Development of Novel Molecular Imaging Contrast Agents for Detection of Oxidative Stress

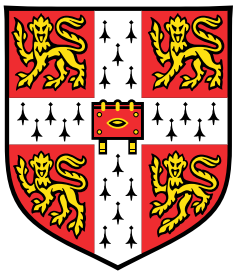

Judith Weber

Supervisors: Dr. Sarah E. Bohndiek

Cancer Research UK Cambridge Institute
University of Cambridge

This dissertation is submitted for the degree of
Doctor of Philosophy

Lucy Cavendish College December 2018

To the most wonderful family ...

Declaration

This dissertation is the result of my own work and includes nothing which is the outcome of work done in collaboration except as declared in the Preface and specified in the text. It is not substantially the same as any that I have submitted, or, is being concurrently submitted for a degree or diploma or other qualification at the University of Cambridge or any other University or similar institution except as declared in the Preface and specified in the text. I further state that no substantial part of my dissertation has already been submitted, or, is being concurrently submitted for any such degree, diploma or other qualification at the University of Cambridge or any other University or similar institution except as declared in the Preface and specified in the text. This dissertation contains fewer than 60,000 words including appendices, bibliography, footnotes, tables and equations.

Judith Weber
December 2018

Abstract

Name: Judith Weber

Title: *Development of Novel Molecular Imaging Contrast Agents for Detection of Oxidative Stress*

An early and precise diagnosis of disease is a crucial requirement for fast and targeted therapy in the era of precision medicine. Most diseases possess molecular alterations in their early stages, which precede noticeable morphological changes. One important molecular change that contributes to dysfunction in a wide range of pathologies, including cancer and neurological disorders, is an increase in levels of reactive oxygen species (ROS) and associated oxidative damage. Our understanding of how ROS influence disease biology is currently limited by our inability to perform sensitive and specific assessment of ROS levels with high spatial and temporal resolution in living systems. The goal of the research described in this thesis was to overcome the challenge of assessing ROS during disease development in cancer and neurodegenerative disease through the design, synthesis and validation of two classes of novel bifunctional, ROS-sensitive contrast agents.

To shed light on the complex redox biology in cancer, the new method of photoacoustic imaging was exploited. A novel activatable, targeted near-infrared cyanine dye is reported that enables specific detection of pathological levels of hydrogen peroxide, a major and abundant ROS in living organisms. This approach uses photoacoustic and fluorescence imaging in cancerous tissue to evaluate the performance of the new probe under *in vitro* and *in vivo* conditions.

In neurodegeneration, there exists a bidirectional interaction between oxidative stress and protein aggregates. To scrutinise this relationship, both bulk and single-molecule fluorescence imaging methods were used to assess the capability of novel bifunctional fluorescence dyes to localise the presence of the two putative disease-causing species, ROS and protein aggregates, simultaneously under *in vitro* conditions.

The data shown here provides a promising foundation for the systematic design of contrast agents based on small molecule dyes, that possess ideal optical and biological characteristics to study oxidative stress in a broad range of pathological applications with high temporal and spatial resolution.

Acknowledgements

To all the wonderful people that supported, helped and guided me, herewith I would like to thank you to make the work presented in this thesis possible.

First, I would like to thank Dr. Sarah Bohndiek for giving me the opportunity to be part of her great research group and for all her support, guidance, patience and encouragements in every aspect of this PhD; our meetings always gave me new energy and determination. I am also especially grateful to Prof. Chris Hunter and Dr. Steven Lee for all your support, interest, enthusiasm and for helping me in so many different aspects - whether it be through scientific advice, letting me take part in your research projects, providing me work space or integrating me into your lovely groups. To Sarah, Chris and Steven, thanks for teaching me how to be a better scientist. It has been a long but great journey, which I would not have been able to make without your support. A massive thank you also to Prof. Sir Shankar Balasubramanian and his group for letting me be your "squatter" and integrating me in such a loving and caring manner.

Thank you very much also to Cancer Research UK (CRUK), not only for funding my project, but also for providing such a friendly and supportive work environment. Especially I would like to mentioned Ann Kaminski - the most caring, helpful and supportive scientific administrator graduate students can wish for.

I would like to extend my thanks to the core facilities at the CRUK Cambridge Institute, whose experimental support was simply fantastic. Here I would like to acknowledge in particular the Research Instrumentation Core - Jane, Ian and Loraine - regardless of whether my Western Blot did not work, the SPR showed unexpected signals or I needed unusual settings for one of your instruments, you supported me throughout my PhD. Special thanks also to Josh from the PKB core for all the help, patience and great company. I don't know how often I mixed up the sequence or asked you for favours and you still kept on smiling and dealing with me. I would also like to thank the Biological Resource Unit staff for looking after my animals everyday, and particularly Mike for all the IV injections but especially for the psychological support and the amazing company. Further, I would like to acknowledge

the great help I received from the Light Microscopy and Histopathology Core. Heather and Ziqiang, thank you for all your support, effort and patience with me and my dyes. Many thanks also to the long list of technical and administrative staff in the Chemistry department - you all helped to make the chemistry part of my project fun.

A big, big thank you goes to all members of the Bohndiek, Hunter, Lee, Balasubramanian and Klenerman group for the wonderful time and endless support in and outside of science. There are too many of you to list individually but please know that I am simply very happy and grateful to have met so many amazing people. Specifically, thank you to Lisa-Maria for being the best collaborator that one can wish for; to Ana - you are my power woman! I don't know where you get your endless energy, motivation, helpfulness and happiness from but I admire you for all of these. Thank you so much for your invaluable help and expertise regarding LCMS/MS; to Laura and Giulia for being the most wonderful and caring "lab-mums", without whom the lab would have been a total chaos; to Marco for sustained chemistry support and guidance; to Juan for being an amazing teacher and showing me the beauty of microscopy; to Maria for all your help with the MS, your smile and positivity; to Isa for all the maravilloso time we had together in and outside the CI and all the biological advice; to Abby for the great running company and your advice on how not to become crazy while writing the thesis; to Elena for all your advice on titrations and general life guidance; to Jo for helping in any possible way; to Michal for being always there when I needed your scientific advice and all the fun we had together; to Ben for all the help with LaTeX and being my saviour in the physic lab.

The last 4 years (and all the years before) would have not been able without my wonderful friends. Firstly, Sarah - you are my best friend and a light in my life. Thank you for always being there for me, listening to everything I am waffling on about and for being so understandable if you did not hear from me for weeks. Sophia, my soul sister and superwoman, there is not a way to express what it meant to me having had you by my side over the last 2 years. I thank you so much for your open ears, the epic sport sessions, sticking with me when I am at my worst and helping me to get better through constant chips and coffee supply. Thi, Karen, Vicki, Robyn, Vasja, Nora, Maryanne, Siri, Betty and Ammar, I am extremely grateful for having you as my close friends here in Cambridge, who supported and entertained me throughout this phase of my life. For nearly 30 years of friendship, lots of patience and understanding and always open ears, I would like to thank Lisa, Steffi and Jessi. You are

bringing endless joy to my life.

Finally and most importantly, I thank my wonderful family. There are not enough words or ways to describe how grateful I am for you - Mama, Papa, Hendrik, Lukas, Oma, Opa, Peter and my love Mathias. Only with you by my side, I got where I am now in my life. You have always supported my dreams and have given everything to make them possible. I owe you so much and it would have not been able to accomplish this without you. I could have not asked for a better family and therefore I dedicate this thesis to you.

Publications

Judith Weber[*], Lisa-Maria Needham[*], Juan Varela, James W. B. Fyfe, Omaru M. Kabia, Dung T.Do, Chatherine Xu, Christopher A. Hunter, Christopher M. Dobson, David Klenerman, Sarah E. Bohndiek[⋆], Thomas N. Snaddon[⋆] and Steven F. Lee[⋆]. "ThX – A next-generation probe for the early detection of amyloid aggregates." In revision.

Judith Weber, Laura Bollepalli, Ana Belenguer, Marco Di Antonio, Nicola De Mitri, James Joseph, Shankar Balasubramanian, Christopher A. Hunter and Sarah E. Bohndiek[⋆]. "An activatable, bifunctional probe for photoacoustic and fluorescence imaging to probe oxidative stress in cancer." In revision.

Lisa-Maria Needham[*], **Judith Weber**[*], James W. B. Fyfe, Omaru M. Kabia, Dung T.Do, Ewa Klimont, Yu Zhang, Margarida Rodrigues, Christopher M. Dobson, Sonia Ghandi, Sarah E. Bohndiek[⋆], Thomas N. Snaddon[⋆] and Steven F. Lee[⋆]. "Bifunctional fluorescent probes for detection of amyloid aggregates and reactive oxygen species." *R. Soc. Open Sci.* 5 (2018): 171399.
https://doi.org/10.1098/rsos.171399

James Joseph, Kevin N. Baumann, Philipp Koehler, Tim J. Zuehlsdorff, Daniel J. Cole, **Judith Weber**, Sarah E. Bohndiek[⋆] and Silvia Hernández-Ainsa[⋆]."Distance dependent photoacoustics revealed through DNA nanostructures." *Nanoscale* 9(42), 16193-16199 (2017).
https://doi.org/10.1039/c7nr05353c

James Joseph, Michal R. Tomaszewski, Isabel Quiros-Gonzalez, **Judith Weber**, Joanna Brunker, and Sarah E. Bohndiek[⋆]. "Evaluation of Precision in Optoacoustic Tomography for Preclinical Imaging in Living Subjects." *J. Nuc. Med.* 58(5), 807-814 (2017).
https://doi.org/10.2967/jnumed.116.182311

Judith Weber, Paul C. Beard and Sarah E. Bohndiek*. "Contrast agents for molecular photoacoustic imaging." *Nature Methods* 13(8), 639-650 (2016).
http://dx.doi.org/10.1038/nmeth.3929

* These authors contributed equally to this work

* Co-corresponding authors

Contents

List of Figures

List of Tables

List of Abbreviations

αSyn	α-Synuclein
Aβ	Amyloid-beta
BODIPY	Boron-DIPYrromethene
CSF	Cerebrospinal Fluid
BSA	Bovine Serum Albumin
MeCN	Acetonitrile
1,2-DCB	1,2-Dichlorobenzene
DCFH-DA	DiChlorodiHydroFluorescein DiAcetate
DCM	Dichlormethan
DFT	Density Functional Theory
DIPEA	Diisopropylethylamine
DMAP	4-(Dimethylamino)-pyridine
DMF	N,N-Dimethylformamide
DMSO	Dimthyl sulfoxide
EDCI	1-Ethyl-3-(3-dimethylaminopropyl)carbodiimide
ELISA	Enzyme-Linked Immunosorbent Assay
eNOS	endothelial Nitric Oxide Synthase
EtOH	Ethanol
FBS	Fetal Bovine Serum
FRET	Foerster Resonance Energy Transfer
FT-IR	Fourier Transform Infrared Spectroscopy
GFP	Green Fluorescent Protein
GPx	Glutathione Peroxidase
GSH	Glutathione
GSSG	Glutathione Disulfide
HOMO	Highest Occupied Molecular Orbital
ICG	Indocyanine green
ICT	Intramolecular Charge Transfer

IS	Internal Standard
ISC	Inter-System Crossing
HCC	Heptamethine carbocyanine
HIF-1α	Hypoxia-Inducible Factor 1-alpha
LCMS	Liquid Chromatography - Mass Spectroscopy
LC-MS/MS	Liquid Chromatography Tandem Mass Spectrometry
LE	Locally Excited
MeOH	Methanol
MI	Molecular Imaging
MPO	Myeloperoxidases
MRI	Magnet Resonance Imaging
MSOT	Multispectral Optoacoustic Imaging
MTT	3-(4,5-dimethylthiazol-2-yl)-2,5-diphenyltetrazolium bromide
NADP(H)	Nicotinamide Adenine Dinucleotide Phosphate
$NaHCO_3$	Sodium Hydrogencarbonate
NaOH	Sodium Hydroxide
NB	Nitrobenzene
2-NBDG	2-(N-(7-Nitrobenz-2-oxa-1,3-diazol-4-yl)Amino)-2-Deoxyglucose
NF-κB	Nuclear Factor kappa-light-chain-enhancer of activated B cells
NIR	Near Infrared
NMR	Nuclear Magnetic Resonance
Nrf2	Nuclear Factor (erythroid-derived 2)-like 2
OD	optical density
PA	Photoacoutsic
PAINT	Point Accumulation for Imaging in Nanoscale Topography
PAI	Photoacoutsic Imaging
PALM	PhotoActivated Localisation Microscopy
PBS	Phosphate Buffered Saline
PEG	Poly(ethylenglycol)
PET	Photoinduced Electron Transfer
PiB	Pittsburgh B
PPAR	Peroxisome Proliferator-Activated Receptor
Prx	Peroxiredoxin
QM	Quinone Methide
QC	Quality Control sample
ROS	Reactive Oxygen Species
(RP)-HPLC	(Reversed Phase) High Pressure Liquid Chromatography

SAVE	Single Aggregate Visualisation by Enhancement
SPR	Surface Plasmon Resonance
STED	STimulated Emission Depletion
STORM	STochastic Optical Reconstruction Microscopy
^{t}Bu	*tert*-Butyl
TEA	Triethylamine
TFA	Trifluoroacetic Acid
TLC	Thinlayer Chromatography
THF	Tetrahydrofuran
ThT	Thioflavin-T
TICT	Twisted Intramolecular Charge Transfer
TIRF	Total-Internal Reflection Fluorescence
TPA	12-O-tetradecanoylphorbol-13-acetat
UV	ultraviolet

Chapter 1

Introduction

This chapter uses material from the review titled: "Contrast agents for molecular photoacoustic imaging",[1] listed in the publication section.

Reactive oxygen species (ROS) are endogenously produced oxidising agents important in essential biological processes. However, increased levels of ROS are critical biological parameters and contribute to dysfunction in a wide range of pathologies, including various types of cancer and neurological disorders (Figure 1.1).

In this context, different approaches have been reported to assess ROS levels but methods with the potential to monitor specific ROS with high spatial and temporal resolution under biological relevant conditions are limited. Potential new methods of cellular analysis are emerging including "activatable" imaging probes, photoacoustic (PA) imaging as well as high resolution microscopy. This thesis examines the properties of these emerging methods including the development of new imaging probes for sensing specific ROS, the compilation of experimental and analytical protocols for PA imaging and high resolution microscopy and the evaluation of the capability of the new imaging probes combined with these imaging techniques to detect ROS under important biological conditions.

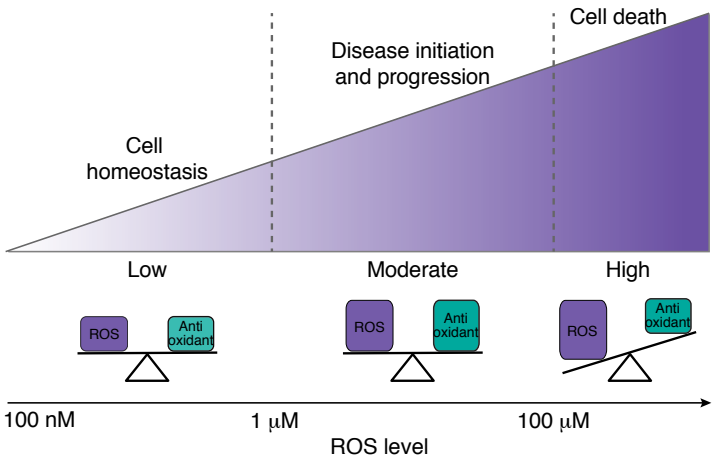

Figure 1.1 Levels of cellular ROS and their differential effects on cells: A low, balanced level of ROS is essential for cell survival and homoeostasis; increased, but balanced levels of ROS can induce oxidative modifications supporting disease initiation and progression; high, unbalanced levels of ROS induces cellular damage and cell death.

1.1 Oxidative Stress and Diseases

1.1.1 Oxidative Stress and Reactive Oxygen Species

Oxygen is crucial for life; the air we breath enables the cells in our body to meet their energy demands. In its molecular form, the role of oxygen in survival is associated with its high redox potential, which allows oxygen to act as electron acceptor during mitochondrial adenosine triphosphate (ATP) synthesis and in enzymatic reactions. During these controlled physiological redox processes, O_2 is mainly converted into H_2O. However, the use of molecular oxygen bears risks. By accepting electrons, it can form highly reactive oxygen species (ROS), including: hydrogen peroxide (H_2O_2); superoxide anion radical ($O_2^{\cdot -}$); hydroxyl radical ($HO^{\cdot}$); and hypochlorous acid (HOCl) (Figure 1.2). Each of these molecules has unique reaction properties (pathway, kinetics, rate), distinctive spatial and temporal distribution and separately regulated production, diffusion and degradation processes [2].

Based on their high reactivity, ROS can induce DNA mutations and damage, activate signal transduction cascades and induce alterations in lipids, proteins and transcription factors. As a consequence, ROS significantly influence the expression of over 500 genes, regulating cell differentiation, cell proliferation and inflammatory responses [3]. Therefore, oxidative stress and increased levels of ROS have long been linked to ageing and the pathogenesis of various diseases, including cancer and neurodegenerations [4, 5].

Counter-intuitively, low levels of ROS have important roles as regulatory molecules in a broad range of important subcellular processes, such as cell signalling, enzyme activation, gene expression, apoptosis, and immune response [6].

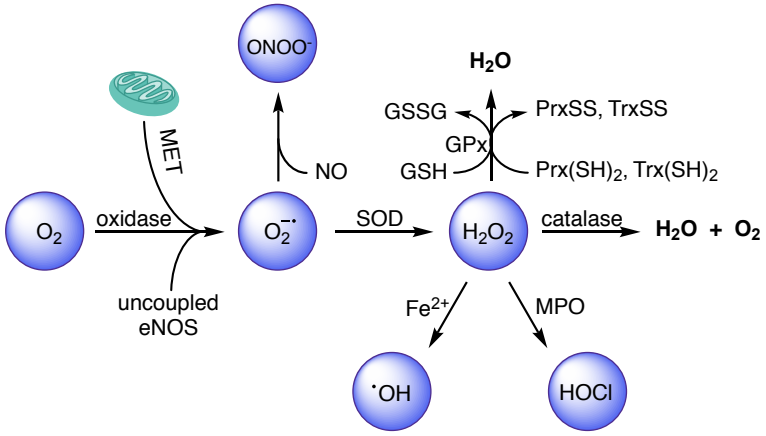

Figure 1.2 Genesis of the major ROS and their detoxification by antioxidants. $O_2^{\cdot -}$ is generated by reduction of molecular oxygen through NADPH/xanthine oxidases, uncoupled endothelial nitric oxid synthase (eNOS) and mitochondrial electron transport (MET). $O_2^{\cdot -}$ can be dismutated into H_2O_2 by superoxide dismutase (SOD) or react with nitric oxide (NO) to form peroxynitrite ($ONOO^-$). H_2O_2 can either be scavenged to H_2O by catalase, glutathione peroxidase (GPx) or peroxiredoxin (Prx) antioxidant enzymes that use thioredoxin (Trx). At inflammatory sites H_2O_2 gets mostly converted into HOCl by myeloperoxidases (MPO). In presence of Fe^{2+} Fenton's reaction leads to the generation of $\cdot OH$ [7].

The major source of cellular ROS are mitochondria, which are double membraned organelles in eukaryotic cells. In general, mitochondria provide energy through the oxidation of glucose, lipids and amino acids. The electrons resulting from the oxidation process are channelled to oxygen as a terminal electron acceptor. In the electron-transport chain, small numbers of electrons escape from the intended pathway and mis-timed interaction with O_2 leads to ROS generation. In addition, other enzymatic (e.g. NADPH-, xanthine-, monoamine-oxidase, cytochrome P450 system) and non-enzymatic reactions (e.g. reactions of oxygen with organic compounds, ionising radiations) can lead to the generation of ROS (Figure 1.2). ROS can also arise from exogenous sources, either being taken up from the extracellular milieu (e.g. ROS released by inflammatory cells), or produced as a consequence of the exposure to environmental pro-oxidants (e.g. pathogens, toxicants, stress) [8].

To prevent cells being damaged by ROS generation, cells have evolved different detoxification mechanisms (Figure 1.2). Such "antioxidants" may be enzymatic (e.g., glutathione peroxidase/reductase, catalase and superoxide dismutase) as well as non-enzymatic (e.g., glutathione (GSH), coenzyme Q and Vitamin A/C/D/E). Cells aim to keep a balanced state

between antioxidants and ROS; an imbalance between the production of ROS and their scavengers is termed oxidative stress and is an early fundamental event in the pathogenesis of several disorders, including cancer and degenerative neurological diseases (Figure 1.1) [7].

1.1.2 Oxidative Stress and Cancer

Cancer is a complex multi-stage process that includes a wide range of cellular and molecular changes mediated by diverse endogenous and exogenous stimuli. Tumourigenesis can be divided into initiation, promotion and progression. ROS are involved at all three stages.

In the initiation stage, oxidation of nucleic acids can produce DNA damages leading to mutations in key genes promoting oncogenic transformation. Common forms of DNA modification linked to genetic mutations and alternation of gene transcription, are formation of hydroxylated bases, sugar lesions, DNA-strand breaks and DNA-protein crosslinks.

During cancer promotion ROS modulate the expression of many genes ultimately supporting tumorigenesis. One of the pathways involved is the hypoxia-response pathway. In this pathway, ROS stabilises the hypoxia inducible factor HIFα, which in turn activates a transcriptional network of genes that help tumour cells to adapt to hypoxic conditions by increasing glycolysis and activating angiogenesis [4, 9].

In the progression stage, ROS can be involved in tumour cell survival, proliferation, migration and angiogenesis [3]. This can be conducted for example by the phosphoinositide 3-kinase (PI3K) pathway, the activity of which being promoted by ROS. PI3K is a critical growth factor response pathway and has been shown to increase tumour proliferation, survival and mobility [10].

Additionally, cancer cells often induce an inflammatory response. Inflammatory processes are characterised by the infiltration of leukocytes, which can release ROS to activate signal transduction cascades subsequently contributing to the elimination of pathogens and the recruitment of additional inflammatory cells. As a result, a sustained inflammatory and oxidative microenvironment emerges. The prolonged exposure to inflammatory related molecules can inflict continuous tissue damage, cell proliferation and enrichment of ROS leading to a protumorigenic environment [11, 7]. Furthermore, the infiltrated, inflammatory cells can protect cancer cells from host immune response as well as support tumour growth (via angiogenic processes for instance), invasion and metastasis [7, 12]. However, the interplay between the different developmental stages of cancer, ROS and inflammation and their cause-correlation relationship remains poorly understood.

1.1.3 Oxidative Stress and Neurodegenerative Disease

Even though, the brain accounts only for ∼2% of our body weight, it consumes more than 20% of the oxygen. Brain cells are divided in two main groups: neurons and glial cells among which are astrocytes. With the exception of a few brain regions, neurons are mostly non-dividing cells with a long life span. Due to the high oxygen consumption and long cell life span, the human brain is particularly prone to the effect of oxidative stress and requires effective antioxidant protection.

ROS production in the brain occurs largely by NADPH oxidase and mitochondria. The activation of the intracellular enzyme NADPH oxidase results in the transfer of protons across the mitochondrial membrane and is accompanied with the generation of large quantities of superoxide [13]. The involvement of NADPH oxidase in oxidative stress generation has been shown in several ways for Parkinson's (PD) and Alzheimer's (AD) diseases. Mitochondrial pathology is evident in many neurodegenerative disorders, including PD and AD. A number of PD related genes (PINK1, DJ-1, Parkin) have been linked to mitochondrial dysfunction with the result of increased levels of ROS [14]. Also, impaired activation of mitochondrial complexes have been shown to influence the redox state in the pathogenesis of AD.

ROS contribute to the development of neurodegeneration by modulating the function of several biomolecules. Highly discussed in the context of neurological disorders are modifications of mitochondrial DNA and proteins. Both possess a bidirectional interaction with oxidative stress. ROS can cause strand breaks, base modifications and DNA-protein crosslinking in (mitochondrial) DNA. These mitochondrial DNA alterations can then lead to respiratory chain dysfunction, reduced ATP production, calcium dysregulation and mitochondrial permeability. All of these have the potential to further increase the ROS generation. Proteins are modified by ROS through the oxidation of both the backbone and side chains which in turn react with other molecules or amino acid side chains. This often results in nonfunctional protein adducts and misfolded proteins. Misfolded proteins are often prone to aggregation, which is a hallmark of many neurodegenerative diseases. These protein aggregates have been shown to increase ROS production by impairing mitochondrial activity, deregulating calcium homeostasis, causing neuro-inflammation and directly activating NADPH oxidase [13, 14]. Neurons with long axons and multiple synapses possess increased energy consumption and their function depends on different ions and a tightly regulated electric potential. This makes these groups of neurons especially vulnerable to additional disease-related oxidative stress, which often leads to impaired synaptic transmission and nonfunctional neurons.

Overall, many processes have been associated with the development of neurological disorders: non- or dysfunctional neurons, protein misfolding and aggregation, perturbed calcium homeostasis, neuro-inflammation and mitochondrial dysfunction. All of these processes can either be a result or a cause of oxidative stress. Even though there are many examples suggesting the importance of oxidative stress in the pathogenesis of neurodegenerations, it remains unknown how critical its impact is and whether it is a primary cause or consequence of the disease.

1.2 Imaging Oxidative Stress and Contributors

Given the high importance of oxidative stress in physiological and pathological processes, many attempts to image ROS and antioxidant species have been reported, each approach aiming to assess the significance of reactive oxygen species and oxidative damage in biological systems.

1.2.1 Requirements for Detection of Oxidative Stress in Disease

A key characteristic of redox signalling is the generation of specific redox species at specific times in specific locations. Cells harbour several interlinked antioxidant systems, including glutathione and thioredoxin (Fig. 1.2), which are subject to independent regulation and respond rapidly to endogenous and exogenous stimuli [15]. Also, ROS production occurs in different, independent ways either enzymatically or through non-enzymatic reactions (cf. section 1.1.1). As the redox reactions are kinetically and sterically separated, thermodynamic equilibriation between the different species does not occur on biologically relevant time scales. This results in a tight temporal and spatial confinement of the different redox reactions and molecules. Thus, to gain a deeper understanding about the function and impact of redox signalling under physiological and pathological conditions, it is crucial to measure a specific redox species at a defined location and time as opposed to assessing the overall redox state. This scenario is technically challenging and the results are often difficult to interpret and prone to artefacts due to the high heterogeneity, reactivity and short half life of ROS.

An ideal redox sensor should be able to monitor dynamic changes of a specific, clearly defined redox molecule with high sensitivity. Furthermore, the signal generated by the sensor should be selective to the specific redox change (no cross-reactivity) and clearly distinguishable from the background signal. To detect an unaffected redox state, the redox

sensor must also be non-disruptive but able to accumulate at the (subcellular) location of interest.

In addition to specific ROS probes, a suitable detection method is needed. Important demands upon the method are high temporal and spatial resolution and, depending on the biological question being asked, sufficient depth penetration for *in vivo* imaging. In addition, it is important that the measurement does not influence the redox states themselves.

1.2.2 Current Methods for the Detection of ROS

In general, there are two approaches to assess ROS: Either detecting the damage caused by the ROS or directly "trapping" or converting a particular ROS and measuring the quantity of the generated molecule.

Ex vivo and *in vitro* Methods

Many conventional approaches are based on measuring the unique chemical fingerprint of ROS such as oxidative DNA damage (e.g. 7,8-dihydro-8-oxo-guanosine), lipid oxidation (e.g. oxidised low-density lipoprotein) and protein oxidation (e.g. protein carbonyls) products [16]. These markers have been studied in different diseases but their specificity is often questionable both with the regard to the biomarker molecule as well as the analytic method (ELISA, HPLC, LC-MS, MS). Furthermore, these methods disrupt the cellular integrity, do not allow detection in a spatial or temporal manner, often suffer poor chemical resolution (in respect to the ROS species) and are subject to fluctuations due to the balance between oxidative damage and removal of the oxidised products [17]. Thus, the results obtained by these indirect measurements of oxidative stress need to be assessed with caution as changes in the clearance of the biomarker can dramatically alter its level with no change in the production of a given ROS [2]. Additionally, ROS can act as regulatory molecules without causing oxidative damage, which will be undetected by these measurements and thus does not allow examination of the physiological roles of ROS.

Another widely used method for ROS sensing *in vitro*, in biofluids or tissue samples are fluorescence dyes such as hydroethidium ($O_2^{\cdot -}$ sensing), dichlorodihydrofluorescein diacetate (DCFH-DA) (ROS sensing) and boronate-based fluorescent probes (H_2O_2 sensing) [18–20]. However, most of these probes are prone to side reactions and a range of associated artefacts, lack of specificity, are unstable or influence the redox state (e.g. calcein, MitoTracker Red) [21, 22, 18, 17]. For instance, although DCFH-DA is often described as a method to measure H_2O_2, it does not react directly with H_2O_2 and requires a peroxidase or transition metal

catalyst. The generated signal depends also on the cellular uptake of DCFH-DA. Additionally, the relationship between ROS concentration and DCFH signal is not linear, DCFH is prone to photo-sensitisation and can promote superoxide production [23, 24]. Hence, there are various factors which affect the signal without changes in ROS.

The use of boronate-based sensors has greatly improved the selectivity of fluorescence dyes for ROS sensing. The boronate functionality enables not only the selective detection of hydrogen peroxide changes at concentrations relevant to oxidative stress but also has been recently refined to detect signalling levels of ROS. In addition, their targeting to specific organelles such as mitochondria allows localisation specific sensing [25, 19]. However, these boronate-based dyes show an optical absorption maximum below 600 nm and thus have a high background signal due to blood absorption and limited potential for *in vivo* optical imaging due to the poor depth penetration (typically less than 2 - 3 mm).

In vivo Methods

An important contribution to the detection of redox species has been the development of genetically encoded redox probes. These probes react selectively and sensitively with a particular ROS, which triggers changes in fluorescence. For example, the redox-sensitive green fluorescent protein (roGFP) enables ratiometric measurement sensitive to the glutathione redox potential on the basis of disulphide formation between two cysteine residues [26]. The disulphide formation facilitates protonation of the chromophore, which induces a change in the absorption spectrum. To ensure a rapid adaptation to the redox state, roGFP was further covalently fused to specific redox enzymes [27]. Also, Foerster resonance energy transfer (FRET)-based probes have been evaluated, in which a redox sensitive peptide linker connects two fluorescent proteins (ECFP and EYFP) [28]. The use of genetically encoded fluorescence proteins enables targeted, transient and reversible live cell imaging and hence the comparison of levels of a specific ROS in response to different stimuli at particular intracellular location, which enables reporting of the localised redox changes within the cell. However, these approaches require adequate cellular expression of the probe and the use of transgenic animals for *in vivo* imaging. Furthermore, the sensitivity of some genetically encoded redox probes depends on the environment and their dynamic response is decreased compared to the dynamic range of small molecule fluorescence probes [29, 2]. Additionally, excitation and emission often occurs below 600 nm limiting *in vivo* applications due to poor penetration depth.

Alternatively, it is possible to employ a boronated caged [^{18}F]Fluorodeoxy thymidine-1 (PC-[^{18}F]FLT) tracer for H_2O_2 detection with positron emission tomography [30]. PC-

[^{18}F]FLT reacts with H_2O_2 to form [^{18}F]FLT, which allows uptake and retention in proliferating cells. This approach is still in an early stage but shows promising results for non-invasive *in vivo* imaging of H_2O_2 with sufficient penetration depth for clinical applications. However, positron emission tomography requires radioactivity, has limited spatial resolution and needs co-registration with another modality such as X-ray computed tomography for anatomical information. This results in a restricted report on the localised redox changes within an organ/cell and the exposure to ionising radiation can affect the the redox state.

Lastly, promising *in vivo* approaches use electron paramagnetic resonance (EPR) and/or (hyperpolarised) magnetic resonance ((HP) MR) contrast [31, 32]. EPR is able to detect unpaired electrons and thus can sense free radicals directly. For example, the contrast provided by paramagnetic nitroxides can assess the redox state. Nitroxides are antioxidants and their rate of reduction has been shown to correlate with cellular partial pressure of oxygen in tumours and brain tissue [31]. However, the contrast achieved by EPR is relatively weak resulting in low sensitivity, the species generating the contrast are often rapidly removed through enzymatic metabolism or reaction with biomolecules and the interaction with antioxidant systems in tissue is poorly characterised. Also, the accessibility of the required specialised instrumentation is limiting their broad application, especially for HP MR imaging.

Overall, the lack of tools for measuring defined redox species together with the uncertainty of interpretation of the data has been a profound limitation for fundamental research in redox biology as well as clinical studies. Most approaches disrupt cellular integrity, influence the redox state themselves, lack specificity and/or spatiotemporal resolution or have limited potential for *in vivo* imaging. Thus, there is a great demand for new approaches that allow the specific detection and quantification of different types of ROS in biological systems, particularly *in vivo* and biofluids.

1.3 Novel Imaging Approaches for the Detection of ROS

In order to understand the biological and pathological impact of ROS, it is important to reveal the nature of the particular ROS in the biological context. Therefore, molecular imaging (MI) techniques are needed that allow the sensitive detection and quantification of a specific ROS at a defined region of interest within the biological environment with high spatiotemporal resolution.

MI uses specialised instrumentation combined with specific molecular markers to visualise and quantify complex biochemical processes present in normal and pathological states

[33, 34]. Data obtained from MI has revolutionised the biomedical understanding of biochemical reactions at a nanoscale level providing insight into mechanisms of pathologies and therapy response. Imaging of molecular processes is performed in several ways and encompasses a broad area of research. In this section, contrast agents used for MI and two important methods, photoacoustic (PA) imaging and single molecule microscopy, will be described and their applicability for imaging ROS will be highlighted.

1.3.1 General Considerations for Contrast Agents for Molecular Imaging

The main goal of MI is to characterise and quantify pathological and physiological processes at the cellular and molecular level in a non-invasive way. To realise this, it is necessary to use finely tuned contrast agents specific for the targeted molecular and biochemical process. The key road blocks to the development of such contrast agents include: physiological delivery barriers (such as the hematoencephalic barrier); suboptimal tissue perfusion (in case of *in vivo* imaging); interactions with molecules in the biological environment (such as protein binding); rapid elimination or biodegradation; imaging instability; and unwanted off-target binding (Figure 1.3).

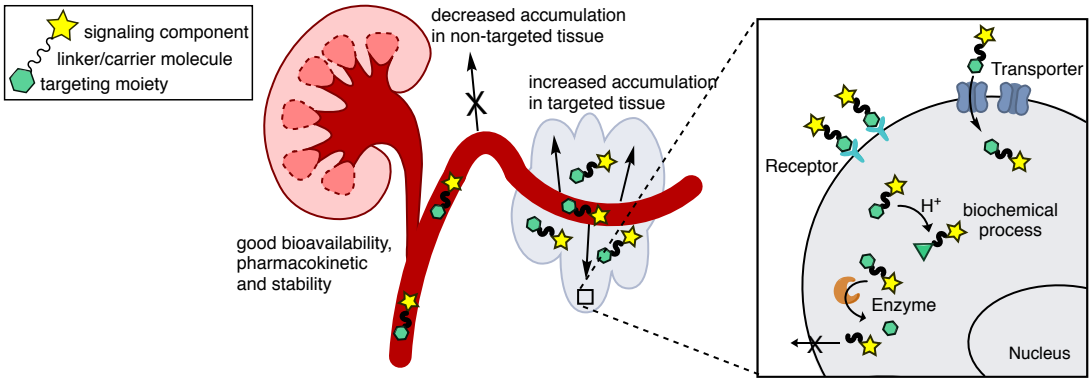

Figure 1.3 Illustration of the complexity of criteria which have to be accomplished by contrast agents for molecular imaging.

The basic principles for overcoming these limitations and improving the biological properties of the contrast agent are:

1. Targeting: The incorporation of functional groups to target the accumulation of the probe in the region of interest.

2. Structural modifications: Variations in size, shape and chemical structure can help to improve interaction with constituents in the biological environment, *in vivo* and imaging stability, pharmacokinetics and rapid elimination.

Taking the above considerations into account, a contrast agent for MI should comprise a signalling compound generating the signal during the imaging session and a targeting moiety restricting the signal to the targeted biological entity or process.

Active Targeting

Most MI agents are actively targeted to cell surface receptors [35], transporters [36], metabolic enzymes [37], biochemical processes [38] or pathogenic species [39] (Figure 1.3). These targets should ideally be (over)expressed at a very early stage of the disease as well as sensitive and specific to biochemical changes. Current structures that can be used to achieve active targeting include small molecules [40], peptides and adhirons [41], affibodies [42], aptamers [43] and proteins [44]. While choosing the targeting structure, particular consideration must be given to biocompatibility (minimising toxicity), interactions with biological compounds (effect on imaging signal, triggering immune response), as well as optimising elimination (from circulatory system and off-target sites) and target tissue penetration.

Using small molecules for targeting maintains the benefits that they can pass physiological barriers easily due to their small size ($<$1 nm). These molecules also clear rapidly through the kidneys, which optimises biocompatibility and reduces off-target accumulation. However, their biochemical properties are prone to changes when coupled to signalling compounds. Peptides are relatively small targeting units and the development of solid-phase peptide synthesis and phage display libraries allows a fast, cheap and efficient synthesis and selection of peptides with high specificity and sensitivity [45]. In general, they show no significant immunogenicity and their biological half-life/metabolic stability can be controlled by cyclisation, insertion of D-amino acids or amino acid mimics and modifications of the amide bond (e.g. N-methylation, reduction). Proteins (especially monoclonal antibodies and their fragments) show high target affinity and specificity, and thus display little cross-reactivity with healthy tissues [44]. Their generation is more difficult, time-consuming and expensive than peptide synthesis and the larger size also results in poorer tissue penetration and clearance, which can cause low signal-to-background ratios. Also, immunogenicity can be a limiting criterion for their use. Antibody fragments such as diabodies and affibodies

solve a few of these limitations, since they are smaller in size but retain high affinity and selectivity [42, 44].

Passive Targeting: EPR Effect

The "enhanced permeability and retention" (EPR) effect is special for cancer imaging and mainly relies on the hyperpermeability of tumour vasculature combined with the lack of an intact lymphatic drainage. This allows the accumulation of macromolecules (10 - 100 nm) inside a tumour; larger entities ($>$ 100 nm) are in general not accumulated and will be cleared through the reticuloendothelial system [46, 47]. Small molecules also diffuse into the tumour tissue but do not accumulate. The EPR effect may exist in various solid tumours, but differs between tumour types and patients depending on the tumour characteristics. The tumour passive accumulation is influenced by inefficient orientation of microvessels in the tumour [48] leading to low delivery of macromolecules and increased interstitial pressure reducing extravasation of macromolecules [49]. Even though some authors have found enhanced accumulation and retention of nanostructures without targeting ligands in tumours for longer than 24 h [50, 51], passive targeting should be avoided as far as possible as uptake is not specific to a biological process.

Activatable Contrast Agents

Activatable contrast agents are able to elicit a signal change upon binding or interaction with their biological target. This reduces the background signal and thus improves quantification and offers the potential for high sensitivity of detection. Additionally, activatable contrast agents increase the range of possible targets and allow dynamic, real-time studies of biological processes such as enzymatic activity, pH sensing or the detection of ROS. Although it is challenging to develop systems that respond to molecules, which are often present in concentrations less than nanomolar, several examples across different MI methods have shown promise.

One class of activatable contrast agents with considerable promise for fluorescence imaging of H_2O_2 are dyes masked with boronic esters (e.g. MitoPY1 [25], Sulfo-QCy7 [52], PF1/PR1 [19]). These sensors react directly and selectively with low levels of H_2O_2 releasing the bright fluorophore and thus allowing to detect H_2O_2 by a turn-on fluorescence enhancement. Similarly, the combination of a fluorescent protein with the hydrogen peroxide–sensitive domain of the transcription factor OxyR resulted in a genetically encoded, activatable redox probe. In the presence of H_2O_2 a dithiol group is oxidised, which triggers a

conformational change releasing the fluorescent protein [53]. Even though these fluorescent probes show encouraging results, most of them are not targeted to a certain pathophysiological location and fluorescence imaging has only limited application for *in vivo* imaging. In MR imaging, one approach to generate a redox-sensitive, activatable contrast agent involves the change in oxidation state of a free radical or a metal ion of the contrast agent. The reduction of the radical or metal ion in the presence of ROS leads to a significant increase in the T_1 relaxation time constant, allowing the non-activated and activated probe to be distinguished [53].

1.3.2 Photoacoustic Imaging

Given the importance of oxidative stress highlighted in section 1.1, the ability to image specific ROS levels *in vivo* would provide powerful insight to the relevance of ROS for physiological and pathological processes. Several approaches have been developed to tackle this problem, yet all of them suffer from certain limitations, facing different challenges on the way to a high-resolution, quantitative *in vivo* image of a specific ROS.

Photoacoustic (PA) imaging is an emerging hybrid imaging technology which has the potential to fulfil this unmet need. PA imaging combines the high contrast of optical imaging with the high spatial resolution and penetration depth of ultrasound [54]. Tissue heating due to the transient absorption of short laser pulses produces acoustic waves, which can be detected by ultrasound transducers and reconstructed to form an image of the absorbed optical energy distribution. Since sound waves are less scattered in tissue than photons, PA imaging bypasses the traditional limits of optical imaging. This enables non-invasive *in vivo* imaging at depths of several centimetres with a resolution on the order of a few hundred micrometres, scaling to $<100\,\mu$m for shallower (<1 cm) penetration depths [55]. Given that PA imaging is relatively affordable and portable, it has the potential to be rapidly incorporated into clinical routine in surgery rooms as well as for diagnosis at the bedside [56]. All of this combined makes PA imaging one of the fastest-growing molecular imaging techniques that has successfully been adopted for preclinical *in vivo* imaging for a wide range of diseases.

Principles of Photoacoustic Imaging

PA signal generation starts with the absorption of photons from pulsed or modulated continuous-wave light sources by intrinsic or extrinsic molecules (Figure 1.4). Subsequent fast, non-radiative conversion of the absorbed light energy into heat leads to a small temperature rise (on a scale of milli-Kelvin). The origin of this thermalisation depends on the nature

of the chromophore and can be attributed to vibrational and collisional relaxation events for small molecule dyes and intrinsic chromophores, and to electron-photon interactions for metallic nanostructures. As PA imaging uses laser pulses in the nanosecond range, no significant thermal diffusion occurs. The local temperature rise leads to a pressure increase in the irradiated sample section, which relaxes into an ultrasonic wave at MHz frequencies. These ultrasonic waves propagate to the sample surface where they are detected by ultrasound transducers. The detected time-resolved ultrasound signals are then reconstructed to form an image mapping the distribution of the absorbed optical energy. A photoacoustic image contrast is therefore considered to be absorption based.

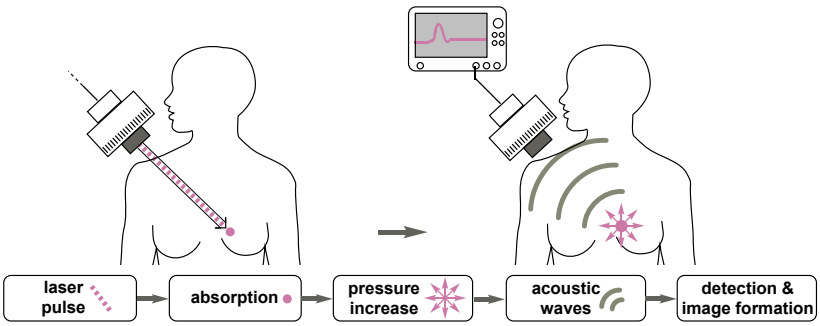

Figure 1.4 Principles of Photoacoustic Imaging.

As the human body possesses its own set of chromophores, PA imaging is able to provide structural and functional information based on these light absorbing molecules (Figure 1.5). The main endogenous chromophores are haemoglobin, lipids, water and melanin.

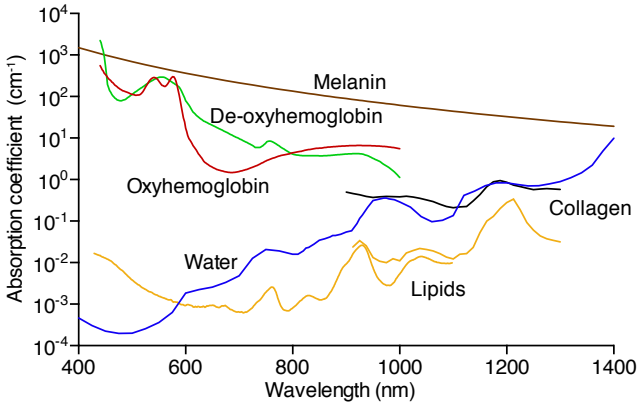

Figure 1.5 Absorption spectra of the main endogenous chromophores: oxyhaemoglobin (red, 150 g/L); deoxyhaemoglobin (green, 150 g/L); water [57] (blue, 80% by volume in tissue); lipids [58] (yellow (20% by volume in tissue); melanin (brown, μ_a corresponds to that in skin); and collagen (black). Data from http://omlc.ogi.edu/spectra/.

A PA image can be formed in several ways [59]. One of the most common configurations is referred to as photoacoustic tomography (PAT). In PAT, a wide-field laser beam with wavelengths in the near-infrared (NIR) range illuminates the sample. As light is scattered in the tissue, a broad area is exposed to the diffused light beam and acoustic signals are generated across this area. The waves, once reaching the surface, are then recorded at low frequencies (few MHz) via multi-element ultrasonic detection. The spatial resolution is in general frequency and thus depth dependent. As PAT aims for deep-tissue imaging with centimetre penetration (up to 6 cm *in vivo*) a submillimetre spatial resolution is reached. To generate the final image, a computer algorithm, typically based on backprojection principles, is used [59]. An important feature of PA imaging is its multi-wavelength data acquisition capability. Recording PA data at multiple wavelengths allows generation of a specific PA spectral profile of the absorbing molecule. This profile can either be generated by following the signal change at the different wavelengths before and after the contrast molecule being present, or through multivariate statistical methods, referred to as "spectral unmixing" (for example, linear regression) [59]. However, spectral unmixing results are strongly dependent on accurate compensation for light fluence and strong (sufficient signal-to-noise ratio), non overlapping spectra. Thus, molecules with broad spectra are often difficult to separate from the systematic noise and their identification *in vivo* is hampered as their spectral profiles often overlap with the biological "background" signal of the haemoglobins.

1.3.3 Photoacoustic Contrast Agents for Molecular Imaging

PA imaging with endogenous contrast can provide structural and functional information through contrast available from hemoglobin, melanin, lipids and water (Figure 1.5). However, oxidative stress and ROS lack sufficient intrinsic contrast and require the introduction of exogenous contrast for MI. As highlighted before, to be used in MI, the contrast agent should consist of a signalling unit and a targeting structure.

Photophysical Properties of PA Contrast Agents

To design an effective contrast agent for PA imaging it is critical to understand the photophysical properties and thermodynamic interactions of the signalling compounds during the signal generation process (cf. section 1.3.2).

The ideal signalling compound for PA imaging should generate a signal that is sufficiently large and distinct relative to the background signal provided by endogenous molecules to allow unambiguous detection. Therefore, a high molar extinction coefficient in the NIR

window (620 - 950 nm) and a sharply peaked, characteristic absorption spectrum are needed. Figure 1.6 shows the specific extinction coefficients and peak absorption wavelengths of the most common contrast agents used in PA imaging.

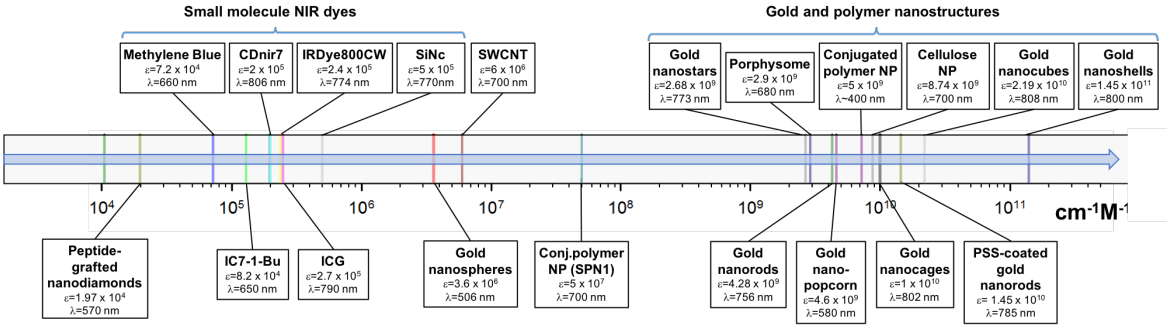

Figure 1.6 Reported extinction coefficients (ε) and peak absorption wavelength (λ) of the most common PA signalling compounds. NP refers to nanoparticle. Values are reported for peptide-grafted nanodiamonds [60], methylene blue [61], IC7-1-Bu [62], CDnir7 [63], IRDye800CW, ICG (http://www.spectra.arizona.edu/), SiNc [64], gold nanospheres [65], SWNTs [66], SPN1 [66], gold nanostars [65], porphysomes [67], GNRs [50], gold nanopopcorn [68], CP NPs [66], cellulose NPs [69], gold nanocages [70], poly(sodium 4-styrenesulfonate) (PSS)-coated GNRs [71], gold nanocubes [72] and gold nanoshells [73].

A high molar extinction coefficient in the NIR range maximises the amount of light absorbed and the penetration depth, as absorption by intrinsic molecules is minimal in this wavelength range (Figure 1.5). To generate a strong PA signal, the signalling compound should also exhibit a good conversion efficiency of the absorbed light energy into pressure. To ensure this, the fluorescence quantum yield should be low to maximise thermalisation. Subsequent transformation of the thermal energy into pressure is characterised by the photoacoustic efficiency, which depends on the absorber and the propagation medium [74]. Additionally, it is important that the contrast agent has good photostability to guarantee that light irradiation throughout the imaging process does not impact the spectral features.

Signalling Compounds for PA imaging

Signalling compounds for PA imaging can be grouped into three broad classes including small-molecule dyes, metallic or semiconducting nanostructures, and organic nanostructures. Figure 1.7 illustrates a schematic overview of the signalling compounds used for PA imaging, including their advantages and disadvantages, and the methodology that enables their targeting for the use in MI. It is important to consider that the targeting ligand and signalling compound should be compatible in terms of their chemical, physical and biological properties.

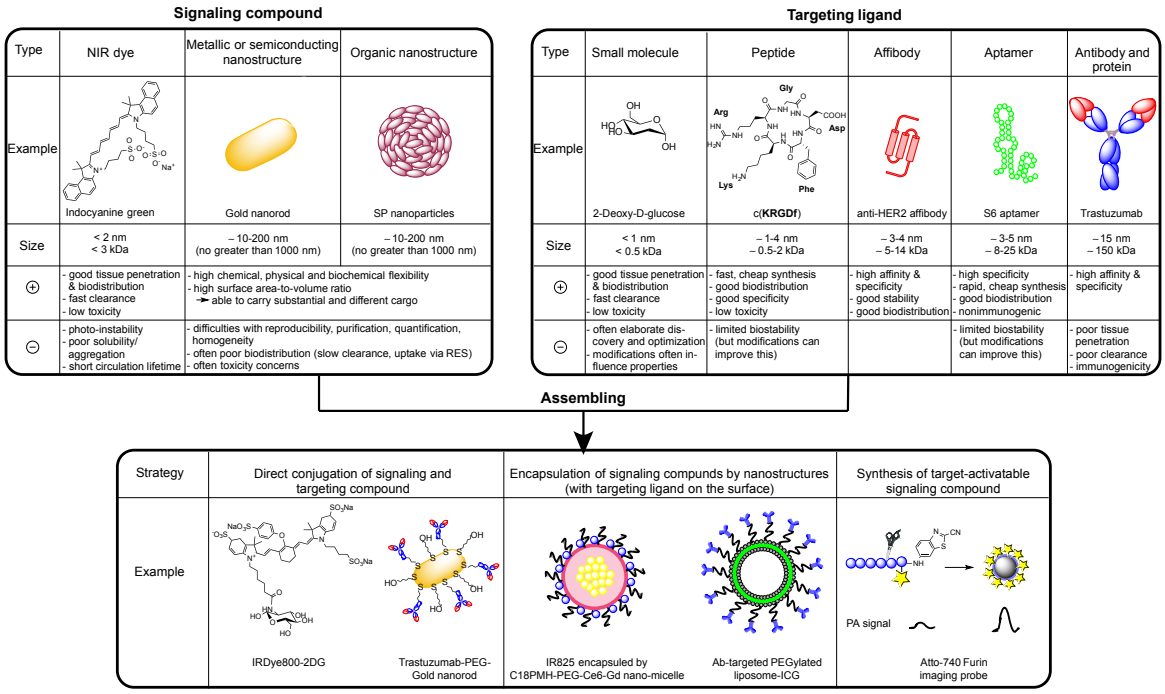

Figure 1.7 Schematic overview of the assembly of molecular imaging contrast agents for PA imaging combining signalling compounds with targeting structures. Examples of each approach are shown and the relative advantages (+) and disadvantages (–) are listed [75, 37, 76–78].

While nanoparticles and organic nanostructures have been applied for the detection of oxidative stress [79, 80, 66], other studies have shown that these species can themselves induce oxidative stress [81]. Therefore, the focus here is directed on contrast agents based on small molecule optical dyes, which are less perturbing to the local biology in the environment that is being imaged.

Small molecule optical dyes are in general good candidates for PA imaging as their small size allows them to easily pass physiological barriers and possess favourable biocompatibility, including good biodistribution, minimal toxicity and immunogenicity as well as minor off-target accumulation. The main classes of dyes used for PA imaging are cyanine dyes, azo dyes, rhodamine dyes and squaraine dyes (Figure 1.8A-D). The chemical basis of these dyes is a series of conjugated double-bonds and/or (mostly aromatic) ring systems. In these π-conjugated structures, the energy gap between the highest occupied energy band (π-band) to the lowest unoccupied energy band (π^*-band) of the molecule is small enough to allow absorption in the NIR range. The wavelength of the absorbed light is defined by π-π^*-energy gap and gives rise to a distinct absorption peak. Relaxation of the excited electrons can occur in radiative (fluorescence or bioluminescence) or non-radiative processes, dependent on the lifetime of the excited states (Figure 1.8E). To obtain a sufficient PA signal, a large

non-radiative relaxation is desired and thus the contribution of fluorescence emission should be minimal (low quantum yield, ϕ_{Fl}).

The challenges associated with the use of small molecule dyes are mostly based on their low molar extinction coefficient ($< 3\mathrm{x}10^5\ \mathrm{M}^{-1}\mathrm{cm}^{-1}$) and limited solubility combined with the tendency to aggregate, bind to proteins and photobleach. However, one of the key features of small molecule dyes is their chemical flexibility. This not only allows some of these limitations to be addressed by attaching hydrophilic groups, introducing triplet-state quenchers [82] and integrating stabilising groups [83] but also enables the spectral properties of the dyes to be tailored through varying the size of the conjugated system and incorporating electron-donating or electron-withdrawing groups. Additionally, the chemical flexibility also facilitates the creation of (redox-) activatable contrast agents, which can in part compensate for their low molar extinction coefficient by minimising the influence of the background signal caused by endogenous molecules.

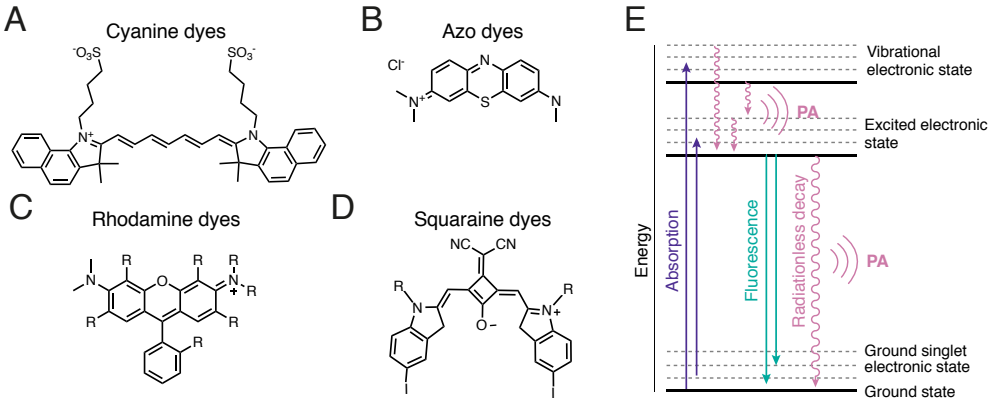

Figure 1.8 Representative structures of the different dye classes used for PA imaging. Molecular structure of A) indocyanine green (ICG) as example for a cyanine dye. Cyanines show photoinduced cis-trans isomerism and transition to triplet states, which leads to low ϕ_{Fl} and thus increased non-radiative relaxation; further they are generally easy to functionalise but possess often poor photostability and their optical properties are highly effected by the environment. B) Methylene blue as example for azo dyes. Limited by absorption in lower NIR range and phototoxicity. C) Rhodamine dye core structure. Rhodamine dyes show intense and sharp absorption peaks and good photostability but are often relatively blue shifted and exhibit high ϕ_{Fl} due to their rigid structure. D) Squarine dye. Squarine dyes possess good photostability but are often limited by insolubility, aggregation and chemical reactivity for modifications. E) Simplified Jablonski diagram showing energetic transitions for an NIR dye after optical excitation.

1.4 Single-Molecule Fluorescence Microscopy

Considering the high spatial and temporal heterogeneity of redox species within a cell, the ability to monitor dynamic changes in specific redox processes with subcellular resolution in the biological environment would enable a shift from inadequate quantification of "cellular redox status" to subcellular measurements, allowing the complex interplay between different redox pathways and major physiological and pathological phenomena to be unmasked.

Fluorescence microscopy is an indispensable tool in biomedical research as it allows biological processes to be imaged on a single-molecule level with a high signal-to-noise ratio while still retaining the key features in the physiological context of native biological samples. By looking at single molecules the ensemble averaging of traditional methods is removed and it is possible to directly measure hidden heterogeneity. Combined with high temporal resolution this reveals fundamental molecular scale processes such as signal transduction [84], DNA replication [84], cell division mechanisms [85] and protein folding.

Principles of Single-Molecule Fluorescence Imaging

Two main techniques for single-molecule fluorescence imaging, which are able to bypass the classical diffraction limit and shift the optical resolution down to molecular levels, include wide-field based single molecular localisation (SML) microscopy and confocal based stimulated emission depletion (STED) microscopy. Both methods are able to resolve structures below 100 nm (Figure 1.9A) and thus allow the direct and localised observation of intracellular redox processes, which cannot be visualised using conventional methods. Hereafter, the focus is placed on SML. A detailed comparison of the two techniques can be found in the literature [86].

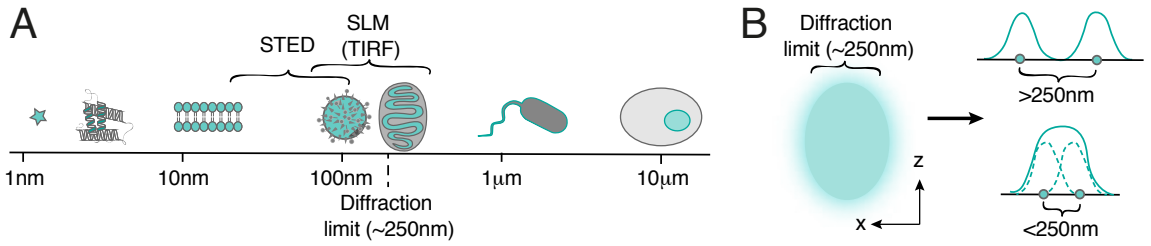

Figure 1.9 Diffraction limited resolution. A) Schematic illustration of the scale of different biological objects and the relative scale of the confinement of SLM and STED. B) Illustration of the blurry focal spot obtained by a high objective lens with a high numerical aperture. The width of this spot defines the diffraction limit, which causes that two fluorophores are not resolved if their distance is below the diffraction limit.

These optical microscopy techniques require the presence of a fluorophore. When imaging the light emitted from the optically active species using the objective of a microscope, the light forms a blurry focal spot instead of a focal point (Figure 1.9B). The scale of this spot depends on the wavelength of the light used and the microscope setup. The intensity profile of this spot is described by the point spread function (PSF). As a result, two fluorophores, which are closer together than the width of the PSF, appear as a single emitter and cannot be separated. This resolution limit is often referred to as the optical diffraction-limit of light and is typically $\sim$250 nm (perpendicular to light propagation) [87]. Many biological processes and structures are smaller than this resolution limit and therefore unresolved by conventional fluorescence microscopy (Figure 1.9B).

Localisation microscopy exploits the knowledge that a PSF is the result of a single point source emitter. Thus, the central position of that emitter can be determined by the use of a Gaussian or a Lorentzian function with an accuracy below the diffraction limit. The precision of the location is thereby determined by the number of photons emitted by a fluorophore, the size of the point spread function, and the background [88]. In order to assume a point source scenario, there must be only a small number of fluorophores emitting at a time as otherwise the fluorescence from these molecules will strongly overlap and the overall image will be blurry. Achieving this by reducing the labelling density does often result in under-sampling accompanied with drastically reduced resolution. Thus, techniques such as STORM (stochastic optical localisation microscopy [89]) and (f)PALM ((fluorescent) photoactivatable localisation microscopy [90, 91]), separate the fluorophore emission in time by ensuring that only one molecule is emitting at a time (Figure 1.10A). Therefore, photoswitchable/photoactivatable fluorophores can be used, which are converted between an "on" state, in which they emit light, and an "off" state, in which they do not emit light, or emit light at different wavelengths.

An alternative SML approach to control the fluorescence emission is PAINT (point accumulation for imaging in nanoscale topography). This method uses freely diffusing dyes or dye-labelled ligands to target molecules of interest [92]. The fluorophores are diffusing in and out of the excitation area and become immobilised when they bind to their target, which then allows localisation. The signal generation and hence their spatiotemporal resolution is not limited by the photophysics of the probe and can be tuned through the rate of interaction between the dye and the target and thus by the affinity of the fluorophore for the biomolecule. Specifically, DNA-based PAINT (DNA-PAINT) has been identified as a promising approach since it adds the specificity and programmability of DNA nanotechnology, which allows spectrally unlimited multiplexing capabilities (Figure 1.10B).

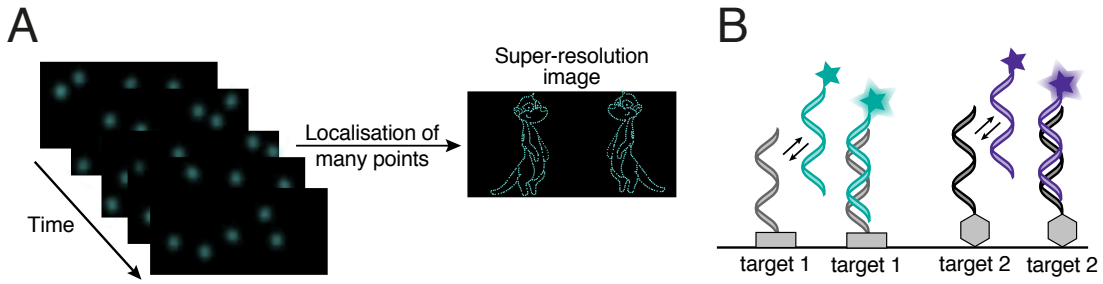

Figure 1.10 Schematic illustration of approaches for SML microscopy. A) SML takes advantage of photoswitching of fluorophores to generate temporally separate images of a subset of spatially overlapping single molecules. After multiple iterations of activation and deactivation the super resolution image can be constructed from the localisations of many single fluorescent points. B) Principle of DNA-PAINT. DNA-PAINT uses short, dye-labelled DNA strands (imager strands) that binds transiently to a complementary strand (docking strand, bound to the target structure) in a sequence-specific way. The DNA sequence allows tuning of on- and off-rates and thus minimises the impact of photobleaching. Additionally, the use of different DNA sequences and different dyes allows the readout of different targets simultaneously.

For all SML approaches, the sample is imaged with low intensity and thus only a small subset of fluorophores is activated to the emitting state resulting in a high resolution image of the individual, excited fluorophores. After deactivating or bleaching this subset of emitters, the process will be repeated until enough or all molecules have been imaged. Subsequent localisation of all detected fluorophores enables the construction of a super-resolution image (Figure 1.10A) [87].

Total Internal Reflection Fluorescence

A major requirement for single-molecule imaging methods, especially when examining biological species present at low concentrations (e.g. ROS), is the ability to sensitively and specifically detect small signals over a high background noise. Different approaches have been used to achieve this. One of the most prominent approaches in cell biology exploits total internal reflection fluorescence (TIRF) illumination at highly inclined angles at the glass–sample interface to excite fluorophores in the sample (Figure 1.11) [93].

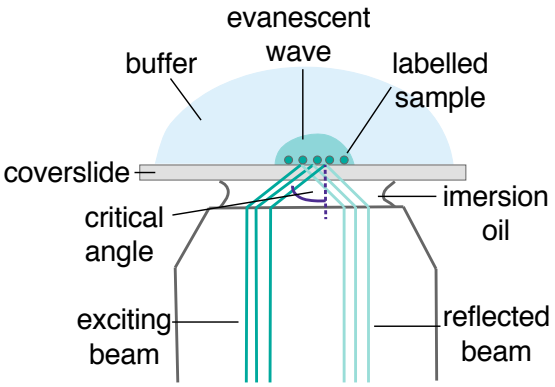

Figure 1.11 Schematic illustration of an objective-based TIRF microscope set-up.

Total internal reflection occurs when light travels through a transparent medium with refraction index n_1, such as a glass cover-slide ($n_1 = 1.5$) and is incident on a dielectric interface with a medium of lower refraction index n_2 (e.g. aqueous medium, $n_2 = 1.33$) at an critical angle. The critical angle of incident light can be determined by Snells's law ($\theta_C = \sin^{-1}(n_1/n_2)$). At or above the critical angle, the incident light is refracted back into the higher medium but a portion of the energy will be converted into an electromagentic field, which propagates as an evanescent wave of exponentially decaying intensity, but same frequency, into the lower medium. Due to the exponential decay of the amplitude with depth of penetration, only fluorophores in a thin region (100-200 nm) of the sample are excited [93]. This reduction in excitation volume increases the signal-to-noise ratio as it excludes signals from unfocused regions and thus allows single molecules to be resolved.

1.4.1 Contrast Agents for Single-Molecule Localisation Microscopy

To study a specific biological process at the molecular level the contrast agents should comprise a signalling unit generating the fluorescence signal and a targeting structure, which confines the signal to the molecular target of interest.

Photophysical Properties of Contrast Agents for SML Imaging

Choosing the right signalling compound is critical for SML microscopy. An ideal probe should fulfil several main criteria. First, it is crucial that the fluorescence probe possesses a fluorescent "on" state at a defined wavelength range and an "off"(dark) state, which does not emit at this range, to allow activation-deactivation cycles and to maximise the signal-to-noise ratio. Second, a high extinction coefficient and quantum yield is needed to generate a large number of photons in the on state, which allows high precision of localisation and

increases sensitivity. Third, as spontaneous activation by thermal energy or the imaging laser (instead of the activation laser (in case of switchable fluorophores)) can occur during image acquisition, it is also critical for the probe to have a low spontaneous activation rate [87]. Fourth, a large Stokes shift is beneficial to separate the emitted light from the excitation light. Finally, the probe should possesses a good photostability at high laser powers.

Signalling compounds for SML Imaging

The main signalling compounds used for SML are small molecule organic dyes and fluorescent proteins. For the purposes of this thesis fluorescent proteins will not be discussed and the focus will remain on organic dyes that can be easily introduced into an arbitrary biological sample.

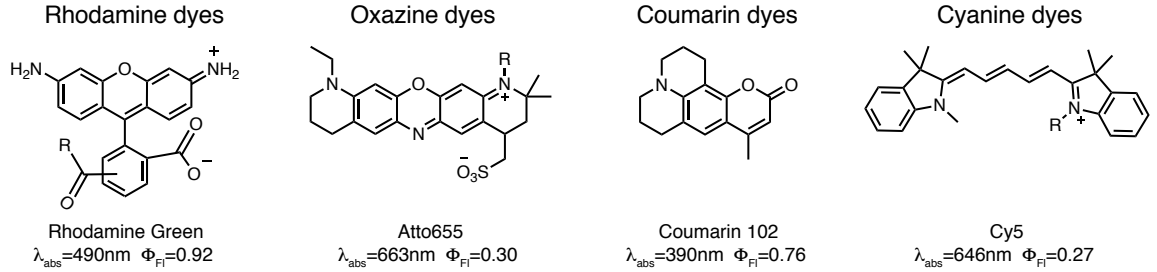

Figure 1.12 Chemical structure of represenative dyes used for SML microscopy and their maximum absorbance wavelength (λ_{abs}) and quantum yields (ϕ_{Fl}). Rhodamine dyes have a rigid dye backbone leading to high ϕ_{Fl}. Oxazine dyes absorb at higher λ_{abs} and show good photostability but possess low ϕ_{Fl}. Coumarin dyes manifest large Stokes shifts due to their polar excited state but are rather photoinstable. Cyanine dyes exhibit photoswitching behaviour due to cis/trans isomerisation and transition to triplet states, which leads to low ϕ_{Fl}.

The main classes of dyes used for SML are rhodamines, oxazines, coumarins and cyanines (Figure 1.12). The chemical structure of organic dyes underlying their capability to absorb and emit light is a conjugated system of π-electrons. Light induces these electrons to move from the highest occupied energy band (π-band) into the lowest unoccupied energy band (π^*-band) of the molecule. The electrons will then relax back and the electronic ground state is restored. The energy gap between these bands defines the wavelength at which absorption and emission takes place. However, due to more complex electron dynamics both absorption and emission occur over a continuum of energies, which gives rise to an absorption and emission spectrum instead of a sharp, discrete atomic line spectrum. The Jablonski diagram provides a schematic representation of the processes involved in the excitation and relaxation process of fluorophores (Figure 1.13A). The probability of this process occurring

is dependent on the quality of the interaction between the electrons and electromagnetic field of light, which induces motion of the delocalised electrons and thus creates an oscillating dipole [94]. The better the interaction, the greater oscillating dipole and thus the absorption.

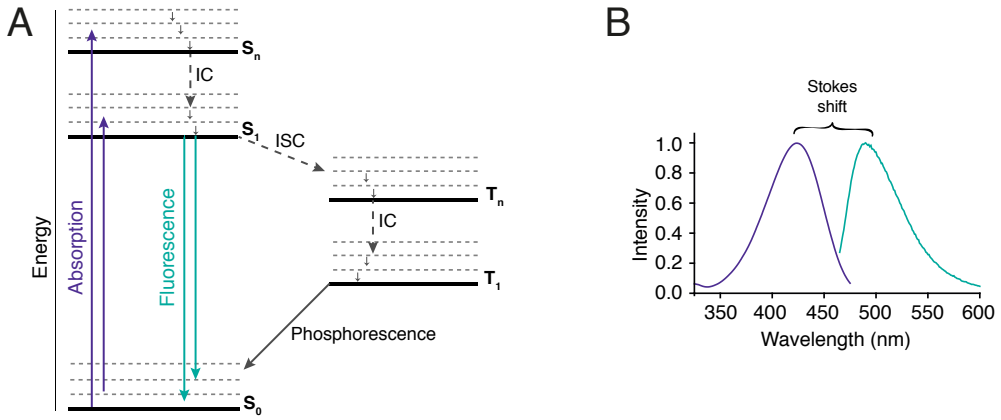

Figure 1.13 A) Jablonski diagram. Solid arrows = electronic transitions, dashed arrows = vibrational transitions, IC = internal conversion, ISC = intersystem crossing. B) Representative absorption and emission spectra of a fluorophore. Excitation promotes the fluorophore often in energy levels greater than S_1. Due to fast vibrational relaxation to S_1 before emission of the photon, the fluorescence is shifted to longer wavelengths than the absorption (Stokes shift). This is a desirable in fluorescence spectroscopy as it allows the two processes to be spectroscopically separated.

Excited fluorophores in the S_1 state can undergo several decay processes, the most desired one for SML imaging being emission of a fluorescence photon, which returns the molecule to its ground state (S_0). Competing de-excitation pathways are non-radiative intersystem-crossing (ISC) to form a triplet excited state (T_n) and non-radiative internal conversion (IC) from S_1 to S_0 (Figure 1.13). However, both processes are rather slow as ISC to T_n involves electron spin conversion and the relative large energy gap between S_1 and S_0 limits IC [94].

For SML microscopy it is desirable that the fluorescent form of the molecule can be recovered after the deactivation process. “Blinking” fluorophores realise this through transition to a reversible off-state. One cause for single-molecule blinking is the transition of the fluorophore into the triplet state by ISC. As the T_1 to S_0 transition is formally forbidden, T_1 possesses a long lifetime (10^{-4} to 10^{-6} sec) and T_1 to S_0 decay (phosphorescence) is not detected in the time regime in which SML operates, manifesting a reduction in total intensity. Also, as oxygen is generally present and has a triplet ground state, it efficiently quenches the dye’s triplet state and repopulates the S_0 state in a non-radiative way, resulting in fast on-off-cycles [95]. However, the interactions with oxygen lead to the generation of singlet oxygen, which can oxidise the fluorophore resulting in irreversible photobleaching [96].

Apart from ISC, the T_1 off-state can also be reached as a result of photoinduced electron transfer reactions of the fluorophore in its excited state [97] or through conformational changes, which can be either photophysical or thermally induced. For example, the presence of rotatable groups can lead to an intramolecular twisting motion in the fluorescent excited state, which can lead to a lower energy excited state, which often decays in a non-radiative way. Several dyes, referred to as molecular rotors, exhibit this property [98].

Organic dyes are promising contrast agents for SML as they possess a high chemical flexibility to tune their properties. Based on this, organic dyes are versatile for labelling with different targeting ligands including small molecules, peptides, affibodies, apatmers, antibodies and proteins (Figure 1.7). However, if extremely high resolution is required, the greater size of antibodies and proteins are limiting. Chemical modifications can also allow adjustment of the optical properties of dyes. It has been shown that integrating electron-donating and electron-withdrawing groups can increase the quantum yield of fluorophores [99]. Furthermore, this push and pull effect, which increases the delocalisation of the π-electrons, can help to induce a bathochromic shift in the absorption and emission spectra, which is favourable due to the reduced background from endogenous chromophores (cf. Figure 1.5).

During SML image acquisition, the fluorophores are surrounded by solvent molecules. After excitation, the polarity of the fluorophore changes and thus the solvent molecules will reorganise. This solvent relaxation helps to stabilise the excited state and contributes to increased Stokes shifts (solvatochromism) (Figure 1.13B), especially for polar fluorophores [100]. Thus modifying the polarity of the organic dye can help to improve their performance in SML. However, when increasing polarity through the introduction of H-bond donor groups, this may lead to an decrease in quantum yield [101, 102].

1.5 Project Objectives and Outline

As outlined in this introduction, there is an unmet need for a robust, accessible and sensitive methods to measure specific types of ROS with high spatial and temporal resolution, particularly *in vivo* and in patient-derived samples. To overcome the current limitations, the fundamental objective of this thesis was to develop new optical probes for the specific detection of ROS in cancer and neurodegenerative disorders and combine these with suitable technologies allowing a specific readout with high spatial and temporal resolution under biologically relevant conditions.

Combining the high temporal and spatial resolution of PA imaging with new cell- and redox species-specific probes is a promising approach for the accurate mapping of cellular redox conditions *in vivo*. Therefore, the aim was to develop a bifunctional small molecule PA probe for detecting a major and abundant ROS, hydrogen peroxide, which elicits a signal change upon redox alterations and is specifically uptaken by cancer cells. Approaches to achieve this aim are described in Chapters 2 and 3 of this thesis and involve the investigation of the following areas:

- Synthesis and chemical and photophysical characterisation of an organic framework that absorbs light in the NIR range, possesses suitable optical properties for PA imaging and provides easily accessible sites for chemical modifications.
- Synthesis and characterisation of different linker-dye conjugates to evaluate their ability to elicit a signal change upon the reaction with H_2O_2 that is detectable with PA imaging.
- Synthesis as well as physicochemical and biological evaluation of a bifunctional H_2O_2-reactive, cancer-targeting dye.
- *In vitro* and *in vivo* application of the new bifunctional probe to study the role of oxidative stress in cancer with the help of PA imaging.
- Development of *ex vivo* methods to cross validate the biological insight provided by the *in vivo* data of the new bifunctional PA probe.

Single molecule fluorescence imaging allows the ultrasensitive detection of individual nanoscale biological species with unsurpassed spatial and high temporal resolution. Merging this technology with new bifunctional probes able to simultaneously sense ROS and pathological species of neurological diseases presents an auspicious method to overcome the hurdle in assessing ROS changes linked to the pathology of neurodegenerations that could in future be applied in patient samples. Chapters 4 and 5 describe the different strategies explored in this thesis to reach this goal and include the following areas:

- Photophysical characterisation on a bulk and single molecule level of a novel fluorophore library for detecting pathogenic protein aggregates in neurodegenerative disorders.
- Characterisation of the binding properties of this novel fluorophore library.
- Establishing the relationship between the chemical modifications of the different fluorophores, their photophysical and binding properties.
- Applying the knowledge gained from the characterisation of the library to develop novel bifunctional dyes capable of simultaneously identifying H_2O_2 and pathogenic protein aggregates.

- Characterisation of the bifunctional sensing capabilities of the new bifunctional dyes at bulk and single-molecule levels.

The thesis concludes with a chapter that summarises the findings and provides and outlook for additional work that would further assess the significance of H_2O_2 and oxidative damage in cancer and neurodegenerative diseases with the two new developed approaches.

Chapter 2

Development of a new Activatable, Bifunctional Photoacoustic Probe

The PA spectrometer used for acquiring PA spectra of the dyes with different concentrations in different solvents was assembled under the guidance of S. Morscher (iThera Medical), who also provided the code for the image reconstruction of these data. The study of the absorption and fluorescence properties of commercial available cyanine dyes was done in collaboration with a summer student L. Birnoschi, under my supervision. Dr. T.J.Zuehlsdorff and Dr. N.De Mitri performed DFT calculations. All other work was performed and analysed myself. Parts of this work are in review for publication.

2.1 Introduction and Motivation

Reactive oxygen species (ROS), oxidative stress and oxidative damage has long been linked to several cancerous conditions promoting tumour initiation, promotion, progression and survival [103, 104]. Whether increased levels of ROS are a primary cause or a downstream consequence of tumorigenesis and how the different disease stages vary from each other in respect of their redox biology is still an open question due to limitations of the current state-of-the-art methods for measuring ROS, particularly *in vivo*. Consequently, research into new imaging probes and early detection methods for deleterious levels of ROS have attracted significant interest in biomedical research. Thus the focus of this chapter was to develop a new imaging probe for specific and sensitive *in vivo* sensing of ROS in cancer. Therefore, PA imaging was used as it operates on a spatial and temporal resolution highly suited to detect ROS in real-time *in vivo* with high spatial resolution.

2.1.1 Near-Infra-Red Dyes and Hydrogen Peroxide Sensing

In the past few decades, new near-infra-red (NIR) fluorescence dyes with fine photophysical properties, high sensitivity and multi-detection capability have been a topic of great interest in bioimaging and therapeutics. Their chemical flexibility facilitates the conjugation with moieties of interest and tailoring the spectral range of the contrast agent, making them ideal candidates for disease targeted imaging and multimodality approaches.

One target for which NIR dyes are broadly exploited are reactive oxygen species (ROS). H_2O_2 is a major and abundant ROS in living organisms and plays an important role as a second messenger in physiological signal transduction and pathological processes. Thus, several NIR dye backbone structures have been chemically modified to be capable of measuring H_2O_2 production. Among them are rhodamine [19, 20, 25], BODIPY [105] or cyanine [52, 106] based dyes. Frequently, a boronate functionality frames the moiety for specific and irreversible H_2O_2 detection.

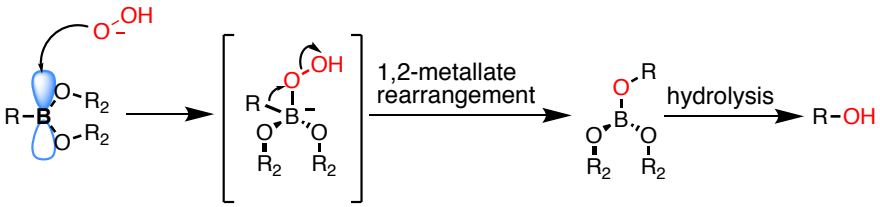

Figure 2.1 Mechanism of the oxidation of boronic esters by H_2O_2.

In this context, the readout is based on an selective increase in fluorescence triggered by H_2O_2 mediated boronate deprotection (Figure 2.1). An added benefit is that neither the boronic esters nor the arising boronic acids show an intrinsic toxicity and their reactivity can be tuned by means of substitution effects on the phenyl unit [107, 108]. Additionally, the sensors have been refined to detect signalling levels of ROS (down to 100-200 nM H_2O_2) and targeting to specific organelles such as mitochondria allows localisation-specific readout [19, 25].

Even though the temporal and spatial regimes in which fluorescence imaging can operate makes it a suitable technique for the study of ROS on a cellular basis, constrained depth of penetration limits the application of the fluorescence based ROS-specific probes in deeper tissues and thus for clinical *in vivo* imaging [33]. Photoacoustic (PA) imaging overcomes these traditional depth limits of ballistic optical imaging and the resolution limits of diffuse optical imaging. Additionally, it uses acoustic waves generated in response to the absorption of pulsed laser light and thus no radiation or other source of external ROS generation is needed

for PA imaging. Logically, using the knowledge gained from boronate-based fluorescent dyes could allow for introduction of an activatable PA contrast agent.

2.1.2 Activatable Contrast Agents for PA Imaging

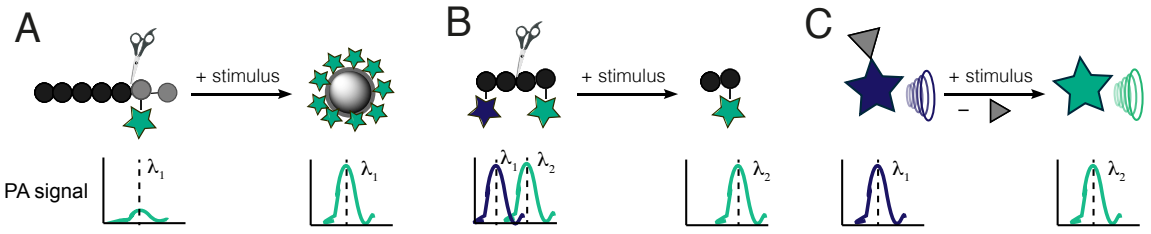

Figure 2.2 Schematic illustration of the mechanisms of activatable probes for PA imaging. A) The non-activated probe generates a weak PA signal with a peak intensity at λ_1. Upon the interaction with the biological stimulus, many probes combine and generate a significant signal increase at λ_1. B) The non-activated probe produces a PA signal at 2 wavelengths (λ_1, λ_2) corresponding to the absorption maxima of the 2 chromophores (green and blue star). After cleavage, only one part of the probe carrying one of the chromophores (green star), accumulates in region of interest and results in a PA signal at only 1 of the 2 wavelengths. C) The interaction with the biological stimulus causes a chemical modification of the probe, which leads to a change in the PA maxima from λ_1 to λ_2.

Activatable probes for PA imaging are designed to elicit a detectable signal change upon enzymatic activity or in response to a specific biomolecular interaction. The PA signal change can be manifested through an increase in signal intensity [109, 37], the disappearance/local separation of one of two initial PA peaks [110, 111] or through a shift in the peak absorption [112] (Figure 2.2). PA images can then be acquired at the wavelengths characteristic for the probe before and after activation, which allows internal normalisation and thus can lead to very high signal-to-background ratios compared with conventional targeted contrast agents. Additionally, they open up the possibility of imaging biological processes in real-time at lower concentrations due to increased sensitivity.

However, to realise these features it is important to consider some key criteria: Firstly, it is crucial that the activatable contrast agent possesses clear distinguishable absorption profile before and after activation without significant signal cross-over with each other and the background to allow spectral unmixing and maximise the signal-to-noise ratio. Furthermore, a low spontaneous or unspecific activation rate is needed to enable the sensitive and specific readout of the biological stimulus of interest. The activation reaction rate and reaction kinetics must also be optimised towards the stimulus to enable the response to stimuli, which are often present in concentrations of less than nanomolar. Finally, it is critical to study the *in vitro* and *in vivo* properties of both the non-activated and activated probes separately

to exclude artefacts due to differences in the interaction with the biological environment, biodistribution, metabolism or clearance. Although relatively few examples of activatable contrast agents exist for PA imaging, targeting matrix metalloprotease [113], metal ions [114, 115], hypoxia [116] or nitric oxide [112] have shown promising results.

2.1.3 Bifunctional Contrast Agents for ROS Sensing

ROS are not only assigned to pathologies and ageing but also play an important role as regulatory molecules in a range of biological processes. Consequently, ROS are present ubiquitously and it needs to be assessed cautiously whether a change in concentration of a particular ROS is indicative of its contribution in a pathology or physiological redox signal [2]. Thus, to study the impact of oxidative stress towards a particular disease, the location of the probe within the organism and the cell must be understood and controlled. This is particularly important in complex, multistage diseases such as cancer, in which a variety of factors lead to disease initiation and progression. Often several of these factors, such as inflammatory processes, lead to an additional enrichment of ROS.

To examine precisely how the different factors and developmental stages vary from each other in respect of their redox biology, we need to be able to not only get a read out of the redox environment but also of the localisation and developmental stage of the pathological process. This can be achieved through bifunctional probes, which on the one hand actively target a disease inherent biomarker (over)expressed at a certain stage of the disease and found at low levels in off-target tissues and on the other hand possess an activatable functionality reactive towards the ROS of interest. Such an approach was explored by Dickinson et al, who targeted a H_2O_2-reactive fluorescence dye towards mitochondria, which allowed mitochondria specific H_2O_2 detection in cell culture and tissue models [25]. Moreover, the active targeting moiety can be exploited to accomplish biological needs such as bypassing physiological delivery barriers, rapid elimination, biodegradation, decreased off-target tissue accumulation and suboptimal tissue perfusion.

2.1.4 Approach

The ideal contrast agent for accurate *in vivo* mapping of cellular redox conditions in cancer by means of PA imaging must fulfil certain requirements (Figure 2.3). One main criterion is a characteristic absorption spectrum in the NIR range with a high extinction coefficient to maximise the amount of light absorbed and to ensure unambiguous identification by spectral unmixing even at low molar concentrations. For the specific and irreversible H_2O_2

detection, a functional group that triggers a signal change upon reaction with H_2O_2 is crucial. Finally, because the spatial and temporal distributions of redox species is usually highly heterogeneous and the redox signalling signature is specific to a certain location, the ideal contrast agent should also comprise a cancer targeting moiety to increase patho-physiological specificity and gain a favourable biodistribution. The target structure should ideally be (over)expressed at a defined stage of the cancer development and found at low levels in off-target tissues.

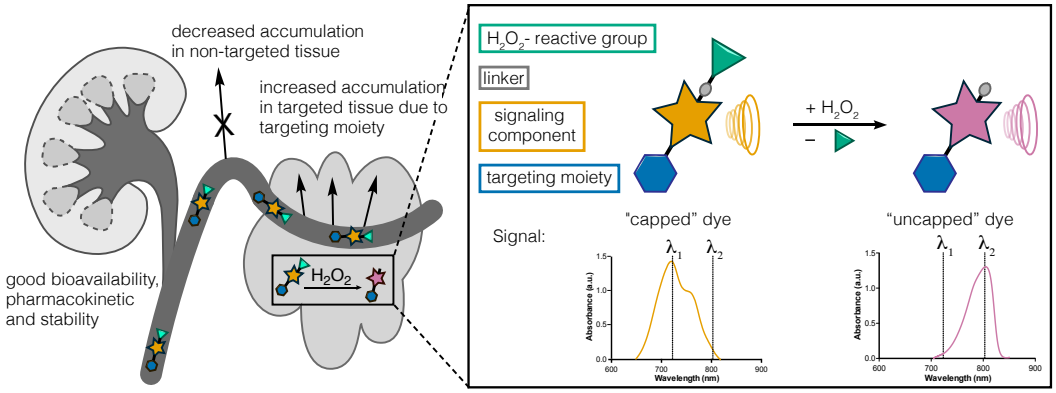

Figure 2.3 Schematic illustration of the design and different features of the new activatable, PA contrast agent.

This chapter will describe the background and fundamentals on how these different requirements were implemented. First, different commercially available NIR cyanine dyes, previously used for fluorescence imaging, have been studied to investigate how structural modifications of the dye backbone influence the suitability of the dye as PA contrast agent. Secondly, the ability of different linkers to elicit a PA signal change upon interaction with H_2O_2 was examined. The chapter will finish by describing the final design, synthesis and photophysical properties of the new bifunctional, activatable contrast agent.

2.2 Results and Discussion

2.2.1 Properties and Characteristics of Commercial Available NIR Cyanine Dyes

The rise of *in vitro* and *in vivo* fluorescence imaging in research and clinical use in the last decades led to a significant number of NIR fluorescent probes being synthesised, characterised and later made commercially available. Heptamethine carbocyanine (**HCC**) dyes have

been described among the different dye scaffolds that satisfy the optical criteria needed for PAI and, importantly, provide easily accessible sites for chemical modifications [117, 118]. However, most of the examinations of cyanine dyes are based on fluorescence imaging and only limited information are available about their absorption and PA characteristics under different, especially biologically relevant, environments. Hence, the aim was to examine the photochemical properties of different NIR cyanine dyes, which possess distinct similarities and differences, with regard to their suitability as PA contrast agents. The structures and characteristics of the chromophores compared are shown in Table 2.1. The main criteria for selection were the ring size of the terminal 3-H-indole structure, the number and position of solubilising, anionic groups and the presence and size of the carbocyclic ring bridging C3' and C5' of the polymethine chain. Representative spectra for different solvents and dyes can be found in the Appendix.

Aggregate Formation

In general, cyanine dyes consist of two nitrogen centres, one positively charged the other neutral, which are linked by a conjugated chain of an odd number of carbons. This structure generates a push and pull effect and forms the basis of their chromophoric unit [118]. The absorption spectrum of cyanine dyes is characterised by a maximum based on the 0-0 electronic transition and often blue shifted sub-bands caused by vibronic transitions [119]. Additionally, H- and J-aggregate formation can occur in different environments leading to hypsochromic or bathochromic shifts, respectively [118]. Dimerisation, in particular, evokes a peak partially overlapping with the vibronic shoulder of the monomer [119]. It is therefore important to assess the nature of aggregation formation in these species in order to understand the spectral shifts that may occur *in vivo*.

The optical examination of the 7 different dyes confirmed the following aggregation trends. The aggregate content appears to increase with solvent polarity and ionic strength. Extending the terminal aromatic system and thus the hydrophobicity increases the aggregation tendency in aqueous solutions (Cy7 vs Cy7.5, Figure 2.4A). The introduction of a six-membered ring in the heptamethine chain seems to promote the formation of additional J-aggregates, which might be caused by the increated rigidity of the dye framework (Cy7.5 vs ICG, Figure 2.4B). The aggregation tendency in solution between dyes with integrated 5- or 6-membered ring (IR783 vs IR806) did not differ. However, the 5-membered ring derivative, IR806, readily precipitated in the presence of ions whereas IR783 was soluble in buffers.

Table 2.1 Structure and characteristics of selected commercial available cyanine dyes.

Dye	Aromatic Rings[1]	Anionic Groups	Carbocyclic Ring[2]	Chemical Structure
ICG	2	2 SO_3^-	No	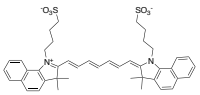
Cy7.5	2	1 CO_2^-	Yes (6)	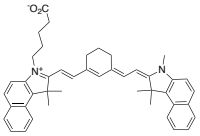
Cy7	1	1 CO_2^-	Yes (6)	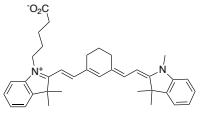
SulfoCy7	1	2 SO_3^-, 1 CO_2^-	Yes (6)	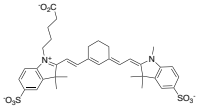
IR800CW	1	4 SO_3^-, 1 CO_2^-	Yes (6)	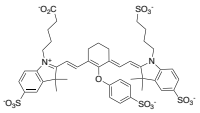
IR783	1	1 SO_3^-	Yes (6)	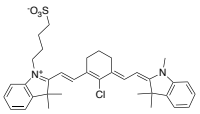
IR806	1	1 SO_3^-	Yes (5)	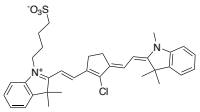
IR680RD	1	3 SO_3^-	No	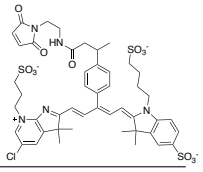

[1] Relating to the aromatic rings of the terminal 3-H-indole structure.
[2] Relating to the carbocyclic ring bridging C3' and C5' of the polymethine chain. The number indicates the ring size.

Addition of fetal bovine serum (FBS) or bovine serum albumin (BSA) to water or buffer led to a significant decrease in aggregation for dyes strongly binding to proteins (Figure 2.4C). This is caused by dye-protein complex formation, which prevents dye-dye interactions. The tendency of dye-protein complex formation was validated by incubating the dyes with phosphate buffered saline (PBS) containing 3 wt% BSA and separating the different dye-protein complexes via gel electrophoresis in native conditions (Figure 2.4D). The two sulfo-cyanine dyes, IR800CW and SulfoCy7, showed no significant change in their spectral shape by adding BSA or FBS, which was consistent with the absence of noticeable protein binding.

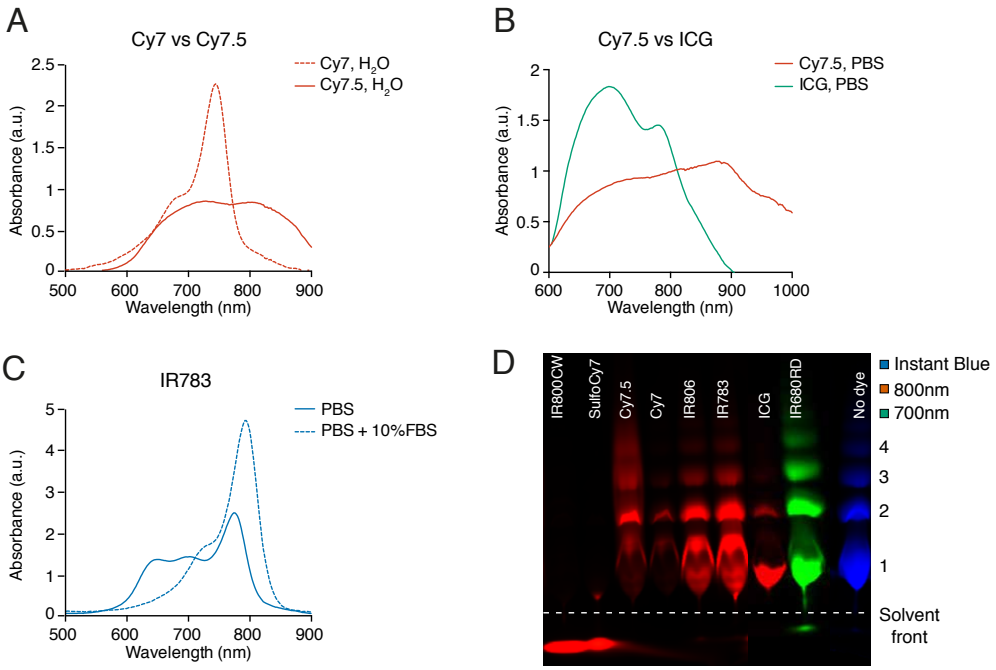

Figure 2.4 Aggregation trends of cyanine dyes. Absorption spectra of A) Cy7 and Cy7.5 (20 μM) in H_2O B) Cy7.5 and ICG (50 μM) in PBS and C) IR783 (20 μM) in PBS and PBS + 10 % FBS are shown, demonstrating A) the increase in aggregation when extending the aromatic framework of the dye, B) the influence of a more ridged backbone caused by an integrated 6-membered ring and C) the decrease in aggregation in the presence of proteins. D) Tendency of the dyes to bind to proteins. Protein binding of the 7 cyanine dyes was assessed in 3 wt% BSA in PBS. The bound and unbound dyes were separated on a native gel and visualised using the 800 nm channel laser source (700 nm channel was used for IR680RD). After scanning the first time, the gel was stained with instant blue and imaged again with the 700 nm channel. Dyes with low protein binding (IR800CW and SulfoCy7), show not detectable signals at the protein bands, whereas those with high protein binding show high signals aligned with the BSA monomer (1), dimer (2), tetramer (3) and hexamer (4) [120].

Absorptivity, Quantum Yield and Photoacoustic Properties

A summary of some of the optical properties of the dyes can be found in Table 2.2. In general, the lowest absorption and quantum yield values are observed in buffer solutions for all dyes. This is most likely due to the formation of self-quenching dye-dye aggregates and the stabilisation of the more dipolar electronic excited state by ions, which decreases the likelihood of emission [121, 118]. No significant difference was observed between different ion contents (e.g. PBS vs. tris-buffered saline (TBS) vs. brine). However, attaching sulfonate groups directly to the conjugated system (IR800CW, SulfoCy7) decreases the effect of ions. The data also confirmed, that adding protein to the solution generally increases the absorptivity (except ICG), sharpens the absorption peak, often leads to a slight red-shift and enhances the quantum yield (Table 2.2). Overall, the most absorbing dye appears to be IR800CW, while the least absorbing dye is IR680RD. This difference was expected on the basis of the structure of their conjugated system. IR800CW and SulfoCy7 possess the same backbone structure and thus - based on this feature alone - similar absorptivity would have been expected. However, the higher absorptivity of IR800CW might be the result of the rather symmetric chemical substitution in comparison to SulfoCy7 [122]. Also, the structure of IR800CW comprises two extra sulfonate groups leading to different interactions with the solvent. Integrating a 5-membered ring in comparison to a 6-membered ring results in a shift of the absorption and emission maxima of around 25 nm.

The PA spectra obtained in the different solvents largely mirror the absorption spectra. However, all dyes exhibited a slight broadening and a blue shift (up to 25 nm) of the spectra compared to their absorption profile (Figure 2.5A). The exception was Cy7, for which PA spectra exhibited a peak 25 nm red-shifted compared to its absorption maximum. The broadening and shift was very minor for the sulfo-cyanine dyes, IR800CW and SulfoCy7. As for the absorption spectra, the presence of proteins did increase the PA amplitude and often sharpened the spectra (Figure 2.5B). Even though IR800CW and SulfoCy7 exhibit a strong and sharp PA profile, photothermal stability studies suggested that the two sulfo-cyanine dyes are the least photostable dyes among the examined dyes, whereas Cy7 showed nearly no photobleaching over the tested time frame (Figure 2.5C). Improved photothermal stability of asymmetric dyes, which was reported in the literature, was not found in our experiments [82].

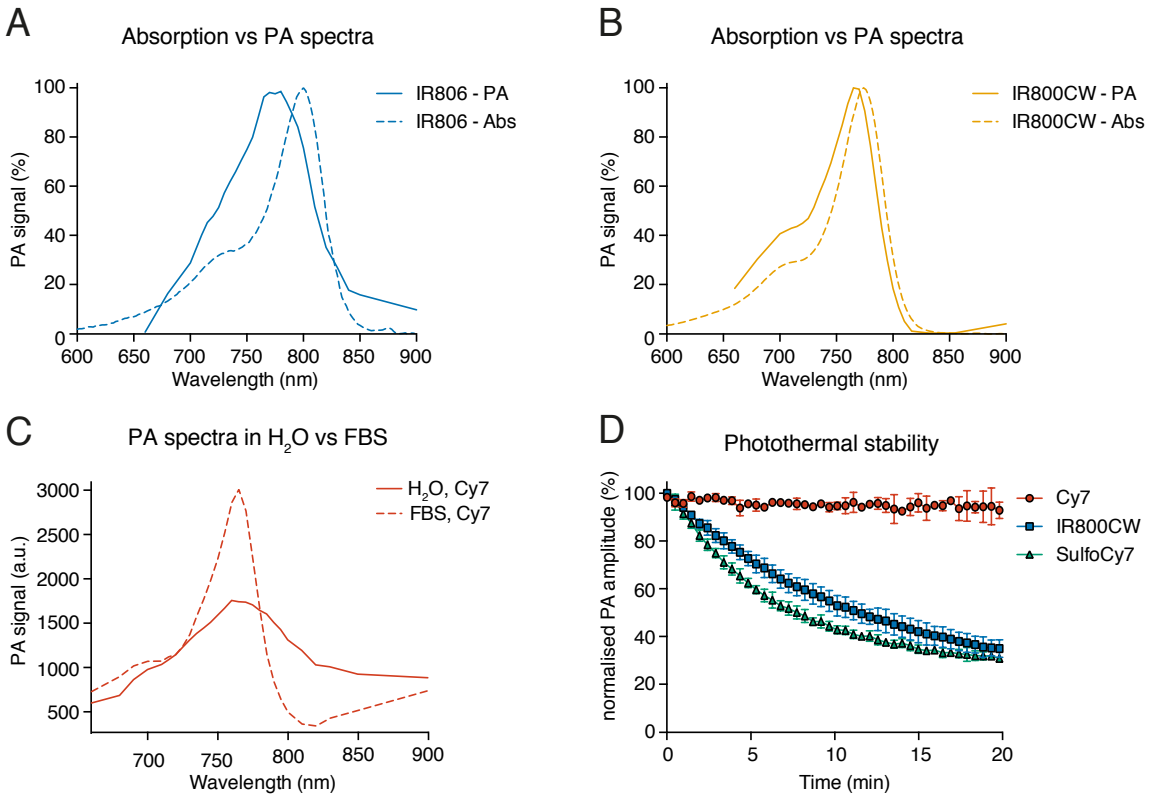

Figure 2.5 Representative PA properties of some commercial available cyanine dyes.PA (solid line) and absorption (dashed line) spectra in water of A) IR806 (5 μM) as example for a non-sulfonated dye and B) IR800CW (5 μM) as example of a sulfonated dye. C) PA spectra of Cy7 (5 μM) in water and FBS. D) Normalised PA amplitude at the PA maximum. D) Photostability of 5 μM dye solutions in FBS under continuous laser exposure (9-ns excitation pulses at a 10-Hz repetition rate) for 20 min at the same position. The normalised PA signal at the PA maximum of the dye is plotted against the time. All PA measurements were performed in tissue mimicking phantoms.

Altogether, the high absorptivity combined with a low quantum yield and a strong, sharp PA signature make IR800CW the best dye for photoacoustic imaging. However, the presence of proteins did significantly improve the optical and photoacoustic characteristics for the non-sulfonated cyanine dyes, making also Cy7 and Cy7.5 attractive candidates, especially due to their good photothermal stability.

Table 2.2 Summary of some properties of commercial available cyanine dyes

Dye	Solvent	$\lambda^{Abs}{}_{max}$ (nm)	$\lambda^{Em}{}_{max}$ (nm)	ε (10^5 $M^{-1}cm^{-1}$)	$\Delta\varepsilon$ (10^5 $M^{-1}cm^{-1}$)[b]	ϕ_{Fl}[c]	$\Delta\phi_{Fl}$[d]	Aggregate formation	Protein binding[e]
ICG	H_2O	710	819	0.721	0.062	0.060	0.007	med	
	H_2O+FBS	794	819	0.257	0.054	0.173	0.014	low	
	PBS	776	818	0.380	0.018	0.027	0.001	high	high
	PBS+FBS	794	819	0.238	0.052	0.324	0.051	med	
	MeOH	784	819	0.0224	0.032	0.022	0.002	no	
Cy7.5	H_2O	727	-[a]	0.342	0.013	-[a]	-[a]	high	
	H_2O+FBS	800	819	0.858	0.029	0.012	0.001	low	
	PBS	879	-[a]	0.197	0.012	-[a]	-[a]	high	med
	PBS+FBS	799	819	0.880	0.024	0.011	0.001	low	
	MeOH	784	819	1.752	0.084	0.014	0.001	no	
Cy7	H_2O	744	777	0.888	0.057	0.005	0.0006	low	
	H_2O+FBS	764	790	2.035	0.024	0.014	0.0028	no	
	PBS	742	777	0.993	0.010	0.008	0.0006	low	med
	PBS+FBS	762	789	1.734	0.142	0.023	0.0037	no	
	MeOH	750	777	1.999	0.178	0.002	0.0002	no	
SulfoCy7	H_2O	750	777	1.381	0.030	0.005	0.001	no	
	H_2O+FBS	750	783	1.527	0.013	0.007	0.001	no	
	PBS	750	777	1.060	0.023	0.006	0.001	no	low
	PBS+FBS	750	777	1.581	0.035	0.005	0.0004	no	
	EtOH	758	789	1.532	0.027	0.013	0.001	no	
IR800CW	H_2O	774	805	2.714	0.112	0.026	0.004	no	
	H_2O+FBS	777	808	3.072	0.374	0.013	0.003	no	
	PBS	774	799	1.151	0.032	0.026	0.003	no	low
	PBS+FBS	774	804	0.841	0.072	0.049	0.014	no	
IR783	H_2O	774	805	0.909	0.018	0.046	0.005	low	
	H_2O+FBS	794	819	1.031	0.037	0.174	0.022	no	
	PBS	774	805	0.469	0.044	0.034	0.003	low	high
	PBS+FBS	794	819	0.910	0.020	0.145	0.014	no	
	MeOH	782	811	0.680	0.092	0.0002	0.00004	no	
IR806	H_2O	800	833	1.006	0.025	0.137	0.013	low	high
	H_2O+FBS	792	834	0.825	0.027	0.185	0.034	med	
	MeOH	806	834	1.236	0.071	0.095	0.013	no	
IR680RD	H_2O	670	702	0.614	0.022	0.003	0.0003	low	
	H_2O+FBS	674	706	0.598	0.038	0.012	0.001	low	
	PBS	670	702	0.527	0.018	0.003	0.0003	low	med
	PBS+FBS	672	704	0.500	0.081	0.013	0.003	low	

[a] no significant fluorescence was detected. [b] Error (SD) of ε

[c] ICG in PBS solution ($\phi_{(Fl)} = 0.0270 \pm 0.0011$) was used as standard. The values were not normalised with respect to the refractive index of the solvent as the non-normalised values are sufficient for observing general trends among the dye solutions for the purpose of this study.

[d] Error (SD) of ϕ [e] Free to bound dye signal ratio: high: < 5, med: 5 - 100, low > 100.

2.2.2 Experimental Linker Evaluation

The knowledge gained from examining the optical and photoacoustic properties of commercially available dyes, lead to the decision to investigate the addition of a linker structure towards H_2O_2 reactivity on a heptamethine cyanine frame with an integrated 6-membered carbocyclic ring linking C3' and C5', terminal 1,1,2-trimethyl-1H-benzo[e]indol units and symmetrical substituted nitrogens (Figure 2.6A, **HCC**). The choice to include the 6-membered carbocyclic ring, even though it may increase the tendency for aggregate formation, was founded on the improved physical properties and stability caused by this structural feature [117]. Additionally, it provided an easily accessible site for chemical modifications and the synthesis of this backbone was well described in the literature [123, 83, 124]. 1,1,2-trimethyl-1H-benzo[e]indol was chosen above 2,3,3-trimethylindolenine due to the more red-shifted absorption and PA maximum.

According to published procedures [123, 83, 124], the heptamethine carbocyanine dye framework (**HCC**) was synthesised over three steps, as depicted in Figure 2.6A. Previous findings, including density functional theory (DFT) calculations by J. Yin *et al.* [125] and by our collaborator T.J. Zuehlsdorff (Figure 2.6B) indicate that the excitation is associated with a redistribution of charge mainly towards the centre of the cyanine backbone. Hence, the linker unit, responsible for the signal change, was integrated on the central hydrophobic core of the π-system.

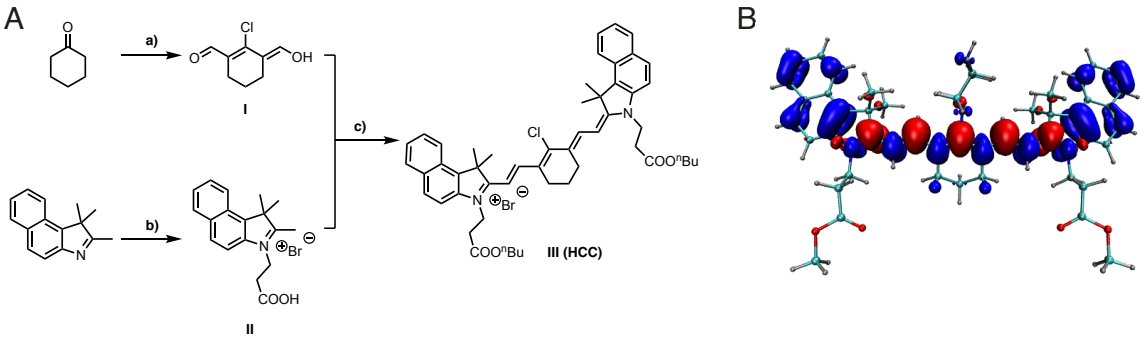

Figure 2.6 A) Synthesis scheme of the heptamethine carbocyanine dye framework (HCC). Reagents and conditions: (a) $POCl_3$, DMF. (b) 1,2-dichlorobenzene, 3-bromopropanoic acid. (c) Butanol/Toluene, ΔT. B) Plot of the electron-hole density of the heptamethine carbocyanine framework. Blue denotes the hole density while red denotes the electron density.

The vinylic chlorine of **HCC** is an attractive functionality for attaching further functional groups to the dye backbone. Previous reports described efficient attachment of N-, O-, S-aryl or piperazine derivatives while retaining their NIR absorptivity [125–127]. To investigate

whether similar substituents are able to tune a signal change for PA imaging, different linker-**HCC** derivatives were synthesised. To start with, 4-aminophenol, benzene-1,4-diamine and piperazine were chosen as linker units to explore the impact of different electronic and steric features on the optical properties. Efforts to synthesise **HCC**-derivatives with benzene-1,4-diamine as linker unit were unfortunately not successful.

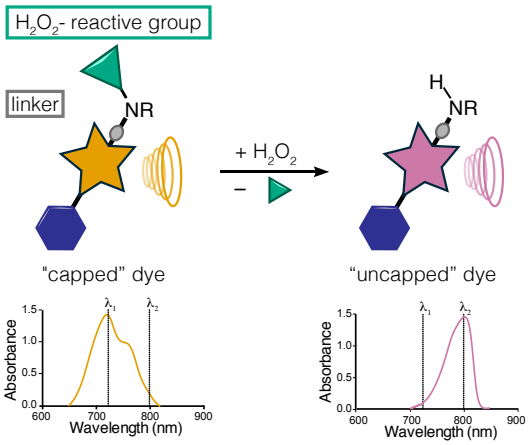

Figure 2.7 Principle of the signal change of the activatable PA probe. In the presence of H_2O_2, the H_2O_2 reactive group will get cleaved and the free linker-dye conjugate, bearing a free amine group, will be released. As a consequence of this structural change, the optical properties of the probe will change allowing the imaging based readout of the presence of H_2O_2.

In the final activatable H_2O_2 PA dye, a redox reactive group will be attached to the linker via an amide bond at the *para*-position to the dye framework. After reaction with the redox species this bond will be cleaved and the free linker-dye conjugate, bearing a free amine group, will be released (Figure 2.7). This approach relies on the structural and electronic effect of the amide bond and the attached group on the optical properties of the dye framework. Therefore, for each linker the corresponding free linker-dye conjugate (free amine group; uncapped dye, Figure 2.7), acetylated linker-dye conjugate (green triangle = Ac) and bocylated linker-dye conjugate (green triangle = Boc) were synthesised to probe the electronic and steric effects.

Synthesis of the Different HCC-Linker Derivatives

An overview of the structure and synthetic routes of the different **HCC**-linker derivatives (**JW7/8/11/13/14/16/17**) is outlined in Figure 2.8. All reactions need to be performed under exclusion of light and below 50 °C to avoid degradation. During the synthesis it was also noticed that only the unmodified piperazine efficiently substitutes the chlorine; as soon as

one nitrogen has been converted into an amide no further reaction occurred. Therefore, the piperazine-nitrogen on **JW8** was modified with substituents in a second step.

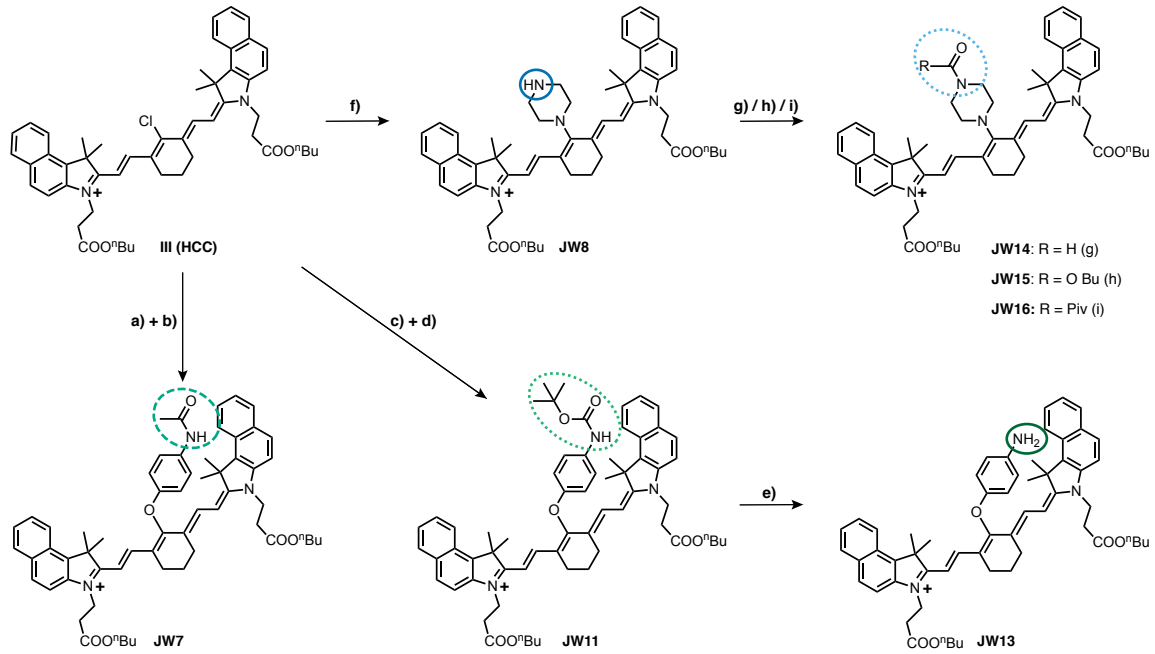

Figure 2.8 Schematic overview of the synthesis of the different HCC-linker derivatives. Reagents and conditions: (a) acetic anhydride, 4-aminophenol, H_2O (47%). (b) HCC, 1-acetylpiperazine, K_2CO_3, MeCN (33%). (c) Di-tert-butyl-dicarbonate, 4-aminophenol, THF (81%). (d) tert-Butyl (4-hydroxyphenyl)carbamate, HCC, TEA, MeCN (94%). (e) JW11, TFA, DCM (82%). (f) HCC, piperazine, TEA, MeCN (91%). (g) JW8, imidazole, acetylchloride, THF (68%). (h) JW8, trimethylacetyl chloride, TEA, THF (42%). (i) JW8, di-tert-butyl dicarbonate, TEA, THF (91%).

Optical Validation of HCC-Piperazine Derivatives

The absorption and fluorescence characteristics of the HCC-linker dyes were examined at different concentrations (1 μM to 100 μM) and conditions (MeOH, EtOH, MeCN, MeOH : H_2O, H_2O, PBS, sodium acetate buffer pH 4.30, ammonium carbonate buffer pH 10.45) to investigate the impact of the environment, the different protonation states of the amino group and aggregation trends. The influence of photoinduced electron transfer (PET) was also analysed since the H_2O_2-reactive group is likely to be involved in PET [128]. This was performed by adding different concentrations of triethylamine (TEA) and 4-dimethylaminopyridine (DMAP). TEA and DMAP are known to be good electron donors to photoexcited chromophores [129, 130]. During the intermolecular PET process, an electron from TEA/DMAP is transferred to the dye molecule (acceptor) resulting in charge separation and quenching of the fluorescence of the acceptor. Representative spectra of the dyes in the different solvents and

concentrations can be found in the Appendix (Figure A.2). The absorption spectra showed that all the dyes tend to aggregate in aqueous solutions, however, a clear spectra could be obtained in organic solvents and for the uncapped derivatives also in MeOH : H_2O mixtures. The spectra recorded in organic solvents revealed that the three different 4-**HCC**-oxyaniline dyes **JW7**, **JW11** and **JW13** possess identical absorption properties (Figure 2.9A). Thus, we can conclude that 4-aminophenol is not suitable as linker for the purpose of this study since no significant absorption shift is noticed between the different derivatives.

The recorded absorption spectra of the **HCC**-piperazine derivatives in organic solvents showed a clear difference for the different nitrogen modifications. As shown in Figure 2.9, the free amino derivative, **JW8**, exhibits an absorption maximum at 718 nm and a weak absorption shoulder close to 800 nm in MeOH. The acetylated derivative **JW14** shows comparable absorption maxima at around 740 nm and 800 nm whereas the bocylated derivative **JW15** features one clear maximum close to 790 nm and an absorption shoulder at 730 nm. To examine whether the spectroscopic differences arise primarily from electronic or steric origins a fourth **HCC**-piperazine derivative with a pivaloyl-functionalised amino group (**JW16**) was synthesised. The recorded absorption spectrum shows similarities to the bocylated derivative **JW15** although further red-shifted (absorption peak at around 815 nm and shoulder at around 745 nm). For all the dyes, PET, experimentally introduced through the addition of TEA or DMAP, did not impact the absorption properties.

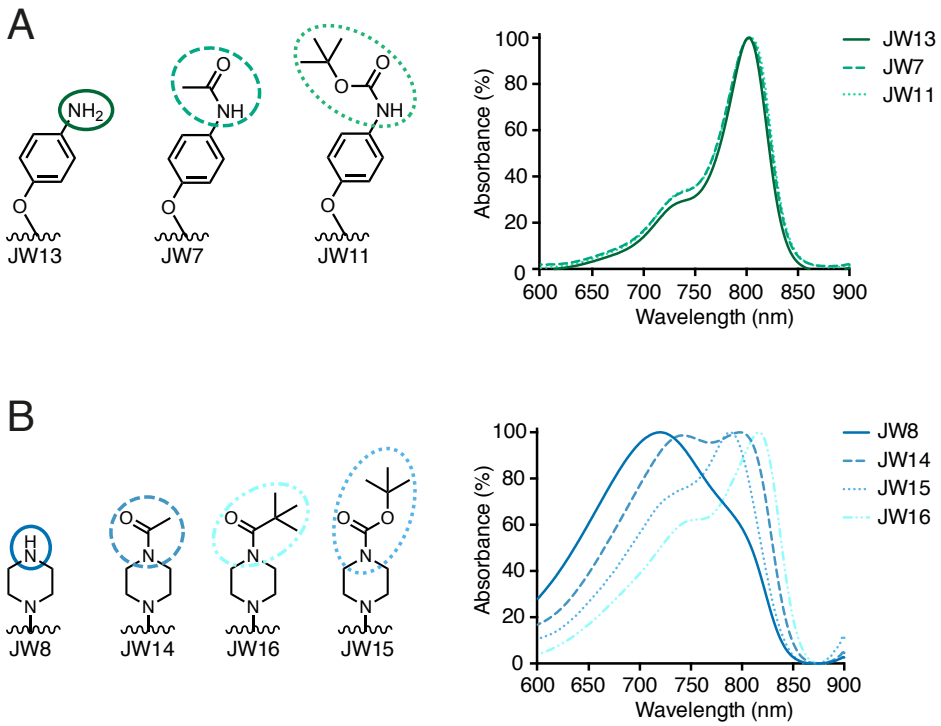

Figure 2.9 Absorption spectra of the different HCC-linker derivatives. Representative, normalised absorption spectra of A) 4-HCC-oxyaniline dyes (10 μM) and B) HCC-piperazine dyes (10 μM) in methanol.

Based on these results it was postulated that the electronic properties of the piperazine substituent have a major impact on the absorption shift. Higher electron density on the nitrogen atom leads to a more red-shifted absorption maximum (c.f. **JW14/JW16** vs **15**). Steric effects seem to influence the intensity of the two absorption bands. The more sterically demanding, the greater the difference between the capped and uncapped dye. These are good properties for a ratiometric imaging approach. Therefore, multi-spectral photoacoustic imaging (i.e. the acquisition of PA data at multiple wavelengths), allows image formation to be based on the ratio of the signals obtained at two wavelengths or the application of spectral unmixing methods. This allows correction of background signals, which do not experience any shift in spectral signature, and artefacts e.g. due to photo-bleaching. Additionally, the fluorescence spectra of **JW8**, **JW14**, **JW15** and **JW16** exhibited an emission peak around 820 nm for all four dyes, which is encouraging for dual imaging purposes (combining fluorescence and PA imaging).

Validation of Piperazine Linker in Aqueous Environment

Having established that the piperazine linker provides suitable spectral shift in organic solvents, it was necessary to undertake the same study in water, to ensure the change would still remain under physiological conditions. To achieve this, the water solubility of the dye had to be increased without changing the backbone structure. First, the generation of an **HCC** derivative bearing free carboxylic acids on the side chains was investigated (Figure 2.10). According to literature [124], this could be achieved by lowering the temperature (105 °C instead of 120 °C) and shortening the reaction time (Figure 2.10A a)). However, under these conditions only the esterified product has been generated. To avoid esterification, the reaction was also carried out in neat toluene, but without success. Finally, the focus was placed on obtaining the free diacid by ester hydrolysis of **HCC** and its derivatives with *t*-BuONa [124] but the desired products were not synthesised.

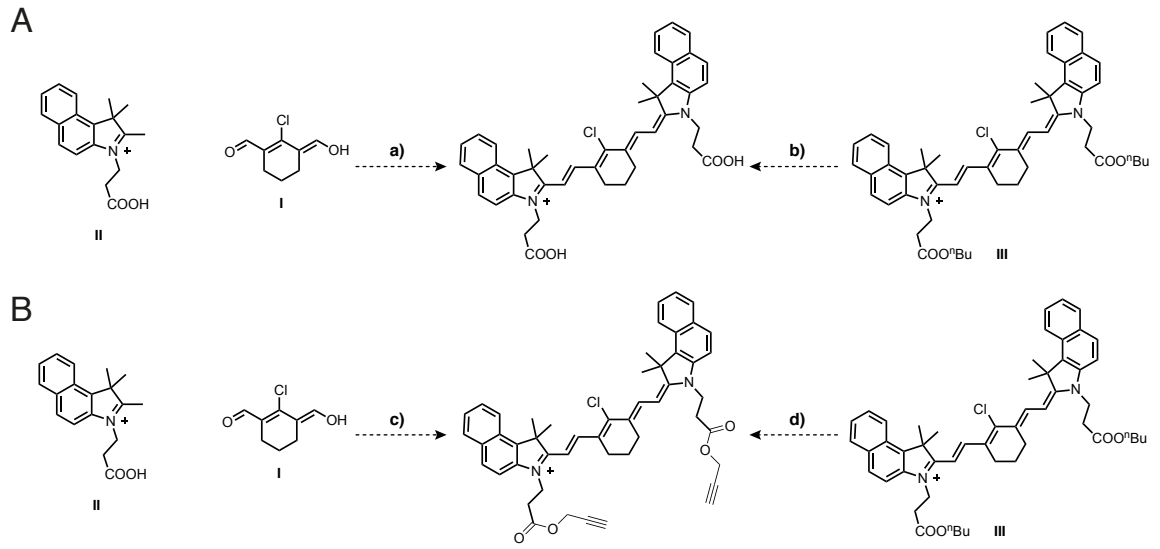

Figure 2.10 Schematic overview of the synthesis trials to modify the HCC-side chain. Reagents and conditions: (a) *n*-BuOH/toluene or neat toluene, $\Delta T = 100\text{-}105\,^{\circ}C$. (b) *t*-BuONa, THF. (c) propargyl alcohol/toluene $\Delta T = 60\text{-}120\,^{\circ}C$, $\pm$ catalyst (d) propargyl alcohol, catalyst, $\pm$ toluene.

A chemically convenient way to attach solubilizing (or later on targeting moieties) to chemical scaffolds is click-chemistry. Therefore, the same reaction was performed with propargyl alcohol instead of *n*-butanol in order to yield ester functionalities with a terminal alkyne (Figure B). Variations in temperature (60 - 120 °C), reaction time (1.5 h - 48 h) and addition of catalysts (tetrazole, imidazole) did not result in the desired product. Also, alternative routes via transesterification of **HCC** did not succeed. Hence, the approach was changed and two terminal alkyne groups were integrated on the side chains (Figure

2.11). These were then used to attach two glucose units as highly hydrophilic solubilizing units, resulting in **JW35** and **JW37** as uncapped and capped dye respectively. The synthesis route is outlined in Figure 2.11. Shortly, N-alkylation of 1,1,2-trimethyl-1H-benzo[e]indole with 4-bromo-1-butyne yielded in the quaternary indolenium salt **IV**. A double Vilsmeier-Haak reaction followed by chlorination and nucleophilic substitutions with aniline afforded intermediate **V**. The dye backbone **VI** was then obtained by a double aldol condensation like reaction of **IV** and **V**. Subsequent substitution of the chloride by piperazine generates intermediate **VII**, which then was modified with 1-azido-1-deoxy-β-D-glucopyranoside via Cu(I)-catalysed azide-alkyne click chemistry reaction yielding in the uncapped dye **JW35**. To synthesise the capped dye, **JW37**, the amine group of **VII** was first converted into the corresponding pivaloyl amide using pivaloyl chloride. The resulting intermediate **VIII** was then converted into **JW37** by attaching D-glucopyranosyl residues via Cu(I)-catalysed azide-alkyne click chemistry reaction.

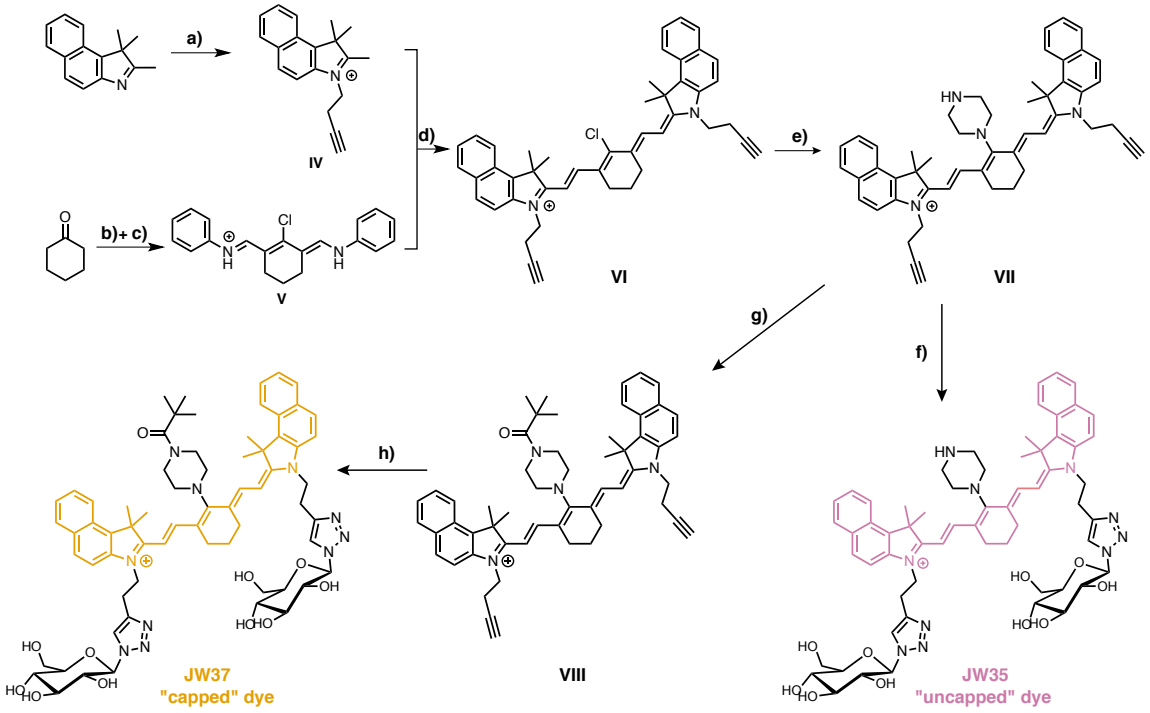

Figure 2.11 Schematic overview of the synthesis of the glucose modified HCC-piperazine derivatives, JW35 and JW37. Reagents and conditions: (a) 4-Bromo-1-butyne, NaI, MeCN, reflux (55%). (b) $POCl_3$, DMF. (c) Aniline, EtOH (72%). (d) NaOAc, EtOH, reflux (42%). (e) Piperazine, Cs_2CO_3, MeCN (85%). (f) 1-azido-1-deoxy-β-D-glucopyranoside, $CuSO_4$, Na-ascorbate, t-BuOH, H_2O (51%). (g) Pivaloyl chloride, TEA, THF (62%). (h) 1-azido-1-deoxy-β-D-glucopyranoside, $CuSO_4$, Na-ascorbate, *t*-BuOH, H_2O (48%).

Both dye derivatives showed good water solubility and the absorption spectra in different solvents (H_2O, MeOH : H_2O, MeOH, EtOH, MeCN, DMSO, PBS, PBS+Glycerol, PBS+polyethylene glycol (PEG)) proved the suitability of piperazine as linker unit (Figure 2.12). In water, the absorption maximum of both dyes appeared in the near-infrared region with an offset of 65 nm. The capped dye, **JW37**, exhibits an absorption maximum at 730 nm and a weak absorption shoulder close to 800 nm. In contrast, the uncapped derivative **JW35** features one clear maximum close to 800 nm and no distinct shoulder (Figure 2.12). Although, the absorption spectra of **JW37** showed different shapes in different solvents, it was promising that the two dyes were distinguishable in the tested solvents. The absorption shape for both dyes were consistent over a range of dye-concentrations in all solvents, suggesting that aggregation might not be the major cause for the different spectral shapes. As observed before, ions lead to broadening of the spectra.

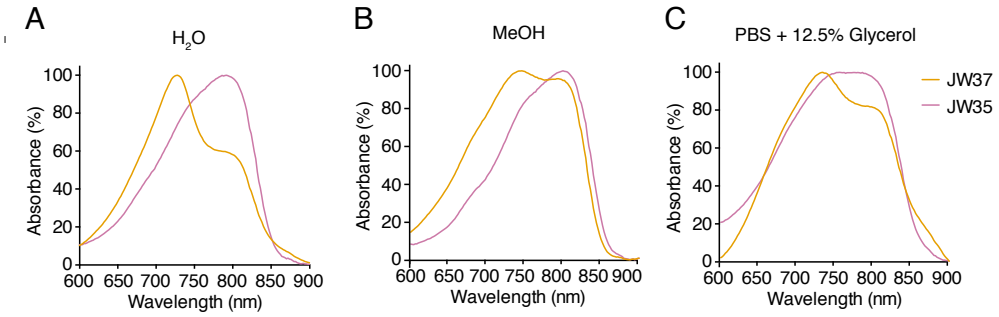

Figure 2.12 Representative absorption spectra of JW35 (20μM) and JW37 (20μM) in A) H_2O B) MeOH and C) PBS + 12.5% Glycerol.

Integrated Linker

Whilst the absorption spectra of the capped and uncapped dye were well distinguishable in water, testing in physiologically relevant buffers led to an increase in overlap in their absorption spectra (Figure 2.12). Thus it was examined if integrating the linker directly into the dye backbone might lead to a bigger difference between the capped and uncapped dye. N. Karton-Lifshin *et al.* published a similar approach in which they integrated a phenol ring at the position of the cyclohexene ring bridging C3' and C5' in the cyanine dye backbone (Figure 2.13) [52]. This generates two positive charged nitrogens with the result of a significantly different conjugation pattern. Deprotonation (or deprotection) of the phenol gives a quinone derivative, which causes a significant change in the optical properties (Figure 2.13). Unfortunately, the published dye possess an absorption maximum below 600 nm making it unsuitable for PAI *in vivo* .

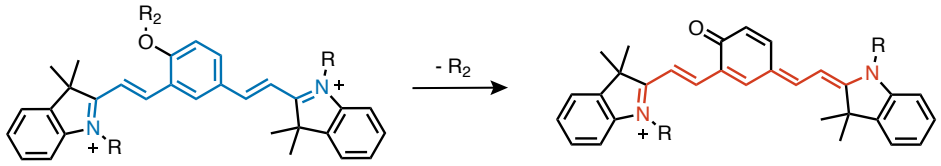

Figure 2.13 Chemical structure and concept behind the signal change of the published cyanine dye with an integrated linker. Deprotection or deprotonantion ($R_2 = H$) of the phenol leads to rearrangement of the π-system generating a free fluorophore.

To introduce a bathochromic shift of the absorption maximum, a similar dye construct was synthesised but using the corresponding benzo[e]indole derivative as a building block to extend the conjugated system. Furthermore, alkyne functionalities were integrated, as before, to then attach glucose as solubilising unit (or later other targeting structures). The synthesis route is outlined in Figure 2.14A.

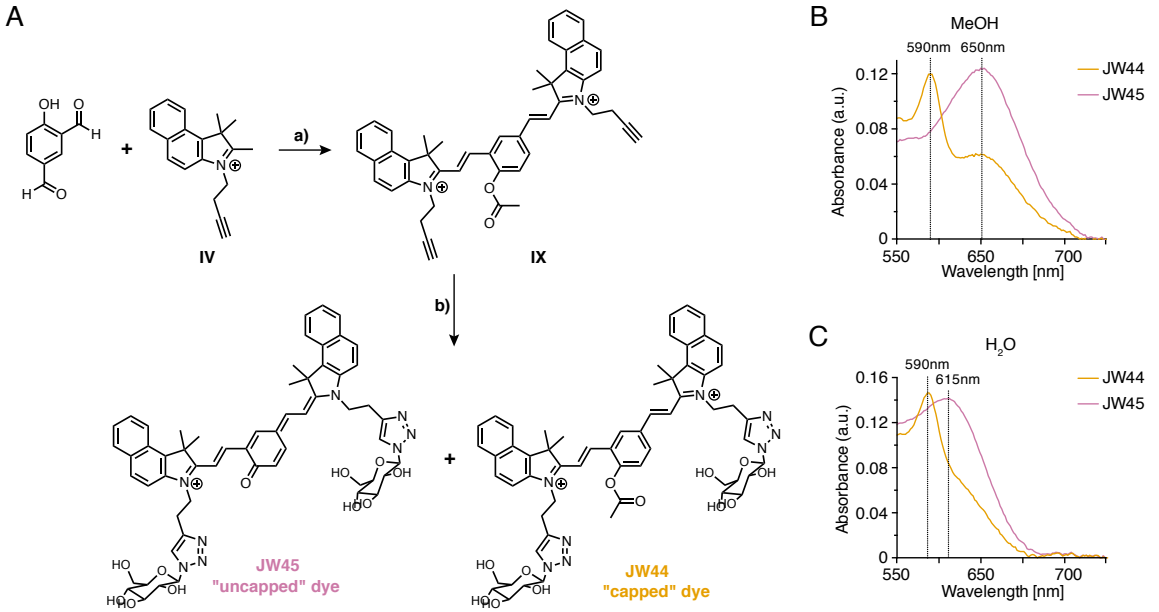

Figure 2.14 A) Schematic outline of the synthesis route for JW44 and JW45. Reagents and conditions: (a) Ac_2O, NaOAc, 80 °C (55%). (b) β-D-Glucopyranosyl azide, $CuSO_4$, Na-ascorbate, t-BuOH, H_2O (13%), on column hydrolysis yielded as well JW45 (13%). B) Absorption spectra of the capped dye, JW44 (10 μM, yellow), and uncapped dye, JW45 (10 μM, magenta), in B) MeOH and C) H_2O.

Optical characterisations of the capped (**JW44**) and uncapped (**JW45**) dye in different solvents (MeOH,MeOH : H_2O mixtures, H_2O, PBS, PBS+10%FBS, FBS) showed that the modifications moved the absorption peak by 30 nm towards the longer wavelength range and that the spectra of the two dyes were clearly distinguishable in all tested solvents. However, the absorption maxima were still below 700 nm in aqueous environment and the offset of

the two maxima amounted to 25 nm, which is far less than the observed 65 nm for the **HCC**-piperazine linker derivatives. Hence, this study confirmed that piperazine attached to the **HCC** backbone features the most promising characteristics as linker unit.

2.2.3 Photophysical Calculations

To investigate the cause of the difference in the spectral shapes between the capped and uncapped dye, computational calculations using density functional theory (DFT) were performed.

Nitrogen Hybridisation States

Central to understanding the changes in spectral properties of the capped and uncapped dyes is an understanding of the differences in the piperazine linker unit. The piperazine ring can exist in chair, boat and twist-boat conformation. Earlier studies have shown that in a similar dye molecule the unmodified piparazine ring exists in a classical chair conformation with the N-H bond axial [125]. Modifications on the nitrogen could first influence the orientation of the N-R residue and/or the hybridisation state of the nitrogen and hence the ring conformation. This might cause different sterical interactions of the piperazine and the N-R residue with the dye backbone, which could influence the optical properties. Additionally, the nitrogen attached to the **HCC** framework might be able to interact with the conjugated dye system. Thus, first the hybridisation state of the piperazinic nitrogens for the capped, uncapped and protonated uncapped dye were examined. It should be pointed out that, atomic electron hybridisation is not a property of a molecule as a whole, whose electronic structure is better described by molecular orbitals that may extend over the entire molecule. As a consequence, within a molecule, each atom can display a mixture of geometrical features commonly associated to different hybridisation states. To compensate for this, the geometry optimisation at the same level of theory was run on six reference cases, namely: pyrrolidine (1), N-methylpyrrolidine (2), protonated pyrrolidine (3), protonated N-methylpyrrolidine (4), pyrrole (5) and N-methylpyrrole (6). These molecules contain easily defined "sp^3-like" pyramidal nitrogens (1-4) and "sp^2-like" planar nitrogens (5, 6). The geometrical features that are being studied are (cf. Figure 2.15):

- δ: the improper dihedral angles defined by N_A-C_{ring}-C_{ring}-R, where R can be either H or the substituent. An entirely planar nitrogen will have all $\delta_i = 0°$.
- θ: the improper dihedral angles defined by N_B-C_{ring}-C_{ring}-C_{HCC} (specific to the piperazine moiety).

- $r_{C\text{-}N_A}$: Bond length of the N_A-C_{ring} bond on the top part of the piperazine structure.
- $r_{C\text{-}N_B}$: Bond length of the N_B-C_{ring} bond on the bottom part of the piperazine structure (attached to the **HCC** backbone; specific to the piperazine moiety).

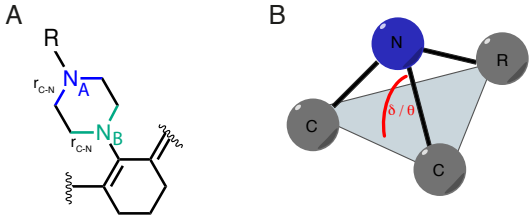

Figure 2.15 Schematic illustration of computational calculated geometrical features of the piperazine linker unit. A) Definition of N_A and N_B and the accompanying N-C bonds. B) Illustration of the improper dihedral angle.

The results are summarised in Table 2.3. In the uncapped dye, the top piperazine nitrogen (N_A) is as pyramidal ($\approx sp^3$) as the reference pyrrolidine ($\delta = 28.9°$ comparable to 28.1°). Upon protonation the angle for the uncapped dye becomes slightly more pyramidal (30.1°) while such change was not observed for the reference compounds (protonating 1 to 3). The enhanced sp^3 character is also highlighted by the elongation of $r_{N\text{-}C}$, which corresponds to a fractionally lower bond order in N_A-C_{ring}. The nitrogen in the capped dye is much less pyramidal than the unsubstituted one with an improper dihedral angle of $\delta = 5.9°$. The totally sp^3 reference (2) has 29.8°, while the corresponding sp^2 planar nitrogen, when substituted, has $\delta = 2.8°$. Thus, the results indicate that substitution makes the nitrogen 89% planar. This can be further observed by looking at $r_{N\text{-}C}$. The bond length decreases only slightly from the unsubstituted case, showing that the added π-contribution to the N-C_{ring}-bond is not significant. For both dyes, the dihedral angle θ of the bottom nitrogen (N_B) was assessed to be similar for the capped and uncapped dye and shows neither a planar nor fully pyramidal geometry. This suggests that the nitrogen hybridisation is not the main reason for the difference in the optical properties of the capped and uncapped dye.

Table 2.3 Summary of the computational investigated geometrical properties of the piperazine linkage.

	uncapped dye a	uncapped dye b	capped dye	1	2	3	4	5	6
δ (°)	28.9	30.1	5.9	28.1	29.8	28.2	28.8	0.0	2.8
θ (°)	11.0	18.1	10.8						
$r_{C\text{-}N_A}$ (Å)	1.46	1.52	1.46	1.46	1.46	1.54	1.52	1.38	1.38
$r_{C\text{-}N_B}$ (Å)	1.47	1.45	1.47						

[1] Computational calculations were performed on the optimised structure of the molecules in gas phase.

[2] Uncapped a referring to the unprotonated state of the uncapped dye, with the free amine group; uncapped b to the protonated one version.

[3] 1-6 referring to the reference compounds: pyrrolidine (1), N-methylpyrrolidine (2), protonated pyrrolidine (3), protonated N-methylpyrrolidine (4), pyrrole (5) and N-methylpyrrole (6).

HCC-Backbone Confirmation

The next approach was to assess the minimum-energy conformations of the capped and uncapped dye through geometry optimisation in the gas phase using DFT. In particular, it was of interest to investigate whether sterically demanding groups attached to the nitrogen together with the different hybridisation of the nitrogen have an influence on the conformation of the **HCC** backbone.

The results suggested a distinct difference in the conformation of the **HCC**-backbone between the two dye derivatives: The two terminal benzoindole moieties in the capped dye, **JW41**, are strongly twisted in respect to each other (74.0°), whereas the uncapped dye, **JW35**, has a twist of only 23.3° (Figure 2.16A, B). This twist-decrease of 50.7° going from the capped to the uncapped dye results in an improved electron-delocalisation, which causes the red-shift in the absorption spectra of **JW35**. To scrutinise if the non-planar piperazine confirmation is the cause for this, the same calculations were performed with the 4-**HCC**-oxyaniline dyes. These dyes bearing a planar aromatic linker, that can easily align orthogonal to the **HCC**-backbone axis and thus minimise the steric interactions of the nitrogen subsituents with the backbone. As clearly evident in Figure 2.16 C and D, in the minimum-energy conformation, the axis of the aromatic linkers are orientated in an 90° angle to the dye backbone axis, leave a nearly planar **HCC** backbone, no matter if the nitrogen is capped or uncapped. This gives rise to the identical absorption for both derivatives, as

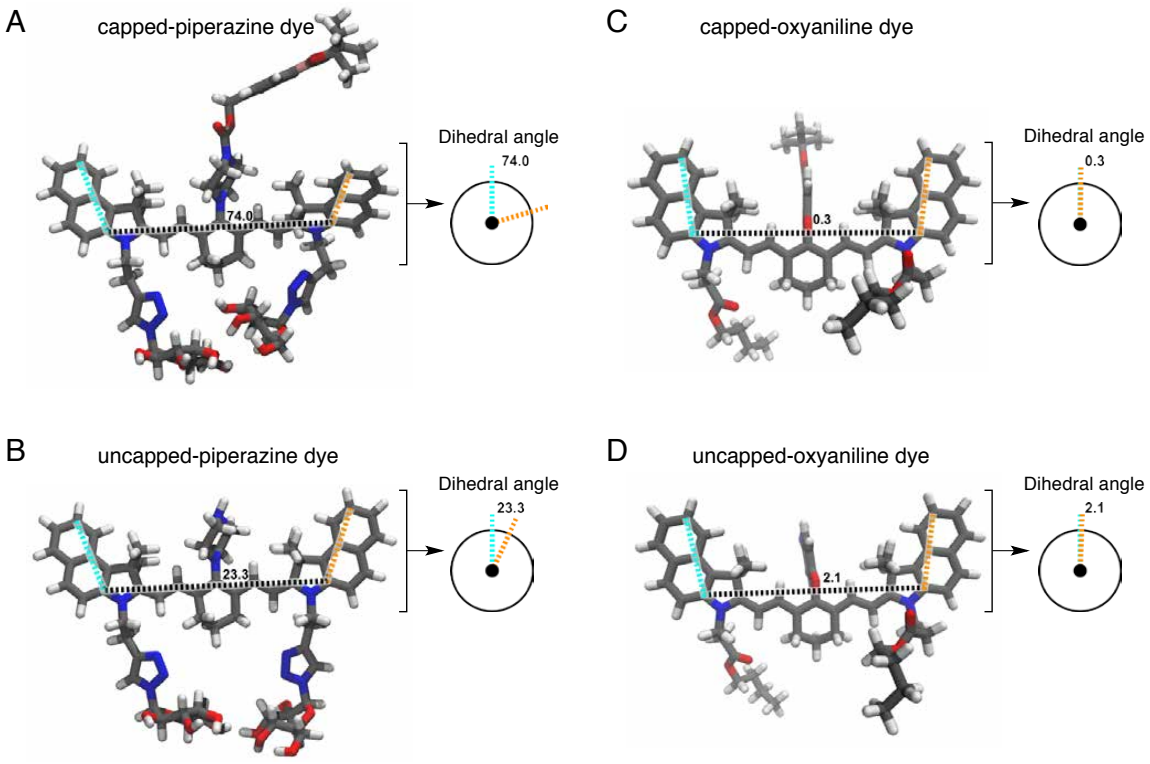

Figure 2.16 Investigation of the effect of the different linker units on the conformation of the dye backbone. The minimum-energy conformations of A) the capped-piperazine dye JW41 (see p. 57), B) the uncapped-piperazine dye (JW35), C) the capped-oxyaniline dye (JW11) and D) the uncapped-oxyaniline dye (JW13) were obtained through geometry optimisation in the gas phase using density functional theory. To quantify the relative orientation of the two terminal polycyclic moieties, a dihedral angle was defined as shown in the picture. (Calculations of the capped-piperazine dye (A) were already performed with the aimed final contrast agent having a boronic ester attached.)

demonstrated previously (Figure 2.9). In conclusion, computational calculations confirmed that piperazine features promising characteristics as linker group.

2.2.4 Targeting and Dye Backbone Modification Trials

Having established a route to induce a spectral shift in the **HCC** framework, the next step was to consider how to target the dye to a particular disease site of interest.

Cancer Targeting

The aim was to design a bifunctional, activatable probe, which is not only able to visualise H_2O_2 generation in general, but is also specific in its read-out to a defined patho-physiological condition. The ability of cancer cells to modify cellular ROS production is important in malignant progression, therapy response and resistance. Combining the high temporal and spatial resolution of PA imaging with a new cancer- and ROS species-specific probes poses a promising approach to address the unmet need for elucidating the role of redox biology in carcinogenesis, tumour progression and treatment response. By targeting the probe to cancer cells, it is also possible to exploit the diversity in well studied, cancer targeting structures and already characterised cancer mouse models in our laboratory that are well suited for PA *in vivo* imaging [131].

The use of a simple one-step functionalisation via click chemistry (see 2.2.2) showed promising results for its use to embed the targeting moiety: The attachment of the two β-D-glucopyranoside groups via a short aliphatic spacer maintained the different optical signatures of the capped and uncapped dyes (cf. **JW8** vs **JW35**, **JW16** vs **JW37**) and the small, hydrophilic units did further support solubility of the probe. Additionally, targeting of glycolysis with 2-deoxyglucose has been reported as a potential strategy for cancer targeting in several studies using small molecules and NIR dyes [40, 132–134]. This targeting approach exploits the increased demand of glucose in tumours, which is accompanied with an over-expression of glucose transporters (GLUTs) [135, 136]. It should, however, be noted that, targeting through 2-deoxyglucose is not exclusively specific for cancer cells and can also lead to accumulation in inflammatory processes, as it was indicated in studies with ^{18}F-fluorodeoxyglucose using positron emission tomography [137]. But as the temporal accumulation profile in malignancy differs from that for inflammatory processes, it is possible to study both simultaneously with dual- or multiple-time-point imaging strategies [137, 138]. Taking all this into account, and having already synthesised the uncapped derivative, **JW35**,

β-D-glucopyranosyl azide was chosen as preliminary, clickable targeting structure to validate the concept of the bifunctional contrast agent.

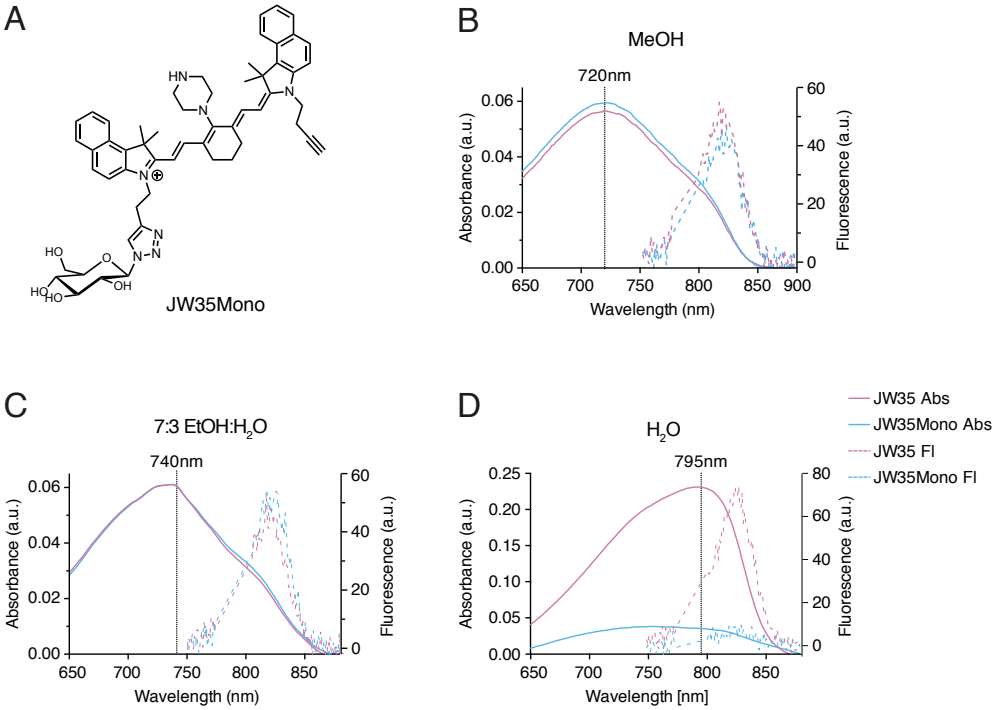

Figure 2.17 Structure and optical properties of JW35 and JW35Mono in different environments. A) Chemical structure of JW35Mono. Average absorption (n = 3, solid line) and fluorescence (n = 3, dashed line) spectra of B) JW35 and JW35Mono (0.3 μM) in MeOH and EtOH : H_2O and C) in water (3 μM). Fluorescence spectra were recorded upon excitation at 785 nm.

Considering that the cellular uptake of 2-deoxyglucose-functionalised probes is based on glucose transporters (GLUTs) [139], which mediate the cellular uptake of glucose and other small molecules [140], it was tried to minimise the size of the new contrast agent by implementing only one targeting unit instead of two. To investigate if one β-D-glucopyranosyl group is sufficient to maintain water solubility and if an asymmetric dye structure does influence the optical properties (decrease in molar absorptivity, see section 2.2.1), the previously described click reaction was performed with only 1 eq. of β-D-glucopyranosyl azide to obtain **JW35Mono** (Figure 2.17) - the mono-functionalised derivative of **JW35**. The absorption and fluorescence spectra of **JW35Mono** in pure organic solvent (MeOH) as well as a solvent mixture with high proportion of organic solvent (ethanol:water (7:3)) did not show any significant difference to those of **JW35** (Figure 2.17B,C) indicating that the asymmetry does not influence the optical properties. However, the absorption as well as fluorescence characteristics of **JW35Mono** in water reveals strong deviations (Figure

2.17D) implying poor solubility in aqueous environment making this approach impractical for biological applications. **JW35** was therefore used for the remainder of the studies.

Dye Backbone Modifications

A main criterion that should be addressed by contrast agents for PA *in vivo* imaging is that their photophysical properties should not be influenced by the physiological environment. For example, the clinically approved cyanine dye, ICG, has been proposed and studied as contrast agent in cancer imaging [141, 142]. However, the optical properties of ICG are highly dependent on its environment, its solubility and stability in aqueous solutions is limited (cf. section 2.2.1) and its strong plasma binding accompanied with rapid hepatic clearance limit its tumour accumulation and restrict its *in vivo* application [143, 144]. To overcome these disadvantages, it was aimed to further increase the hydrophilicity of the probe, as it was shown to reduced plasma protein binding (cf. section 2.2.1). This should facilitate the extravasation of the dye into the extracellular space and slow down the hepatic clearance [144]. Another advantage of hydrophilic dyes is their reduced tendency to form aggregates and enhanced photophysical stability in different environments (cf. section 2.2.1).

One common approach to improve the hydrophilic character of cyanine dyes is to integrate sulfonate- or carboxyl-groups on the terminal indole moieties (e.g. SulfoCy7 vs Cy7, section 2.2.1) [144, 145]. Sulfonate groups were also shown to not strongly influence the wavelength of the absorption and fluorescence peaks. However, most approaches are based on modifying terminal trimethyl-3H-indole functionalities instead of benzo[e]indole analogue. Changing the dye's backbone towards the bicyclic structure would have been unfavorable: reducing the number of aromatic rings causes a hypsochromic shift in the optical properties (cf. Cy7 vs Cy7.5 (section 2.2.1 and section 2.2.2) and the decreased size of the terminal polycyclic functionality is likely to influence the capability of the piperazine linkage to generate a significant signal change, which is based on steric and electronic interactions with the terminal aromatic groups (cf. section 2.2.2). It was therefore aimed to use a sulfonated 2-methyl-1H-benzo[e]indole building block to generate a more hyrophilic dye backbone [146, 147].

Different strategies based on sulfonation reactions of 2,3,3-trimethyl-3H-indole in patents have been exploited to reach this aim. Attempts to do so are summarised in Figure 2.18. In brief, even though some of the intermediates could be confirmed by mass spectrometry analysis, most were highly viscous, poorly soluble and difficult to purify, which made it challenging to ensure the formation of the correct compounds and to synthesise the complete dye backbone based on these scaffolds. Thus this method was not further pursued. A future

approach would be to synthesise the mono- or disulfonated building block starting from 6-amino-1,3-naphthalenedisulfonic acid [121].

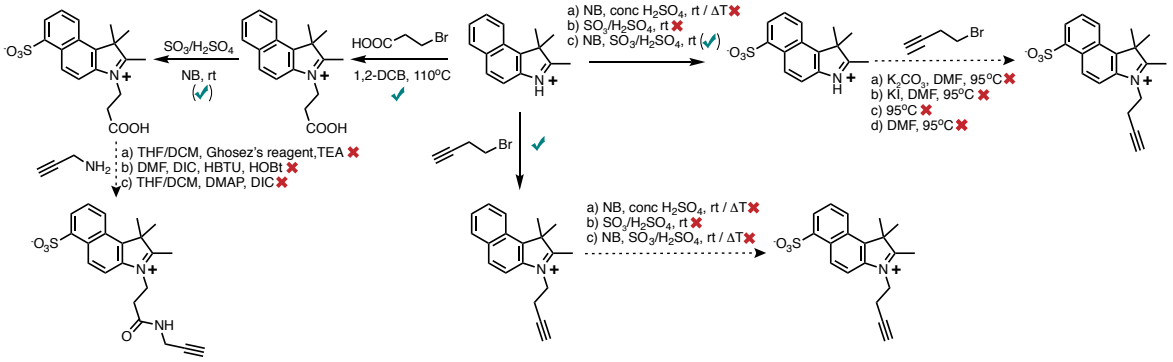

Figure 2.18 Schematic illustration of the unsuccessful attempts to generate sulfonated 1,1,2-trimethyl-1H-benzo[e]indol derivatives.

2.2.5 Final Design, Synthesis and Photophysical Examination of the new Activatable, Bifunctional PA Probe

Having found a suitable dye backbone, linker and targeting approach, it was next aimed to integrate the H_2O_2-reactive group beyond the linker unit. In designing a chemoselective H_2O_2-reactive PA imaging probe, the focus was placed on the well established oxidation-immolation of an aryl boronate attached to a benzylic leaving group in para-position [30, 128]. The additional carbamate linkage increases the elimination kinetics upon oxidation to release the uncapped dye bearing the free amine group.

Synthesis of the new Bifunctional, Activatable Probe

The synthesis route of the final bifunctional, activatable probe, **JW41**, is outlined in Figure 2.19.

Shortly, intermediate **VII** (synthesised as described before, cf. Figure 2.11) was treated with boronate **X**, generated by reaction of 4-nitrophenylchloroformate with 4-(4,4,5,5-tetramethyl-1,3,2-dioxaborolan-2-yl)phenyl)methanol. The resulting intermediate **XI** was then converted into **JW41** by attaching D-glucopyranosyl residues via Cu(I)-catalysed azide-alkyne click chemistry reaction.

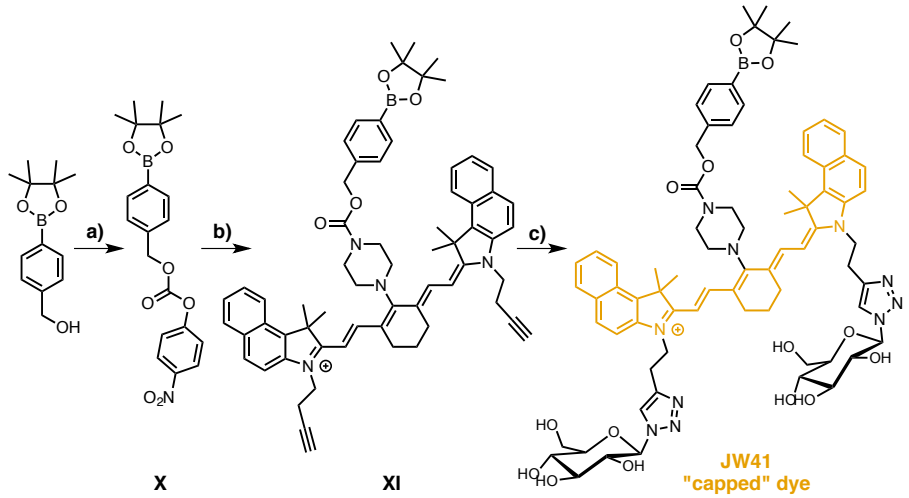

Figure 2.19 Schematic outline of the synthesis route for the final bifunctional, activatable probe, JW41. Reagents and conditions: (a) 4-Nitrophenylchloroformate, Pyridine, DCM. (b) VII, DIPEA, DMF (39%). (c) 1-Azido-1-deoxy-β-D-glucopyranoside, $Cu(CH_3CN)_4PF_6$, TBTA, MeCN (33%).

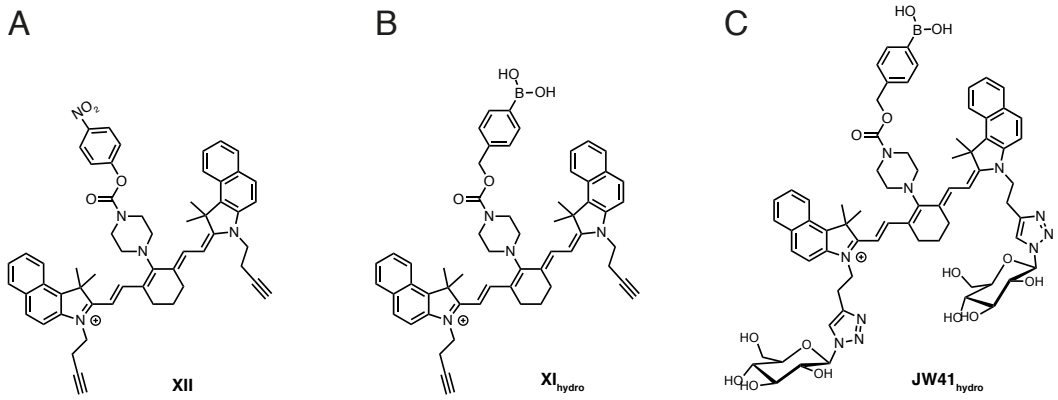

Figure 2.20 Chemical structures of side products of XI and JW41. A) 4-nitrophenyl-piperazine derivative XII B) hydrolysed boronic acid derivative, XI_{hydro} of XI C) hydrolysed boronic acid derivative, $JW41_{hydro}$, of JW41.

It is worth mentioning that during the synthesis of intermediate **XI** the main product was the corresponding 4-nitrophenyl-piperazine derivative **XII** (Figure 2.20A), which could be isolated and characterised by HRMS and NMR. In addition, intermediate **XI** is prone to hydrolysis forming $\mathbf{XI}_{hydro}$ (Figure 2.20B) and degrades during purification by column chromatography. Different columns for normal phase (silica, alumina) and reversed phase chromatography as well as different solvents, including MeCN, THF, EtOH, MeOH, H_2O with the addition of either acetic acid (AcOH), formic acid (FA), trifluoroacetic acid (TFA) or NH_4OAc buffer adjusted to the higher buffering range of pH 5.7, have been tested. Summarising the findings, none of the tested conditions were able to elute the **XI** from the

column by normal phase silica chromatography; using neutral alumina as stationary phase did allow the elution of the desired product, **XI**, but only by applying a steep gradient to 20% methanol causing co-elution with the 4-nitrophenyl by-product **XII** and the hydrolysed product $\mathbf{XI}_{\text{hydro}}$. Using a longer gradient increased the retention time leading to further hydrolysis and degradation. As methanol was found to promote hydrolysis, other solvents were tested but none eluted the product **XI** from the neutral alumina column.

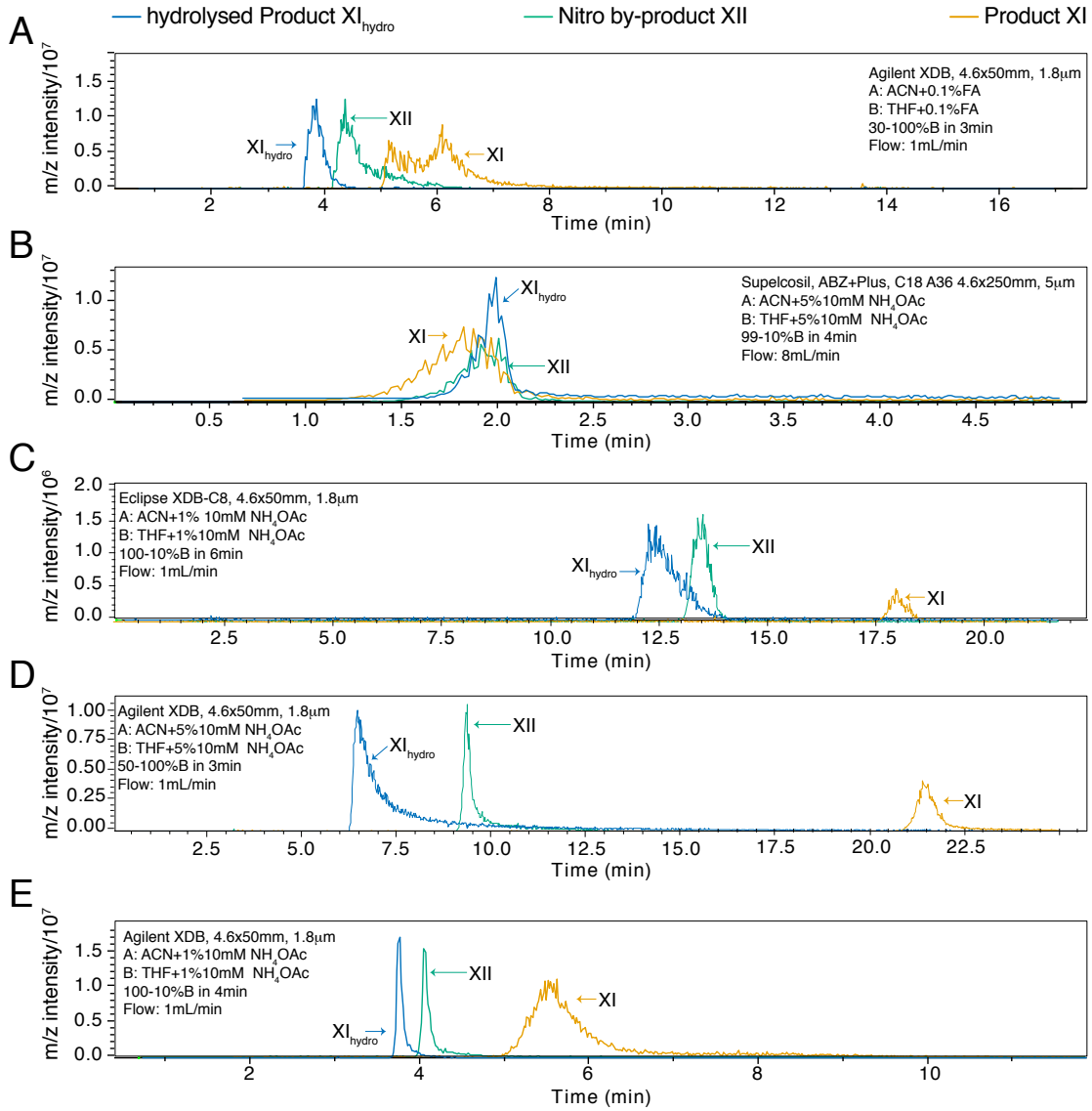

Figure 2.21 Examples of purification trials for XI. A) and B) Representative chromatograms of conditions which allowed early elution but suboptimal separation. C) and D) Representative chromatograms of conditions which lead to too late elution of the product. E) Conditions which led to best purification in respect of elution time and separation.

The hydrolysis of boronic esters is acid catalysed transforming the ester (**XI**) into the dihydroxy boronic acid, $\mathbf{XI}_{\text{hydro}}$. Under typical reverse phase HPLC conditions (aqueous solvent A, organic solvent B e.g. MeCN, MeOH or THF), **XI** did not elute from the column as a MeCN : water mobile phase was not strong enough to elute these highly lipophilic analytes. Thus, a non-conventional reverse-phase mode was tested using a nearly water-free mobile phase where two organic solvents (MeCN and THF) with different selectivities were used for solvent A and solvent B with a C18 HPLC column. THF is a H-bond acceptor while MeCN has a dipole. Arbitrarily, solvent A was MeCN while solvent B was THF. Using this system without a modifier, no separation between **XI**, **XII** and $\mathbf{XI}_{\text{hydro}}$ was achieved. Only through the addition of 0.1% FA to both, solvent A and solvent B, some separation was obtained with $\mathbf{XI}_{\text{hydro}}$, being the first to elute while **XI** being the most lipophilic and thus most retained compound (Figure 2.21 A). As the separation of the product **XI** was suboptimal (broad peak overlapping with **XII**), the pH of the mobile phase was increased to reduce the hydrolysis of **XI**. Therefore, 10 mM NH_4OAc at pH 5.7 was investigated as the hydrolysis of **XI** should be reduced at higher pH. Using 1-5% of 10 mM NH_4OAc (pH 5.7) as a modifier for solvent A and B, some separation could be achieved depending on the start and end ratio of solvent A to solvent B as well as the gradient rate (Figure 2.21B-E). The chromatograms in Figure 2.21B,C and E illustrating the separation obtained with a MeCN gradient, while Figure 2.21D shows a separation with a THF gradient. Both gradients led to the elution order with $\mathbf{XI}_{\text{hydro}}$ being first, closely followed by **XII** and much later the product **XI**. The separations were found to be very sensitive to the gradient used and in all cases the product **XI** eluted as a very broad peak. Although using MeCN + 1% 10 mM NH_4OAc (pH 5.7) and THF + 1% 10 mM NH_4OAc (pH 5.7) as solvents did enable a relatively fast elution and good separation of intermediate **XI** (Figure 2.21E), this method could not be applied for purification as the product degraded in THF as soon as MeCN evaporated. Thus, the best compromise was the purification with neutral alumina and using impure **XI** in the next step.

Similarly to intermediate **XI**, the final probe, **JW41**, was prone to on-column hydrolysis resulting in the formation of $\mathbf{JW41}_{\text{hydro}}$ (Figure 2.20C) and degradation into smaller fragments. However, due to the increased hydrophilicity of **JW41**, fast elution with good separation could be obtained by reversed phase HPLC with MeCN + 0.1% TFA and H_2O + 0.1% TFA (Figure 2.22A). The use of aqueous phase and the addition of the strong acid TFA, is unfavourable, since both promote on-column hydrolysis and degradation. Unfortunately, weaker acids (AcOH or FA) or buffers (NH_4OAc buffer (pH 5.7)) and/or the use of only organic solvent (MeCN and THF) systems were unable to wash the dye off the column on a preparative HPLC system having an internal diameter of 1 inch, using flow rate of

20 mL/min. Using smaller, analytical columns with an internal diameter of 4.6 mm permitted less loading of the sample but faster chromatography resulting in reduced time of **JW41** on the column and in contact with the acidic mobile phase (Figure 2.22B). It also enabled the use of FA as acid instead of TFA. Thus, although limiting the purification to small quantities at a time, purification was carried out on an analytical column (internal diameter of 4.6 mm) with MeCN 0.1% FA and H_2O + 0.1% FA as solvents.

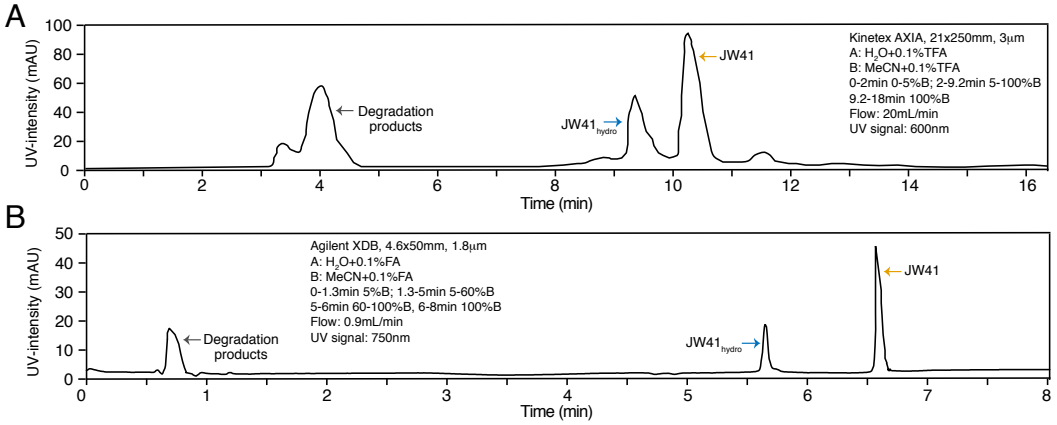

Figure 2.22 Examples of purification approaches of JW41. A) Representative chromatogram of purification on a preparative HPLC system. The UV signal at 600 nm is plotted. B) Representative chromatogram of purification on a analytical HPLC system. The UV signal at 750 nm is monitored.

Photophysical Properties of the New Bifunctional, Activatable Probe

It is an essential requirement for the determination of H_2O_2-changes to precisely distinguish the capped (**JW41**) and uncapped (**JW35**) probe. Thus, to initially characterise the efficacy of the new probe, the optical and photoacoustic properties of **JW41** were assessed at different concentrations and in different environments and compared to those of **JW35**. The results obtained from absorption, fluorescence and PA spectroscopy suggest that the capped and uncapped contrast agents are well distinguishable in aqueous environment with all three modalities (Figure 2.23).

The absorption of **JW41** and **JW35** appears in the near-infrared region with peak absorption at 730 nm for **JW41** and 795 nm for **JW35**, leading to an offset of 65 nm. It was shown to be independent from the concentration (Appendix Figure A.5), which reinforces the assumption that the effect is not aggregation-based. The emission maximum is located at ∼825 nm for both forms, leading to a large Stokes shift of about 95 nm for **JW41**, which supports an increase in signal to noise ratio for fluorescence imaging. Even though the capped and uncapped dyes showing an emission maxima at around the same wavelength, the fluorescence intensity

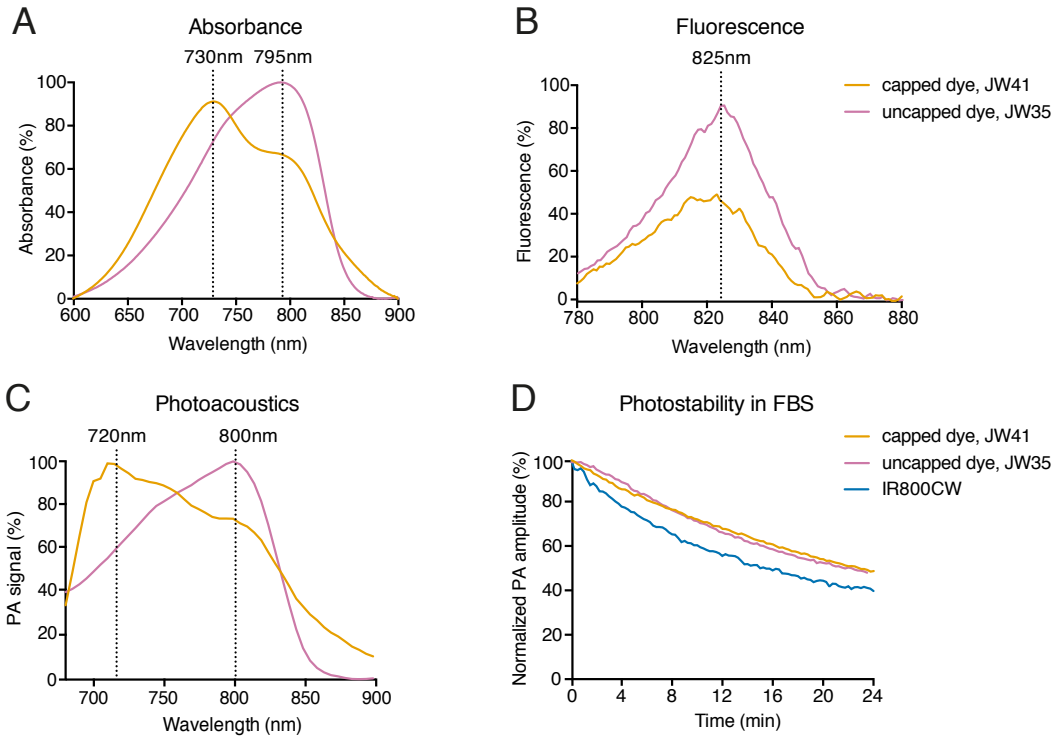

Figure 2.23 Optical and PA properties of the capped dye, JW41, and uncapped dye, JW35. Normalised absorption (A), fluorescence (excitation at 740 nm) (B) and PA (C) spectra of JW41 and JW35 (10 μM in H_2O) are shown, illustrating the different Optical and PA properties of the capped and uncapped dye. The absorption spectra are normalised to 100 % at the peak of JW35, the PA spectra are separately normalised both to 100 % at their peak. D) Photothermal stability study of JW41 and JW35 with IR800CW as reference (2.5 μM in FBS).

of the uncapped dye ($\phi_{Fl(JW35,ex:740nm)} = 0.01234 \pm 0.00146$) in aqueous environment increased by over 100% relative to the one of the capped dye ($\phi_{Fl(JW41,ex:740nm)} = 0.00626 \pm 0.00086$), which can be reasoned by photon-induced electron transfer in the case of **JW41**. This is mirrored by the total integrated emission intensity (brightness, B) of the capped dye (B = 456.6) in water being half the brightness of the free dye (B = 950.95), with molar extinction coefficients of $\varepsilon_{JW41(730nm)} = 61400\,M^{-1}cm^{-1}$ and $\varepsilon_{JW35(790nm)} = 77450\,M^{-1}cm^{-1}$ (Figure 2D). An overview of the optical properties of **JW41** and **JW35** in three different environments is given in Table 2.4. The PA characteristics appeared similar to those obtained by absorption spectroscopy (Figure 2.23C). The PA maxima of **JW41** was located at 720 nm and the PA maxima of **JW35** at 800 nm, resulting in an off-set of 80 nm - a promising feature for ratiometric measurements. Additionally, both dyes showed encouraging photothermal stability for *in vivo* applications (Figure 2.23D) compared to IR800CW, the dye showing the most promising results in previous studies (cf. section 2.2.1) and is already used in PA imaging [148, 149].

Table 2.4 Photophysical properties of JW41 and JW35. These were obtained from bulk UV-vis absorption and fluorescence measurements of the dyes.

Dye	Solvent	λ_{Abs} (nm)	λ_{Em} (nm)	λ_{Em} - λ_{Abs} (nm)	ε_{max} ($M^{-1}cm^{-1}$)	$\phi_{(Fl)}$	B (a.u.)
JW41	H_2O	730	826	96	61400	0.0063	456
	MeOH	740	826	86	385150	0.0338	17393
	EtOH:H_2O 7:3	805	823	18	385150	0.0351	11313
JW35	H_2O	790	822	32	77450	0.01234	951
	MeOH	718	821	103	232300	0.0515	7635
	EtOH:H_2O 7:3	720	821	101	126200	0.0571	4010

Validation of Spectral Unmixing Feasibility

In order to get a precise read-out of the H_2O_2-production *in vivo* by the means of PA tomography, it is essential that multispectral PA imaging is capable to accurately detect and quantify the relative concentrations of the capped and uncapped dye if present simultaneously. For this purpose, different concentrations and mixtures of **JW41** and **JW35** in tissue-mimicking phantoms were measured (Figure 2.24B). Subsequently, spectral unmixing was performed to distinguish the probes from each other and the background and to calculate the relative concentrations of the probes.

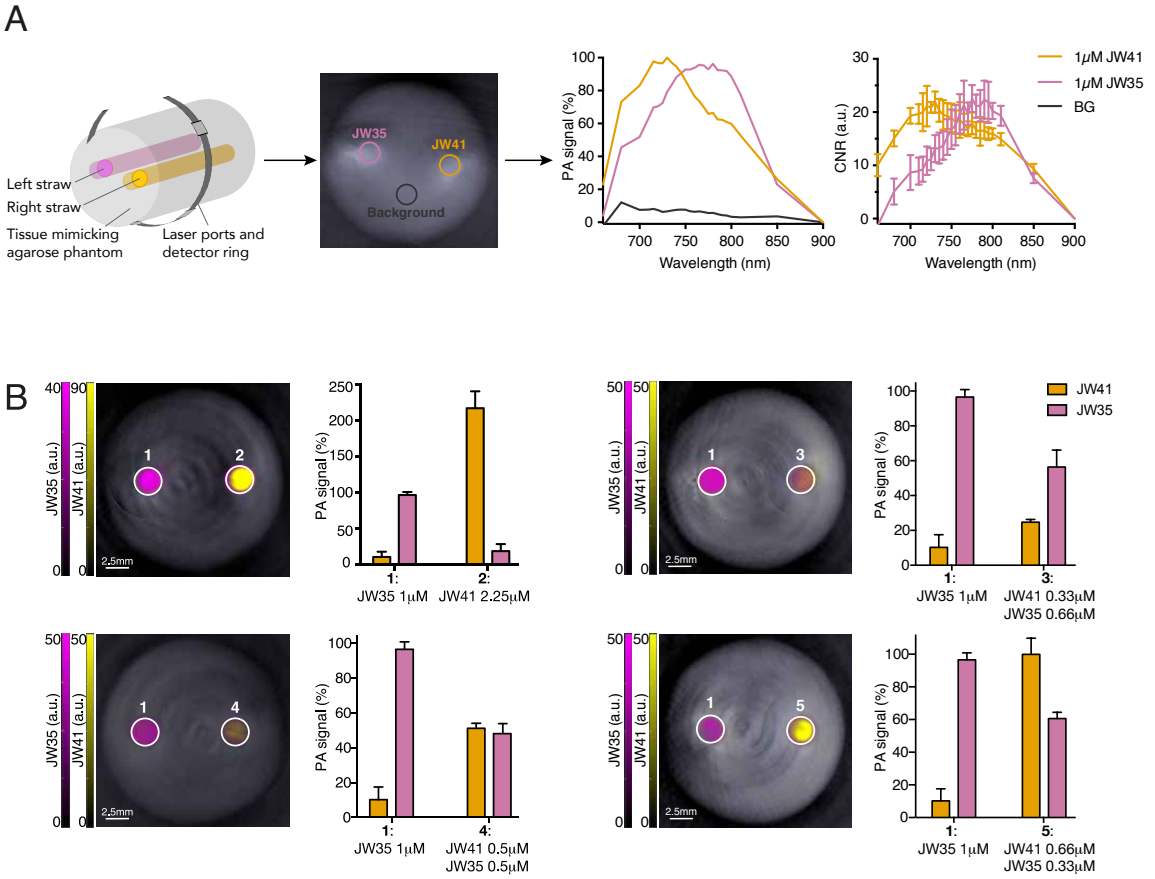

Figure 2.24 Spectral unmixing study of JW41 and JW35 in tissue-mimicking phantoms. A) Schematic graphic of experimental set up (left) and image of the tissue mimicking phantom (middle) with ROIs used for analysis are illustrated. The normalised, offset corrected PA spectra, which form the foundation for subsequent multispectra processing by linear regression, and the contrast-to-noise ratio (n = 3) obtained in the tissue mimicking phantom are plotted. B) Phantom images containing straws filled with different aqueous JW41-JW35 solutions are outlined in column 1 and 3, the results obtained by linear regression in column 2 and 4 right to the associated phantom image. The weights contributed by the JW41 and JW35 spectra to each straw signal are plotted relative to a reference straw (1) containing 1 μM JW35. The relative accuracies for the different mixtures are: straw 2: - 3.4% (JW41), + 18.4% (JW35); straw 3: - 25.9% (JW41), - 15.4% (JW35); straw 4: + 2.5% (JW41), - 3.7% (JW35); straw 5: + 49.9% (JW41), +81.8% (JW35), 10.7% (JW41, JW35 in respect to mixture ratio).

Basis of the analysis were the PA spectra of **JW41**, **JW35** and the background obtained in a tissue mimicking phantom (Figure 2.24A), which were used for multispectra processing by linear regression. The results are summarised in Table 2.5. The data obtained with spectral unmixing showed a relative accuracy (% deviation from the known concentration) between 2.5% and 25.9% for sample 1 to 4 in respect to reference straw 1 containing 1 μM **JW35**. The relative accuracy of the mixture in test straw 5 (0.66 μM **JW41** and 0.33 μM **JW35**) in respect to the **JW41**-**JW35** ratio was 10.7%, but above 45% when compared to the reference straw with 1 μM **JW35**. This demonstrates one of the limitations of the study. Even within the same imaging acquisition session, the absolute signal intensity varied often between different slices and time points. The variations were more pronounced when comparing the values obtained for the same dye solution from different imaging acquisition sessions. Additionally, some signal-crossover is present, which can cause result in signal misclassification. However, taking these considerations into account during the image analysis process and normalising the values against the reference straw (1 μM **JW35**) present in the same phantom (see 2.24, these findings illustrate the effective detection and separation of the two dyes from each other in phantoms and the background with a preciseness suited to detect changes in H_2O_2 under pathological conditions.

Table 2.5 Spectral unmixing studies of JW41 and JW35 in tissue-mimicking phantoms.

Concentration (%)		PA signal (a.u.)		PA signal (%)[1]	
JW35	JW41	JW35	JW41	JW35	JW41
100	0	42.1 ± 9.3	4.0 ± 2.5	97	10
0	225	7.7 ± 4.1	90.9 ± 9.8	18	217
66.6	33.3	32.3 ± 5.6	14.1 ± 0.9	56	25
50	50	16.7 ± 1.9	17.7 ± 0.9	48	51
33.3	66.6	22.8 ± 1.5	37.5 ± 3.7	61	100

[1] Normalised to reference straw with 1μM JW.

2.3 Summary and Conclusions

The aim described in this chapter was the development of an activatable, bifunctional contrast agent for PA and fluorescence imaging.

The optical and photoacoustical behaviour of different commercially available dyes have been assessed in different environments to gain a better insight into how different structural features influence those properties.

Thereafter, different linker-derivatives of a heptamethine carbocyanine (**HCC**) dye backbone were synthesised and evaluated. Piperazine was found to possess beneficial features as linker unit: the piperazinyl-**HCC** derivatives imitating the capped probe showed, depending on the sterical demand of the nitrogen substituent, different absorption profiles clearly distinguishable from the uncapped derivative. Computational calculations using density functional theory have been applied to investigate the cause of the difference in the spectral shapes between the capped and uncapped dye. These calculations suggest that the absorption change is caused by a decreased twist in the relative orientation of the two terminal benzoindole moieties going from the capped dye to the uncapped derivative.

Improved solubility and cancer targeting were achieved by conjugating two glucose units to the side chains of the NIR dye via click-chemistry. Click-chemistry is a chemically convenient way to conjugate biomolecules to chemical scaffolds and hence this linkage opens the opportunity to easily exchange the glucose moieties with other targeting structures specific for different molecular markers expressed by cancer or other pathological cells. Further functionalisation of linker unit of the optimised dye structure with an aryl boronate attached to a benzylic leaving group in para-position, resulted in the new activatable, bifunctional contrast agent, **JW41**, promising for application in PA and fluorescence imaging. The use of **JW41** and its uncapped counter dye, **JW35**, in tissue-mimicking phantoms demonstrated that the spectral unmixing of the obtained PA images can be achieved and allows the relative quantification of the dyes concentration with accuracies between 2.5% and 25.9%. However, truly quantitative PA measurements of the concentration of the dyes would require further factors to be taken into account such as the light distribution over the total illuminated volume, the generation of the photoacoustic signal as well as the influence of the dyes on the fluence. Therefore, more complex phantoms and unmixing models should be considered. Additionally, although phantom studies can only give a limited insight into the dye's performance *in vivo* and the molecular structure of the dye could perhaps be optimised to increase the difference in their spectral shapes, the optical and photoacoustic properties of the new contrast agent in its existing configuration seem sufficient for specific H_2O_2 imaging under biological conditions.

2.4 Material and Methods

2.4.1 Chemical Synthesis

General Considerations

All reagents and materials used in the synthesis of the compounds described below were bought from commercial sources, without prior purification. Solvents were either dried (THF from $LiAlH_4/CaH_2$ with triphenylmethane as indicator; CH_2Cl_2, MeOH and ACN from CaH_2) and distilled in house or used as supplied.

Thin layer chromatography was carried out using with silica gel 60F (Merck) on glass plates. Compounds were visualised by UV light (254 and 366 nm) or by using a vanillin or basic potassium permanganate stain (3 g $KMnO_4$, 20 g K_2CO_3, 2.5 mL 10 % aq. NaOH, in 400 mL deionised H_2O) followed by heating. Flash chromatography was carried out either on an automated system (Combiflash Rf+ or Combiflash Rf Lumen; UV detector was set to a wavelength of 254 nm and 280 nm) using prepacked RediSep cartridges of silica or alumina (pH = 7) or manually using silica gel high-purity grade (9385, Merck, pore size 60 Å, 230-400 mesh particle size) or C18-reversed phase silica gel (Merck 60757, pore size 90 Å, 230-400 mesh particle size). LCMS analysis of samples was performed on different systems:

a) A 3000 LC system connected to a Bruker amaZon X Ion Trap mass spectrometer using 0.1 % formic acid in water and acetonitrile as mobile phase and a Kinetex C18 column (Phenomenex, 50 x 2.1 mm, 2.6 μm). Water + 0.1 % formic acid (solvent A) and acetonitrile + 0.1 % formic acid (solvent B) were used as mobile phase. The gradient was adopted to the compounds.

b) Waters Acquity H-class UPLC coupled with a single quadrupole Waters SQD2 and a ACQUITY UPLC CSH C18 column (130 Å, 1.7 μm, 2.1 mm x 50 mm). The conditions of the UPLC method are as follows: Solvent A: Water + 0.1 % Formic acid; Solvent B: Acetonitrile + 0.1 % Formic acid; Gradient of 0-2 minutes 5 % - 100 %B + 1 minute 100 % B with re-equilibration time of 2 minutes. Flow rate: 0.6 mL/min; Column temperature of 40 °C; Injection volume of 2 μL. The signal was monitored at 254 nm, 280 nm and 680 nm.

c) A modular Agilent 1200 Series HPLC system connected to an Agilent/Bruker ionTrap model XCT with MSMS capabilities. Agilent XDB C18 Column (1.8 μm, 4.6 mm x 50 mm) was used as the UPLC column. The conditions of the UPLC method are as follows: Solvent A: Water +0.1 % Formic acid; Solvent B: Acetonitrile +0.1 % Formic acid; Gradients: 0-1.3 minutes 5 % B; 1.3-5 minutes 5-60 % B, 5-6 minutes 60-100 % B, 6-8 minutes 100 % B with

re-equilibration time of 3 minutes. Flow rate: 0.9 ml/min; Column and injector temperature set to 25 °C. The signal was monitored at 254 nm and 750 nm with 360 nm as reference wavelength.

High performance liquid chromatography (HPLC) was performed either on a Varian ProStar system or an or an Agilent HP-1100 preparative HPLC system equipped with a Varian Pursuit C18 column (3 μm, C18, 100 Å, 250 x 30 mm) or a Kinetex AXIA packed HPLC column (5 μm, C18, 100 Å, , 250 x 21.2 mm). The UV detector was set to a wavelength of 214 nm and/or 680 nm. As eluants, mixtures of acetonitrile (MeCN) (HPLC-grade) and millipore H_2O with addition of different acids (stated in the synthesis procedure) were used.

NMR spectra were recorded on a Bruker DRX-400 (400 MHz), Bruker DPX-400 (400 MHz) and Bruker AVANCE III HD (500 MHz, DUL $^{13}C/^{1}H$) at room temperature using deuterated solvents. Calibration of the spectra was achieved using the solvent signals [150]. All chemical shifts (δ) are quoted in ppm and coupling constants given in Hz. Splitting patterns are given as follows: s (singlet), bs (broad singlet), d (doublet), t (triplet), q (quadruplet), m (multiplet).

An overview of the synthetic routes of the different linker derivatives, the different attempts to synthesise sulfonated building blocks as well as of **JW35**, **JW37** and **JW41** is outlined in Results and Discussion of this chapter (section2.2).

Intermediates **I** (2-Chloro-1-formyl-3-(hydroxymethylene)cyclohex-1-ene) [83], **II** (1-Hydroxycarbonylethyl-2,3,3-trimethylbenzoindoleninium bromide) [124], the heptamethine carbocyanine dye framework **III (HCC)** [124], N-(4-hydroxyphenyl)acetamide [151], **V** (N-[5-anilino-3-chloro-2,4-(propane-1,3-diyl)-2,4- pentadiene-1-ylidene]anilinium chloride) [152] were synthesised according to literature procedure, the analytical data corresponded. 3-(but-3-yn-1-yl)-2-((E)-2-((E)-3-((E)-2-(3-(but-3-yn-1-yl)-1,1-dimethyl-1,3-dihydro-2H-benzo[e]indol-2-ylidene)ethylidene)-2-chlorocyclohex-1-en-1-yl)vinyl)-1,1-dimethyl-1H-benzo[e]indol-3-ium **VI** was synthesised based on a previous described procedure [62].

Synthesis of 4-HCC-Oxyaniline Derivatives

Synthesis of JW7

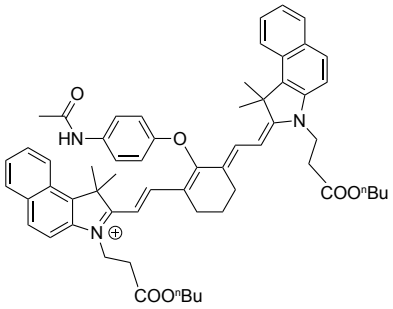

To a solution of **HCC** (50 mg, 0.056 mmol) in dry MeCN (0.6 mL), *N*-(4-hydroxyphenyl)-acetamide **IV** (11.2 mg, 0.074 mmol) and K_2CO_3 (12 mg, 0.087 mmol) were added and stirred at room temperature for 48 h. The insoluble K_2CO_3 was removed by filtration and the filtrate concentrated *in vacuo* to give a dark red solid. The crude product was purified by flash column chromatography (0 - 5 % MeOH in DCM) to yield **JW7** as green solid (19.52 mg, 0.018 mmol, 32 %).

R_f: 0.49 (DCM : MeOH 10 : 1)
HRMS: m/z calculated for $[M^+] = 926.5103$, found m/z = 926.5070.
^{1}H-NMR: (400 MHz, $CDCl_3$) δ [ppm] = 10.29 (s, 1H), 8.14 - 8.06 (m, 6H), 7.89 (d, $J_{H,H} = 9.2$ Hz, 6H), 7.64 (t, $J_{H,H} = 7.6$ Hz, 2H), 7.46 (t, $J_{H,H} = 7.5$ Hz, 2H), 7.35 (d, $J_{H,H} = 8.8$ Hz, 2H), 6.98 (d, $J_{H,H} = 9.1$ Hz, 2H), 6.04 (d, $J_{H,H} = 14.2$ Hz, 2H), 4.43 (t, $J_{H,H} = 7.0$ Hz, 4H), 4.06 (m, 4H), 2.85 (t, $J_{H,H} = 7.0$ Hz, 4H), 2.71 (t, $J_{H,H} = 6.3$ Hz, 4H), 2.29 (s, 3H), 2.17 - 1.25 (20 H), 0.85 (t, $J_{H,H} = 7.4$ Hz, 6H).

tert-Butyl (4-hydroxyphenyl)carbamate

This compound is known and fully characterised (Ref.[153])

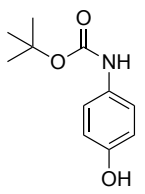

To a solution of 4-aminophenol (296 mg, 2.71 mmol) in dry THF (4 mL), di-tert-butyl-dicarbonate (591.5 mg, 2.71 mmol) was added over 20 min. The reaction mixture was stirred at room temperature for 2 h. After the solvent was concentrated *in vacuo*, the residue was dissolved in ethyl acetate and washed with aqueous $NaHCO_3$. The organic layers were washed with brine and dried over $MgSO_4$. The solvent was removed *in vacuo* and *tert*-butyl (4-hydroxyphenyl)carbamate was achieved as white solid (459 mg, 2.2 mmol, 81 %).

MS: m/z calculated for [M] = 209.1052, found m/z = 209.2511.
^{1}H-NMR: (400 MHz, CD_3CN) δ [ppm] = 7.20 (d, $J_{H,H}$ = 8.8 Hz, 2H), 6.72 (d, $J_{H,H}$ = 8.9 Hz, 2H), 1.46 (s, 9H).

Synthesis of JW11

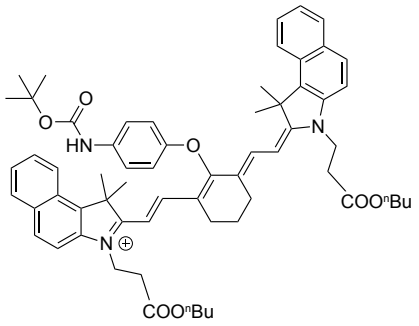

To a solution of **HCC** (50 mg, 0.056 mmol) in dry ACN (3 mL), 4-hydroxyphenyl)carbamate **III** (17 mg, 0.081 mmol) and TEA (44.3 mg, 0.44 mmol) were added and stirred at room temperature for 36 h. The solvent was removed *in vacuo* and the crude product was purified by flash column chromatography (0 - 5 % MeOH in DCM) to yield the desired product **JW11** as green solid (56.63 mg, 0.053 mmol, 95 %).

R_f-value: 0.51 (DCM : MeOH 10 : 1)
HRMS: m/z calculated for [M^+] = 984.5521, found m/z = 984.5494.
^{1}H-NMR: (400 MHz, $CDCl_3$) δ [ppm] = 8.04 - 8.01 (m, 4H), 7.90 (d, $J_{H,H}$ = 8.6 Hz, 4H), 7.57 (ddd,$J_{H,H}$ = 8.4, 6.8, 1.3 Hz, 2H), 7.54 - 7.47 (m, 4H), 7.05 (d, $J_{H,H}$ = 9.1 Hz, 2H), 6.23 (d, $J_{H,H}$ = 14.2 Hz, 2H), 4.62 (t, $J_{H,H}$ = 6.7 Hz, 4H), 4.02 (t, $J_{H,H}$ = 6.8 Hz 4H), 2.94 (t, $J_{H,H}$ = 6.6 Hz, 4H), 2.80 (t, $J_{H,H}$ = 6.1 Hz, 4H), 2.07 (t, $J_{H,H}$ = 6.0 Hz, 2H), 1.66 (s, 12H), 1.50 (s, 9H), 1.54-1.47 (m, 4H), 1.31 - 1.22 (m, 6H), 0.83 (t, $J_{H,H}$ = 7.4 Hz, 6H).

Synthesis of JW13

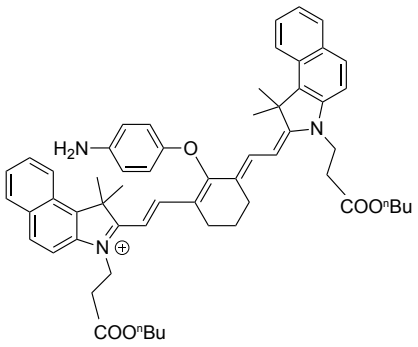

To a solution of **JW11** (41 mg, 0.038 mmol) in dry DCM (3 mL), TFA (65 μL, 0.85 mmol) was added and stirred at room temperature for 36 h. The solvent was removed *in vacuo* and the crude product was purified by flash column chromatography (0 - 10 % MeOH in DCM) to yield the desired product **JW13** as green solid (30.42 mg, 0.032 mmol, 83 %).

R_f: 0.39 (DCM : MeOH 10 : 1)
HRMS: m/z calculated for $[M^+] = 884.5002$, found m/z = 884.4984.
^{1}H-NMR: (400 MHz, $CDCl_3$) δ [ppm] = 8.05 - 8.02 (m, 4H), 7.90 (d, $J_{H,H} = 8.6$ Hz, 4H), 7.56 (ddd, $J_{H,H} = 8.4, 6.8, 1.3$ Hz, 2H), 7.49 - 7.41 (m, 4H), 6.94 (d, $J_{H,H} = 8.7$ Hz, 2H), 6.83 (d, $J_{H,H} = 8.5$ Hz, 2H), 6.20 (d, $J_{H,H} = 14.2$ Hz, 2H), 5.30 (s, 1H), 4.59 (t, $J_{H,H} = 6.7$ Hz, 4H), 4.03 (t, $J_{H,H} = 6.7$ Hz 4H), 2.93 (t, $J_{H,H} = 6.6$ Hz, 4H,), 2.77 (t, $J_{H,H} = 6.1$ Hz, 4H), 1.68 (s, 12H), 1.54 - 1.47 (m, 4H), 1.30 - 1.24 (m, 6H), 0.84 (t, $J_{H,H} = 7.4$ Hz, 6H).

Synthesis of HCC-piperazine derivatives

Synthesis of JW8

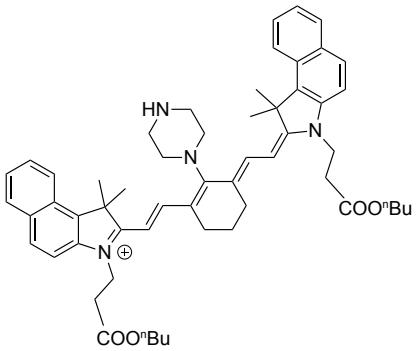

To a solution of **HCC** (50 mg, 0.056 mmol) in dry ACN (3 mL), piperazine (21.2 mg, 0.24 mmol) and TEA (44.3 mg, 0.44 mmol) were added and stirred at room temperature for 20 h. The solvent was removed *in vacuo* and the crude product was purified by flash column chromatography (0 - 20 % MeOH in DCM with addition of 0.1 % TEA) to yield the desired product **JW8** as green solid (48 mg, 0.051 mmol, 91 %). For absorption and fluorescence measurements, HPLC purification was performed (aqueous ACN addition of 0.1 % TFA: 0-100 % in 30 min).

R_f: 0.44 (DCM : MeOH 10 : 1 with addition of 0.1 % TEA)
HRMS: m/z calculated for $[M^+] = 861.5319$, found m/z = 861.5305.
^{1}H-NMR: (400 MHz, $CDCl_3$) δ [ppm] = 8.15 (d, $J_{H,H} = 7.6$ Hz, 2H), 7.89 - 7.85 (m, 4H), 7.77 (d, $J_{H,H} = 14.3$ Hz, 2H), 7.59 (ddd, $J_{H,H} = 8.4$, 6.9, 1.3 Hz, 2H), 7.41 (ddd, $J_{H,H} = 8.3$, 6.9, 0.8 Hz, 2H), 7.30 (d, $J_{H,H} = 10.9$ Hz, 2H), 5.81 (d, $J_{H,H} = 12.9$ Hz, 2H), 4.37 (t, $J_{H,H} = 6.8$ Hz, 4H), 4.20 (bs, 4H), 4.07 (t, $J_{H,H} = 6.7$ Hz 4H), 3.35 (bs, 4H), 2.84 (t, $J_{H,H} = 6.9$ Hz, 4H), 2.53 (t, $J_{H,H} = 6.6$ Hz, 4H), 2.02 (s, 12H), 1.90 - 1.87 (m, 2H), 1.57 - 1.50 (m, 4H), 1.33 - 1.28 (m, 4H), 0.85 (t, $J_{H,H} = 7.4$ Hz, 6H).

Synthesis of JW14

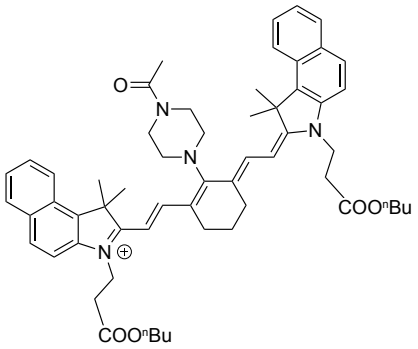

To a solution of **JW8** (10 mg, 0.011 mmol) in dry THF (3 mL), imidazol (1.5 mg, 0.022 mmol) and acetylchloride (1.5 μL, 0.021 mmol) were added and stirred at room temperature for 16 h. The solvent was removed *in vacuo* and the crude product was purified by flash column chromatography (0 - 10 % MeOH in DCM) to yield the desired product **JW14** as blue solid (7.33 mg, 0.0075 mmol, 68 %).

HRMS: m/z calculated for $[M^+] = 903.5424$, found m/z = 903.5411.

^{1}H-NMR: (400 MHz, $CDCl_3$) δ [ppm] = 8.10 (d, $J_{H,H}$ = 8.5 Hz, 2H), 7.92 - 7.89 (m, 4H), 7.85 (d, $J_{H,H}$ = 13.5 Hz, 2H), 7.59 (ddd, $J_{H,H}$ = 8.4, 6.9, 1.3 Hz, 2H), 7.46 - 7.39 (m,4H), 6.03 (d, $J_{H,H}$ = 13.5 Hz, 2H), 4.50 (t, $J_{H,H}$ = 6.9 Hz, 4H), 4.06 (t, $J_{H,H}$ = 6.7 Hz, 4H), 3.97 - 3.93 (m, 4H), 3.88 - 3.86 (m, 2H), 2.91 (t, $J_{H,H}$ = 6.8 Hz, 4H), 2.60 (t, $J_{H,H}$ = 6.4 Hz, 4H), 2.34 (s, 3H), 1.98 (s, 12H), 1.93 - 1.86 (m, 2H), 1.57 - 1.50 (m, 4H), 1.32 - 1.25 (m, 4H), 0.85 (t, $J_{H,H}$ = 7.4 Hz, 6H).

Synthesis of JW15

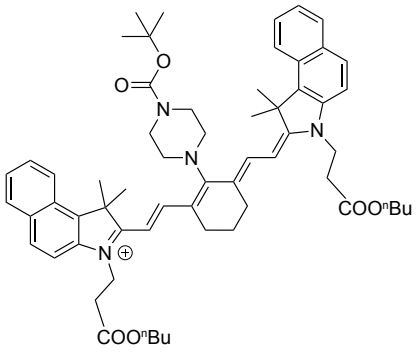

To a solution of **JW8** (30 mg, 0.032 mmol) in dry THF (3 mL), di-*tert*-butyl dicarbonate (9.5 mg, 0.044 mmol) and TEA (20 μL, 0.14 mmol) were added and stirred at room temperature for 15 h. The solvent was removed *in vacuo* and the crude product was purified by flash column chromatography (0 - 20 % MeOH in DCM) to yield the desired product **JW15** as blue solid (14.06 mg, 0.013 mmol, 42 %).

HRMS: m/z calculated for [M^+] = 961.58, found m/z = 961.5811.
^{1}H-NMR: (300 MHz, $CDCl_3$) The peak intensities of the obtained spectrum was too weak why accurate data analysis could not be performed.

Synthesis of JW16

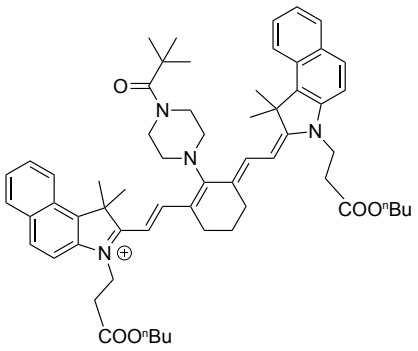

To a solution of **JW8** (30 mg, 0.032 mmol) in dry THF (3 mL), TEA (1.5 μL, 0.021 mmol) was added and the solution was cooled down to 0 °C. Then, a solution of trimtheylacteyl chloride (1 μL, 0.089 mmol) in 500 μL THF was added and the reaction mixture was stirred at room temperature for 19 h. The solvent was removed *in vacuo* and the crude product was purified by flash column chromatography (0 - 15 % MeOH in DCM with addition of 0.1 % TEA) to yield the desired product **JW16** as green solid (30 mg, 0.029 mmol, 91 %).

MS: m/z calculated for $[M^+] = 945.5894$, found m/z = 945.5881.
^{1}H-NMR: (400 MHz, $CDCl_3$) δ [ppm] = 8.09 (d, $J_{H,H} = 8.4$ Hz, 2H), 7.92 (m, 4H)), 7.85 (d,$J_{H,H} = 13.5$ Hz, 2H), 7.68 - 7.63 (m, 2H), 7.58 (ddd, $J_{H,H} = 8.5, 6.8, 1.3$ Hz, 2H), 7.45 - 7.41 (m, 2H), 6.08 (d, $J_{H,H} = 13.5$ Hz, 2H), 4.51 (t, $J_{H,H} = 6.8$ Hz, 4H), 4.04 (t, $J_{H,H} = 6.8$ Hz, 4H), 4.02 - 3.99(m, 4H), 3.76 - 3.72 (m, 4H), 2.91 (t, $J_{H,H} = 6.8$ Hz, 4H), 2.61 (t, $J_{H,H} = 6.5$ Hz, 4H), 1.97 (s, 12H), 1.54 - 1.47 (m, 8H), 1.40 (s, 9H), 1.25 (m, 4H), 0.84 (t, $J_{H,H} = 7.4$ Hz, 6H).

Synthesis of Quinone-Cyanine dyes JW44 and JW45

Synthesis of IX

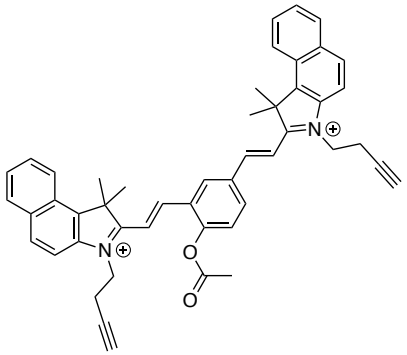

Intermediate **IV** (182 mg, 0.70 mmol), 5-formylsalicylaldehyde (50 mg, 0.33 mmol) and NaOAc (84 mg, 1 mmol) were dissolved in Ac_2O (2 mL) and stirred for 2 h at 80 °C. The solvent was removed *in vacuo* and the crude product was purified by flash column chromatography (0 - 20 % MeOH in DCM) to yield the desired product **IX** as blue solid (122.6 mg, 0.18 mmol, 55%).

$R_f = 0.2$ (MeOH : DCM 1 : 10).
HRMS: m/z calculated for [M] = 679.33, found m/z = 679.3331.

Synthesis of JW44 and JW45

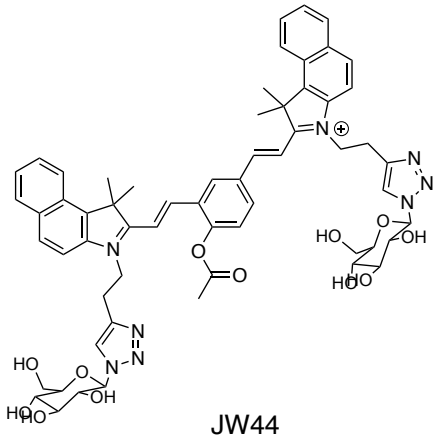

JW44

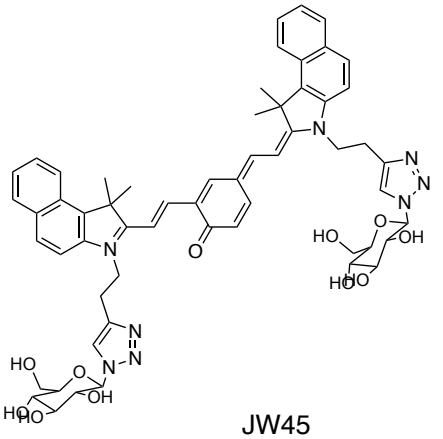

JW45

To a mixture of **IX** (21 mg, 0.031 mmol), β-D-Glucopyranosyl azide (17.5 mg, 0.09 mmol) and $CuSO_4$ (5 mg, 0.031 mmol) in *t*-BuOH:H_2O (1:1, 3 mL), Na-ascorbate (10 mg, 0.05 mmol) was added and the resulting reaction mixture was stirred at room temperature for 3 h. The solvent was reduced *in vacuo* and the crude product was purified with reverse-phase HPLC (Kinetex, 5 μm, C18, 100 Å, AXIA packed HPLC column, 250 x 21.2 mm) using H2O + 0.1% formic acid and MeCN + 0.1% formic acid as solvents. **JW44** as well as the uncapped derivative, **JW45**, were obtained as blue solids (**JW44**: 4.5 mg, 0.004 mmol, 13%; **JW45**: 4.2 mg, 0.004 mmol, 13%). The obtain amount of product was too little to perform accurate analysis with these compounds.

HRMS (JW44): m/z calculated for [M] = 1090.48, found m/z = 1090.4820.
HRMS (JW45): m/z calculated for [M] = 1047.46, found m/z = 1047.4619.

Synthesis Attempts of Sulfonated Building Blocks

3-(But-3-yn-1-yl)-1,1,2-trimethyl-1H-benzo[e]indol-3-ium-6-sulfonate

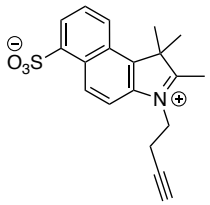

Method a: 3-(but-3-yn-1-yl)-1,1,2-trimethyl-1H-benzo[e]indol-3-ium (168 mg, 0.64 mmol) was dissolved in 5 mL nitrobenzene and cooled down to 0 °C. Concentrated sulfuric acid (70 mg, 0.71 mmol) was slowly added and the reaction mixture was kept at 0 °C for further 30 min. Afterwards, the reaction was stirred for 24 h at room temperature followed by 20 h at 100 °C. No formation of product was observed under this conditions.

Method b: To solid 3-(but-3-yn-1-yl)-1,1,2-trimethyl-1H-benzo[e]indol-3-ium (168 mg, 0.64 mmol) was added oleum (30%, 270 μL, 1.5 mmol) at 0 °C. The reaction mixture was stirred at room temperature for 12 h and further 8 h at 60 °C. No product formation was observed under this conditions.

Method c: 3-(but-3-yn-1-yl)-1,1,2-trimethyl-1H-benzo[e]indol-3-ium (435 mg, 1.7 mmol) was dissolved in 2.5 mL nitrobenzene and cooled down to 0 °C. Oleum (65%, 0.4 mL) was slowly added and the reaction mixture was kept at 0 °C till no further fume formation was observed. The reaction was then brought to room temperature and stirred for additional 12 h. No product formation was observed under this conditions.

1,1,2-Trimethyl-1H-benzo[e]indol-3-ium-6-sulfonate

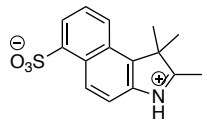

Method a: 1,1,2-trimethyl-1H-benzo[e]indole (500 mg, 2.5 mmol) was dissolved in 2.5 mL nitrobenzene and cooled down to 0 °C. Concentrated sulfuric acid (294 mg, 3 mmol) was slowly added and the reaction mixture was kept at 0 °C for further 30 min. Afterwards, the

reaction was stirred for 24 h at room temperature followed by 20 h at 100 °C. No formation of product was observed under this conditions.

Method b: To solid 1,1,2-trimethyl-1H-benzo[e]indole (500 mg, 2.5 mmol) was added oleum (30%, 540 μL, 3 mmol) at 0 °C. The reaction mixture was stirred at room temperature for 12 hours and further 8 hours at 60 °C. No product formation was observed under this conditions.

Method c: 1,1,2-trimethyl-1H-benzo[e]indole (700 mg, 3.3 mmol) was dissolved in 3.5 mL nitrobenzene and cooled down to 0 °C. Oleum (65%, 0.7 mL, 5.3 mmol) was slowly added and the reaction mixture was kept at 0 °C till no further fume formation was observed. The reaction was then brought to room temperature and stirred for additional 12 h. Distillation using a Kugelrohr apparatus under reduced pressure yielded in a brown, highly viscous oil, which was purified by reverse-phase chromatography using H_2O and MeCN + 0.1% formic acid. The crude product was used in the next step without further purification.

$R_f = 0.1$ (MeOH : DCM 2 : 10). MS: m/z calculated for $[M^+] = 290.08$, found $m/z = 290.12$.

3-(but-3-yn-1-yl)-1,1,2-trimethyl-1H-benzo[e]indol-3-ium-6-sulfonate

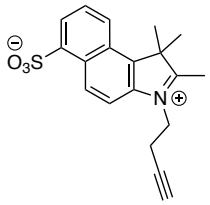

Method a: Crude 1,1,2-trimethyl-1H-benzo[e]indol-3-ium-6-sulfonate (500 mg, ∼ 1.7 mmol) and K_2CO_3 (553 mg, 4 mmol) were dissolved in dry DMF (2 mL) under argon. 4-Bromo-1-butyne (368 mg, 2.8 mmol) was added and the reaction mixture was stirred at 95 °C for 8 h. No product formation was observed under this conditions.

Method c: Crude 1,1,2-trimethyl-1H-benzo[e]indol-3-ium-6-sulfonate (500 mg, ∼ 1.7 mmol) and 4-Bromo-1-butyne (368 mg, 2.8 mmol) were heated at 95 °C for 6 h under argon. The reaction mixture was cooled down to room temperature and 15 mL Et_2O was added. After stirring for 20 min at room temperature the suspension was further cool down to 4 °C, filtered

and washed three times with ice cold Et_2O. No product was isolated.

Method c: Crude 1,1,2-trimethyl-1H-benzo[e]indol-3-ium-6-sulfonate (500 mg, $\sim$ 1.7 mmol) was dissolved in dry DMF and 4-Bromo-1-butyne (368 mg, 2.8 mmol) was added. The reaction mixture was heated at 95 °C for 3.5 h under argon. KI (644 mg, 4 mmol) was added and the reaction was stirred at 95 °C for further 3 h. Reaction monitoring with LCMS and TLC indicated product as well as byprodcut formation, thus the reaction was stopped and purified by reverse-phase chromatography using H_2O and MeCN + 0.1% formic acid. Even though, different buffers and acids have been used to try to elute the product from the column, no product was isolated.

3-(2-carboxyethyl)-1,1,2-trimethyl-1H-benzo[e]indol-3-ium-6-sulfonate

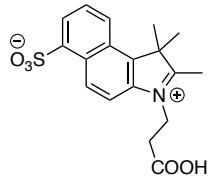

3-(2-carboxyethyl)-1,1,2-trimethyl-1H-benzo[e]indol-3-ium (100 mg, 0.35 mmol) was dissolved in 1.5 mL nitrobenzene and cooled down to 0 °C. Oleum (65%, 0.137 mg, 0.53 mmol) was slowly added and the reaction mixture was kept at 0 °C till no further fume formation was observed. The reaction was then brought to room temperature and stirred for 3 days. 5 mL water was added and the aqueous phase was washed four times with EtO 2. Water was removed by lyophilisation. The crude product was used in the next step without further purification.

MS: m/z calculated for [M] = 361.10, found m/z = 361.82.

1,1,2-trimethyl-3-(3-oxo-3-(prop-2-yn-1-ylamino)propyl)-1H-benzo[e]indol-3-ium-6-sulfonate

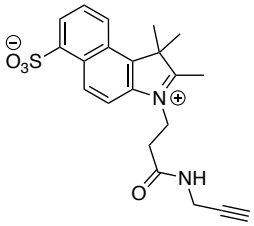

Method a: Ghosez's reagent (25.2 mg, 0.19 mmol) in dry DCM/THF (0.8 mL, 3/1) was added to crude 3-(2-carboxyethyl)-1,1,2-trimethyl-1H-benzo[e]indol-3-ium-6-sulfonate (31 mg, 0.09 mmol). The mixture was stirred for 30 min at room temperature before cooling down to 0 °C. TEA (19.2 mg, 0.19 mmol) was added at 0 °C and the reaction was then stirred at room temperature for 1 h. Propagylamine (10 mg, 0.18 mmol) in 0.5 mL DCM : THF (3 : 1) was added and the reaction mixture was stirred at room temperature for 2 days. No product formation was observed under this conditions.

Method b: Crude 3-(2-carboxyethyl)-1,1,2-trimethyl-1H-benzo[e]indol-3-ium-6-sulfonate (100 mg, ∼ 0.27 mmol) was dissolved in 1 mL dry DMF under argon atmosphere. HBTU (102 mg, 0.27 mmol) and HOBt (41 mg, 0.27 mmol), dissolved in 1 mL dry DMF were added, followed by DIC (34 mg, 0.27 mmol). After 10 min, the mixture was cooled down to 0 °C, propagylamine (15 mg, 0.27 mmol) was added and the reaction was stirred at room temperature for 1.5 days. The reaction mixture was extracted with water and DCM. No product could be isolated.

MS: m/z calculated for [M] = 398.13, found m/z = 398.95.

Method c: Crude 3-(2-carboxyethyl)-1,1,2-trimethyl-1H-benzo[e]indol-3-ium-6-sulfonate (500 mg, ∼ 1.38 mmol) and DMAP (17 mg, 0.14 mmol) were dissolved in 4 mL dry THF/DMF (1/1) under argon atmosphere. DIC (174 mg, 1.38 mmol) was added and the reaction mixture was cooled down to 0 °C. Propagylamine (114 mg, 2.1 mmol) was added and the reaction was stirred for 1 day at room temperature. The solvent was reduced under reduced pressure and the residue was extracted with water and DCM. No product could be isolated.
MS: m/z calculated for [M] = 398.13, found m/z = 398.95.

Synthesis of JW35, JW35Mono, JW37 and JW41

Synthesis of IV

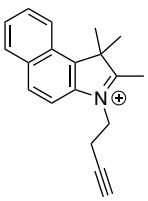

1,1,2-Trimethyl-1H-benzo(e)indole (600 mg, 2.9 mmol) and 4-bromo-1-butyne (572 mg, 4.3 mmol) were heated at 100 °C under argon for 2 h. The reaction mixture was cool down to room temperature and 15 mL Et_2O was added. After stirring for 20 min at room temperature the suspension was cooled down to 4 °C, filtered and washed three times with ice cold Et_2O. The crude product was obtained as a light blue solid (497.7 mg, 1.9 mmol, 55 %), which was used for the next step without further purification.

$R_f = 0.4$ (MeOH : DCM 1 : 10).
HRMS: m/z calculated for $[M+H^+] = 262.1596$, found m/z = 262.1590.

Synthesis of VI

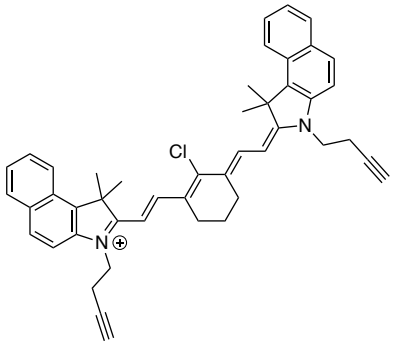

Freshly synthesized **IV** (653 mg, 2.49 mmol) and (N-[5-anilino-3-chloro-2,4-(propane-1,3-diyl)-2,4- pentadiene-1-ylidene]anilinium chloride) (**V**) (404.5 mg, 1.13 mmol) were dissolved in EtOH and together with KOAc (244.4 mg, 2.49 mmol) refluxed overnight under light exclusion and N_2-atmosphere. After completion of the reaction, the mixture was cooled down to room temperature, concentrated *in vacuo* and redissolved in DCM. After three washes with brine, and one wash with H2O, the organic layer was dried over anhydrous magnesium sulphate ($MgSO_4$) and DC was evaporated. The crude reaction product was then purified by flash column chromatography (0 - 20% MeOH in DCM) to obtain compound **VI** (309 mg, 42%).

HRMS: m/z calculated for $[M+H^+] = 659.3193$, found m/z = 659.3206.
^{1}H-NMR: (400 MHz, $CDCl_3$) δ [ppm] = 8.46 (d, $J_{H,H} = 14.2$ Hz, 2H), 8.15 (dd, $J_{H,H} = 8.5$, 1.0 Hz, 2H), 7.97 (d, $J_{H,H} = 8.5$ Hz, 4H), 7.65 – 7.59 (m, 4H), 7.50 (dd, $J_{H,H} = 8.0$, 1.0 Hz, 2H), 6.48 (d, $J_{H,H} = 14.1$ Hz, 2H), 4.67 (t, $J_{H,H} = 8.0$ Hz, 4H), 2.95 (td, $J_{H,H} = 6.6$, 2.7 Hz, 4H), 2.81 (t, $J_{H,H} = 6.2$ Hz, 4H), 2.06 (s, 12H), 2.03 (m, 2H), 1.95 (t, $J_{H,H} = 2.6$ Hz, 2H).

^{13}C NMR: (126 MHz, CD_3CN) δ [ppm] = 175.6, 150.1, 144.1, 140.8, 134.8, 132.9, 131.3, 130.9, 128.7, 128.2, 126.2, 123.3, 112.5, 102.6, 80.9, 72.9, 52.1, 43.5, 27.9, 27.1, 21.7, 18.0.

Synthesis of VII

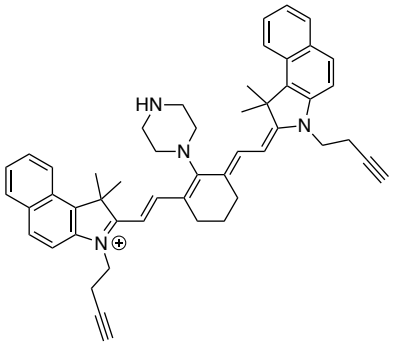

VI (351 mg, 0.53 mmol) and piperazine (69 mg, 0.80 mmol) were dissolved in dry MeCN (10 mL) and stirred for 8 h at room temperature under argon atmosphere. Cs_2CO_3 (130 mg, 0.40 mmol) was added and the reaction mixture was heated for 90 min at 40 °C. The reaction mixture was allowed to cool to room temperature and concentrated under reduced pressure. Purification by flash column chromatography (Al_2O_3, pH = 7, 0 - 20% MeOH in DCM) yielded the desired product **VII** (323 mg, 0.45 mmol, 85%).

HRMS: m/z calculated for [M^+] = 709.4270, found m/z = 709.4321.
^{1}H-NMR: (500 MHz, CD_3CN) δ [ppm] = 8.20 – 8.15 (m, 2H), 7.95 -7.89 (m, 4H), 7.67 (d, $J_{H,H}$ = 13.2 Hz, 2H), 7.57 (ddd, $J_{H,H}$ = 8.5, 6.8, 1.4 Hz, 2H), 7.46 (d, $J_{H,H}$ = 8.5 Hz, 2H), 7.40 (ddd, $J_{H,H}$ = 8.5, 6.8, 1.4 Hz, 2H), 5.90 (d, $J_{H,H}$ = 13.2 Hz, 2H), 4.22 (t, $J_{H,H}$ = 6.8 Hz, 4H), 3.88-3.84 (m, 4H), 3.16-3.12 (m, 4H), 2.74 (td, $J_{H,H}$ = 6.8, 2.7 Hz, 4H), 2.56-2.51 (m, 4H), 2.22 (t, $J_{H,H}$ = 2.7 Hz, 2H), 1.85-1.79 (m, 2H). The 12H belonging to the 4 methyl groups of the 1,1-dimethyl-1,3-dihydro-2H-benzo[e]indole unit are underneath the solvent peak at 1.94 ppm.
^{13}C NMR: (126 MHz, CD_3CN) δ [ppm] = 176.8, 170.2, 141.6, 140.4, 132.2, 131.8, 130.8, 129.2, 128.2, 124.8, 124.4, 122.9, 111.8, 95.5, 81.6, 72.2, 57.6, 50.3, 48.5, 42.5, 28.8, 25.5, 22.5, 17.4.

Synthesis of JW35

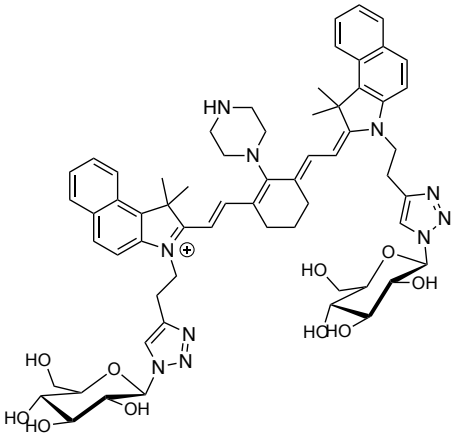

VII (32 mg, 0.045 mmol), 1-Azido-1-deoxy-β-D-glucopyranoside (20 mg, 0.097 mmol) and $CuSO_4$ (7 mg, 0.045 mmol) were dissolved in ^{t}BuOH : H_2O (1 : 1, 1.3 mL). Sodium ascorbate (15 mg, 0.075 mmol) was added and the reaction mixture was sonicated for 30 seconds followed by stirring at room temperature for 2 h. The reaction mixture was diluted with MeCN : H2O (1 : 1) and purified with HPLC (Kinetex, 5 μm, C18, 100Å, AXIA packed HPLC column, 250 x 21.2 mm) using H_O + 0.1% formic acid and MeCN + 0.1 formic acid as solvents. **JW35** was obtained as green-blue solid (25.7 mg, 0.023 mmol, 51%). JW35Mono was synthesised accordingly but with the use of only 1 eq. 1-Azido-1-deoxy-β-D-glucopyranoside. Under this conditions also some **JW35** was generated but **JW35Mono** was well separated by HPLC (Kinetex, 5 μm, C18, 100Å, AXIA packed HPLC column, 250 x 21.2 mm) using H_O + 0.1% formic acid and MeCN + 0.1 formic acid as solvents.

The 4H from the CH_2 groups directly attached to the triazole are underneath the solvent peak at 3.31 ppm and thus not visible. Also, due to the low concentration of the sample not all 13C-NMR signals are distinguishable from the background noise but coupling pattern could be observed with HMBC.

HRMS: m/z calculated for $[M+H^+] = 1119.57$, found m/z = 1119.5759.
^{1}H-NMR: (500 MHz, CD_3OD) δ [ppm] = 8.43 (s, 2H), 8.21 (d, $J_{H,H} = 8.5$ Hz, 2H), 8.02 (s, 1H), 7.99 - 7.96 (m, 4H), 7.84 (d, $J_{H,H} = 13.5$ Hz, 2H), 7.63 - 7.59 (m, 2H), 7.50 (d, $J_{H,H} = 8.8$ Hz, 2H), 7.46 - 7.43 (m, 2H), 5.92 (d, $J_{H,H} = 13.5$ Hz, 2H), 5.53 (d, $J_{H,H} = 9.2$ Hz, 2H), 4.52 - 4.46 (m, 4H), 3.86 - 3.75 (m, 8H), 3.71 - 3.64 (m, 4H), 3.56 - 3.52 (m, 4H), 3.50 - 3.43 (m, 4H), 2.61 - 2.52 (m, 4H), 2.00 (d, $J_{H,H} = 2.6$ Hz, 12H), 1.94 - 1.90 (m, 2H).

^{13}C NMR: (126 MHz, CD_3OD) δ [ppm] = 142.3, 131.57, 130.07, 129.67, 128.51, 125.24, 123.81, 123.15, 111.56, 111.39, 97.98, 89.51, 81.02, 78.46, 74.08, 70.87, 62.38, 56.47, 54.28, 51.37, 44.23, 29.44, 29.27, 29.12, 28.95, 26.06, 23.01, 22.72, 22.57, 22.42, 22.27, 22.10, 20.51, 18.25, 15.07, 13.56, 13.41, 13.26, 13.11, 12.96, 12.80.

Synthesis of VIII

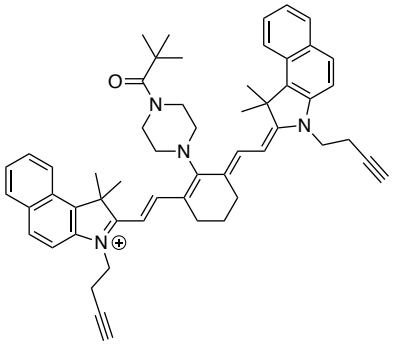

VII (29.3 mg, 0.039 mmol) and TEA (4 mg, 0.040 mmol) were dissolved in dry THF (2.5 mL) under argon atmosphere and cooled down to 0 °C. Pivaloyl chloride (6 mg, 0.05 mmol) in 0.5 mL dry THF was slowly added and the reaction was then stirred at room temperature for 15 h. The reaction mixture was concentrated under reduced pressure, redissolved in DCM and washed three time with water to yield **VIII** as green-blue solid (19.2 mg, 0.024 mmol, 62%).

HRMS: m/z calculated for [M^+] = 793.48, found m/z = 793.4833.

Synthesis of JW37

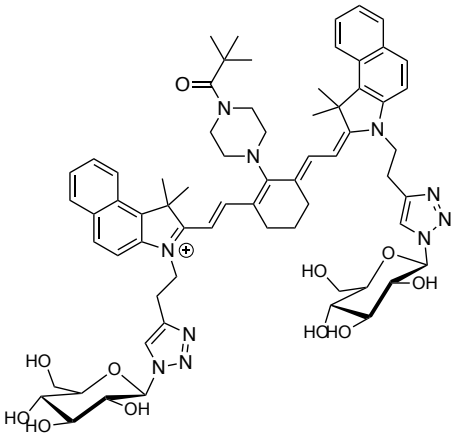

VIII (15 mg, 0.019 mmol), 1-Azido-1-deoxy-β-D-glucopyranoside (12 mg, 0.058 mmol) and $CuSO_4$ (5 mg, 0.031 mmol) were dissolved in ^{t}BuOH : H_2O (1 : 1, 1.5 mL). Sodium ascorbate (7.5 mg, 0.038 mmol) was added and the reaction mixture was sonicated for 30 seconds followed by stirring at room temperature for 2 h. The reaction mixture was diluted with MeCN : H2O (1 : 1) and purified with HPLC (Kinetex, 5 μm, C18, 100Å, AXIA packed HPLC column, 250 x 21.2 mm) using H_O + 0.1% formic acid and MeCN + 0.1 formic acid as solvents. **JW37** was obtained as blue solid (10.8 mg, 0.009 mmol, 48%).

All the NMRs were measured in a very diluted sample and the solvent peaks are overlapping with the signals from the methyl groups. Additionally, due to the low concentration of the sample the ^{13}C-NMR could not be analysed. Thus not all protons of the 7 methyl groups are stated.

HRMS: m/z calculated for $[M^+] = 1203.62$, found m/z = 1203.6230.
^{1}H-NMR: (500 MHz, CD_3CN) δ [ppm] = 8.30-8.10 (m, 4H), 8.04-7.85 (m, 4H), 7.72 (s, 2H), 766-7.55 (m, 2H), 7.55 - 7.33 (m, 4H), 5.78 (d, $J_{H,H}$ = 15 Hz, 2H), 5.39 (d, $J_{H,H}$ = 10 Hz, 2H), 4.40 (bs, 4H), 4.04-3.82 (m, 8H), 3.72-3.50 (m, 8H), 3.33 (dd, $J_{H,H}$ = 15, 10 Hz, 2H), 3.25 (bs, 2H), 3.14 (t, $J_{H,H}$ = 5 Hz, 4H), 2.99 (bs, 2H), 1.32-1.21 (m, 12H).

Synthesis of X

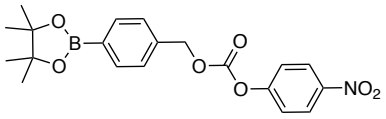

4-Nitrophenylchloroformate (120 mg, 0.595 mmol) were dissolved in dry DCM (1.5 mL) under argon atmosphere and pyridine (53 mg, 0.670 mmol, dissolved in 1.5 mL dry DCM) was added. After cooling down to 0 °C, (4-(4,4,5,5-tetramethyl-1,3,2-dioxaborolan-2-yl)phenyl)-methanol (140 mg. 0.598 mmol) was added in 1 mL dry DCM and the reaction mixture was stirred for 2 h. The reaction was stopped by washing once with H_2O and twice with brine. The organic layer was separated, dried over anhydrous $MgSO_4$ and concentrated under vacuum. The colourless solid was unstable and thus used immediately in the next step without further purification .

Synthesis of XI

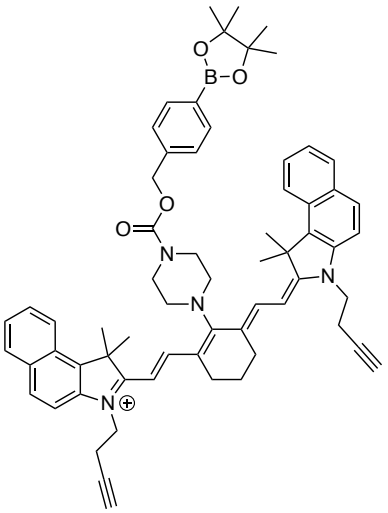

VII (40 mg, 0.056 mmol) and 18 mg (0.060 mmol) N,N-diisopropylethylamine were dissolved in dry DMF (0.5 mL) under argon atmosphere. After cooling down to 0 °C, **X** (33.6 mg, 0.084 mmol) was added in 0.2 mL dry DMF and the reaction mixture was stirred at room temperature overnight. The mixture was diluted with ethyl acetate and washed with water and brine. After drying over anhydrous $MgSO_4$ and concentrating under vacuum, the crude product was purified by flash column chromatography (Al_2O_3, pH = 7; 0 - 20% MeOH in DCM). Since the product was subject to degradations during the purification step (different conditions have been exploited), **XI** (dark blue solid, 21.1 mg, 0.022 mmol, 39%) with some impurities was used for the next step. The 4-nitrophenylpiperazine by-product, could be isolated and analysed via NMR.

HRMS: m/z calculated for $[M+H^+] = 969.55$, found m/z = 969.5377.

Synthesis of JW41

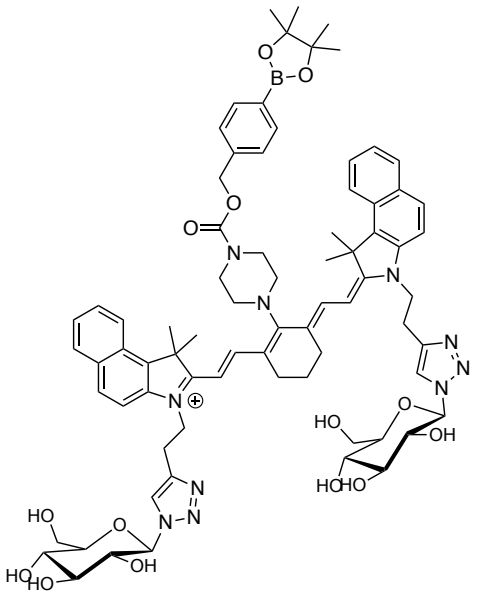

XI (20 mg, 0.021 mmol), $Cu(CH_3CN)_4PF_6$ (4 mg, 0.011 mmol), TBTA (5.6 mg, 0.011 mmol) and 1-Azido-1-deoxy-β-D-glucopyranoside (10 mg, 0.048 mmol) were dissolved in dry MeCN (1.5 mL) and stirred at room temperature under argon atmosphere for 24 h. The reaction mixture was purified by HPLC (Agilent XDB C18, 5 - 100% MeCN in H2O + 0.1% TFA). **JW41** was obtained as dark blue solid (9.6 mg, 0.007 mmol, 33%).

The hydrogens of the OH groups might be underneath the broad peak at 2.50 ppm. Also, due to the low concentration of the sample not all ^{13}C-NMR signals are distinguishable from the background noise but coupling pattern could be observed with HMBC.

HRMS: m/z calculated for $[M+H^+] = 1380.69$, found m/z = 1380.6700.
^{1}H-NMR: (500 MHz, CD_3CN) δ [ppm] = 8.15 (s, 2H), 8.01 – 7.88 (m, 6H), 7.77 – 7.71 (m, 6H), 7.60 (m, 2H), 7.50 – 7.36 (m, 6H), 5.80 (bs, 2H), 5.46 (d, $J_{H,H}$ = 9.2 Hz, 2H), 5.28 (s, 2H), 4.40 (bs, 4H), 3.79 (s, 4H), 3.77 – 3.67 (m, 4H), 3.64 (s, 4H), 3.56 (dd, $J_{H,H}$ = 12.0, 5.2 Hz, 2H), 3.48 (t, $J_{H,H}$ = 8.9 Hz, 4H), 3.42 – 3.35 (m, 2H), 3.25 (bs, 4H), 2.07 (dt, $J_{H,H}$ = 4.9, 2.5 Hz, 2H), 1.89 (s, 12H), 1.85 – 1.83 (m, 2H), 1.80 (dt, $J_{H,H}$ = 4.9, 2.5 Hz, 2H), 1.29 (s, 12H).
^{13}C NMR: (126 MHz, CD_3CN) δ [ppm] = 155.92, 144.34, 141.33, 135.56, 130.98, 130.75, 128.35, 127.74, 122.80, 118.44, 111.72, 88.37, 84.81, 79.99, 77.82, 73.40, 70.70, 67.62, 62.33, 54.9546.20, 43,89, 28.61, 25.13, 25.09, 22.46.

νmax (solid): 3337, 2977, 2930, 2888, 1677, 1544, 1501, 1440, 1354, 1274, 1229, 1202, 11138, 1108, 1065, 1046, 1007, 914, 901, 861 cm^{-1}.

2.4.2 Photophysical Calculations

The nitrogen hybridization states as well as minimum-energy conformations were analysed computationally by geometry optimisation in gas phase and frequency calculations were run using Gaussian 03 [154], at the density functional theory level, using the B3LYP functional and the cc-pvDz basis set [155, 156]. Although used by the intuitive valence bond theory, atomic electron hybridisation is not a property of a molecule as a whole, whose electronic structure is better described by molecular orbitals that may extend over the entire molecule. Even though transformations can be applied to the molecular orbitals in order to obtain a set of localised molecular orbitals, these are neither unambiguous nor they have a definite energy level. As a consequence, within a molecule, each atom can display a mixture of geometrical features commonly associated to different hybridisation states. Thus, we compared the results for the hybridisation states of the nitrogens with reference cases, namely: pyrrolidine (1), n-methylpyrrolidine (2), protonated pyrrolidine (3), protonated n-methylpyrrolidine (4), pyrrole (5) and n-methylpyrrole (6). These molecules contain easily defined "sp3-like" pyramidal nitrogens (1-4) and "sp2-like" planar nitrogens (5, 6). To determine the twist in the HCC backbone, we quantified the relative orientation of the two terminal polycyclic moieties by defining a dihedral angle with the main axis across the central aliphatic chain and terminating in the two distal benzene rings (as shown in Figure 2.16 and measured on the optimised structures.

2.4.3 Optical Characterisations

General Considerations

Absorption and fluorescence spectra were recorded at 25 °C using a fluorescence spectrophotometer (Cary Eclipse, Varian) and a UV-VIS spectrophotometer (Cary 300, Varian). Therefore, samples were placed into Suprasil® quartz cuvettes with a 10 mm pathlength. Separate absorption and emission measurements were performed at 25 °C on a microplate reader (CLARIOstar, BMG Labtech or SPECTROstar, BMG Labtech). All measurements were repeated with $n \geq 3$ separately prepared dye samples and errors are represented as standard deviations.

PA spectra of the dyes in different environments at different concentrations were recorded in micro plastic cuvettes (Y200.1, ROTH; V(dye solution) = 800μL) in a custom PA spectrometer built using a laser module (SplitLight 600 OPO) coupled into a silica fiber (CeramOptec), an ultrasound transducer (PANAMETRICS, 500kHz) and the data acquisition unit of a commercial multispectral optoacoustic tomography (MSOT) system (InVision 256, iThera Medical). The set-up was assembled and optimised together with Stefan Morscher from iThera Medical. Figure 2.25 shows a schematic illustration of the set-up.

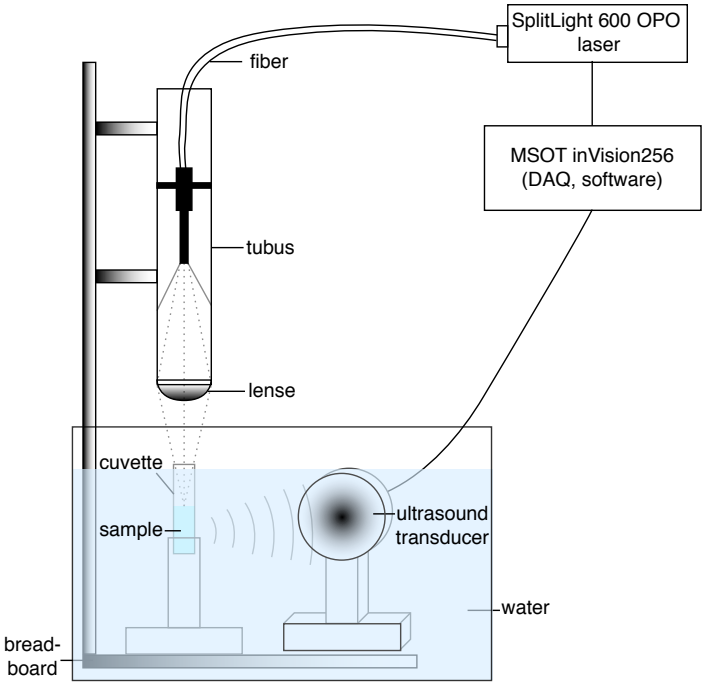

Figure 2.25 Schematic illustration of custom PA spectrometer set-up.

PA spectra for assessing photothermal stability and obtaining PA spectra for spectral unmixing were recorded in a commercial multispectral OT (MSOT) system (inVision256-TF; iThera Medical). Detailed information of the system are described elsewhere [157, 158]. In short, 9 nanosecond (ns) excitation pulses at a 10-Hz repetition rate are generated from a tuneable (660 nm – 1300 nm) optical parametric oscillator (OPO) pumped by an Nd:YAG laser with a peak pulse energy of 90 mJ at 720 nm. A uniform diffused ring of illumination over the image plane is provided by ten arms of a fibre bundle. Ultrasound detection was achieved with 256 toroidally focused ultrasound transducers at a centre frequency of 5 MHz with a 60% bandwidth. The array of transducers is organised in a concave array with a radius of 4 cm and covers an angle of 270 degree. The samples are coupled to the transducer via a water bath filled with heavy water.

Optical Characterisation of Commercially Available Dyes

All dye solutions were prepared in UV-transparent 96 well plates (Corning Costar, Sigma-Aldrich) and absorption and fluorescence spectra were acquired using a microplate reader (CLARIOstar, BMG Labtech). All measurements were conducted at 37 °C. For each dye and solvent combination, 0.5,μM, 1,μM, 5,μM, 10,μM, 20,μM and 50,μM solutions were prepared in triplicates, with the exception of Cy7 and Cy7.5 in ethanol, where no 0.5 μM samples were used.

Table 2.6 Conditions used for optical characterisation of commercially available dyes.

Solvent	ICG	Cy7.5	Cy7	SulfoCy7	IR800CW	IR783	IR806[1]	IR680RD
H_2O	x	x	x	x	x	x	x	x
H_2O+3wt.% BSA	x	x	x	x	x	x	x	x
H_2O+10% FBS	x	x	x	x	x	x	x	-
PBS	x	x	x	x	x	x	-	x
PBS+10% FBS	x	x	x	x	x	x	-	x
FBS	x	x	x	x	x	x	-	-
TBS	x	x	x	x	x	x	-	-
normal brine	x	x	x	x	x	x	-	-
MeOH	x	x	x	-	x	x	x	-
EtOH	-	x	x	x	-	-	-	-

[1] IR806 readily aggregates in the presence of ions and is insoluble in all the buffers used in this experiment.

Optical Characterisation of the Dyes for Linker Evaluation

The absorption spectra of the different HCC-linker derivatives, **JW7** - **JW16**, and **JW37**, **JW44**, **JW45** were recorded with different solvents and concentrations (Table 2.7 and 2.8). To obtain the corresponding emission spectra, the samples were excited at 720 nm (**JW8**) or 770 nm (**JW14**, **JW15**, **JW16**) and emission was collected between 750 and 900 nm for **JW8** and 780 and 900 nm for **JW14**, **JW15** and **JW16**. Slit emission and excitation were defined as 10 nm.

Table 2.7 Conditions used for optical characterisation of HCC-piperazine derivatives.

Solvent	JW7 (μM)	JW8 (μM)	JW11 (μM)	JW13 (μM)	JW14 (μM)	JW15 (μM)	JW16 (μM)
H_2O	1, 5, 10, 15 20, 50, 100	1, 5, 10, 15 20, 50, 100	1, 5, 10, 15 20, 50, 100	1, 5, 10, 15 20, 50, 100	1, 5, 10, 15 20, 50, 100	1, 5, 10, 15 20, 50, 100	1, 5, 10, 15 20, 50, 100
MeOH	1, 5, 10, 15 20, 50, 100	1, 5, 10, 15 20, 50, 100	1, 5, 10, 15 20, 50, 100	1, 5, 10, 15 20, 50, 100	1, 5, 10, 15 20, 50, 100	1, 5, 10, 15 20, 50, 100	1, 5, 10, 15 20, 50, 100
PBS	1, 5, 10, 15 20	1, 5, 10, 15 20	1, 5, 10, 15 20	1, 5, 10, 15 20	1, 5, 10, 15 20	1, 5, 10, 15 20	1, 5, 10, 15 20
NaOAc (pH 4.3)	1, 5, 10, 15 20	1, 5, 10, 15 20	1, 5, 10, 15 20	1, 5, 10, 15 20	1, 5, 10, 15 20	1, 5, 10, 15 20	1, 5, 10, 15 20
$(NH_4)_2CO_3$ (pH 10.45)	1, 5, 10, 15 20	1, 5, 10, 15 20	1, 5, 10, 15 20	1, 5, 10, 15 20	1, 5, 10, 15 20	1, 5, 10, 15 20	1, 5, 10, 15 20
MeOH	5, 10	5, 10	5, 10	5, 10	5, 10, 20	20	-
MeOH+5eq.DMAP	5	5	5	5	5	-	-
MeOH+1eq.TEA	10	10	10	10	10	-	-
MeOH+100eq.TEA	10	10	10	10	10	-	-
MeOH+20mM NaOH	-	-	-	-	20	-	-
MeOH+30mM NaOH	-	-	-	-	20	-	-
MeOH+20mM NaOH	-	-	-	-	20	-	-
MeOH+1.5eq. TFA	-	-	-	-	-	20	-
DCM	-	-	-	-	-	100	-
DCM+3eq. TFA	-	-	-	-	-	20	-

Table 2.8 Conditions used for optical characterisation of JW37, JW44, JW45.

Solvent	JW37 (μM)	JW44 (μM)	JW45 (μM)
H_2O	5, 10, 20	10	10
H_2O+10%DMSO	5, 10, 20	-	-
PBS	5, 10, 20	10	10
PBS+2.5%PEG_{24}	5, 10, 20	-	-
PBS+5%PEG_{24}	5, 10, 20	-	-
PEG+5%glycerol	5, 10, 20	-	-
PEG+12.5%glycerol	5, 10, 20	-	-
PBS+10%FBS	-	10	10
FBS	-	10	10
MeOH/H_2O 3/1	5, 10, 20	10	10
MeOH/H_2O 1/1	5, 10, 20	10	10
MeOH/H_2O 1/3	5, 10, 20	10	10
MeOH	5, 10, 20	10	10
EtOH	5, 10, 20	-	-
MeCN	5, 10, 20	-	-
Hexane	5, 10, 20	-	-

Optical Characterisation of JW35 and JW41

JW35 and **JW41** were optically characterised in various conditions and concentrations, including: MeCN, DMF, DMSO, EtOH, EtOH : H_2O 7 : 3, MeOH, MeOH : H_2O 3 : 1, MeOH : H_2O 1 : 1, MeOH : H_2O 1 : 3, H_2O, H_2O+10% DMSO, PBS, PBS+10%FBS, PBS+2.5% PEG_{24}, PBS+5% PEG_{24}, PEG+12.5% glycerol, PEG+5% glycerol, FBS. Fluorescence spectra of **JW35** and **JW41** were recorded by exciting close to their absorption maximum at 740 nm, 780 nm and/or 785 nm.

Several photophysical quantities were determined from absorption and emission data at various concentrations. These included absorption maxima (λ_{Abs}), emission maxima (λ_{Em}), Stokes shift, molar extinction coefficient (ε), fluorescence quantum yield (ϕ_{Fl}) and brightness (B). Stokes shifts were calculated from the difference of λ_{Em} and λ_{Abs}. ε was determined using the Beer–Lambert law from dilutions of solutions with known concentrations. ϕ_{Fl} of **JW41** and **JW35** in water, MeOH and EtOH : H_2O (7 : 3) were measured at the excitation wavelength of 785 nm and referenced against 1,1',3,3,3',3'-Hexamethylindotricarbocyanine

iodide (HITC, Sigma-Aldrich, 252034) in MeOH (ϕ_{Fl}=0.28) (cf. Appendix, Figure A.6) [159]). Discrepancies in absorbency and solvent refractive index were corrected for with the following equation [160].

$$\theta_{Fl} = \theta_{Fl,Ref} \cdot [(\wr I / \wr I_{Ref}) \cdot ((1 - 10^{-A_{Ref}})/(1 - 10^{-A})) \cdot (n^2/n^2{}_{Ref})]$$

with θ_{Ref} being the fluorescence quantum yield of the reference dye, HITC, I is the fluorescence intensity and n is the refractive index of the medium. Fluorescence emission spectra of θ_{Fl} HITC were collected at several concentrations in MeOH (see Appendix A.2, Figure A.6 for calibration curve).

Photoacoustic Characterisation

The PA spectra of the commercial available cyanine dyes as well as **JW41** and **JW35** were recorded at various concentrations ranging from 0.125 μM to 25 μM on the spectroscopic set up described previously (cf. Figure 2.25) in different solvents including MeCN, EtOH, H_2O, H_2O + 3 wt.% BSA, H_2O + 10% FBS and PBS.
To investigate the resolution of the commercial small-animal, multispectral optoacoustic systems (MSOT), which would be used for *in vivo* studies, and the influence of biological tissue, we additionally acquired PA spectra of the commercial available cyanine dyes as well as **JW41** and **JW35** in tissue-mimicking phantoms on the MSOT. The phantoms possess defined optical properties closely mimicking the optical properties of biological tissue and were fabricated as described previously [161]. 150 μL of dye solution (5 μM for commercial available dyes, 2.5 μM for **JW41** and **JW35**) in (a) water and (b) FBS were inserted into thin-walled plastic straws, sealed and placed in holes inside the phantom as illustrated in Figure 2.24. The phantom was clamped into a supplied rigid phantom holder and placed into the imaging chamber of the MSOT system. To allow the phantom to adapt the water bath temperature of 34 °C, measurements were recorded starting 5 min after placing the phantom into the imaging system.

Photobleaching Studies

Photothermal stability studies were carried out in tissue-mimicking phantoms on the commercial small-animal, multispectral optoacoustic systems (MSOT), as described before (see 2.4.3). For examining the photothermal stability of commercial available dyes, 150 μL of 5 μM dye solution in (a) water and (b) FBS was used; for **JW41** and **JW35**, 150 μL of

2.5 μM dye solution in (a) water and (b) FBS was measured. 150 μL of 2.5 μM IR800CW in water or FBS served as reference for the assessment of the photothermal stability of **JW41** and **JW35**. Imaging was performed at one imaging position at 680 nm, 850 nm and from 710 to 800 nm in 5 nm steps with constant 9 ns excitation pulses at a 10 Hz repetition rate. Graphs are plotted with the values obtained at their PA maxima wavelength. Photobleaching was confirmed by fluorescence imaging of the dye containing straws with a fluorescence imaging system (IVIS 200, Xenogen) before and after the photothermal stability study.

2.4.4 Spectral Unmixing Evaluation

The same preparation procedure as described in section 2.4.3 was used for obtaining the PA spectra of the dyes in tissue mimicking phantoms and evaluating the possibility of unmixing the spectra of **JW41** and **JW35** using linear regression. The dye solutions used for this purpose were prepared in deionised water at concentrations of 2.25 μM **JW41**, 1 μM **JW35**, and mixtures of 0.33 μM **JW41**- 0.66 μM **JW35**, 0.5 μM **JW41** - 0.5 μM **JW35**, 0.66 μM **JW41** – 0.33 μM **JW35**. Imaging was performed over 5 scanning positions covering the different straw positions in 1-mm steps and at 25 different wavelengths between 660 nm and 900 nm.

The acquired images were reconstructed offline with linear reconstruction and analysed with linear regression multispectral processing, both available within the ViewMSOT software package (version 3.8; iTheraMedical). Mean pixel intensities were extracted from the regions of interest (ROIs) drawn within the plastic straw and the average values over the different scan positions were used for further analysis. To obtain the PA spectra profile, offset correction was performed by subtracting the signal at 900 nm from the other values. The contrast-to-noise ratio (CNR) of signals in the photoacoustic images were calculated using the following equation[122]:

$$CNR = | S_i - S_0 | / \sigma_0$$

where S_i is the mean of the image data within the ROI located inside the straw, S_0 the means of the image data within the background ROI and σ_0 is the standard deviation of the data of the background ROI. Linear regression with spectra for **JW41**, **JW35** and the phantom background extracted from the phantom study were used to produce images in arbitrary units to obtain information about the relative weight that each spectrum redounds to a specific image pixel. For quantifying the accuracy of the spectral unmixing, the values obtained through linear regression were background corrected to the phantom signal, and normalised against the value of the reference straw containing 1 μM **JW35**. These relative values (%)

obtained by spectral unmixing for **JW41** and **JW35** in the test straw were then compared with the actual concentration (%), which was present in the straw. The relative accuracy is stated as the difference (%) between the actual concentration (%) and the calculated concentration (%).

2.4.5 Protein-Binding Assay

To test the binding of commercially available cyanine dyes to proteins, the dyes were added to 3 wt.% bovine serum albumin solution in PBS to reach a final concentration of 1 μM and incubated for 15 min, 30 min or 60 min at 37 °C. Next, nativePAGE sample buffer (Invitrogen) was added to the sample in a 1:3 ratio and the samples were loaded into a nativePAGE Bis-Tris gel (Invitrogen). The gel was run in nativePAGE running buffer (Invitrogen) at 4 °C for 70 min at 150 V followed by 20 min at 200 V. The gel was imaged on an Odyssey CLx system (LI-COR) using the 700 nm and 800 nm channel. Afterwards, the gel was stained with InstantBlue for 1 h at room temperature and imaged again an an Odyssey CLx system (LI-COR) using the 700 nm channel. Protein binding was classified by forming the ratio of unbound (free) dye to protein bound dye. Therefore the average signal intensity of the solvent front and the protein bands was determined with Fiji. A free to bound dye signal ratio smaller than 5 was classified as high, a ratio between 5 and 100 as medium and a ratio higher than 100 as low protein binding ability.

Chapter 3

Application of the New H_2O_2-Activatable Photoacoustic Probe in Cancer

Dr. Laura Ansel-Bollepalli performed the Incucyte proliferation measurements as shown in Figure 3.7A and the TPA-assay shown in Figure 3.12. LC-MS/MS studies of tissue samples were performed with the help of Joshua Kent. All other work was performed and analysed myself. Parts of this work is in review for publication.

3.1 Introduction and Motivation

Among several cancer pathways it has been shown that increased levels of reactive oxygen species (ROS) have a broad impact on tumorigenesis and linked inflammatory processes in breast, colon, liver, gastric, lung and pancreatic cancers [162]. For a better characterisation and definition of their physiology and pathology, specific redox-activatable and bifunctional contrast agents for photoacoustic imaging (PAI) possess promising features for translatable detection of ROS with high spatial and temporal resolution *in vivo*.

In Chapter 2, the design and synthesis of a cancer-targeted, ROS-activatable probe, **JW41**, for PAI was described, which is responsive to one of the major and most abundant ROS, hydrogen peroxide (H_2O_2) (Figure 3.1). The putative bifunctional probe uses a heptamethine carbocyanine dye scaffold for signal generation, glucose for cancer localisation and boronic ester oxidation to specifically detect H_2O_2. The optical properties of the novel probe, **JW41**, and the uncapped reference, **JW35**, were characterised using absorption, fluorescence and photoacoustic measurements. These data indicated a distinct change in the photophysical profile when comparing the capped (**JW41**) and uncapped (**JW35**) probe.

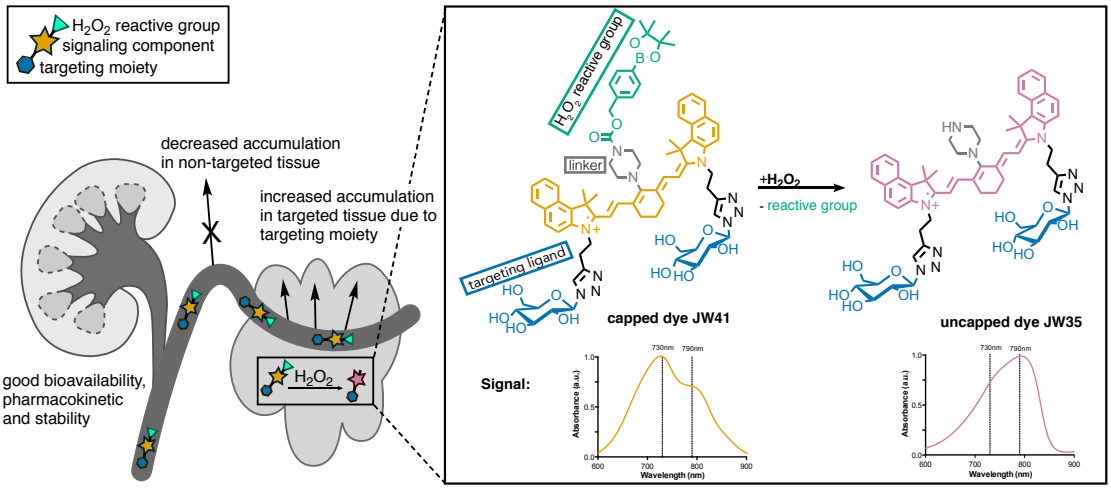

Figure 3.1 Design and structure of the new bifunctional PA probe: JW41, a NIR dye designed to exhibit a H_2O_2-dependent change in its optical and photoacoustic properties as well as an increased accumulation in the targeted tissue due to a clickable targeting moiety (glucose was chosen as a preliminary cancer targeting moiety).

In the light of the previous data, the broader challenge of biocompatibility, biodistribution and *in vivo*-performance are now the key steps, which need to be evaluated. For successful molecular imaging, the probe must be non-toxic and overcome physiological delivery barriers (circulatory and cellular) while ensuring appropriate biodistribution (avoiding off-target tissue accumulation) and elimination (Figure 3.1). Thus, the goal of this Chapter was to establish the abilities of the capped dye, **JW41**, to operate as an activatable, bifunctional contrast agent for PA *in vivo* imaging by examining the sensitivity and selectivity of **JW41** towards H_2O_2, its cancer targeting ability and its performance *in vitro* and *in vivo*.

3.2 Results and Discussion

3.2.1 ROS Sensing

The ability of the capped dye, **JW41**, to respond to H_2O_2 with a change in its photophysical properties was evaluated with absorption, fluorescence and PA spectroscopy. Spectral transformations were characterised following the addition of 100 μM H_2O_2, a physiologically realistic concentration in a cellular environment undergoing oxidative stress, to solutions of the probe [163]. A rapid ratiometric change in the absorption and PA profile, which allows data normalisation, were observed following the addition of 100 μM H_2O_2. The optical absorption peak at 730 nm shifted by 65 nm to 795 nm and the absorbance at 790 nm was found to increase by over 45% (Figure 3.2A). Similarly, the photoacoustic peak shifted from

705 nm to 775 nm with an increase of the 775 nm signal by 25% (Figure 3.2B). Furthermore, the addition of H_2O_2 elicits a prompt increase in the fluorescence signal at 825 nm by over 100% (Figure 3.2C). The kinetics of this reaction was followed with all three modalities, and revealed a fast conversion of the capped dye into the uncapped dye over a period of 10 minutes based on the absorption signal (Figure 3.2D). All measurements were cross validated via liquid chromatography mass spectrometry (LCMS) confirming that the signal changes were caused by the conversion of **JW41** to **JW35**.

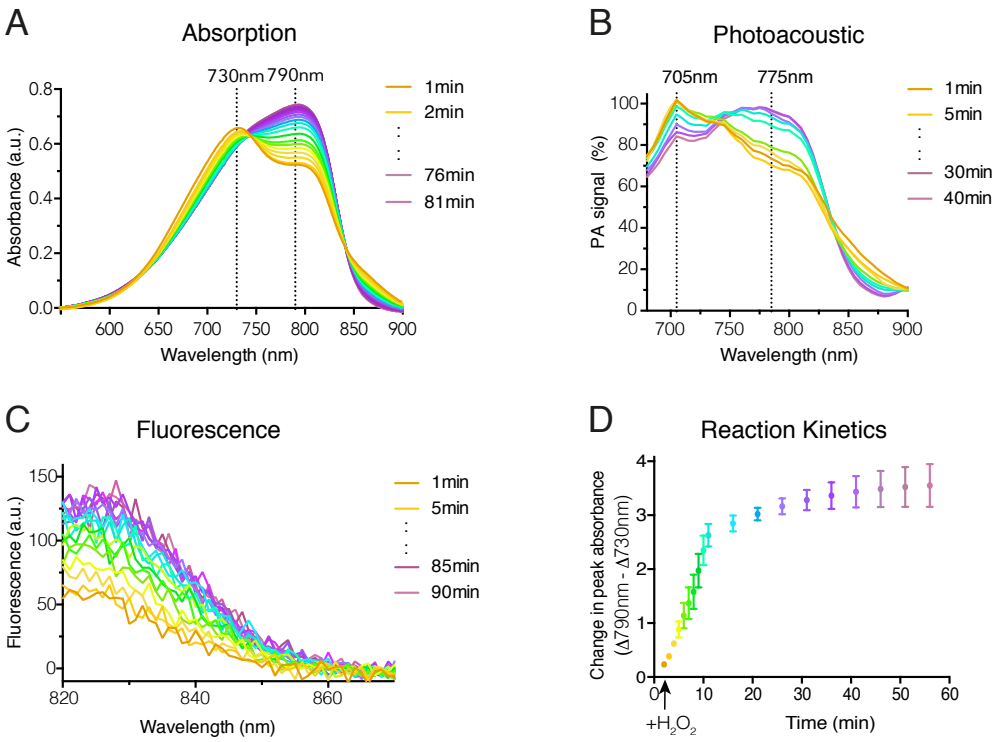

Figure 3.2 Reactivity of JW41 towards H_2O_2. A) - D) Monitoring the reaction of the capped dye (JW41; 10 μM) with H_2O_2 (100 μM) via absorption (A), photoacoustic (B) and fluorescence (C) measurements. The change (Δ) in peak absorbance at 730 nm and 790 nm was used to generate the reaction progress curve (D).

Importantly, LCMS studies demonstrated that the above stated properties are selective for the ROS H_2O_2 with no or only minor cross-reactivity observed with a wide range of other reactive species (Figure 3.3). The generation of the different ROS was verified by independent tests with commercially available products (see section 3.4). It should be noted that **JW41** partially hydrolyses to the corresponding boronic acid (**JW41$_{\mathbf{hydrol}}$**) under aqueous conditions. However, it was ensured that this does not significantly affect the optical properties as the photophysical characteristics did not change in the control solutions of **JW41**, which were incubated in water for up to 2 h (Appendix Figure A.7). Additionally,

the H_2O_2 reactivity and specificity retained for the hydrolysed form of **JW41**, **JW41$_{\text{hydrol}}$**. As the oxidation reaction is irreversible, this probe records the total H_2O_2 exposure to the system, rather than the equilibrium value.

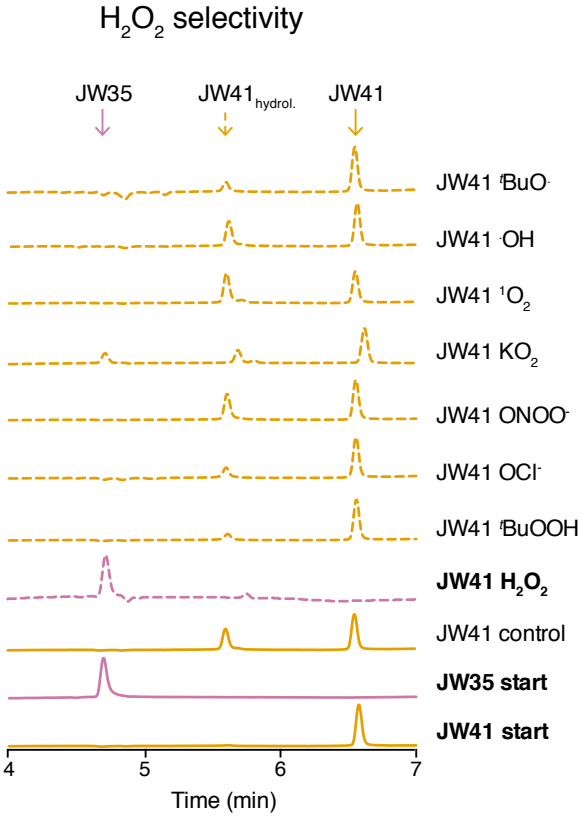

Figure 3.3 LCMS monitoring of the response of JW41 (10 μM) towards different ROS after 60 min incubation ([ROS] $\sim$ 100 μM). JW35 (10 μM) was used as endpoint-reference. UV traces at 750 nm are plotted.

3.2.2 *In Vitro* Evaluation

A good contrast agent must meet the following crucial requirements: high stability throughout the imaging time frame, being non-toxic and non-disruptive, bypassing physiological delivery barriers (e.g. cell membrane) and the ability to accumulate in targeted tissue but not in off-target tissue. Thus the next goal was to exploit the behaviour of the new H_2O_2-specific probe under *in vitro* conditions to gain insight into serum stability, protein binding, cellular toxicity, cellular uptake, cell localisation and targeting efficiency.

A first set of experiments sought to characterise the stability of the capped and uncapped dye in biological conditions. For this **JW41** and **JW35** were incubated in plasma at 37 °C for

up to 2 hours. Both dyes showed good stability with no formation of degradation products detected (Figure 3.4).

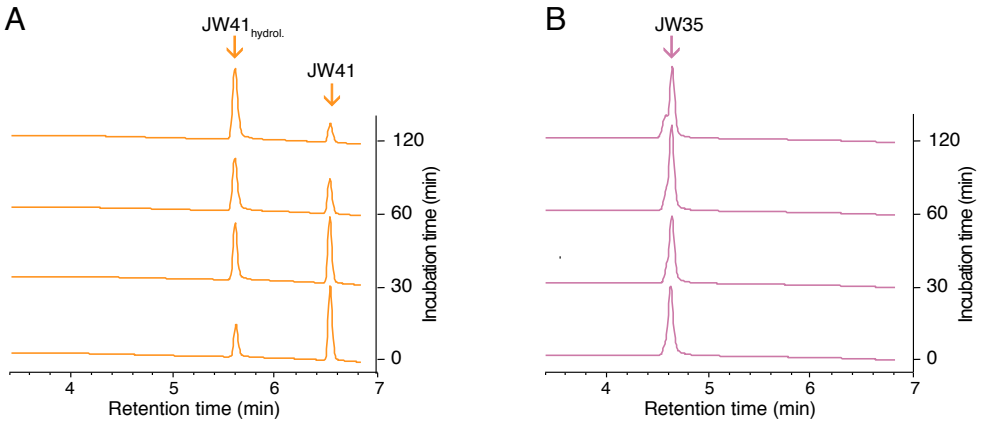

Figure 3.4 Serum stability of A) JW41 and B) JW35 over 2 h in FBS at 37 °C. UV traces at 750 nm of the LCMS analysis of the dyes after 30 min, 60 min and 120 min incubation are shown (concentration at time point of injection: 8 μM).

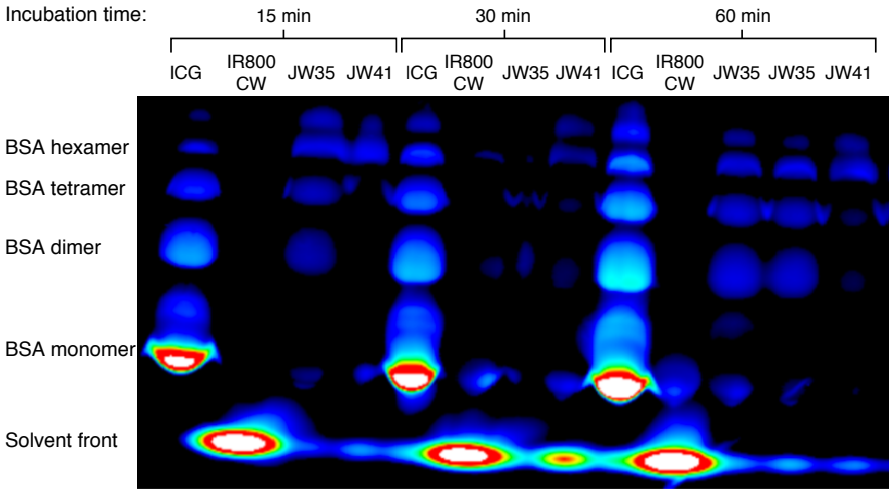

Figure 3.5 Protein binding of JW41 and JW35 assessed in 3 wt.% BSA in PBS. ICG (1 μM) and IR800CW (1 μM) are used as reference for a strong protein binding and a low protein binding dye respectively. The bound and unbound dyes were separated on a native gel after 15 min, 30 min and 60 min incubation and visualised using the 800 nm channel laser source. 1-BSA monomer, 2-BSA dimer, 3-BSA tetramer, 4-BSA hexamer [120]

.

Protein binding can not only influence the optical properties of dyes but also hamper extravasation and hence affect the biodistribution of a contrast agent (e.g. by increasing hepatic clearance). Thus, the protein binding properties of **JW41** and **JW35** were evaluated

using 3 wt.% BSA in PBS. IR800CW was used as reference for a low protein binding dye and Indocyanine green (ICG) as a strong protein binding dye (cf. Section 2.2.1). Both dye derivatives were found to show stronger binding than IR800CW but considerably less binding than ICG (Figure 3.5).

To establish the toxicity and uptake profiles of the new probe, two established breast cancer cell lines, MCF-7 and MDA-MB-231, were used. These two cell lines are of particular interest to test the properties of the new probe as they differ significantly in their ROS production abilities with MDA-MB-231 cells producing intracellular ROS levels three times higher than those of MCF-7 cells [164].

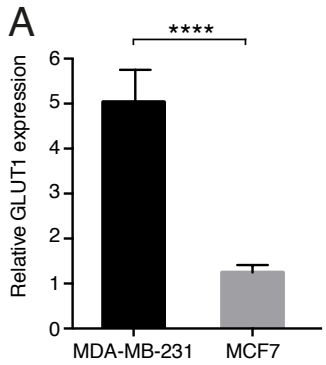

Figure 3.6 Glut1 mRNA expression.

Furthermore, MDA-MB-231 cells typically feature Warburg effect characteristics and express higher levels of glut1 mRNA than MCF7 cells [165, 166, 164]. This observation was confirmed by quantitative real-time polymerase chain reaction (Figure 3.6). However, one needs to keep in mind that higher gene expression does not always translate into higher protein levels, and it is the latter that dictates cellular uptake of the contrast agent. Unfortunately, multiple attempts to quantify the protein expression levels of MDA-MB-231 and MCF7 cell lines via Western blot failed. Nonetheless, these two observations from the literature justified the choice of the MDA-MB-231 and MCF7 cells lines to investigate the biological properties of the new probe.

Because the ideal contrast agent should maintain the cellular integrity and be non-toxic, the cytotoxicity of the capped and uncapped probe was tested using 3-(4,5-dimethylthiazol-2-yl)-2,5-diphenyltetrazolium bromide (MTT) viability assays and IncuCyte proliferation assays. Through these two assays the acute toxicity (MTT assay) as well as the long term impact of the probes towards cell proliferation (Incucyte assay) were assessed. Cells exposed to 0.5% DMF were used as a reference as the dyes were dissolved in that solvent. The toxicity of the capped and uncapped probe was compared to that of ICG as this dye presents a very low toxicity profile and is FDA-approved. Encouragingly, neither form of the new probe showed any significant cytotoxicity in any of the assays performed (Figure 3.7), with the notable exception of time points between 54 and 60 h for MDA-MB-231 and 72-78 h for MCF7 cells after which the dye groups recovered confluence levels similar to the control group. Cells exposed to ICG and 0.5% DMF showed a greater impact towards cell division than **JW41** and **JW35**, reinforcing no decisive toxicity of the new probes.

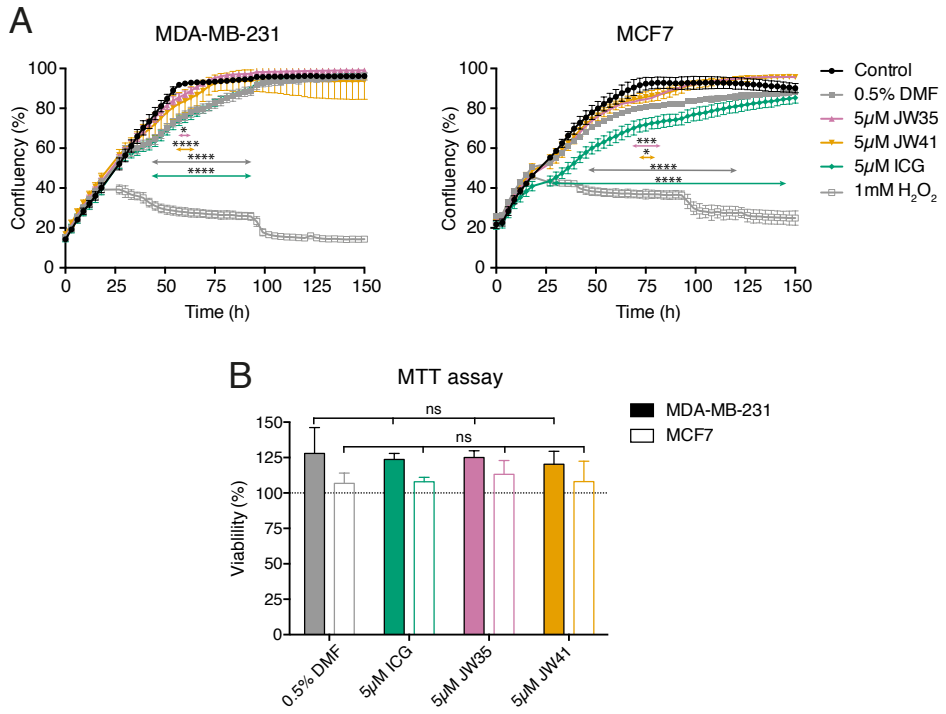

Figure 3.7 Cellular toxicity of JW41 and JW35. A) Real-time evaluation of the effect of 5 μM JW41 and JW35 towards cell proliferation of MDA-MB-231 (left) and MCF7 (right) cells was performed by IncuCyte Zoom. ICG (5 μM) was used as FDA approved control dye, H_2O_2 (1 mM) as toxic control compound and DMF (0.5%) to correct for possible effects of the solvent the dye-stocks were prepared in. The substances were added 24 hours after the cells were seeded. Images were acquired every 3 hours for 150 hours. Statistical significance was assessed by 2way ANOVA; $****p < 0.0001$; $*p > 0.024$. B) Cell viability was tested by MTT assay. Cells were incubated prior with 5 μM of JW41, JW35, ICG, 0.5% DMF or medium (=control) for 8 hours. Viability is stated relative to the control cells. Statistical significance was assessed by unpaired t-test.

Next, the cellular uptake of the new probes were investigated. The addition of 5 μM **JW41** or **JW35** to MDA-MB-231 or MCF7 cells resulted in a rapid cellular uptake (15 min post exposure) progressively increasing over 4 hours (Figure 3.8).

To establish the intracellular distribution of the probes, microscopic examination of live and fixed MDA-MB-231 and MCF7 cells by wide field microscopy were performed. Briefly, the cells were co-stained with NucBlue or Hoechst (DNA binding dyes; nucleus), WGA-AF488 (membrane-bound dye; plasma membrane), MitoTracker orange (a dye containing a thiol-reactive chloromethyl moiety specifically accumulating into the mitochondria) and LysoTracker green (a weakly basic amine accumulating in low pH organelles; lysosomes). The fluorescent signal signal from **JW41** and **JW35** was localised to the cytosolic compartment with no nuclear or cell surface co-localisation (Figure 3.9).

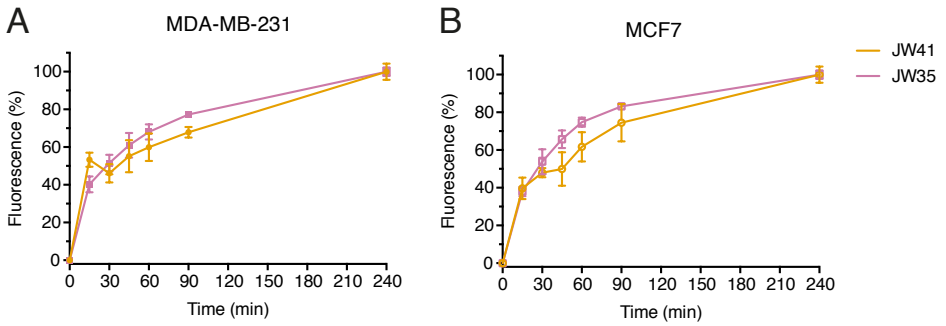

Figure 3.8 Cell uptake kinetics of 5 μM JW41 and JW35 in A) MDA-MB-231 and B) MCF7 cells. The fluorescence signal is normalised and stated relative to the baseline signal of the cells without dye.

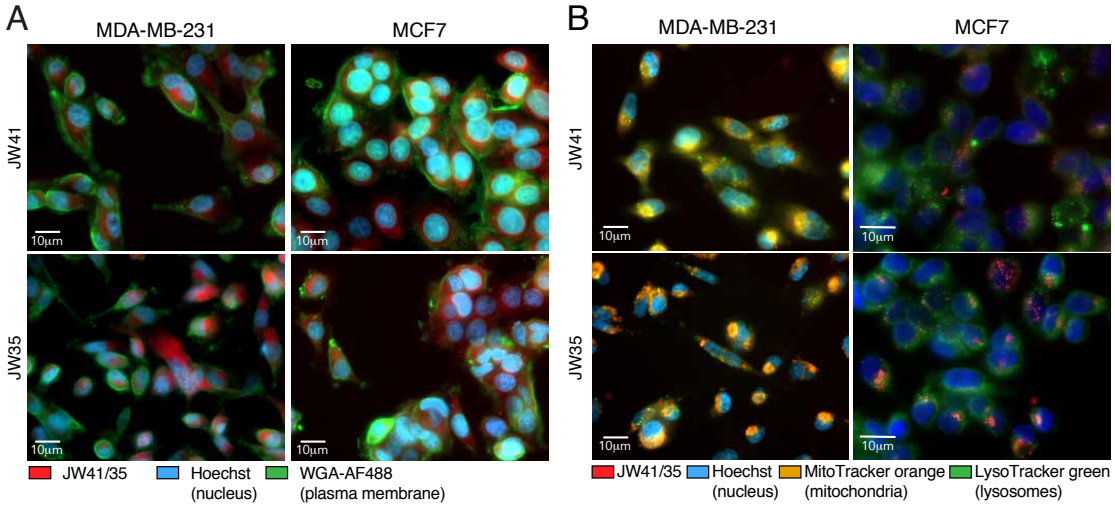

Figure 3.9 Cellular localisation of JW41 and JW35. Widefield fluorescence images of: A) fixed MDA-MB-231 and MCF7 cells stained with JW41 / JW35 (red; 2.5 μM), WGA-AF488 (green) and Hoechst (blue); B) live MDA-MB-231 cells incubated prior with JW41/JW35 (red, 2.5 μM), NucBlue Live ReadyProbes (blue), MitoTracker (orange) and LysoTracker green (green) and of live MCF7 cell incubated prior with JW41/JW35 (red, 2.5 μM), NucBlue Live ReadyProbes (blue) and LysoTracker green (green).

Furthermore, the GLUT-targeting ability of the H_2O_2-specific probe and whether the cellular uptake is facilitated via GLUT-mediated diffusion was questioned. This was investigated by inhibition assay, competition assay and pharmacological activation of glucose transport *in vitro*. ICG and IR800CW were used as negative, non-targeted controls and IR800CW-2DG as positive control [167]. These controls were chosen due to the same targeting structure (2-DG) and molecular weights and near-infrared absorption and fluorescent signals in the same range as **JW41**. The specificity of 2-deoxyglucose targeting was examined by pre-incubation of MDA-MB-231 and MCF7 cells with either 2-deoxyglucose (competition assay, Figure 3.10)

or D-glucose (competition assay, Figure 3.11). The response curves indicating that a strong decrease in **JW41** uptake occurs around 50 mM 2-DG or 20 mM D-glucose addition.

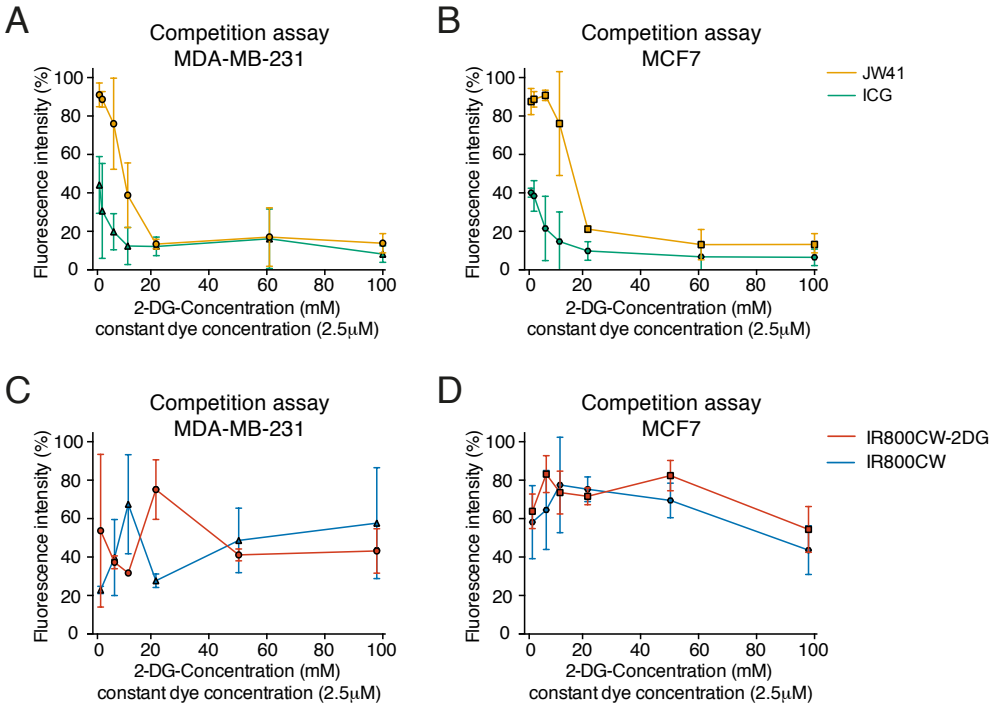

Figure 3.10 Competition binding assay in MDA-MB-231 (A and C) and MCF7 (B and D) cells with increasing concentrations of 2-deoxyglucose. The near-infrared dyes ICG and IR800CW were used as a non-targeted control, IR800CW was intended as positive control. All dyes were used at 2.5 μM concentration.

However, it is important to mention that the negative control ICG exhibited a similar cellular uptake trend although to a smaller degree and with a smaller overall signal (Figure 3.10 and 3.11). Additionally, all the error bars (expressing standard deviations) were relatively large and neither the competition nor inhibition study of the positive control IR800CW-2DG resulted in the expected uptake curve. Different parameters were varied to optimise the assay but without success. Consequently, the results of these two assays can not yet be used to claim targeting specificity of **JW41**.

Finally, cellular uptake of 2-DG targeted compounds by GLUT transporters can be pharmacologically modified by drugs either enhancing surface translocation and activity of GLUT transporters or decreasing glucose transport. Thus, we strived to establish one assay for each case of pharmacological alteration. To inhibit glucose uptake, the chemical compound STF-31, which has been described to specifically inhibit GLUT1, was used

[168, 166]. Unfortunately, the different conditions tested did not influence cellular uptake of **JW41** nor the positive or negative controls.

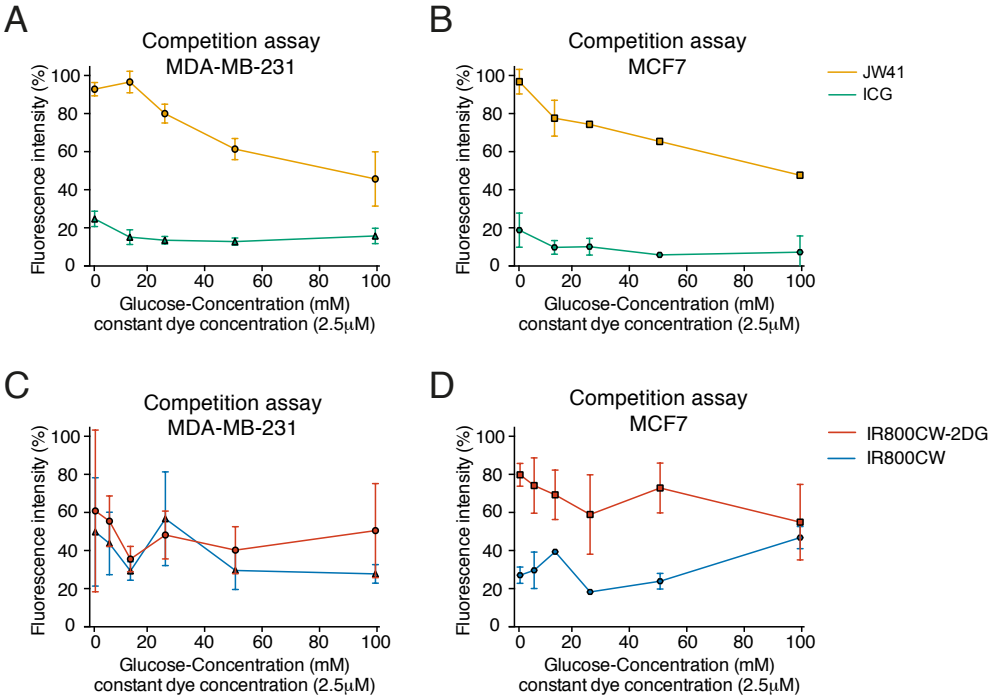

Figure 3.11 Competition binding assay in MDA-MB-231 (A and C) and MCF7 (B and D) cells with increasing concentrations of D-glucose. The near-infrared dyes ICG and IR800CW were used as a non-targeted control, IR800CW was intended as positive control. All dyes were used at 2.5 μM concentration.

To induce pharmacological activation of glucose transport, a 12-O-tetradecanoylphorbol-13-acetate (TPA) uptake assay was established. The phorbol ester TPA leads to the phosphorylation of serine 226 in GLUT1 causing a rapid enhanced cell surface localisation of GLUT1 and an increased glucose uptake [169, 170]. Thus, treatment of the cells with TPA was expected to result in an increase in **JW41** uptake. A fluorescence increase of greater than 44% in MDA-MB-231 and greater than 35% in MCF7 cells occurred for IR800CW-2DG and **JW41** when treated with TPA (13 μM) 1 h prior dye incubation, whereas there was no fluorescence enhancement observed in cells treated with IR800CW (Figure 3.12). These results may be due to the specific recognition of **JW41** by tumour cells via glucose transporters and thus its targeting capability.

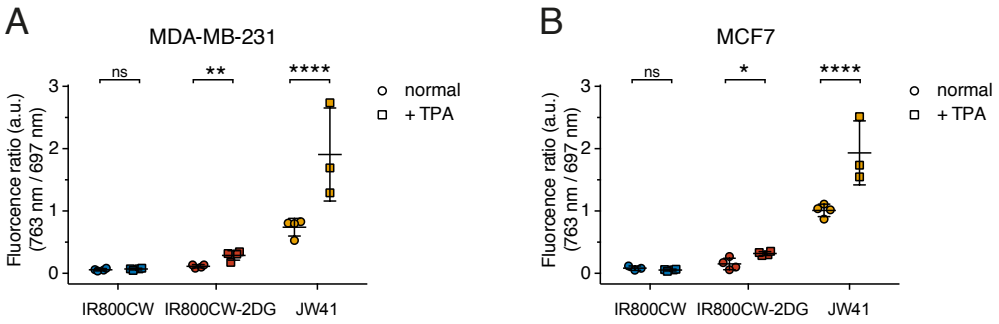

Figure 3.12 TPA assay to investigate GLUT specific uptake of JW41. Pharmacological activation of glucose transport in A) MDA-MB-231 and B) MCF7 cells were induced with TPA (13 μM) 1 h prior to dye addition and led to increased uptake of JW41 and the positive control IR800CW but not of the negative control IR800CW. Statistical significance was assessed by unpaired 2 tailed t-test; $*p < 0.05$, $**p < 0.01$, $****p < 0.0001$.

3.2.3 *In Vivo* Characterisation - Biodistribution and Tumour Accumulation

Having obtained promising *in vitro* results, the next goal was to investigate the biodistribution, toxicity, tumour detection efficacy and reactivity of **JW41** *in vivo* and to ensure a unique optical signature.

The ability to detect the dyes PA and fluorescence signal in living subjects was first studied in female nude mice bearing bilateral subcutaneous MDA-MB-231 tumours. For a 20 g mouse, 150 μL of 150 μM **JW41** was injected intravenously into the tail vein, resulting in $\sim$15 μM circulating concentration (assumption: 58.5 ml blood per kg; https://www.nc3rs.org.-uk/mouse-decision-tree-blood-sampling). The PA signal was recorded between 660 nm and 900 nm for a period of 30 minutes post-injection. As illustrated in Figure 3.13, an increase in PA signal intensity as well as a change in the PA spectrum was observed in the tumours, liver, kidneys and spleen within the first 5 to 10 minutes post-injection and remained high up to 30 minutes post-injection (Figure 3.13A,B). The accumulation kinetics could successfully be monitored following the signal at 760 nm (Figure 3.13C).

The specific accumulation of the contrast agent in tumour and liver was confirmed with fluorescence imaging acquired before probe injection, 1 h post-injection and 24 h after injection (Figure 3.14). The strong PA and fluorescence signals persisted for 24 h in the tumours and liver, whereas the signals in spleen and kidney were decreased close to baseline level. This indicates a specific retention of the dye in the tumours and liver, but not in the kidneys and spleen.

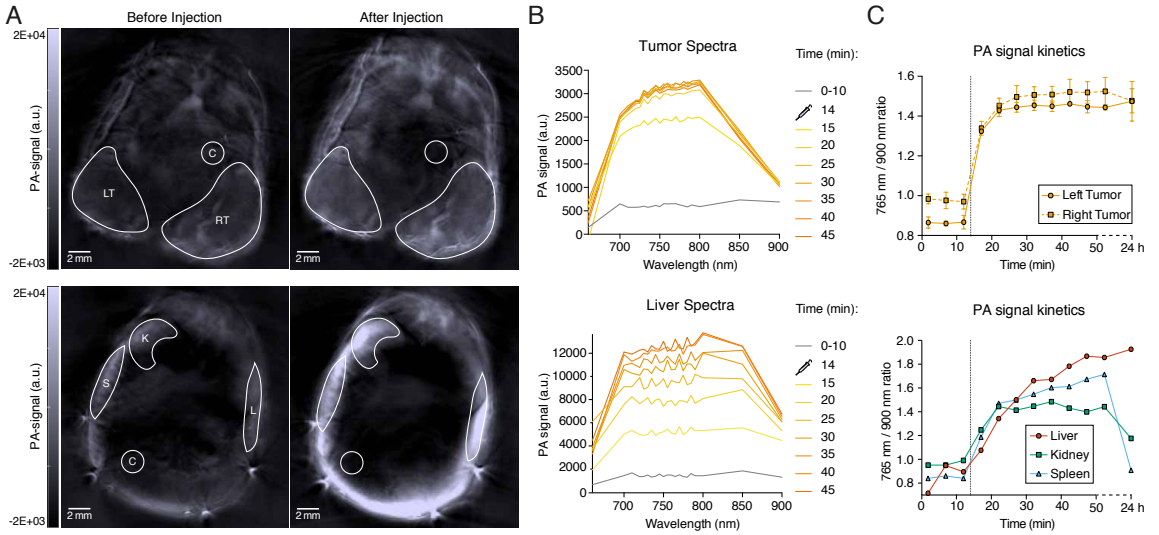

Figure 3.13 PA *in vivo* characterisation of JW41 in subcutaneous MDA-MB-231 tumours in nude mice. A) Representative PA tomography slice through MDA-MB-231 tumours (top) and kidney, spleen and liver (bottom) before and 30 min after injection of JW41 (150 μL of 150 μM for 20 g mouse). The regions of interest are indicated with white borders (LT = left tumour, RT = right tumour, L = liver, S = spleen, K = kidney, C = control region). B) Specific changes in the PA spectra and an increase in the PA signal between 700 and 810 nm were detected in the regions of interest upon injection of JW41. Representative graphs for tumour (top) and liver (bottom) are presented. The spectra recorded between 0 and 10 min represent the intrinsic tumour / liver spectrum (grey). The contrast agent was injected at 14 min. C) The increase in PA signal at 765 nm up to 24 h after injection is shown and suggests specific retention of the dye in the tumours (top) and liver, but clearance in kidney and spleen (bottom). PA signal changes in the control regions confirm that the PA signal kinetic data are specific to the ROIs (Appendix Figure A.8).

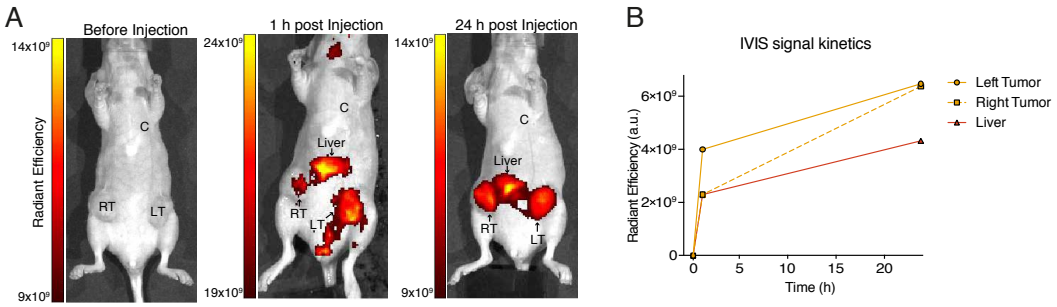

Figure 3.14 Fluorescence *in vivo* characterisation of JW41 in subcutaneous MDA-MB-231 tumours in nude mice. A) IVIS images before as well as 1 h and 24 h post injection of JW41. (LT = left tumour, RT = right tumour, L = liver, C = control region). B) The specific increase in radiant efficiency in the tumours and liver upon JW41 injection (values from the control region, C, were used for background correction).

To enable PA imaging of H_2O_2 it is necessary to differentiate the capped, **JW41**, and uncapped, **JW35**, dye *in vivo*. Thus, the same study was performed with an injection of **JW35**

but at a 3-times lower dose as used for **JW41** (50 μM instead of 150 μM). The objective of this was to investigate if a conversion of one third of **JW41** into **JW35** is detectable *in vivo*. Similar PA signal changes and biodistribution results were observed (Figure 3.15). However, the clearance of **JW35** occurred faster with only a low signal remaining in the tumours, liver, kidneys and spleen after 24 h (Figure 3.15C).

These results were affirmed with fluorescence imaging acquired before probe injection, 1 h post-injection and 24 h after injection (Figure 3.16), which indicated a strong increase in the fluorescence signal in the tumours and the liver but a fast clearance over the following 23 hours.

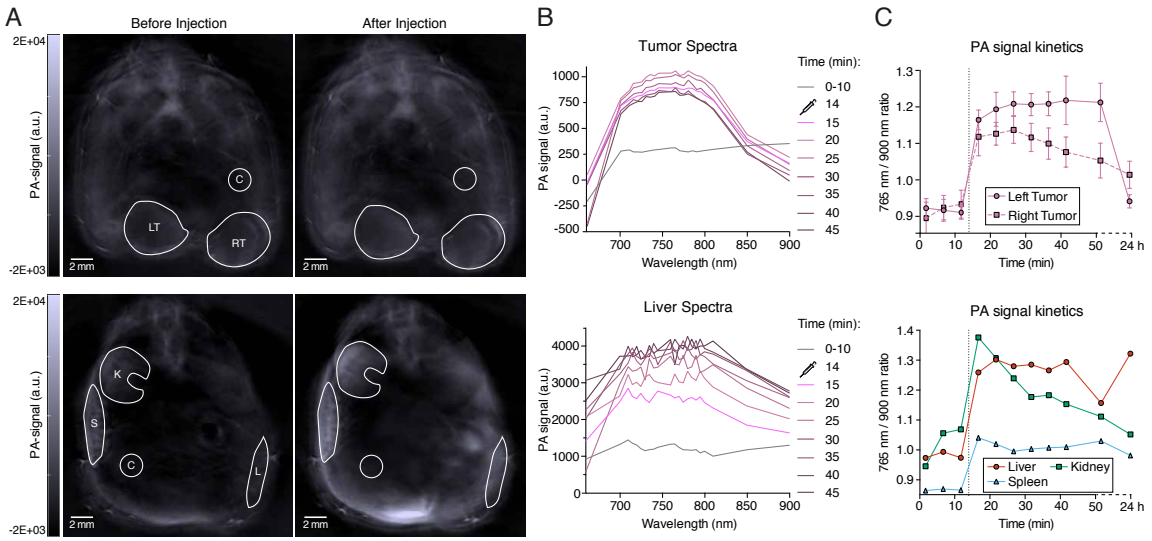

Figure 3.15 PA *in vivo* characterisation of JW35 in subcutaneous MDA-MB-231 tumours in nude mice. A) Representative PA tomography slice through MDA-MB-231 tumours (top) and kidney, spleen and liver (bottom) before and 30 min after injection of JW35 (150 μL of 50 μM for 20 g mouse). The regions of interest are indicated with white borders (LT = left tumour, RT = right tumour, L = liver, S = spleen, K = kidney, C = control region). B) Specific changes in the PA spectra as well as a PA signal increase were detected in the regions of interest upon injection of JW35. Representative graphs for tumour (top) and liver (bottom) are presented. The spectra recorded between 0 and 10 min represent the intrinsic tumour / liver spectrum (grey). The contrast agent was injected at 14 min. B) The increase in PA signal at 765 nm up to 24 h after injection is shown and suggests accumulation of the dye in the tumours (top) and liver and to smaller extend in kidney and spleen (bottom). PA signal changes in the control regions confirm that the PA signal kinetic data are specific to the ROIs (Appendix Figure A.8).

The *in vivo* characterisation of **JW41** and **JW35** showed that both versions of the new contrast agent can be detected separately in mice. It was therefore next examined whether spectral unmixing is able to accurately detect and quantify the relative concentrations of the capped and uncapped dye if present simultaneously *in vivo*. Even though it is assumed that

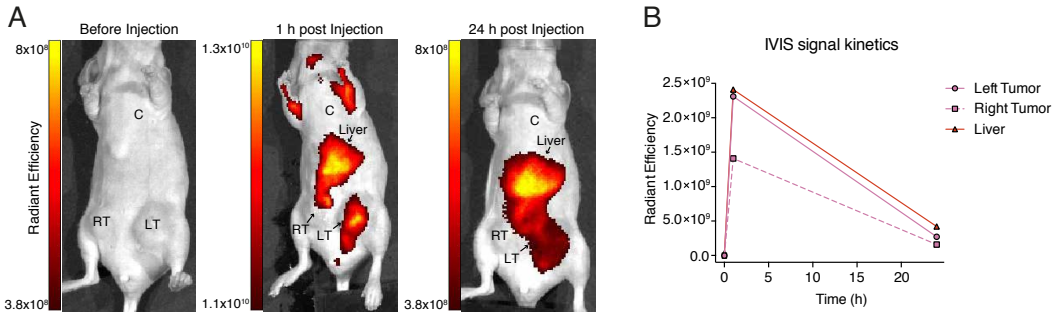

Figure 3.16 Fluorescence *in vivo* characterisation of JW35 in subcutaneous MDA-MB-231 tumours in nude mice. A) IVIS images before as well as 1 h and 24 h post injection of JW35. (LT = left tumour, RT = right tumour, L = liver, C = control region). E) The specific increase in radiant efficiency in the tumours and liver upon JW35 injection monitored over 24 h. (Values from the control region, C, were used for background correction).

JW41 will be partially converted into **JW35** in the tumours, to ensure that both dyes were present for the evaluation of spectral unmixing *in vivo*, the same *in vivo* study was performed, but on this occasion with a 2 : 1 mixture of **JW41** : **JW35** (150 μL of 100 μM **JW41** and 50 μM **JW35**). Analysis of the PA *in vivo* data with linear regression multispectral processing using the spectra of **JW41** and **JW35** obtained previously in tissue mimicking phantoms (Figure 2.24) and published spectra for oxy- and deoxyhemoglobin (http://omlc.org/spectra/) was applied to produce images indicating the relative weight that each dye spectrum contributes to a given image pixel (Figure 3.17) and thus allowing the readout of H_2O_2 being present in different regions of interest (ROI). Both probes could be successfully distinguished from the background signal and visualised. In addition, it was possible to distinguish the two forms of the contrast agent, **JW41** and **JW35**, from each other *in vivo* by means of spectral unmixing (Figure 3.17A-C). Furthermore, monitoring the accumulation kinetics with spectral unmixing resulted in a similar biodistribution profiles of the dyes to those obtained by monitoring the signal increase at 765 nm (Figure 3.13 and 3.15).

Comparing the weights of **JW41** and **JW35** in the ROIs of the mice injected with either only **JW41** or a 2 : 1 mixture of **JW41** : **JW35** indicate a conversion of 57$\pm$14% of **JW41** into **JW35** (average across 7 tumours). Spectral unmixing in the liver - the organ with the highest signal - of mice treated with the 2 : 1 mixture of **JW41** : **JW35** mirrors the injected ratio with an accuracy of 11% (% deviation from the known concentration). However, as it was shown in previous phantom studies (cf. Chapter 2, Section 2.2.5) the unmixing approach did not match perfectly and some signal crossover was obtained resulting in background signal and contribution of **JW35** to the **JW41** signal and vice versa, causing signal misclassification to some extent. In addition, each single data point represents the average of multiple

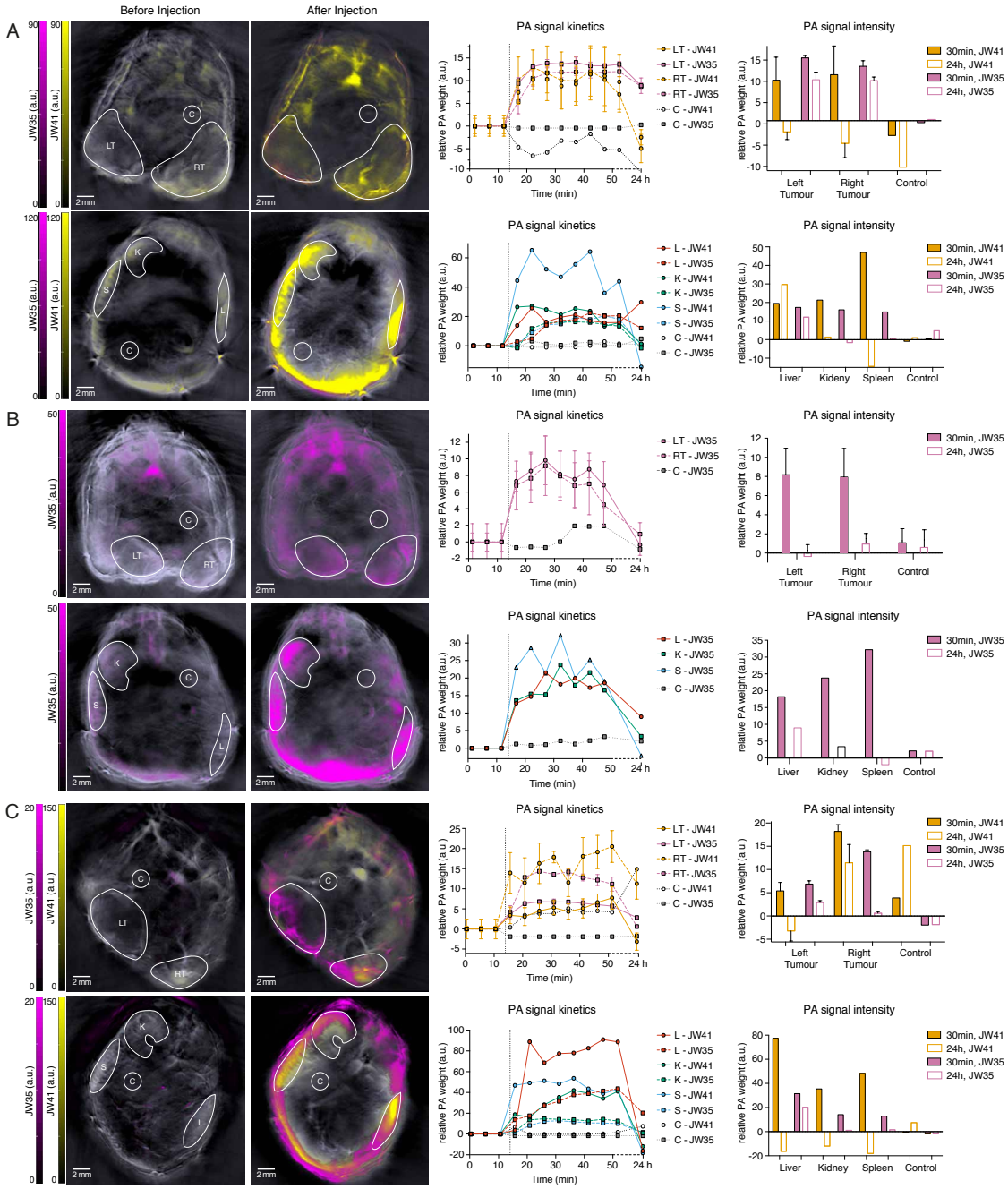

Figure 3.17 *In vivo* spectral unmixing of JW41 and JW35. Column 1&2: representative PA tomography slice through MDA- MB-231 tumours, kidney, spleen and liver before and after injection of A) JW41 (150 μL, 150 μM) B) JW35 (150 μL, 50 μM) C) 2 : 1 JW41 : JW35 mixture (150 μL, 100 μM JW41, 50 μM JW35) analysed by spectral unmixing with linear regression. The signal of JW41 is shown in yellow, JW35 in magenta. Signal intensity indicates the relative weight that each dye spectrum contributes to a given image pixel. White borders indicate ROIs (LT = left tumour, RT = right tumour, L = liver, S = spleen, K = kidney, C = control region). Column 3: representative PA signal kinetics curves obtained by spectrally unmixing of the outlined ROIs. The plotted values derived by linear unmixing are zeroed to the mean of the first 3 measurements, which were performed before probe injection. Column 4: PA signal increase (obtained by spectrally unmixing for JW41 and JW35) relative to the baseline signal (average of the first 3 measurements) in the outlined ROIs at 30 min and 24 h after injection.

slices through the tumour (number of slices were dependent on tumour size). The tumour heterogeneity together with the unmixing approach explaining the relatively large error bars (representing standard deviation). Nevertheless, the results suggest a good tumour detection efficiency (also compared to the intrinsic signal of Hb and HbO_2, cf. Appendix Figure A9) and demonstrate the applicability of the dye to monitor oxidative stress *in vivo*. Finally, the contrast agent was also injected into healthy mice, which were kept alive for a month after injection. No signs of any toxicity were observed in these mice.

3.2.4 *In vivo* Evaluation - Therapy Monitoring

The next aim was to evaluate the capability of the new contrast agent to monitor oxidative stress response in tumours upon treatment. As highlighted previously, the two breast cancer cell lines, MDA-MB-231 and MCF7, feature different characteristics regarding their *glut1* expression and H_2O_2 production. Additionally, MCF7 cells are characterised as less aggressive, less prone to metastasise, recruiting a more complex microenvironment and exhibiting a better differentiated phenotype associated with a pronounced paracrine activity. In comparison, MDA-MB-231 cells are more aggressive and less differentiated, they tend to acquire mesenchymal characteristics and are inclined to metastases [171]. Therefore, it was expected that these two cells lines would respond differently to therapy when subcutaneously implanted in mice. Taking this as the starting point, the aim was to further investigate the *in vivo* H_2O_2 reactivity of **JW41** and the capability to monitor treatment response in subcutaneous MDA-MB-231 and MCF7 tumour bearing mice. Liposomal doxorubicin (Doxil), was used as anti-cancer treatment. Doxorubicin is an anthracyline chemotherapy drug, which is routinely used in the treatment of several cancers including breast cancers. One of the proposed mechanisms by which doxorubicin acts in cancer cells is the generation of oxidative stress through reactive oxygen species, which damages cellular membranes, DNA and proteins [171]. The liposomal version of doxorubicin acts in the same way but was shown to reduce cardiac toxicity and increase tumour accumulation [171]. The study design is outlined in Figure 3.18.

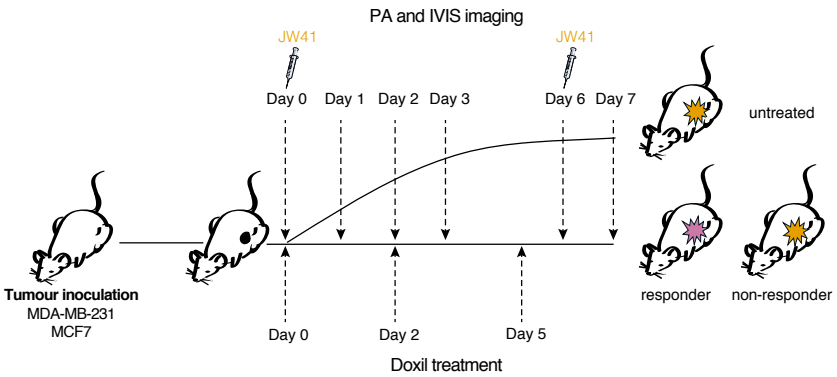

Figure 3.18 Schematic illustration of the design of the *in vivo* study to examine the capability of JW41 to monitor the response to the anticancer drug Doxil. On day 0, subcutaneous MDA-MB-231 and MCF7 tumour bearing mice were dosed with JW41 and imaged with MSOT and IVIS. After the imaging session, the mice were treated with Doxil for the first time. Further MSOT and IVIS imaging was performed on day 1, 2 and 3 and additional Doxil treatments were given on day 2 and 5. On day 6, mice were imaged before and after administration of a second dose of JW41. 24 h later, the mice were imaged, culled and organs were collected for *ex vivo* examination. One cohort of mice for each tumour type did not receive Doxil treatment but passed the same imaging process. One subcutaneous MDA-MB-231 tumour bearing mouse was only treated with Doxil but not with JW41 to investigate possible signals arising from Doxil.

PA and fluorescence imaging revealed a similar biodistribution and accumulation kinetics to those observed in previous *in vivo* studies (cf. Section 3.2.3). The specific accumulation of the contrast agent in the 2 different tumour types was confirmed (Figure 3.19 and 3.20). Unfortunately, this study was confounded by some technical difficulties as the PA data acquisition stopped regularly in between running imaging session, which required that the mouse needed to be taken out of the scanner and placed in after restarting, along with issues due to low and variable laser energy due to a faulty flashlamp. Additionally, mouse health related issues did emerge during this study: the oestrogen dependent MCF7 tumours required the implantation of oestrogen pellets. These pellets caused skin rashes as well as bladder obstruction, which made the MCF7 tumour bearing mice rather weak. Amongst other issues, this forced **JW41** to be injected 5 minutes after the mouse was placed in the MSOT, prohibiting baseline stabilisation before the start of the biodistribution study. These circumstances led to an unstable baseline and variable PA data with low signal sensitivity, which did not lead to acceptable and trustable results using spectral unmixing analysis.

On the other hand, fluorescence data revealed a slower signal reduction in the tumours when compared to the liver, especially after the injection of the contrast agent in Doxil treated mice (Figure 3.20). This may indicate either an overall prolonged retention of the

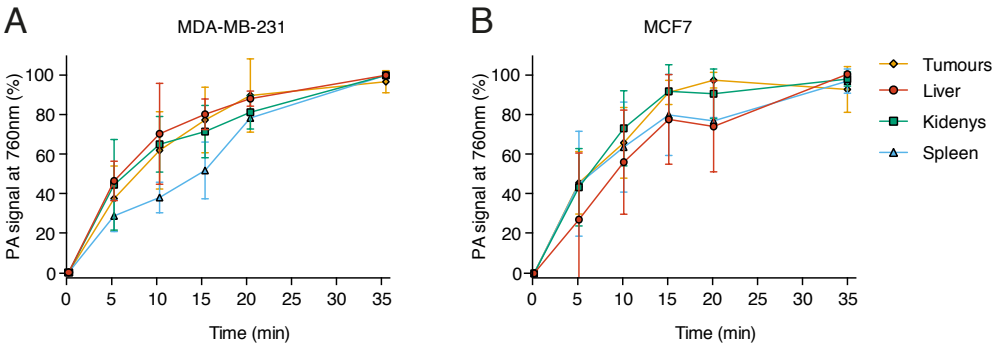

Figure 3.19 PA signal kinetic data of the first injection of JW41 for A) MDA-MB-231 and B) MCF7 tumour bearing mice of treatment response study. The plotted PA signal at 760 nm is normalised for each organ separately.

dye in tumours or the partial conversion of **JW41** into **JW35**, which is accompanied with a fluorescence signal increase. As the fluorescence imaging instrument used cannot distinguish the two forms of the dye, it is not possible to draw further conclusions from these data.

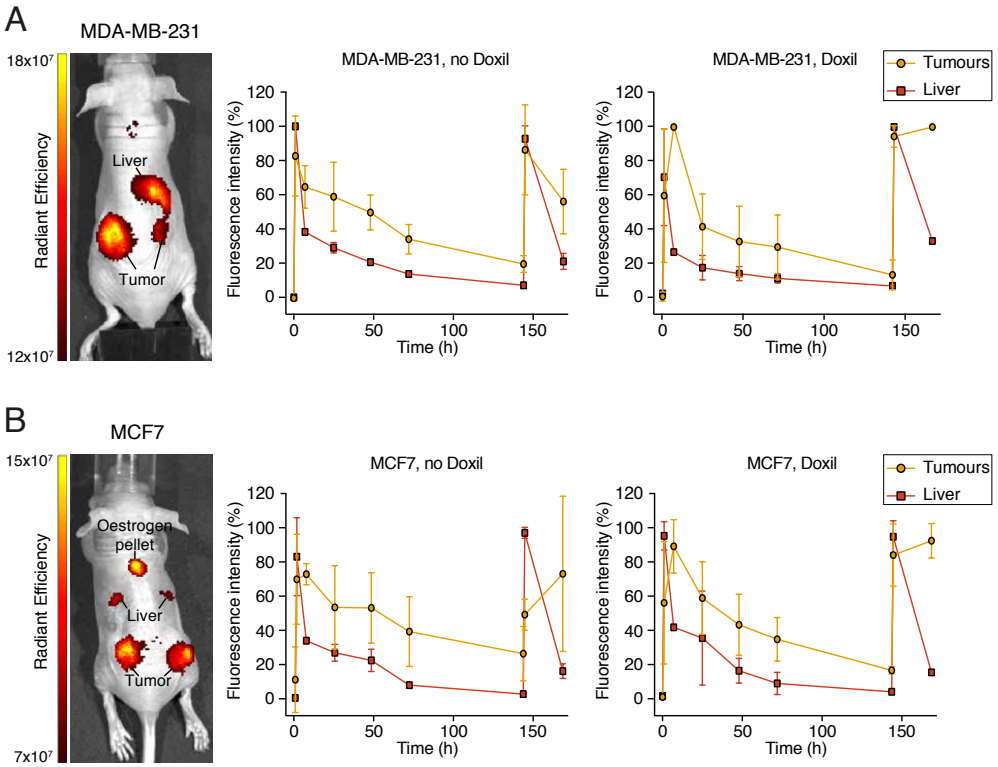

Figure 3.20 IVIS image (left) of A) MDA-MB-231 and B) MCF7 tumour bearing mice of treatment response study 24 h after the first injection of JW41. IVIS signal kinetic curves over the time frame of the whole treatment response study for A) MDA-MB-231 and MCF7 tumour bearing mice (n = 3) divided into two cohorts, non treated (middle) and Doxil-treated (right) mice.

3.2.5 Histopathology and Microscopy *ex vivo* Analysis

To examine the behaviour of the new contrast agent in greater depth, the localisation of the dye in the tumours was investigated by *ex vivo* histopathological analysis on consecutive sections that were either processed with Haemotoxylin and Eosin (H&E) or Caspase 3 (an apoptosis maker) stainings or directly imaged to detect the **JW41** and **JW35** signal. Comparing necrotic areas of tissue, as assessed by H&E staining with the **JW41** and **JW35** signal by wide-field microscopy suggests that the dye accumulates to a greater extent in viable areas or more **JW41** gets converted into **JW35** in these areas (Figure 3.21). Co-staining with DAPI also provided confirmation that the dye gets uptaken into the cytosol of the cells *in vivo* as was shown before for *in vitro* conditions (zoom, Figure 3.21). Further experiments would be needed to differentiate **JW41** and **JW35** in these sections.

To confirm this observation, the tumour fluorescence intensity (determined on the IVIS after necropsy) was compared to the tumour viability assessed by H&E staining (Figure 3.22A). Three out of the four tumours seem to support the assumption that less necrotic areas present either an increased dye accumulation and/or greater conversion of **JW41** into **JW35**. However, it must be taken into account that viability assessment was performed on one section through the tumour and hence does not reflect the whole tumour viability, which is often heterogeneous.

Histopathological analysis was also used to investigate the effect of the doxil treatment. Firstly, the level of tissue necrosis was assessed with H&E staining, but no significant difference was observed between the treated and non-treated cohorts (Figure 3.22B). Next, sections were stained for cleaved caspase-3. Caspase-3 is a critical executioner of apoptosis and thus used as apoptosis marker [172]. Again, no response was seen to the Doxil treatment (Figure 3.22C). Hence, for the tumour models and treatment conditions used here, Doxil treatment was not observed to induce cell death. The target in this case was to induce oxidative stress rather than necrosis, which was validated separately using LC/MS (see section 3.2.6), so it was expected that little or no significant difference would be observed between the cohorts.

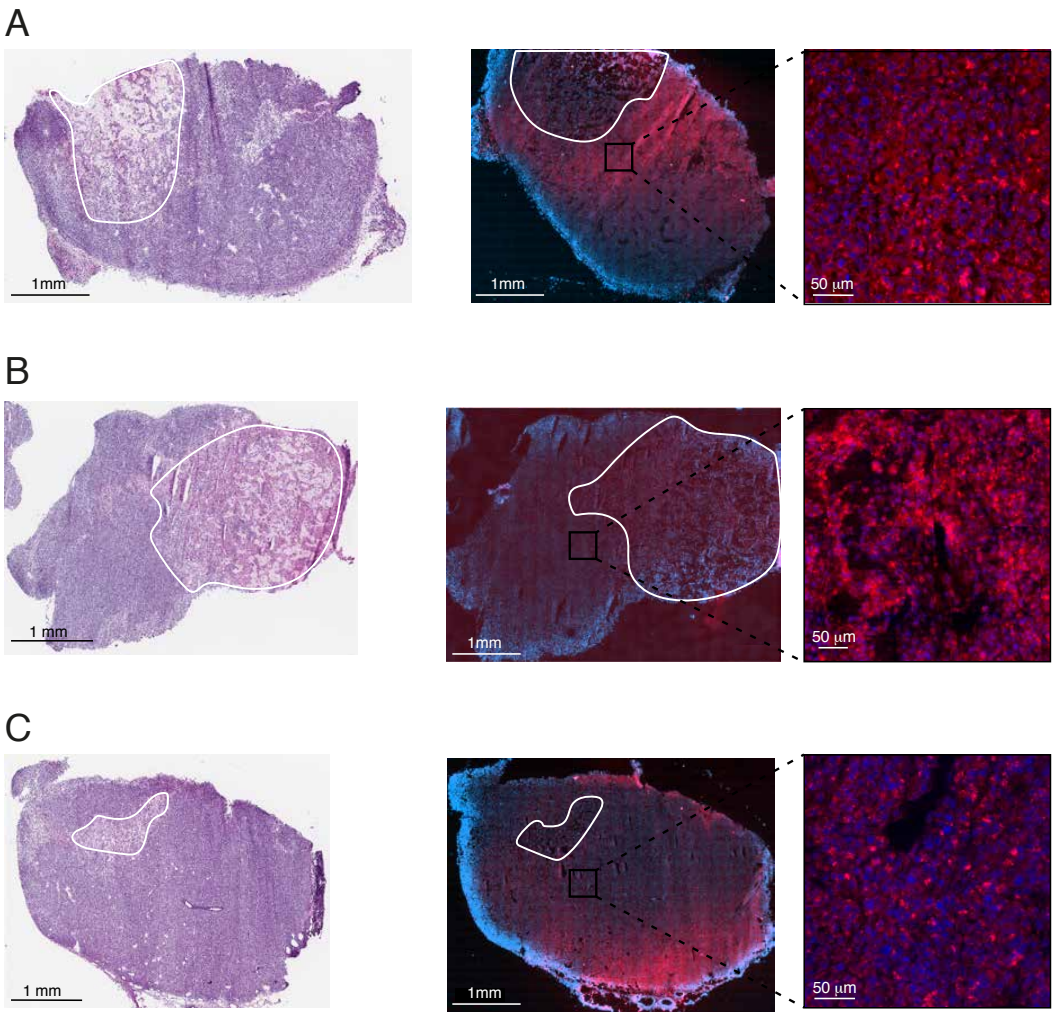

Figure 3.21 Histopathological and microscopy *ex vivo* characterisation of tumour tissues from *in vivo* studies with A) JW41, B) JW35 and C) 2-1 JW41-JW35 mixture. First column illustrates representative H&E stained section of frozen MDA-MB-231 tumours. The necrotic area is indicated with the white line. Representative wide-field fluorescence images of a consecutive tumour section section after formaldehyde fixation and staining with DAPI in mounting media (blue), are displayed in the middle column. On the right, a magnification of the wide-field image is pictured, allowing the localisation of the dye signal into the cytosol of the cells.

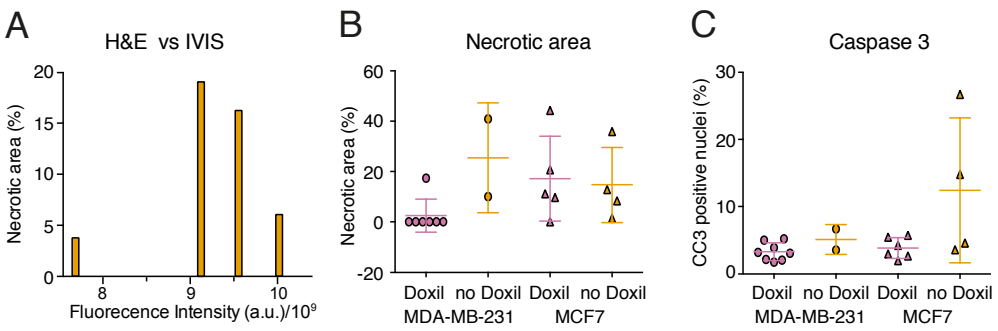

Figure 3.22 A) Relationship between necrotic areas assessed by H&E staining and fluorescence signal measured in the tumours after necropsy. Each bar represents a tumour from a mouse treated with JW41. A) and B) Histopathological *ex vivo* examination of tumours from treatment response *in vivo* study questioning the correlation between the different tumour types and between the treated and non-treated cohorts.

3.2.6 *Ex Vivo* Evaluation by LC-MS/MS

It is important to cross-validate the *in vivo* conversion of **JW41** into **JW35**. Fluorescence imaging confirmed the specific accumulation of the contrast agent in tumour and liver but because both, the capped and uncapped probe, share the same emission profile, it was not possible to determine if a stronger fluorescence intensity is caused by a higher tumour accumulation of **JW41** or by the conversion of **JW41** into **JW35**. Liquid chromatography tandem mass spectrometry (LC-MS/MS) is a powerful, sensitive and discriminating tool for the accurate detection of different molecules. Especially, when combined with multiple reaction monitoring mass spectrometry (MRM-MS) methods, it enables highly sensitive quantification of molecules in complex biological matrixes. In contrast to traditional mass spectrometry methods, which attempt to detect all the chemicals in the sample in an indiscriminate manner, MRM allows the MS to be calibrated to detect only the compounds of interest at the expected range of concentration.

Thus it was sought to use this method to accurately quantify the relative concentrations of **JW41** and **JW35** in tumours and livers to confirm the conversion of the capped dye into the uncapped dye and to validate the accuracy of the spectral unmixing analysis. Additionally, an established LC-MS/MS method was used to question the efficacy of the Doxil treatment by quantifying the amount of glutathione (GSH) and glutathione disulfide (GSSG) in each sample [173].

Workflow for LC-MS/MS Analysis of JW41 and JW35

The target molecules, **JW41**, **JW41$_{\text{hydrol}}$** and **JW35**, were extracted from homogenised tissue samples with MeCN : H_2O (8 : 2) and separated by their chromatographic retention. Subsequent mass analysis with MRM-MS was performed, where the specified parent ion of each dye derivative was isolated from all other ions entering the MS and targeted for further fragmentation. The detected MRM signal was then integrated and used to determine the concentration of the dye within the tissue sample, by comparing it with a calibration line of dye standards in tissue matrix. To validate the calibration line and the status of the analytical system, six quality control (QC) samples at three known concentrations were run before and after the biological samples [174]. Reproducible extraction of analytes from a biological matrix is challenging and often affects the accuracy of mass quantification. This can be improved by the use of an internal standard (IS), which is added to the biological samples, calibration standards and QCs and helps to correct for variability in the extraction efficiency and matrix effects [175]. Quantification is then performed by calculating the ratio of the integrated areas of the MRM peak of the dye and that of the internal standard. An overview of the workflow is illustrated in Figure 3.23.

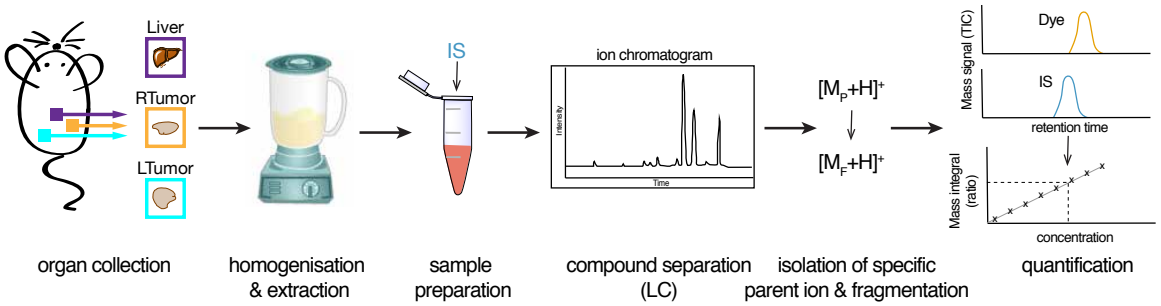

Figure 3.23 Schematic illustration of LC-MS/MS workflow for *ex vivo* evaluation studies. After the sample preparation, which includes organ collection, homogensiation, extraction and spiking with the IS, the samples are separated by chromatographic retention and eluted into the MS ionsource. There the selected compounds are isolated as the parent ions and fragmented in the MS-MS mode. Only the selected fragments ("daughter ions") are then further isolated and detected. The MRM transition from parent to daughter ion is quantified as a peak area.

Internal Standard and Validation of Matrix Effects, Calibration Curves and Detection Limits

Ideally, the internal standard is embodied by an isotopically labelled version of the analyte itself, since it bears the same chromatographic and ionisation characteristics but exhibits a unique mass signal, which can be used for separate integration. Unfortunately, the

synthesis requirements and instability of the dye molecules under certain conditions made it challenging to synthesise an isotopically labelled derivative.

Thus, a structurally similar molecule was synthesised, which possesses a specific fragmentation pattern and a retention time similar to those of the analytes. The first attempt, was to prepare the boc-protected derivative of **JW35**, **JW56** (Figure 3.24). Even though **JW56** gave a distinct mass signal (m/z = 1220.624 (z = 1) transition to m/z = 282.82), which could be used for integration, and eluted similarly to the analytes, its signal intensity and profile showed great variability indicating **JW56** to be unstable in the matrix and under the LC-MS/MS chromatographic conditions. During the dye development process, the **JW35**-derivative **JW35Mono** was synthesised, which carries only one glucose moiety (cf. Chapter 2.2.4, Figure 2.17). Its structural features looked promising for its suitability as IS due to the similarity to **JW35** and **JW41**. LC-MS/MS analysis confirmed that **JW35Mono** eluted similarly to **JW35** and **JW41** and showed a unique and stable mass signal for quantification (Figure 3.25) (consistency was validated over a range of four concentrations in matrix as well as MeCN : H_2O (8 : 2)). Although, **JW35Mono** was contaminated with trace levels of **JW35**, the signal of this impurity was below the threshold in the noise range and thus negligible.

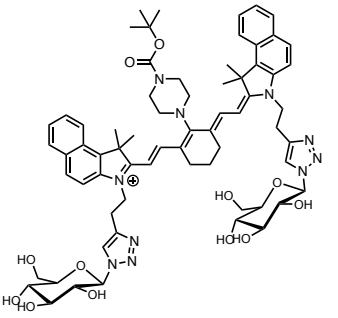

Figure 3.24 Molecular structure of JW56.

Next, the most abundant fragments for **JW41** and **JW35** were identified, which will be used for quantification (Figure 3.25B-D). The strongest parent ion for **JW35** appeared to be the doubled charged ion (m/z = 560.30 (z = 2)) and hence this was used for fragmentation (Figure 3.25). Due to the tendency of **JW41** to hydrolyse in aqueous solutions and especially on-column under the acidic conditions (solvent A: H_2O+0.1% FA; solvent B: MeCN+0.1% FA), the fragmentation pattern for $\mathbf{JW41_{hydrol}}$ was also determined (Figure 3.25C). All three analytes (**JW41**, $\mathbf{JW41_{hydro}}$ and **JW35**) were well distinguishable through their fragmentation patterns (Figure 3.25B-D) as well as their retention times (Figure 3.25E-F). The nearly simultaneous elution of the IS (**JW35Mono**) with **JW35** and $\mathbf{JW41_{hydro}}$ did not influence the quantification process, as MRM operates by targeting the defined parent ions separately (Figure 3.26). For quantification of the IS (**JW35Mono**), in the first quadrupole segment Q1 only the ions with m/z = 914.5 are isolated from all ions entering the MS. Subsequently, the isolated m/z = 914.5 ions entering the collision chamber Q2, where they get fragmented into their daughter ions (m/z = 161.11, 172.11, 187.12, 201.14, 215.15) (Figure 3.25E). When entering the third quadrupole segment Q3, all daughter ions are removed except the

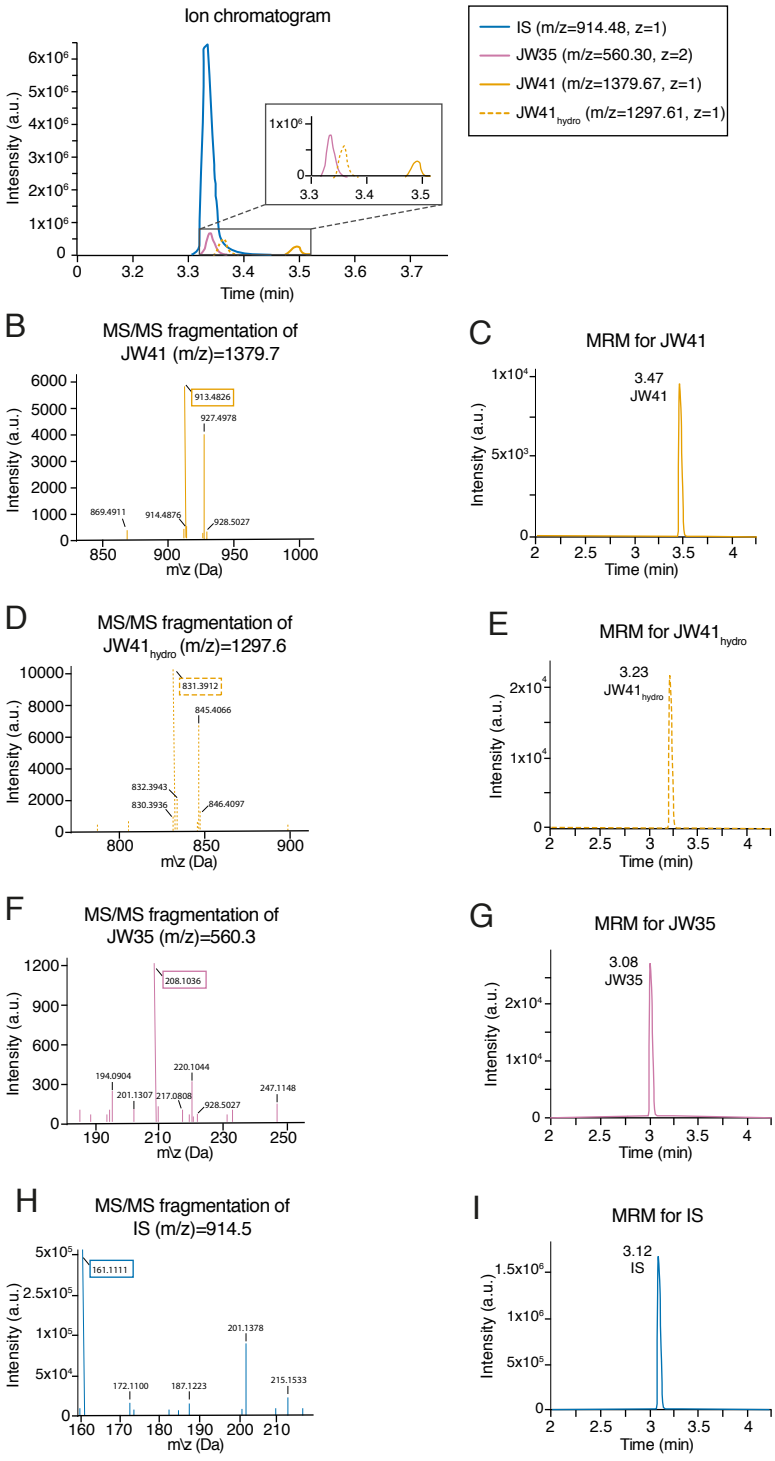

Figure 3.25 LC-MS/MS chromatograms of JW41(75 nM), JW35 (38 nM) and the IS (JW35Mono, 190 nM). A) Representative ion chromatogram of of JW41, JW35 and the IS. B), D), F) and H) Fragmentation of the parent compounds JW41 (m/z=1379.67), $JW41_{hydro}$ (m/z=1297.61), JW35 (m/z=560.30) and IS (M/z=914.48), respectively. MRM peaks for JW41 (monitoring m/z=1379.67 transition to m/z=913.48), $JW41_{hydro}$ (monitoring m/z=1297.60 transition to m/z=831.39), JW35 (monitoring m/z=560.30 transition to m/z=208.10) and IS (monitoring m/z=914.48 transition to m/z=161.11) are shown in C), E), G) and I), respectively.

selected daughter ion (m/z = 161.11), which then gets detected. This selective process results in a characteristic and very sensitive MRM peak for the IS (**JW35Mono**; transition from m/z = 914.5 to m/z = 161.1; Figure 3.25). Similarly, the specific **JW35** ions with m/z = 560.1 (z=2) are isolated in Q1, entering the collision chamber Q2, where they are fragmented into the daughter ions (m/z = 220.1, 217.1, 208.1, 201.1, 194.1 (all with z = 2)). In Q3 only the daughter ion with m/z = 208.1 gets directed to the detector and a characteristic and very sensitive MRM peak for **JW35** manifests (transition m/z = 560.2 (z = 2) to m/z = 208.1 (z = 2), Figure 3.25). The same procedure generates the unique MRM peak for $\mathbf{JW41_{hydrol}}$ (transition m/z = 1297.6 to m/z = 831.4) and **JW41** (transition m/z = 1297.6 to m/z = 831.4).

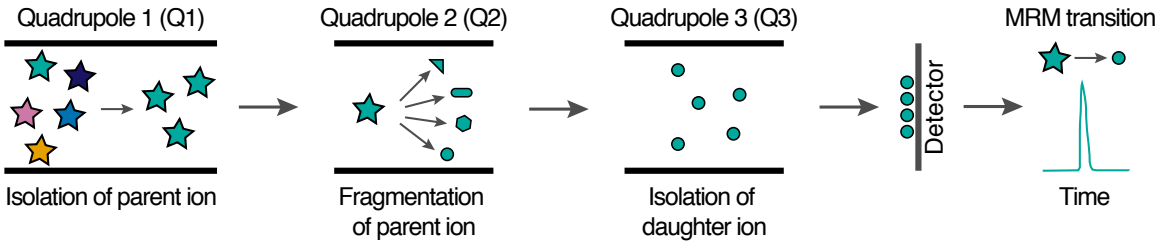

Figure 3.26 Schematic illustration of MRM quantification.

Evaluation of matrix effects and extraction recovery of the dyes and IS was performed in liver matrix and tumour matrix ($n \geq 3$). Therefore, standard solutions were added either to the tissue, the tissue matrix (tissue homogenate) or MeCN : H_2O (8 : 2) and processed the same way. The matrix effect led to a signal increase of 2.9% for **JW35Mono** and of 4.4% for **JW35**, while for **JW41** a signal suppression of 21.5% was observed.

As work was carried out with frozen tissue samples, it was assumed that frozen tissue is unable to take up any of the dye and thus in the following studies the calibration standards and IS solutions were only added after homogenisation of the tissue.

The lower limit of quantification was determined using samples with known concentrations of analytes and defined as the lowest concentration of analyte that was quantifiable in a matrix sample with a precision within 20% and an accuracy of 80–120%. This was 473 pM for **JW35** and 945 pM for **JW41**. The higher detection limit for **JW41**, which is double the value of **JW35**, is likely due to the hydrolysis of **JW41** leading to two separately detected compounds and thus reducing the effective concentration for each. Calibration lines in both tumour and liver matrix were constructed for each dye with an accuracy of 80–120% (Figure 3.27A,B). The calibration lines were cross-validated by six QC samples at three different concentrations.

As discussed in Chapter 2 (section 2.2.5), **JW41** undergoes hydrolysis in aqueous solutions, which increases greatly on-column and under acidic conditions. Unfortunately, it was necessary to extract the dyes from the tissues with 20% water content and to use acidic conditions to obtain fast elution of the dyes. As a consequence of this, the MRM peak area of **JW41** in the standard samples run at later time points of the assay, the concentrations were lower than expected due to hydrolysis of **JW41** to **JW41$_{hydr}$**. However, the loss appeared to be compensated by the increase in the MRM peak area of the **JW41$_{hydr}$**. Based on these data and given that the hydrolysis of **JW41** could not be avoided under the experimental conditions, the peak area of the MRM transitions of **JW41** and **JW41$_{hydr}$** were added together to represent the original concentration of **JW41**. This assumption was reinforced by two linearity curves, each run at four concentrations ten times over a time frame of 10 hours (Figure 3.27C). The robustness of the method was validated by measuring five of the tumour samples at different concentrations and three of them again on a different day. The intra- and inter-batch variation of the relative concentrations was below 3%.

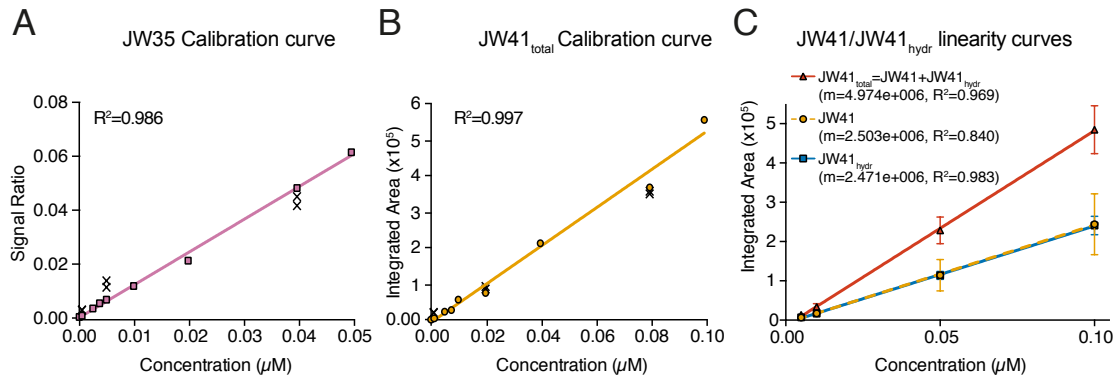

Figure 3.27 Calibration lines for *ex vivo* quantification of A) JW35 and B) JW41 by LC-MS/MS. For each study a new calibration curve was acquired before and after running the samples. One representative calibration line for JW35 and JW41 is shown. The coloured symbols representing values obtained from the calibration samples, the crosses are indicating the values of the QC samples validating the calibration curve. C) Linearity curves for JW41, JW41$_{hydr}$ and JW41$_{total}$ being the sum of JW41 and JW41$_{hydr}$.

Detection and Quantification of JW41 and JW35 in Tissue Samples

The optimised and validated method was used to quantify the relative concentrations of **JW35** and **JW41** in tumour and liver samples to investigate differences in the conversion rate of **JW41** into **JW35** in tumour vs. liver, MDA-MB-231 tumours vs. MCF7 tumours and Doxil treated tumours vs. non-treated tumours.

Examining the tumours from the biodistribution and tumour accumulation *in vivo* study (cf. section 3.2.3) via LC-MS/MS in multiple reaction monitoring mode (MRM-MS) indicated that the total concentration of dye (**JW41** + **JW41$_{\mathbf{hydro}}$** + **JW35**) being present in the tumours was between 726 pmol/g and 1261 pmol/g for the mice treated with **JW41** (150 μL, 150 μM) and between 103 pmol/g and 247 pmol/g for the mice treated with the 2-1 mixture of **JW41**-**JW35** (150 μL, 100 μM **JW41**, 50 μM **JW35**) (Figure 3.28A). Unfortunately, as the boronate groups of **JW41** are partially hydrolysed to give **JW41hydro** by the aqueous and acidic conditions required for the LC-MS/MS analysis, the resulting values of total **JW41$_{\mathbf{total}}$** concentration and thus also the total dye concentration cannot be interpreted as absolute. Hence, only the relative values were considered for interpretation. This led to the following observations: A significant difference between the conversion of **JW41** into **JW35** in the livers and tumours was detected. In the liver less than 8% of **JW41** reacted with H_2O_2, whereas in the tumours more than 36% was transformed (Figure 3.28B). This was expected as the H_2O_2 production in the liver should be relatively small in comparison to the tumour. The ratio of **JW35** to **JW41** was also calculated for the mice treated with the 2-1 **JW41**-**JW35** mixture. However, as shown before, **JW35** presents a different biodistribution profile than **JW41** and gets nearly completely cleared after 24 hours. Since the organs were only collected 24 hours after injection of the contrast agent, very little increase in the amount of **JW35** in the tumours was observed, as was the case for the mice treated only with **JW41**. This is confirmed by the data obtained via LC-MS/MS analysis since the conversion ratio mirrored the one from the mice where pure **JW41** was administered. To exclude mistakes made during the sample preparation, samples were measured at different concentrations and on different days. The concentration and batch-to-batch variation was less than 3%.

Next, the difference in **JW41**-transformation between Doxil treated and non-treated mice was investigated. For both tumour types, the mice treated with Doxil showed a higher conversion than the mice that did not receive Doxil treatment (Figure 3.28B). These results suggest that while both tumour types responded to the Doxil treatment in terms of oxidative stress, the MCF7 tumours generate slightly more oxidative stress than MDA-MB-231 tumours.

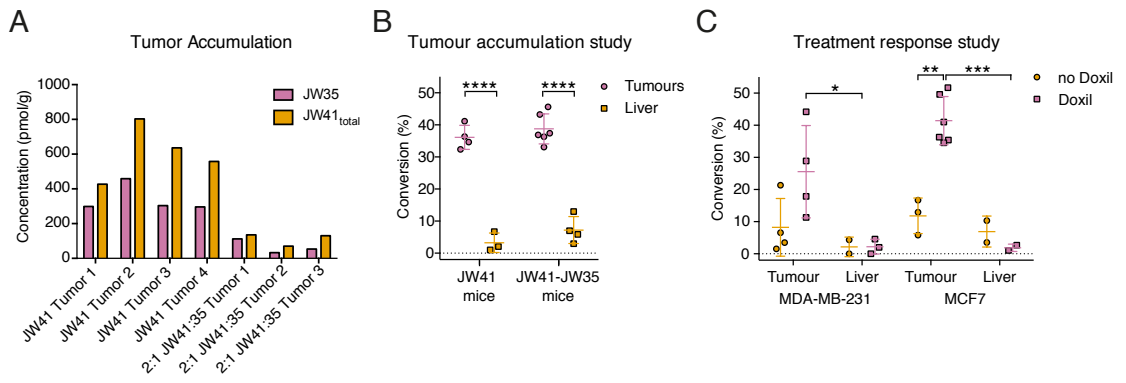

Figure 3.28 Results of JW35 and JW41 *ex vivo* LC-MS/MS analysis of tumour and liver samples. A) Calculated total concentration of $JW41_{total}$ and JW35 24h after injection of JW41 or the 2 : 1 mixture of JW4 : JW35. The results of 4 tumors where the mice received an injection of JW41 alone and 3 tumors where mice received an injection of 2 : 1 JW41 : JW35 solution are shown. B) Comparison of the relative amount of JW41 that got converted into JW35 in MDA-MB-231 tumours and livers of mice treated either pure JW41 or a 2 : 1 mixture of JW41 : JW35. C) Comparison of JW41-conversion in Doxil treated and non-treated MDA-MB-231 and MCF7 tumour bearing mice. Statistical significance was assessed by 2way ANOVA; $****p < 0.0001$; $***p = 0.0002$, $**p = 0.008$, $*p < 0.05$.

Detection and Quantification of GSH and GSSG in Tumour Tissue

The redox balance in a cell does not exclusively depend on the generation of ROS. Glutathione (GSH) is one of the most abundant sources of cellular reducing equivalents and is crucial for the redox balance. Consequently, the effect of Doxil on GSH levels was examined following an established procedure to detect GSH and its oxidation product Glutathione disulfide (GSSG) in tumour homogenates by LC-MS/MS [173, 176]. As IS, commercially available ^{13}C and ^{15}N labelled GSH and GSSG (GSH-glycine-$^{13}C_2$,^{15}N; GSSG-glycine-$^{13}C_2$,^{15}N) were used. The data indicated that there was no significant changes in the total glutathione concentration nor in the GSH/GSSG ratio following Doxil treatment. Moreover, no difference was observed between the two tumour types (Figure 3.29). Hence, Doxil does not appear to influence the GSH to GSSG ratio or the total glutathione concentration in the examined tumours. Prior work demonstrated that Doxil leads to an increase in GSH in A2780 tumours (Dr. Tim Witney, not yet published results). However, discrepancies between this work and previous findings can be explained by tumour diversity and the fact that the spatial and temporal distribution of different redox species is highly heterogeneous in tumours and regulated by different, independent systems.

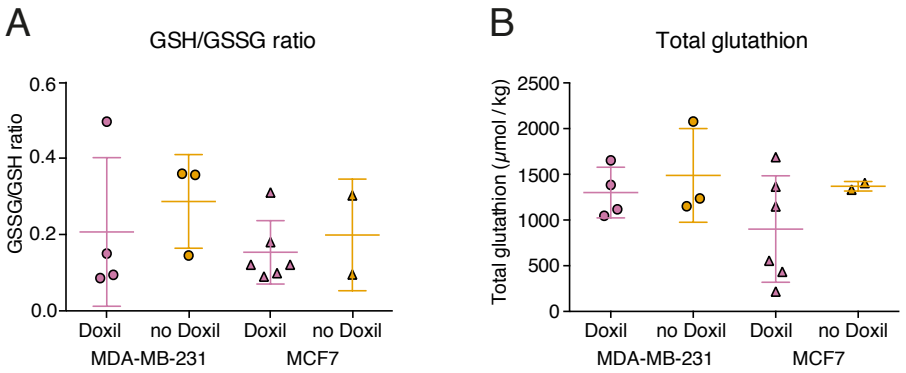

Figure 3.29 Results of GSH/GSSG LC-MS/MS analysis in tumour samples of treatment response study. The A) GSH/GSSG ration as well as B) the total glutathion concentration is shown for the different cohorts.

3.3 Summary and Conclusions

New methods for the specific detection and quantification of ROS *in vivo* will be critical to advance the clinical understanding of severe diseases. Accordingly, the goal of this chapter was to evaluate the new activatable, targeted contrast agent towards its application in H_2O_2 imaging in cancer.

The ability of the new probe to detect rapidly and specifically physiological amounts of H_2O_2 via PA, absorption and fluorescence spectroscopy was demonstrated. In addition to this, it was shown that spectral unmixing allows the relative quantification of the concentration of the original probe, **JW41**, and the H_2O_2-transformed probe, **JW35** in tissue mimicking phantoms.

In vitro studies indicated the new contrast agent has no significant toxicity and demonstrated the specific uptake of the dye into the cytosol of cells. Furthermore, the cellular uptake could be effectively increased by treating the cells with TPA suggesting effective GLUT targeting.

In vivo studies yielded promising results with the absence of toxicity over four weeks, the accumulation of the contrast agent in tumour tissue accompanied with specific changes in the PA tumour spectra and the H_2O_2-dependent conversion of the contrast agent into its uncapped form. Additionally, spectral unmixing approaches were introduced to successfully generate images indicating the presence of the new activatable contrast agent and its conversion product.

Finally, *ex vivo* analyses revealed a heterogeneous cytosolic localisation of the contrast agent in tumour tissue with a decreased accumulation in necrotic tumour areas. Additionally,

LC-MS/MS analysis confirmed the transformation of **JW41** into **JW35** in tumour tissue and indicated the applicability of the activatable contrast agent for treatment response monitoring.

However, further work is required to improve the unmixing approach described in this manuscript. Currently signal misclassification exists, this is caused by signal cross over, shadowing, motion and fluence effects. Signal misclassification can occur when using a linear regression approach due to the similarity in the *in vivo* spectra of **JW41**, **JW35** and intrinsic chromophores. The latter issue could be partially evaluated by studying the influence of the blood oxygenation state on the dye's signal in phantoms and by evaluating more precisely the detection limit and resolution depending on the concentrations of the dyes. Furthermore, spectral colouring, the process whereby shorter wavelengths are preferentially attenuated in tissue, may distort the spectra measured at depth *in vivo*. Therefore, applying a fluence correction to the data and using more complex unmixing models coping with further nonlinear interactions may improve the quantification capabilities but was not possible in the software used for analysis during this study. Spectral unmixing could also be improved with structural modifications generating narrower peaks and greater spectral differences between the capped and uncapped dye. Modifying the dye structure would also allow the use of different disease-specific targeting moieties and extend the use of this new activatable contrast agent to the study of oxidative stress in a broad range of pathological conditions, with a high temporal and spatial resolution in living subjects.

3.4 Material and Methods

3.4.1 ROS Sensing

Absorption and fluorescence spectra were recorded at 25 °C using a fluorescence spectrophotometer (Cary Eclipse, Varian) and an UV-VIS spectrophotometer (Cary 300, Varian). Samples were placed into quartz cuvettes (Suprasil) with a 10 mm pathlength. Monitoring the reaction with H_2O_2 by PA spectroscopy was recorded in micro plastic cuvettes (Y200.1, ROTH) in a PA spectrometer using a laser module (SplitLight 600 OPO) coupled into a silica fiber (CeramOptec), an immersion transducer (A392S, Olympus-NDT) and the data acquisition unit of MSOT inVision256. The set-up was assembled and optimised together with Stefan Morscher from iThera Medical and a schematic illustration can be found in the Chapter 2, Section 2.4.3).

To assess the optical responses of **JW41** to H_2O_2, the dye (10 μM) was incubated with 100 μM H_2O_2 and the absorption, fluorescence and PA spectra were recorded before and

up to 90 minutes after addition of H_2O_2 at either 5 minute intervals over the whole period or at 1 minute intervals for the first 10 minutes followed by 5 minute intervals. **JW41** in water without the H_2O_2 supplement served as controls. To prove that the product of the reaction, **JW35**, does not react further, the same measurements were performed with **JW35**. All experiments were repeated with n$\geq$3 separately prepared dye samples and errors are represented as standard deviations.

LCMS analysis of the reaction of the dyes with H_2O_2 was performed using an Agilent LC-MSD ionTrap model XCT LCMS equipment in electrospray mode. Agilent XDB C18 Column (1.8 μm, 4.6 mm x 50 mm) was used as the UPLC column. The conditions of the UPLC method are as follows: Solvent A: Water +0.1% formic acid; Solvent B: Acetonitrile +0.1% formic acid; Gradients: 0 - 1.3 minutes 5% B; 1.3 - 5 minutes 5 - 60% B, 5 - 6 minutes 60 - 100% B, 6 - 8 minutes 100% B with re-equilibration time of 3 minutes. Flow rate: 0.9 ml/min; Column and injector temperature set to 25 °C; Injection volume of 20 L. The signal was monitored at 254 nm and 750 nm with 360 nm as reference wavelength.

In order to verify that the optical changes triggered by 100 μM H_2O_2 are due to the conversion of **JW41** into **JW35**, the 10 μM **JW41** reaction solution from the UV-VIS and fluorescence measurements were subjected to LCMS analysis at multiple time points without further modifications.

To prove the oxidative cleavage of the boronic esters is selective to H_2O_2, aqueous 10 μM **JW41** solution was incubated at 37 °C for 1 hour with different ROS. 100 μM H_2O_2, 100 μM *t*BuOOH, 100 μM OCl^-, 100 μM $ONOO^-$ and 100 μM KO_2 were prepared by directly diluting commercially available H_2O_2 (9.7 M), ^{t}BuOOH (70 wt.% in water), NaOCl (10-14% W/W), KO_2 (solid). 200 μM $^1O_2$ was produced from H_2O_2 catalysed by Na_2MoO_4 and 100 μM $\cdot$OH and *t*BuO$\cdot$ were generated from Fenton reaction between H_2O_2 or *t*BuOOH and $Fe(ClO_4)_2$ [177, 178]. The presence of ROS in the solution used for the assay was validated with DCF-DA, CellRoxGreen and/or Quantofix peroxides test sticks. For CellRox green based cross validation, unspecific double stranded DNA (length of 30 basepairs) was added.

Serum Stability

Serum stability of the dyes was assessed with LCMS using the same method as described in the previous section 3.4.1.

20 μM dye solutions in FBS were incubated for 0, 30, 60 and 120 min at 37 °C. After the incubation period, 35 μL sample was taken, 50 μL cold MeCN was added and the sample was centrifuged for 15 min at 4 °C at 5000 rpm. The supernatant was collected and injected

directly into the LCMS (20 μL injection volume). Measurements were repeated three times with separately prepared dye solution.

3.4.2 Protein-Binding Assay

To test the binding of **JW41** and **JW35** to proteins, both dyes as well as ICG and IR800CW were added to 3 wt.% bovine serum albumin solution in PBS to reach a final concentration of 1 μM and incubated for 15 min, 30 min or 60 min at 37 °C. Next, native-PAGE sample buffer (Invitrogen) was added to the sample in a 1:3 ratio and the samples were loaded into a nativePAGE Bis-Tris gel (Invitrogen). The gel was run in nativePAGE running buffer (Invitrogen) at 4 °C for 70 min at 150 V followed by 20 min at 200 V. The gel was imaged on an Odyssey CLx system (LI-COR) using the 700 nm and 800 nm channel. Afterwards, the gel was stained with InstantBlue for 1 h at room temperature and imaged again an an Odyssey CLx system (LI-COR) using the 700 nm channel.

3.4.3 *In vitro* Cell Experiments

General Considerations

The two human adenocarcinoma cell lines MDA-MB-231 (Oestrogen Receptor neg, OR neg) and MCF-7 (Oestrogen Receptor pos, OR pos) were obtained from the Cancer Research UK (CRUK) Cambridge Institute Biorepository from the University of Cambridge. The experiments were performed when cells were between passage 22-35 for MCF-7 and between passage 30 to 43 for MDA-MB-231. Authentication using Genemapper ID v3.2.1 (Genetica) by STR Genotyping (11/2017) showed exact match with the reference sequence in both cases. Cells were maintained in Dulbeccos Modified Eagle Medium (21885-025, ThermoFisher Scientific, UK) with 10% heat inactivated fetal calf serum (1050064, ThermoFisher Scientific, UK) at 37 °C in 5% CO_2. The cells were routinely subcultured when reaching 85% confluence (1:10 for MCF-7 and 1:20 for MDA-MB-231).

Quantification of GLUT Expression by rtPCR

To confirm the different GLUT expression levels of MDA-MB-231 and MCF7 cell lines quantitative PCR was performed. Cells were grown in 6-well plates to reach 90% confluency. RNA was isolated using solutions, materials and protocol supplied by ThermoFisher within the PARIS kit. Reverse transcription of the isolated RNA was performed using the high-capacity cDNA reverse transcription kit (appliedBiosystems) and quantitative real-time

polymerase chain reaction (PCR) was carried out with the use of TaqMan Gene Expression Master Mix and SLC2A1-specific PCR primers (Hs00892681 m1, ThermoFisher). TATA sequence binding protein (TBP) served as reference gene. The thermal cycling conditions were as follows: 2 min at 50 °C, 10 min at 95 °C and 40 cycles of 15 sec at 95 °C followed by 1 min at 60 °C.

Cell Toxicity Studies

Cellular toxicity of the dyes was examined by quantifying cell proliferation and viability via standard MTT (3-(4,5-dimethylthiazol-2-yl)-2,5-diphenyltetrazolium bromide) assay and IncuCyte proliferation assay. For the MTT assay, cells were seeded at 40 000 cells per well in a 96-well plate and grown to 80% confluency. The media was replaced by 100 μL fresh media containing either 5 μM **JW41**, 5 μM **JW35**, 5 μM ICG, 0.5% DMF or no supplements (control) and incubated for in total 8 hours. After 5 hours of incubation, MTT reagent was added to each well to reach a final concentration of 0.5 mg/mL and the cell were incubated for the remaining hours. After the incubation time, 100 μL lysis buffer (20% SDS in 50% dimethylformamide) was added per well and incubated at room temperature overnight. The absorbance was measured at 590 nm. The values are normalised against the control group. Error bars are expressed as standard deviation (n = 4).

Cellular proliferation measurements were conducted with an Incucyte Zoom System (Essen Bioscience, UK). Cells were seeded in complete medium in 48-well plates (Corning, UK) at a density of 50 000 cells per well and immediately placed in the Incucyte for imaging. Twenty-four hours later, the cells were exposed to the following compounds for 6 hours: **JW35** (5 μM), **JW41** (5 μM), ICG (5 μM) or vehicle (DMF 1%). A reference group (not exposed to any compounds) as well as a positive control group exposed to 1 mM H_2O_2 (H1009, Sigma-Aldrich, UK) were also included. Four replicates were performed for each condition. At the end of the 6 hour incubation, a media change was performed and well confluence was tracked for a further 120 hours. Images were analysed with the Incucyte Zoom software version 2016.

General Cell Uptake Studies

Cellular uptake kinetics of **JW41** as well as **JW35** were examined in MDA-MB-231 and MCF7 cells. Cells were seeded at 50000 cells per well in phenol red free media in 24-well plates. After reaching 90% confluency, the media was replaced with fresh phenol red free media containing 5 μM **JW41** or 5 μM **JW35** and incubated for 15 min, 30 min, 45 min,

60 min, 90 min or 240 min. The assay was stopped by washing three times with PBS (2 min each) followed by imaging with Odyssey CLx (LI-COR) using the 800 nm channel. Error bars are represented as standard deviations ($n \geq 3$); the normalised intensity was calculated as percentage of the maximum obtained fluorescence intensity within a group.

Cellular localisation was assessed by wide-field microscopy. MDA-MB-231 and MCF7 cells were seeded at 40 000 cells per well in a 96-well plate and grown to 80% confluency. For live cell imaging, the medium was aspirate and replaced with phenol red free media containing 2.5 μM **JW41/35**. 45 min before completion of the incubation time, MitoTracker orange was added (final concentration of 300 nM), 30 min into the incubation time LysoTracker green was added (final concentration of 60 nM) and 15 min before the end of the incubation time NucBlue Live ReadyProbes Reagent was added. Next, the cells were washed three times with PBS and kept under phenol red free media for imaging. Fluorescence imaging was performed on a wide-field fluorescent microscope (Zeiss Axio Observer Z1) in a CO_2 and temperature-controlled incubation chamber (set to 5% CO_2, 37 °C) under a 63x oil-immersion objective lens. Fixed Cells were used for co-staining with Wheat Germ Agglutinin-Alexa Fluor 488 (WGA-AF488). As before, cells were incubated in phenol red free media containing 2.5 μM **JW41/35** for 60 min. 45 min before completion of the incubation time, MitoTracker orange was added to reach a final concentration of 300 nM. After incubation, cells were washed three time with PBS and fixed with 4% paraformaldehyde solution in PBS at 37 °C for 15 min. Following fixation, cells were stained with WGA-AF488 (5 μg/mL) and Hoechst (5 μg/mL) for 10 minutes at room temperature, washed three times with PBS and imaged on a wide-field fluorescent microscope (Zeiss Axio Observer Z1) under a 63x oil-immersion objective lens. The fluorescence of **JW41/35** was collected upon excitation, which was centred at 770 nm, 580 nm centred excitation was used for MitoTracker orange, 490 nm centred excitation for LysoTracker green and 365 nm centred excitation for NucBlue/Hoechst. Zen 2.3 (blue edition) was used for imaging analysis.

GLUT Dependent Cellular Uptake Studies

Binding and specificity of **JW41** were tested by fluorescence based inhibition, competition and pharmacological induction/suppression assays using MCF-7 and MDA-MB-231 cells. ICG, IR800CW were used as a non-targeted control dye, IR800CW-2DG and 2-NBDB were used as positive controls (results for 2-NBDB are not shown since the assay needs further optimisation). Cells were grown in high/low glucose media in a 96-well plate to 80-90 % confluency.

2-DG Inhibition Assay

For 2-DG inhibition assay, the cells were starved for 2 h in no-glucose DMEM supplemented with 10% FBS and 1 x GlutaMAX supplement (100 x concentrate, ThermoFisher). After the starvation period, the media was replaced with no-glucose DMEM containing 2.5 μM **JW41/JW35**/ICG/IR800CW/IR800CW-2DG or 100 μM 2-NBDG and increased concentrations of unlabeled 2-Deoxyglucose (0, 1, 6.25, 12.5, 25, 50, 100 mM) and incubated for an additional hour at 37 °C. For 2-NBDG the cells were incubated for only additional 20 min. The inhibition assay was stopped by washing with PBS and fixation with 4% formaldehyde solution for 20 min at room temperature. The fixed cells were then washed three times with 1x PBS + 0.02% Triton to permeabilise the cells and remove unbound dye. Following this step, the plates were blocked in Odyssey Blocking Buffer (1x in PBS; LI-COR Bioscience) for 60 min and consecutively stained for 5 min with DRAQ5 (5 μM in PBS; 5 min at room temperature) to normalise for the cell number per well. After three washing steps with 1 x PBS + 0.02% Tween-20 and one washing step with 1x PBS, the 96-well plates containing the NIR dyes **JW41/JW35**/ICG/IR800CW/IR800CW-2DG were imaged with Odyssey® CLx (LI-COR Bioscience). The dye fluorescence signal detected from the 800 nm channel was normalised in a ratiometric way using the 700 nm signal generated by DRAQ5. For the wells containing 2-NBDG the read out was performed on a Typhoon imaging system using the Cy2 channel (488 nm excitation) for 2-NBDG and the short-red channel (685 nm excitation) for DRAQ5.

Pharmacological STF-31 Inhibition Assay

GLUT1 specific inhibition was carried out by pre-incubating the cells in low glucose DMEM with STF-31. For MDA-MB-231 cells a STF-31 concentration of 10 μM was used and the cells were pre-incubated for 8 h, 16 h, 24 h and 32 h. For MCF-7 cells a STF-31 concentration of 5 μM was used and the the pre-incubation times were set to 2 h, 4 h, 6 h and 8 h. After the pre-incubation period, the media was replaced with low glucose DMEM containing the above stated concentration of STF-31 and 5 μM ICG or 2.5 μM **JW41/JW35**/IR800CW/IR800CW-2DG and incubated for an additional hour.

Glucose Competition Assay

To evaluate the competitive effect of glucose in respect of the cellular uptake of **JW41** and **JW35**, the cells were pre-incubated with no-glucose DMEM (supplemented with 10% FBS and 1 x GlutaMAX supplement (100 x concentrate, ThermoFisher)) and increasing concentra-

tions of D-glucose (0, 5, 10, 25, 50, 100 mM) for 3 h. After the incubation period, the media was replaced with no-glucose DMEM containing 2.5 μM **JW41/JW35/**ICG/IR800CW/ IR800CW-2DG or 100 μM 2-NBDG and the same concentrations of D-glucose (0, 5, 10, 25, 50, 100 mM) as used for the starvation period. After an additional hour (20 min for 2-NBDG) of incubation at 37 °C, the plates were washed with PBS and fixed, permeabilised, blocked, stained, imaged and analysed as described above.

Pharmacological TPA Activation Assay

GLUT dependent uptake was evaluated by immunofluorescent assay. Cells were grown to 60-90% confluency in 96-well plates and incubated with 13 μM TPA in media for 1 h at 37 °C. After washing twice for 2 min with PBS, glucose free media supplemented with IR800CW, IR800CW-2DG or **JW41** (2.5 μM) was added and incubated for an additional hour at 37 °C. After 1 h of incubation DRAQ5 was added to each well to reach a final concentration of 5 μM and incubated for 10 min. The assay was stopped by washing three times with PBS (2 min each) followed by imaging with a microplate reader (ClarioStar, BMG Labtech), exciting at 763-15 nm and 646-15 nm with emission collected at 810-14 nm (LP785 dichroic filter) and at 697-20 nm (670.2 dichroic filter) respectively. Quantification was normalised by ratiometric analysis of the fluorescent signals obtained from both channels. Error bars are represented as standard deviations (n = 4).

3.4.4 *In vivo* Studies

General Considerations

All mice procedures conducted meet the standards required by the UKCCCR guidelines and were performed under the authority of project and personal licenses issued by the Home Office, U.K., reviewed by the Animal Welfare and Ethical Review Board at the CRUK Cambridge Institute [179]. 300000 MDA-MB-231 and 500000 MCF7 cells in a final volume of 100 μL of 1:1 DMEM (GIBCO) and matrigel (BD) were inoculated orthotopically in the mammary fat pad of both flanks of 10 seven to eight-week-old immunodeficient female nude (BALB/c nu/nu) mice (Charles River). For MCF-7, endogenous oestrogen levels were supplemented by surgical implantation of oestrogen pellet (0.18 mg/pellet, 90 days release; Innovative Research of America) in the scruff of the neck. All mice were kept with 5R58 diet (PicoLab) in Tecniplast Green Line cages, individually ventilated in 12/12 h ON/OFF light cycles. Tumours were measured externally with Vernier callipers and the tumour volumes were calculated with a x b x b with a being the longest axis of the tumour and b the shortest. It

was ensured that the overall tumour size was less than 1.5 cm diameter and the overall tumour volume was less than 10% of the body weight of the mouse. The contrast agent was injected and the mouse imaged when tumour size was between 0.5 and 1 cm diameter. Animals were killed by exsanguination and cervical dislocation as confirmation of death. Tumours, liver, kidney, spleen, heart and brain were collected for *ex vivo* fluorescence imaging. Afterwards, tumours and livers were divided into 3 to 4 parts for histopathology, microscopy and LC-MS/MS analysis. Kidney, spleen, heart and brain were collected for paraffin embedding. Tumours which were too small were not analysed *ex vivo*.

All PA *in vivo* imaging was performed with the multispectral optoacoustic tomography (MSOT) system described above (inVision 256-TF, iThera Medical GmbH). The mice were prepared for imaging following our standard operating procedure [180]. Briefly, $<3\%$ isoflurane was used to anaesthetise the mice before they were placed in a custom animal holder (iThera Medical), wrapped in a thin polyethylene membrane. A thin layer of ultrasound gel (Aquasonic Clear, Parker Labs) was used to couple the skin to the membrane. The holder was then placed within the MSOT system and immersed in heavy water maintained at 36 °C. The respiratory rate of the mice was maintained in the range of 70-80 b.p.m. with 1.5-2% isoflurane concentration for the entire scan time.

In vivo fluorescence imaging was carried out on a fluorescence *in vivo* imaging system (IVIS 200, Xenogen). Scans were recorded with filter set 4 using 705-780 nm as excitation passband, 810-885 nm as emission passband and 665-696 nm as background passband. Auto-fluorescence was corrected by subtracting the background filter image from the primary filter image. ROI were drawn on the black and white image without displaying the fluorescence signal. The average radiant efficiency obtained in the control region C was subtracted from the average radiant efficiency within the ROI.

Biodistribution and Tumour Accumulation Study

5 minutes after the animal was placed into the PA imaging system, the scan was initialised and the baseline was monitored for further 14 minutes, to stabilise the signal. 14 min into the scan 150 μL (for a 20 g mouse) of the contrast agent was injected intravenously in the tail vein. The concentration used were 150 μM **JW41**, 50 μM **JW35** or 100 μM **JW41** + 50 μM **JW35** for the 2-1 mixture. Images were acquired at one slice centred on the liver, one slice centred on the kidneys, spleen and liver, and several slices covering the whole length of both tumours in 1-mm steps. Scans were recorded at 21 wavelengths between 660 nm and 900 nm with 10 averages (continuous averaging) for up to 50 min in 5 min intervals. 24 h after injection of the contrast agent the mouse was imaged once again before culling.

Fluorescence *in vivo* imaging was performed before the injection of the probe, after the PA image acquisition (50-60 min post injection of the contrast agent) as well as 24 h post injection.

Treatment Response Study

5 minutes after the animal was placed into the PA imaging system, the scan was initialised and the baseline was monitored for 4.5 minutes. Then, 150 μL (for a 20 g mouse) of 75 μM **JW41** was injected intravenously in the tail vein. Images were acquired at one slice centred on the liver, one slice centred on the kidneys, spleen and liver, and several slices covering the whole length of both tumours in 1 mm steps. Scans were recorded at 22 wavelengths between 680 nm and 900 nm with 10 averages (continuous averaging) for up to 65 min in 5 to 15 min intervals. Further PA images were acquired 24 h, 48 h and 72 h after the first injection of the contrast agent. 6 days after the first injection of **JW41**, the procedure of the first day was repeated and 150 μL (for a 20 g mouse) of 75 μM **JW41** was injected again and monitored for up to 60 min. 24 h after the second injection, the mouse was imaged once again before culling. Fluorescence imaging was acquired before and after the injection of the contrast agent as well as before the PA imaging sessions on day 1, 2, 3 and 7. Doxil (10 mg/kg eq. active doxorubicin) was injected IP on day 0 after the imaging session, day 2 and 5.

Image Analysis of PA *in vivo* Data

The acquired images were reconstructed off-line with linear reconstruction and analysed with linear regression multispectral processing, both available within the ViewMSOT software package (version 3.8; iTheraMedical). Linear regression was performed with published spectra for oxy- and deoxyhemoglobin (http://omlc.org/spectra/) as well as **JW41** and **JW35** spectra obtain from phantom studies described above. ROI were drawn around the liver, left kidney, spleen and tumours as indicated in the Figures on the appropriate tomographic sections. Reference values from ROIs drawn as indicated were taken in the same anatomical plane. The PA spectra in the imaged organs were generated by averaging the mean pixel signal intensities of each ROI from every section. For the PA tumour spectra, the average of all tumour spectra of each tomographic section was formed. To correct for the intrinsic background signal, the spectra acquired at $t = 0$ was subtracted from the subsequent images. For the biodistribution and tumour accumulation study, to monitor the enrichment kinetics of the probe in the different organs, the raw mean pixel intensity values at 760 nm and 900 nm were used and the ratio was formed. To generate the PA signal kinetic plot based on spectral

de-mixing data obtained by linear regression, the values obtained before injection of the contrast agent in the ROI were averaged and used as baseline to allow comparison with the 24 h time point signal. In case of the treatments response study, the 760 nm signal was plotted against the time to generate the enrichment kinetics curve.

3.4.5 Histophathology and Widefield Microscopy of Tissues from *in vivo* Studies

For histopathological analysis organs were fixed in neutral buffered 10% formalin (24 h) for haematoxylin and eosin (H&E) and cleaved caspase 3 staining. For comparable histopathology and wide-field microscopy examination, tumours were mounted on a cork base using OCT solution (VWR Chemicals) and snap frozen in an isopentane bath cooled on dry ice . Formalin fixed, paraffin embedded tumours and livers were sectioned with 3 μm and imaged at ×20 magnification using an Aperio ScanScope (Leica Biosystem) scanner. Frozen blocks were sectioned with 6 μm thickness. Two consecutive slices were generated, of which one was stained with haematoxylin and eosin (H&E); the other section was fixed with 4% PFA for 5 min at room temperature, washed carefully twice with PBS, mounted in mounting media with DAPI (ProLong Gold Antifade Mountant with DAPI, LifeTechnologies) and scanned using a wide-field fluorescent microscope (Zeiss Axio Observer Z1) with excitation wavelengths centred on 365 nm (for DAPI) and on 740 nm for **JW41/JW35** under a 63x oil-immersion objective lens.

3.4.6 LC-MS/MS Analysis of Tumour and Liver Samples

Sample Preparation for LC-MS/MS Analysis of JW41 and JW35

Synthesis of JW56

General experimental details are the same as stated in Chapter 2, Materials and Methods 2.4.1.

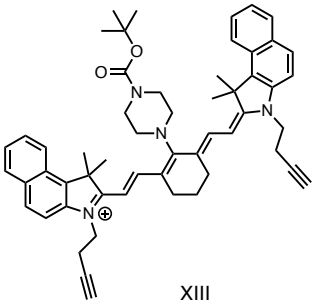

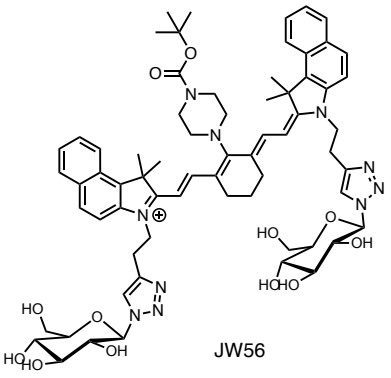

VII (32 mg, 0.045 mmol) and DIPEA (15 *mu*L, 11.1 mg, 0.086 mmol) were dissolved in dry THF (1.5 mL) and cooled down to 0 °C. Di-*tert*-butyl dicarbonate (12.8 mg, 0.056 mmol) dissolved in 1 mL THF was added and the reaction mixture was stirred at room temperature for 10 h. After concentrating under reduced pressure, the reaction was purified by flash chromatography (silica, gradient: 0-20% MeOH in DCM), yielding the intermediate **XIII** as blue solid (12 mg, 0.015 mmol, 33%).

XIII (12 mg, 0.015 mmol), 1-Azido-1-deoxy-β-D-glucopyranoside (7 mg, 0.033 mmol) and $CuSO_4$ (2.3 mg, 0.015 mmol) were dissolved in H_2O : ^{t}BuOH 1:1 (1 mL). Sodium ascorbate (5 mg, 0.025 mmol) was added and the reaction mixture was sonicated for 30 seconds followed by stirring at room temperature for 5 h. The reaction mixture was diluted with MeCN/H2O (1/1) and purified with HPLC (Kinetex, 5 μm, C18, 100Å, AXIA packed HPLC column, 250 x 21.2 mm) using H_O + 0.1% formic acid and MeCN + 0.1 formic acid as solvents. **JW56** was obtained as blue solid (1.1 mg, 0.001 mmol, 6%).

HRMS(**XIII**): m/z calculated for $[M^+] = 809.48$, found $m/z = 809.4781$.
HRMS(**JW56**): m/z calculated for $[M+H^+] = 1220.62$, found $m/z = 1220.6240$.
^{1}H/^{13}C-NMR: (400/126 MHz, CD_3CN) The peak intensities of the obtained spectrum were too weak why accurate data analysis could not be performed.

Preparation of Standard, QC and IS Solutions

All work was done on ice and in the dark. A 2 μM IS spiking solution was prepared in MeCN : H_2O (8 : 2) from a 1 mM stock solution in DMSO. To prepare the standard and QC solutions, a 1 mM stock solution of **JW41** (in DMF) and a 1 mM stock solution of **JW35** (in DMF) were diluted into MeCN : H_2O (8 : 2) to give a final concentration of 10 μM for **JW41** and 5 μM for **JW35**. This dilution was then used to generate the different standard spiking solutions (SSS) and QC spiking solutions (QSS) (cf. Table 3.1). 7 μL of the respective

spiking solution was than added together with 7 μL of the IS solution (2 μM) to 60 μL of either MeCN : H_2O (8 : 2) or liver / MDA-MB-231 or MCF7 tumour homogenate from mice, which did not receive any treatment. The spiking solutions were only added after the homogenisation step due to the assumption that frozen tissue does not take up any of the dye. The samples were vortexed, centrifuged (2 min, 4 °C, 13000 g) and 60μL of the supernatant was transferred into a 96 well plate used for injecting onto the LC-MS/MS system for analysis.

Table 3.1 Concentrations of standard and QC samples for LC-MS/MS analysis.

Solution ID	JW41 concentration (μM)	JW35 concentration (μM)
SSS1	0.01	0.005
SSS2	0.05	0.025
SSS3	0.075	0.0375
SSS4	0.1	0.05
SSS5	0.2	0.1
SSS6	0.4	0.2
SSS7	0.8	0.4
SSS8	1	0.5
QSS1	0.05	0.025
QSS2	0.2	0.1
QSS3	0.8	0.4

Preparation of Tissue Samples from *in vivo* Studies

All work was done on ice and in the dark. Snap frozen tissue samples were cut, balanced and homogenised in MeCN : H_2O (8 : 2, LCMS grade, Fisher) to give a 100 mg/mL homogenate. 60 μL of tissue homogenate were transferred into an eppendorf tube and 7 μL of the IS spiking solution as well as 7 μL MeCN : H_2O (8 : 2) were added. The samples were vortexed, centrifuged (2 min, 4 °C, 13000 g) and 60μL of the supernatant was transferred into a 96 well plate used for injecting onto the LC-MS/MS system for analysis.

LC-MS/MS Method Details for JW41 and JW35 Analysis

The concentration of the activatable contrast agent **JW41** and its conversion product, **JW35**, in tissue samples were determined by LC-MS/MS against a reference standard solution of **JW35Mono**. **JW41** hydrolyses under aqueous, acidic conditions gradually to

JW41$_{\text{hydrol}}$. Thus, **JW35**, **JW41** and **JW41$_{\text{hydrol}}$** were identified from their retention time and from their specific mass transition in multiple reaction monitoring mode. **JW35** elutes at 3.08 min, with a transition from 560.30 to 208.106, **JW41** elutes at 3.47 min, with a transition from 1379.67 to 913.44, **JW41$_{\text{hydrol}}$** elutes at 3.23 min, with a transition from 1297.60 to 831.36 and the IS elutes at 3.12 min with a transition from 457.25 to 160.62. **JW41** and **JW41$_{\text{hydrol}}$** share 652.33 as a common fragmentation ion. The concentration of **JW35**, **JW41** and **JW41$_{\text{hydrol}}$** was determined as the peak area obtained from their mass transition in multiple reaction monitoring mode. The analysis was performed using the hybrid Quadrupole-TOF LC/MS/MS mass spectrometer (TripleTOF 6600, AB Sciex Instruments) with a Shimadzu LC-30AD system. The details of the method are as follows. Column: Acquity UPLC HSS T3 column from Waters (1.8 μm, 2.1 ID x 100 mm length); Chromatographic conditions: Solvent A: Water +0.1% Formic acid; Solvent B: Acetonitrile +0.1% Formic acid; Gradient: 0 - 1. minutes 0% B; 1.2 - 3 minutes 0 - 95% B, 3 - 5 minutes 95% B, 5 - 5.1 minutes 95 - 0% B; 5.1 - 9 minutes 0% B; Flow rate: 0.4 ml/min; Injector module temperature: 5 °C; Column temperature: 25 °C; Injection volume: 20 μL.

The assay of liver and tumour samples were always performed separately to be able to use the correct matrix. All assays were run the same way, starting with the injection of a test solution in MeCN : H_2O (8 : 2), followed by 2 washes, then injecting standard solution 1, 3, 5 and 7, 3 washes, QC1, QC2, QC3, 2 washes, tissue samples, 3 washed, QC1, QC2, QC3, 2 washes, standard solution 2, 4, 6 and 8, 2 washes, test solution in MeCN : H_2O (8 : 2).

In order to evaluate the potential for hydrolysis of **JW41**, a kinetic study was performed over 10 hours. The peak area of the 1379.67 to 913.44 transition of **JW41** lost through hydrolysis appeared to be compensated by the increase in the peak area of the 1297.60 to 831.36 transition of **JW41$_{\text{hydrol}}$**. Therefore based on this data and impracticality to avoid the hydrolysis under the acidic chromatographic conditions, the peak area of the MS transitions of **JW41** and **JW41$_{\text{hydrol}}$** were added together to assume the concentration of **JW41** if this had not suffered hydrolysis.

The calibration line was calculated by linear regression with GraphPad Prism6. The calibration line was accepted as long as a minimum of 10 out of the 14 samples showed accuracy in between 80 and 120% (8 calibration samples, of which minimum 5 needed to pass the accuracy criteria, and 6 QC samples, minimum of 4 needed to pass the accuracy criteria). Exception was the calibration line for **JW41** for the assay run with the liver samples of the treatment response study. In this case, the calibration curve was calculated only by the calibration samples run after the samples, due to fluctuations at the beginning of the assay. This assumption was reinforced by the R^2 value of 1.0 for the calibration curve calculated

this way and by the six QC samples, which showed good accuracy with this calibration and of which three were run before the liver samples and three afterwards.

Statistical analysis was performed using GraphPad Prism6. Each tumour was considered as an independent biological replicate. All data are shown as mean $\pm$ SD.

LC-MS/MS Measurement of Reduced and Oxidised Glutathione

GSH and GSSG were measured following the protocol previously described in the literature [173, 176]. Briefly, tissue samples were homogenised at 50 mg mL^{-1} in 25 : 75 water : methanol containing 1.25 mM 4 fluoro-7-sulfamoylbenzofurazan (ABD-F, thiol-derivatizing reagent),0.025 M sodium borate and 0.25 mM EDTA disodium salt to derivatise GSH to prevent oxidation of GSH and thus enable reliable analysis. Derivatised GSH and GSSG were separated on a Waters Acquity UPLC HSS T3 column (1.8 μm, 2.1 ID x 100 mm length) with the following chromatographic conditions: Solvent A: Water +0.1% Formic acid; Solvent B: Acetonitrile +0.1% Formic acid; Gradient: 0 - 1.2 minutes 0% B; 1.2 - 3 minutes 0 - 95% B, 3 - 4 minutes 95% B, 4 - 4.01 minutes 95 - 0% B; Flow rate: 0.3 ml/min; Column temperature: 25 °C; Injection volume: 2.5 μL. The corresponding ions were identified in MRM-MS using their specific mass transition (GS-ABD: 505.02 to 376.11, GSSG: 613.06 to 355.01) and retention time (GS-ABD: 3.59 min, GSSG: 3.30 min). The analysis was performed using the hybrid Quadrupole-TOF LC/MS/MS mass spectrometer (TripleTOF 6600, AB Sciex Instruments) with a Shimadzu LC-30AD system. GSH-glycine-$^{13}C_2{}^{15}N$ and GSSH-glycine-$^{13}C_2{}^{15}N$ were added as internal standard.

Chapter 4

Development of Novel Fluorescent Probes for the Study of Amyloids

The synthesis of the ME- and E-derivatives was performed by James Fyfe, Omaru Kabia and Dung Do. αSyn was purified by Ewa Klimont and Aβ by Dimitri Sideris. Catherine Xu supplied the stable oligomers. Juan Valera performed the analysis of the degree of modulation shown in Figure 4.20, 4.21 and 4.22. Bulk fluorescence and absorption measurements and analysis of the dyes were equally performed by Lisa-Maria Needham and I. I performed αSyn aggregations, all fluorescence and SPR based binding assays, αSyn and Aβ kinetic and inhibition assays, single aggregate fluorescence anisotropy measurements and the synthesis of the DNA-PAINT probe.

4.1 Introduction and Motivation

A growing number of diseases such as cancer, Alzheimer′s and Parkinson′s disease are associated with protein aggregation. Most of these pathologies share the common hallmark of converting soluble proteins into insoluble amyloid deposits, which often impairs essential cellular functions, initiating and/or promoting the development of diseases [181, 182]. Since the formation of protein aggregates occurs in the early stages of the disease preceding noticeable symptoms, the aggregates can serve as biomarker for early disease detection, prognosis and treatment response. However, at the present there is a lack of tools for measuring defined protein aggregates at low concentrations with high specificity, which would allow the detection of the different pathologic oligomers and fibrils in patient samples at an early disease stage [183]. Consequently, research into new imaging probes and early

detection methods for deleterious oligomeric species have attracted significant interest in biomedical research.

Thus the focus of this chapter was to investigate new imaging probes with improved binding and imaging properties to detect, characterise and study the formation of early pathological species and their role in the development of neurodegenerative disorders. Therefore, high resolution fluorescence microscopy was used as it operates on a spatial resolution highly suited to detect low populations of small, heterogeneous oligomeric species.

4.1.1 Protein Aggregation and Diseases

Proteins are involved in almost every biological process. A typical mammalian cell expresses around 30 000 different proteins, synthesised as linear chains composed of up to several thousand residues [184]. In order to function, these chains undergo post-translational modifications and fold into defined 3-dimensional structures. However, these folded structures possess only limited stability and somatic or hereditary mutations as well as changes in intracellular environment can tip the balance towards misfolded protein structures and subsequent protein aggregation. Various forms of protein aggregates exist and most of them get cleared by several control systems in our body. However, a subset of so called amyloid fibrils are resistant to common proteolytic "cleaning"-pathways and their accumulation is involved in the pathogenesis of many diseases [185].

The insoluble amyloid aggregates possess the main structural hallmark of an ordered arrangement of a double row of β-sheets, which run along the length of the fibril [186]. Their formation follows mainly a nucleation dependent growth model starting with a lag phase. In this phase, soluble, misfolded monomeric species are formed, which then assemble to soluble oligomeric species and protofibrils. In the following elongation phase, the oligomeric precursors act as template to accumulate other monomers or oligomers resulting in the rapid formation of insoluble fibrillar aggregates (Figure 4.1) [184, 187].

Recent studies suggest that small soluble oligomeric species, formed early on in the aggregation process, are the primary cytotoxic components [188, 189]. Unfortunately, these potentially toxic oligomers are highly heterogeneous in their size and structure and rare in abundance (in the order of pg/mL) making them challenging to identify and characterise [190, 191].

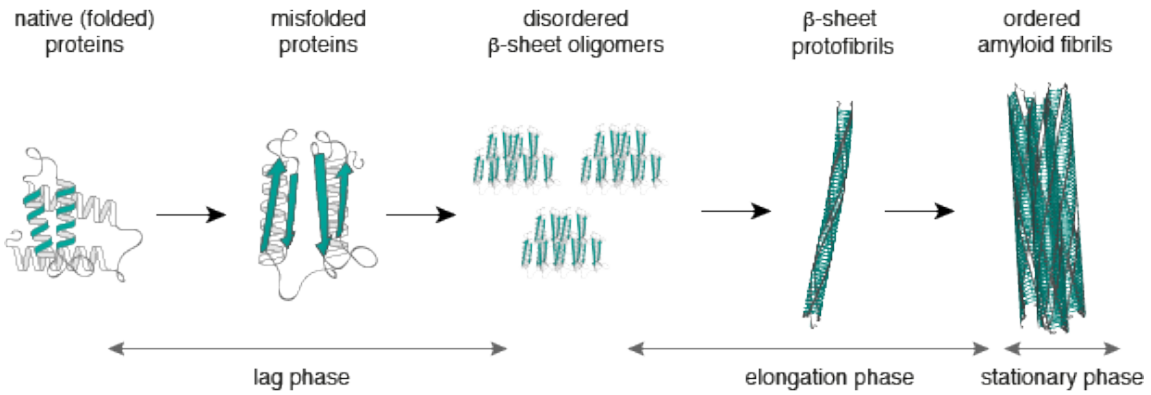

Figure 4.1 Schematic illustration of the nucleated pathway of amyloid fibril formation starting from monomeric proteins.

4.1.2 Imaging Protein Aggregates

To expand our understanding of the pathology of neurological disorders, it is important to visualise, characterise and quantify the toxic protein aggregates associated with these diseases. Fluorescence imaging is widely used for this purpose. To quantify the presence of fibrils or the kinetics of amyloid fibril formation, several fluorophores have been exploited. Among those are Congo Red, conjugated oligothiophenes, Nile red and thioflavin T (ThT) (Figure 4.2) [192–195].

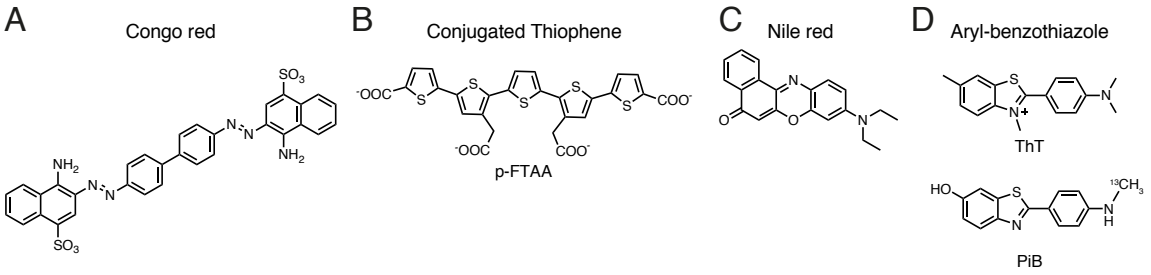

Figure 4.2 Chemical structures of five important and broadly used dyes for protein aggregate sensing - A) Congo Red, B) p-FTAA as example for a conjugated thiophene, C) Nile red and D) ThT and Pittsburgh compound B (PiB), the most used aryl-benzothiazoles.

Congo red was discovered as a stain for amyloid fibrils nearly 100 years ago and since then has been commonly used as diagnosis marker (Figure 4.2A). The detection mechanism of amyloid fibrils by Congo red relies on its birefringence when bound to fibrils. In the bound state, the molecule is arranged along the fibril in a way that all light absorbing atomic-bonds are in the same orientation causing the appearance of anomalous colours. In solution, Congo

red molecules are randomly orientated and thus the specific optical signature is not detectable [194, 192]. However, Congo red is thought to interfere with the aggregation of various different amyloid proteins and the exact binding mechanism between the dye and the fibrils is not well understood [196, 197]. Thus, its use for *in situ* detection of aggregates is limited.

In the last decade, conjugated thiophenes have attracted interest as dyes for amyloid aggregate detection (Figure 4.2B). Binding to amyloid evokes an environment specific conformation change in the thiophene backbone, which leads to a change in its spectral characteristics. This spectral change is specific towards the protein environment as well as the binding site and thus it allows the detection of aggregated species preceding amyloid fibril formation [193].

Nile red represents another fluorophore used for the detection of amyloid fibrils (Figure 4.2C). Its hydrophobic structure causes poor solubility in aqueous environment accompanied by fluorescence quenching. The binding to hydrophobic surfaces of proteins, revealed in misfolded proteins, leads to a turn on response in its fluorescence signal. As the generated fluorescence is dependent on the environment and binding site, Nile red is able to detect early stage aggregates and to compare fibrils from different proteins. However, due to the high affinity towards lipids and other biological structures, Nile red is restricted to *in vitro* studies and incompatible with tissue imaging [198, 195].

One of the main tests for studying amyloid fibril formation relies on the use of aryl-benzothiazoles. Aryl-benzothiazoles are sensitive to β-sheet rich structures and have been used across different imaging modalities. The uncharged, radiolabelled aryl-benzothiazole Pittsburgh compound B (PiB) is able to cross the blood-brain barrier and was the first probe used for positron emission tomography (PET) that allowed the detection of insoluble β-amyloid fibrils in Alzheimer's patients [39]. PiB possess a high binding affinity (nM) for fibrils but rarely detects soluble and oligomeric species, meaning a significant proportion of misfolded protein aggregates are not visualised *in vivo* [199]. Its charged analogue, ThT, has become the most common fluorescent dye used for the detection of amyloid fibrils and for the *in vitro* kinetic study of amyloid formation [200]. Upon binding to β-sheet rich structures, the fluorescence quantum yield of ThT increases by several orders of magnitude, making it a sensitive and efficient reporter of the amyloid structure [201, 202]. However, as with PiB, ThT binds predominantly to late stage aggregates with extended β-sheet structures limiting the effectiveness of ThT to monitor the early stages of amyloid fibril formation. Nevertheless, ThT possesses unique photophysical characteristics, which are subject of great interest in current research.

4.1.3 Characteristic Features of Thioflavin-T

Photophysical Nature of ThT

Over the last few decades, ThT has become the gold-standard among amyloid dyes for studying amyloid formation due to thr large fluorescence enhancement observed upon fibril binding [203].

ThT consists of a dimethylaminobenzene ring coupled to a positively charged benzothiazole ring by a rotatable C-C bond. The internal rotation around this bond is responsible for the presence of two electronic excited states of ThT - the locally excited (LE) and twisted intramolecular charge transfer (TICT) state (Figure 4.3).

In low viscosity solvents, a low-energy barrier allows free rotation around the C-C bond. This results in the conversion of the LE fluorescent state (S_1; $\varphi \sim 37\,^\circ$) to a non-fluorescent TICT state (S_1') with favourable energy. In the TICT state, the twist angle between the two ring systems and thus the corresponding π orbitals is $\varphi \sim 90\,^\circ$.[205] This geometric arrangement prohibits the efficient delocalisation of the π-electrons across the whole chromophoric structure causing a shift in the excitation and emission maximum from $\sim$450 nm to $\sim$385 nm and from $\sim$482 nm to $\sim$445 nm respectively [203]. In addition, due to geometric relaxation and reduction of the oscillator strength in the twisted confirmation, the energy level of the TICT state S_1' is close to the energy level of the ground state, resulting in a non-radiative relaxation and thus poor fluorescence in solution ($\phi_{Fl} = 0.0001$, in water at room temperature) [206, 204, 207]. However, the nonradiative rate constant, $k_{LE\text{-}TICT}$, is highly dependent on the environment. High viscosity solvents, or binding to fibrils, limit the rotation around the C-C bond hindering in turn the adoption of the TICT state. The fluorescence emission from the LE state is therefore dominant, which results in a strong increase in the fluorescence quantum yield (e.g. $\phi_{Fl} = 0.43$, bound to insulin fibrils) [207, 203, 208]. This is the foundation of the amyloid detection property of ThT, the fluorescence quantum yield enhancement attained upon binding to β-sheet containing species. However, ThT suffers

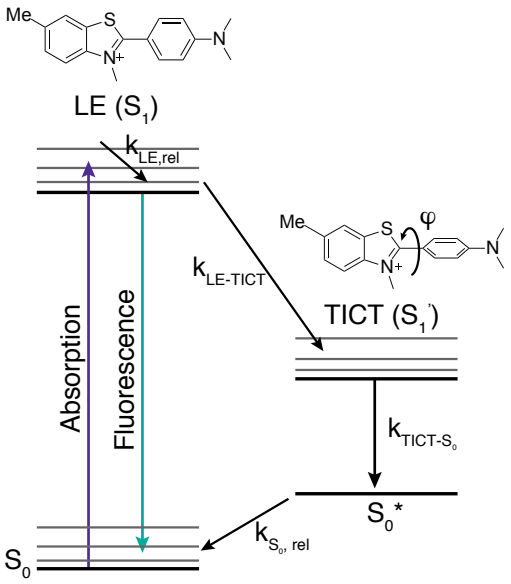

Figure 4.3 Jablonski excited-state deactivation scheme for ThT in solvents with low viscosity. (adapted from ref.[204])

from a relatively small Stokes shift and fluorescence intensity, even in the bound state, which in addition to its poor oligomer detection, limits the effectiveness of ThT to monitor the early stages of amyloid fibril formation in biological samples with high background signals.

Protein Binding

As the photophysical properties of ThT are highly dependent on the environment, it is important to understand the binding properties of ThT under pathological conditions. ThT is able to bind to amyloid aggregates formed from a large variety of proteins and thus it is most likely, that it recognises a common structural motif of amyloids [209].

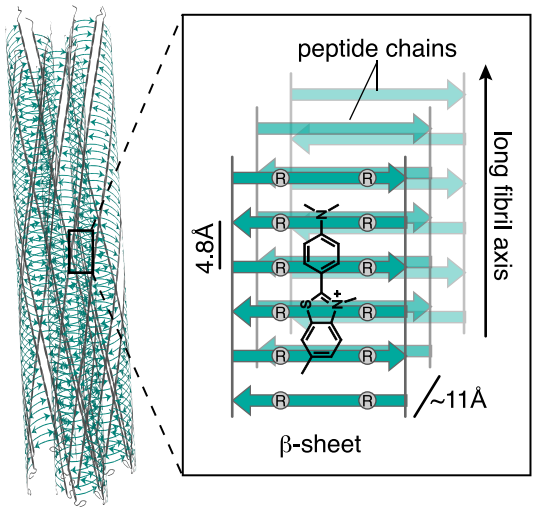

Figure 4.4 Common cross-β sheet motif of amyloid fibrils and proposed ThT binding mode. The common cross-β sheet motif of amyloid fibrils is formed by layers of cross-β sheets, which leads to a specific arrangement of side-chains (R) forming a channel-motif parallel to the fibril axis. ThT is thought to bind transiently along this channel.

One key structural feature common between different amyloid fibrils is the layers of cross-β sheets, which run parallel to the fibril axis (Figure 4.4). The β-strands within a β-sheet layer present an ordered array of side chains towards the surface. These side chains form a channel-like motif also running parallel to the long fibril axis. It has been suggested that the channels are rich in aromatic and hydrophobic amino acids, which strengthens the binding of ThT through π-π stacking and hydrophobic interactions [203, 200]. The distance between the β-strands and thus the side chains was defined by X-ray diffraction to be 4.8 Å. This distance did not change upon binding of ThT, indicating that ThT binds on the β-sheet surface aligned with the channel. Since the length of the long axis of ThT accounts for 14-15 Å, it is thought that ThT recognises 4 continuous β-strands in a β-sheet [210]. As fibrils contain extended β-sheet structures, several ThT molecules can bind along the fibril axis leading to a regular arrangement of ThT molecules. As binding induces a planar conformation of ThT, this leads to the specific "light-up" response of ThT in the presence of β-sheet aggregates. It was further shown, that aryl-benzothiazoles with increased hydrophobicity bind deeper inside the binding groove, which strengthens the aromatic and hydrophobic interactions resulting in an

improved binding affinity. This is mirrored by the ∼135-fold increased binding affinity of the neutral aryl-benzothiazole PiB towards Aβ aggregates compared to ThT [211].

Even though the surfaces of cross-β structures with the channel-arrangement of side chains is thought to be the main recognition motif, ThT is also capable to bind to other protein sites, of which not all result in the characteristic fluorescence increase [211–214]. However, the lack of high resolution structural data and appropriate methods prevents detailed understanding of the different binding sites and binding modes of ThT.

ThT and High Resolution Imaging Techniques

A key requirement in understanding the pathogenic properties of misfolded proteins is the identification and detailed characterisation of these species. Until recently, it was difficult to detect and visualise protein species with such transient nature and a size less than 200 Å. Due to the development of new high resolution fluorescence techniques it is now possible to resolve structures of around 50 nm, which brings research a step closer to the study of the initial stages of protein aggregation [215].

The high resolution technique SAVE, single aggregate visualisation by enhancement, makes use of the unique optical profile of ThT and couples its low fluorescence signal in solution, the rapid quantum yield increase upon amyloid binding and the accompanied Stokes shift with single-molecule instrumentation [216]. The method is based on direct imaging and counting of the number of amyloid aggregates that bind ThT and become fluorescent and uses total internal reflection fluorescence (TIRF) to enhance the signal to background noise. Additionally, as the binding affinity of ThT towards the amyloid structure is in the low μM range, there is a fast exchange of dye molecules on the surface of amyloid fibrils, which prevents photobleaching restrictions [200]. Combining these advantages enables the observation of amyloid aggregates at high resolution both *in vitro* as well as in human biofluids [216].

Despite this promising achievement, the photophysical and binding properties of ThT have limited the potential of these high resolution methods. The poor oligomer detection ability and binding affinity in combination with a relatively small Stokes shift, molar extinction coefficient and quantum yield, makes it poorly suited for the detection of smaller, low concentration oligomeric species, particularly in biological samples with high background signals. Thus, there is a great demand of new dyes with improved photophysical and binding properties to detect, characterise and study the formation of these early species and their role in the pathogenesis of neurodegenerative disorders.

To address this unmet need, the aim of this chapter was to find variants of ThT with improved fluorescence and binding properties, which would enable one to sensitively and specifically detect and quantify the concentration and composition of oligomers and fibrils in cerebrospinal fluid (CSF) or plasma at an early disease stage.

4.1.4 Approach

During the aggregation process a large number of structurally similar binding sites are generated. This provides the opportunity to exploit a multivalent probe design for the generation of new ThT analogoues with improved properties. This hypothesis is supported by published work of Qin et al, which shows a 70-fold enhanced affinity for Aβ40 amyloids of ThT dimers linked by short polyethylene glycol (PEG) chains [217]. However, there was no significant improvement of the specificity of aggregate detection nor of the optical properties. To advance optical and binding properties simultaneously the following key features were aimed to be explored and optimised: the ligand group (by introducing structural modifications onto ThT (R^1, R^2)), the linker length, the linker composition and the multivalent structure and design (R^3) (Figure 4.5).

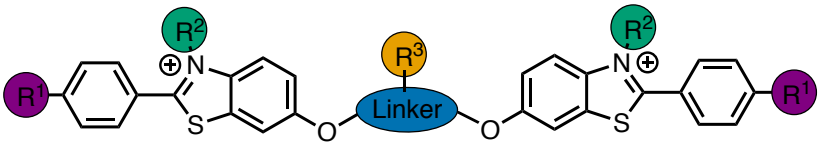

Figure 4.5 Possible modification sides to generate ThT analogues with improved properties.

In addition to the improvement based on structural modifications of ThT, it was also aimed to use the multivalent design and combine it with the single-molecule localisation microscopy technique, DNA-PAINT (cf. Chapter 1.4), which can be used to improve the imaging sensitivity and resolution independent from the optical properties of ThT and thus may allow the detection of small, low concentrated early stage oligomers in biological samples [218].

4.2 Results and Discussions

4.2.1 Ligand Group Modifications - new ThT Analogues

As highlighted above, the photophysical characteristics of ThT make it an interesting fluorescent probe for the study of amyloid. However, the photophysical properties as well

as binding affinities and specificity of ThT are poorly suited for fluorescence imaging in biological samples with high background and for the detection of early stage oligomers. Hence, there is a great demand of new ThT analogues, that outperform ThT in its binding and optical characteristics but keeps the most significant property of ThT, the specific fluorescence quantum yield enhancement attained upon binding to β-sheet containing species. To achieve this, a library of neutral ("E-derivatives") and charged ("mE-derivatives") ThT derivatives with different head groups (R^1, Figure 4.6) were synthesised by our collaboration partners, which we then analysed towards their photophysical and binding affinities in comparison to ThT.

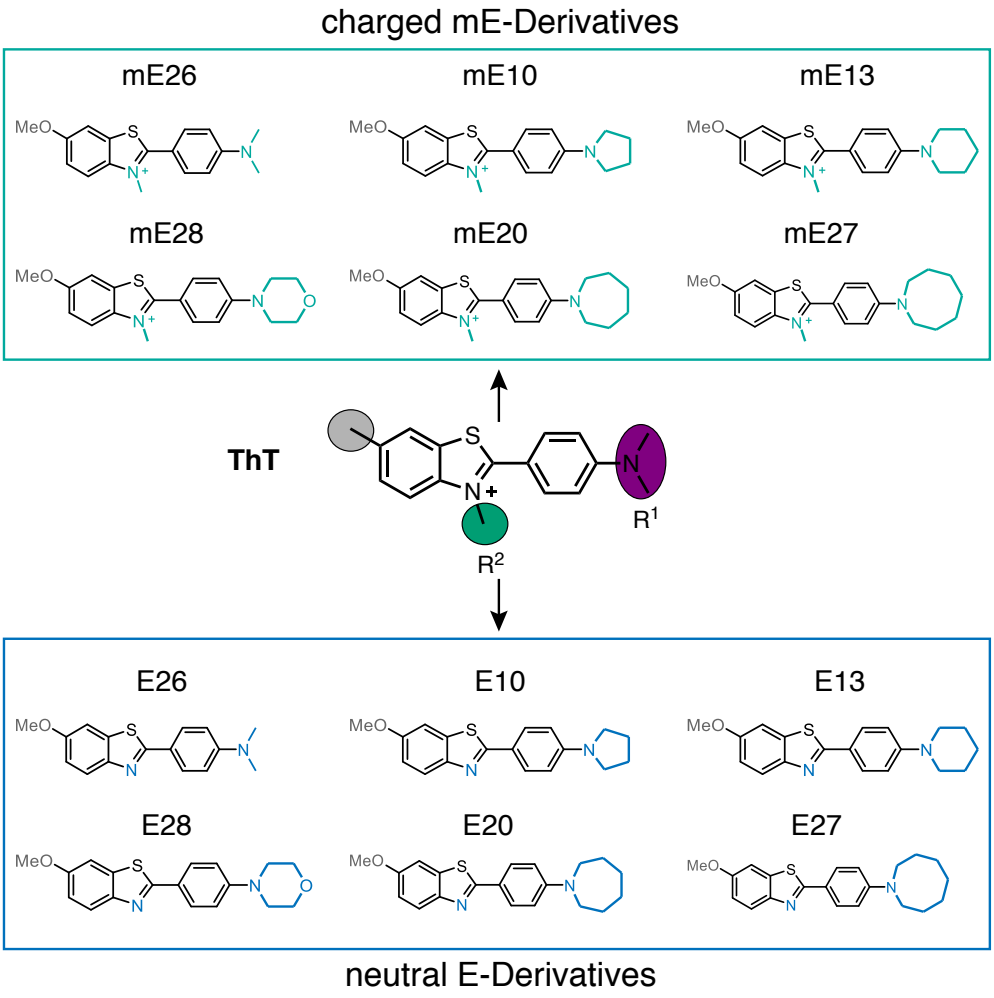

Figure 4.6 Chemical structures of the new charged (mE, green) and neutral (E, blue) ThT derivatives. The structural differences between the derivatives and ThT are highlighted by the coloured circles on the ThT structure as well as through colours in the chemical structures of the derivatives.

To ensure specific amyloid binding and the unique fluorescence turn on response of ThT, it is essential to maintain the aryl-benzothiazole core with its rotatable C-C bond (Figure 4.6). To increase the electron density of the core structure, we converted the aromatic methyl group of ThT into a methoxy functionality and expanded the aliphatic unit on the dimethyl amino moiety. To further question the relationship between the chemical structure and the binding and optical properties, different modification of the dimethyl amino moiety were explored. Therefore, special attention was paid on how increased sterical demand, a more restrained amino moiety and increased lipophilicity influence the properties of ThT. This was realised by introducing different aliphatic ring systems on the dimethyl amino moiety (R^1, purple circle, Figure 4.6). It was already shown, that the lack of positive charge leads to a deeper insertion of the aryl-benzothiazole core into the surface groove and thus strengthens the dye-amyloid binding [211]. To separate the influence of the charged methyl amino group and the modification on the "head" of the aliphatic unit (R^1), the charged (mE, green) as well as neutral (E, blue) ThT derivatives were synthesised. Even though previous reports have demonstrated that modifications on position 6 of the benzothiazole unit (grey circle) do not significantly influence the amyloid binding ability, the ThT analogue bearing only this modification was synthesised as well (mE26, Figure 4.6), to confirm previous results and question its influence towards the optical properties.

Photophysical Properties

One of the goals of this chapter was to generate new dyes with improved optical characteristics (higher quantum yield and greater molar extinction coefficient than ThT) while keeping the most significant property of ThT, the fluorescence quantum yield enhancement attained upon binding to β-sheet containing species. Thus, it is essential to initially characterise the bulk photophysical properties of the different mE and E derivatives under physiologically relevant conditions in PBS (pH 7.4) and in the presence of amyloid aggregates as well as under different viscosity environments to ensure that the behaviour as molecular rotor stays unaffected by the structural modifications made. αSynuclein (αSyn) was chosen as test system for our validation studies. αSyn is presynaptic nerve terminal protein and the major constituent of Lewy bodies, the hallmark of Parkinson′s disease [219].

Photophysical Properties in PBS and 2-Propanol

The main characteristic of molecular rotors is the distinct difference in fluorescence signal of the "free" dye (unbound/low-viscosity solvent) and the "confined" dye (bound/high-

viscosity solvent), caused by the ability of the dye to undergo an intramolecular twisting motion in the fluorescent excited state (cf. section 4.1.3) [220]. In the case of ThT, this is manifested by non-radiative relaxation in its "free" state (twisted intramolecular charge transfer (TICT) conformation) and a strong fluorescent quantum yield increases in its "confined" state (planar (LE) conformation). Thus, to test the suitability of the new ThT derivatives to function as suitable molecular rotor, it is important to first examine their optical properties in a biological relevant environment (PBS) but in the absence of protein aggregates, to ensure low background fluorescence. Next, to affirm the general ability of an turn-on response, the analysis of the photophysical features in a high-viscosity solvent is required. For this, 2-propanol was chosen as representative solvent with higher viscosity (viscosity(2-PrOH) = 2.1 vs viscosity(H_2O) = 0.9).

The results obtained from absorption and fluorescence measurements of ThT in PBS were in good agreement with values reported in the literature and confirmed a moderate extinction coefficient of $\varepsilon_{\lambda=413\text{nm}} = 36000\,\text{M}^{-1}\text{cm}^{-1}$ at $\lambda_{\text{abs,max}} = 413\,\text{nm}$ with a negligible quantum yield of $\phi_{\text{Fl}} < 0.01$ [200, 220].

The charged mE derivatives exhibited well defined absorption and fluorescence spectra with maxima - and consequently Stokes shifts - similar to those of ThT (Table 4.1, Figure 4.8). Exceptions were the two analogues bearing a six-membered ring, mE28, with $\delta_{\text{abs}} = 380\,\text{nm}$ and $\delta_{\text{em}} = 513\,\text{nm}$, and mE13, with $\delta_{\text{abs}} = 326 + 416\,\text{nm}$ and $\delta_{\text{em}} = 512\,\text{nm}$. A summary of the optical properties of the mE derivatives can be found in table 4.1. It was promising, that mE26, which only differs from ThT by the methoxy functionality on position 6 of the benzothiazole ring (grey circle, Figure 4.6), possess a nearly identical absorption and fluorescence maximum to those of ThT with $\delta_{\text{abs}} = 414\,\text{nm}$ and $\delta_{\text{em}} = 484\text{nm}$. However, it showed clear differences in the extinction coefficient, quantum yield and brightness. The extinction coefficient was decreased by more than 2.5-fold compared to ThT. This was a common characteristic across all mE derivatives, which might be caused by the increase in electron density through the methoxy group. As there are now two electron donating moieties attached to the aryl-benzothiazole systems (methoxy group on the benzothiazole ring and dimethylamino group on the aryl ring), the oscillator strength might be lowered and thus also the transient dipole moment leading to a decreased extinction coefficient. In contrast to the trend of the extinction coefficient, the quantum yield of mE26 as well as the remaining mE derivatives, was increased by minimum 10-fold, accompanied with an overall increase of the brightness of the dyes, but to a lesser extent than their quantum yield. These results indicate, that the replacement of the methyl group on position 6 of the benzothiazole ring by a methoxy-group does not influence the absorption and emission range but has an impact

towards their performance as photon absorbers and background fluorescence in their "free" conformation.

Table 4.1 Summary of photophysical properties[1] of the charged mE derivatives and ThT in PBS.

Dye	λ_{abs} (nm)	λ_{em} (nm)	$\lambda_{em} - \lambda_{abs}$ (nm)	ε_{abs} ($M^{-1}cm^{-1}$)	ϕ_{Fl}	B (a.u.)	R^1-structure
ThT	413	488	75	36000	0.001	39.4	
mE26	414	484	70	14088	0.02	281.8	
mE10	420	494	74	31130	0.04	1245.2	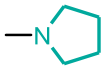
mE13	326 / 416	512	96	4394	0.01	43.9	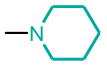
mE28	380	513	133	20638	0.03	619.1	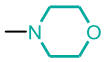
mE20	423	500	77	26318	0.03	789.5	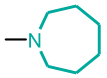
mE27	423	498	69	19471	0.05	973.6	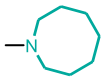

[1] Values were obtained from bulk UV-vis absorption and fluorescence measurements of the dyes in PBS buffer (pH 7.4).

Table 4.2 Summary of photophysical properties of the neutral E derivatives and ThT in PBS.[1]

Dye	λ_{abs} (nm)	λ_{em} (nm)	$\lambda_{em} - \lambda_{abs}$ (nm)	ε_{abs} ($M^{-1}cm^{-1}$)	ϕ_{Fl}	B (a.u.)	R^1-structure
ThT	413	488	75	36000	0.00	39.4	
E26	301	432	131	2542	0.04	101.7	
E10	370	429	59	5394	0.01	53.9	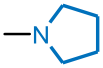
E13	328	433	105	1305	0.02	26.1	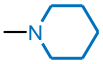
E28	325	439	114	4822	0.02	96	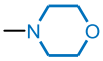
E20	371	445	74	1963	0.01	19.6	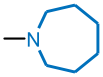
E27	300	440	141	1346	0.02	26.9	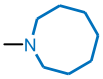

[1] Values were obtained from bulk UV-vis absorption and fluorescence measurements of the dyes in PBS buffer (pH 7.4).

The neutral E derivatives showed absorption maxima at lower wavelength than the charged dyes and ThT (between 300 nm and 371 nm) and a more than 6-fold decrease in the extinction coefficients ($\varepsilon < 6000\,M^{-1}cm^{-1}$) (Table 4.2, Figure 4.9). This finding might be explained by the greater electron-withdrawing ability of the positively charged nitrogen atom. This leads to greater delocalisation of the electrons from the aryl amino group and a decrease in the energy gap between the HOMO and LUMO, thus shifting the absorption to longer wavelength. In addition, the removal of the positive charge may reduce the oscillator strength, which in turn can result in an decrease in extinction coefficient. The emission maxima of the neutral derivatives were, as for the absorption maxima, hypsochromically shifted relative to ThT ($\lambda_{em,ThT} = 488$ nm vs $\lambda_{em,E} = 429$ - 445 nm). In addition, the quantum

yield and brightness of the neutral dyes in PBS was increased compared to ThT and similar to their charged equivalents. This behaviour is supported by previous results from the literature stating a higher energy barrier between the LE and the TICT state caused by the absence of the methyl group and thus positive charge, which in turns results in a higher quantum yield [221]. The increased quantum yield is unfavourable for the use of these analogues as turn-on imaging probes, as the baseline signal increases and thus the signal to background ratio decreases. Nevertheless, the Stokes shifts were comparable with those of ThT and the charged analogues, which might be caused among others by the molecular rotor behaviour [220, 222].

Having established the influence of the methoxy group and the charged nitrogen atom, it was then necessary to examine the influence of the modifications on the aryl nitrogen. Comparing the different structural modifications made on this nitrogen with the results gained from determining the optical properties of the mE and E derivatives, revealed the following trends. Converting the two methyl groups into a 5-membered ring and thus generating a more conformationally restricted benzothiazole salt with increased lipophilicity, induced a bathochromic shift of the absorption maxima and an increase in the extinction coefficient (cf. (m)E26 vs (m)E10). Increasing the ring size by one or more carbons leads to a greater sterical demand and causes different confirmation of the ring, evoking the opposite effect: the maxima shifted hypsochromically and the extinction coefficient decreased. Adding an oxygen to the 6-membered ring did not significantly influence the absorption maximum but enhanced the extinction coefficient ((m)E13, (m)E28), probably due to the increase in polarity. Expanding the ring size even further positively influenced the absorption properties of the charged mE derivatives (raised extinction coefficient for mE20, mE27) but was less favourable for the neutral analogous, E20 and E27, which might be caused by the decreased solubility of these hydrophobic E derivatives in PBS.

As it was shown that the hydrogen bonding capabilities of the aryl nitrogen do effect the twist between the benzothiazole and aryl unit and thus the efficiency of the π-orbital overlap, this might be one of the reasons explaining the observed trends - different ring sizes and conformations result in different hydrogen-bond patterns and thus different twists [223, 224]. The greater the twist, the poorer the π-orbital overlap, the more hypsochromically shifted the absorption maxima. Another aspect which could have an impact is the difference in hybridisation state of the nitrogen, going from predominantly sp^3-hybridised nitrogen in ThT and 6-membered rings to a nitrogen with more sp^2-character in 5-membered rings. The greater the sp^2-character the stronger the interactions of the nitrogen with the aryl unit.

In respect to the quantum yield and brightness, no correlation between the ring size and the obtained values were observed. However, when interpreting the data obtained from bulk absorption and fluorescence measurement in PBS, it is important to keep in mind the unique nature of the photophysical properties of these molecular rotor based dyes and their high environment dependence, which can be strongly influenced by their solvation state. This is especially relevant for the neutral derivatives as they suffered from poor solubility in aqueous environment, aggregate or micelle formations at concentrations higher than 2 μM was observed. This might also cause the broad absorption spectra observed for these dyes. However, the spectral shapes of the absorption and emission curves did not change in the concentration range tested (0.1 -10 μM) and all the calculations were performed by only taking the linear part of the concentration curves into account.

To finally prove that the introduced modifications did not impact the ability of the dyes to function as molecular rotors, UV-Vis absorption and fluorescence spectra of ThT and a subset of E and mE derivatives ((m)E10, (m)E13, (m)E26) were assessed in 2-propanol, as representative high-viscosity solvent. The absorption spectra of both derivatives were unaffected by 2-propanol. However, the fluorescence spectra showed the desired increase in quantum yield by increasing solvent viscosity (Figure 4.7).

The charged mE-derivatives showed an increase of over 4-fold in the total integrated emission in 2-propanol compared to water (Figure 4.7B, D). For the neutral E-derivatives, when changing the solvent from water to 2-propanol, the increase was greater than 30-fold (Figure 4.7C, D). These results suggest, that both, the neutral as well as charged ThT analogues, behave as a molecular rotor and a change in viscosity in the environment leads to the restriction of the carbon-carbon bond torsion resulting in preservation of the fluorescent excited state. The effect of 2-propanol towards this behaviour was more significant for the neutral derivatives, which showed a >100 times higher integrated emission in higher viscosity solvent than ThT and the charged equivalents (Figure 4.7D). However, this can not be directly transferred to the dyes behaviour bound to amyloid aggregates as not only the viscosity but also other properties of the micro-environment are influencing the complex behaviour of molecular rotors [98, 225]. Nevertheless, the results are encouraging, suggesting that all dyes of the library can function as molecular rotors and thus are suitable for amyloid detection.

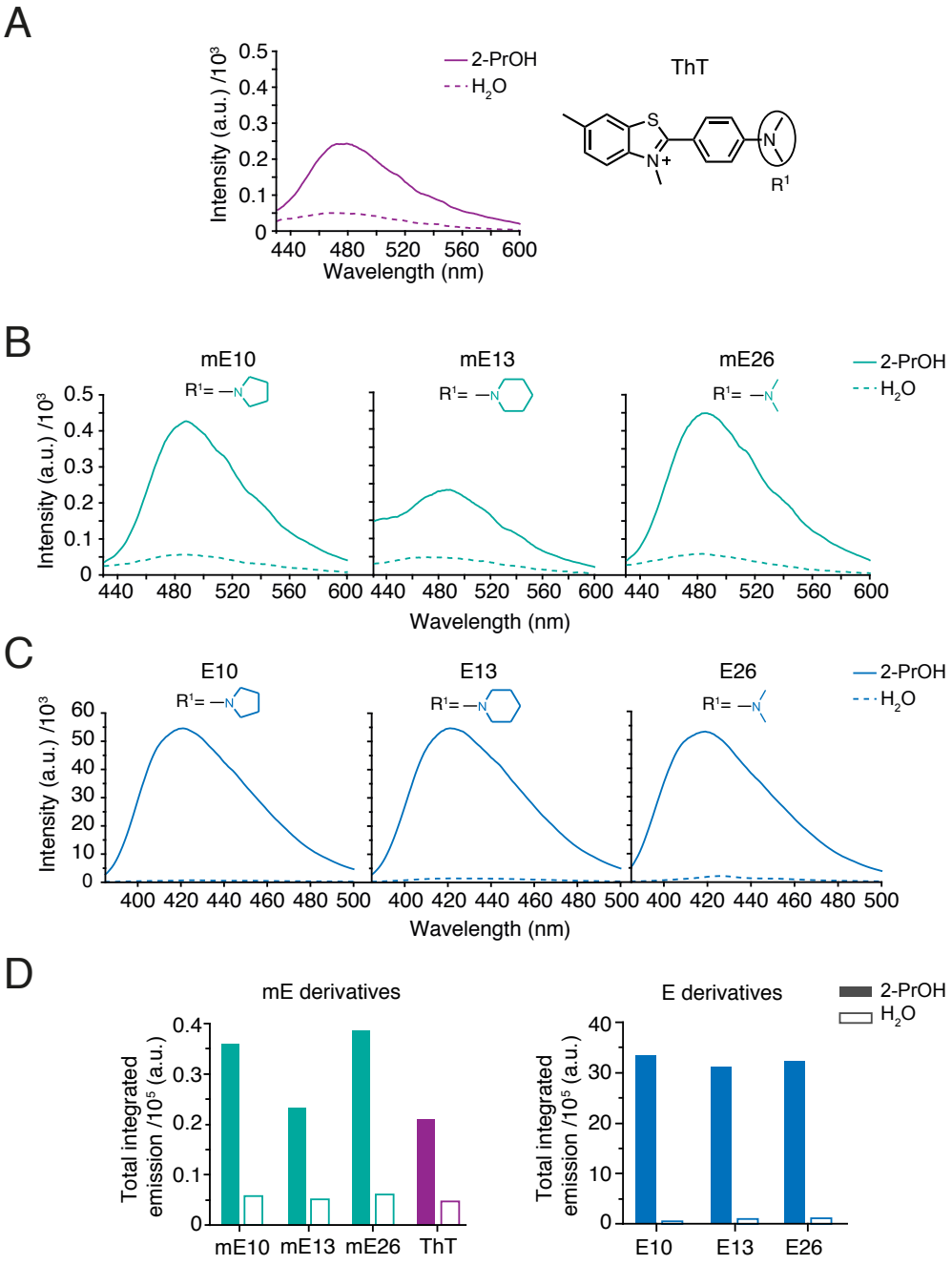

Figure 4.7 Fluorescence spectra of A) ThT (10 μM), B) mE10, mE13, mE26 (10 μM) and C) E10, E13, E26 (10 μM) in H_2O and 2-PrOH. D) Bar graph illustrating the fluorescence increase of ThT, mE derivatives (left) and E derivatives (right) in 2-PrOH compared to H_2O.

Photophysical Properties in Presence of αSynuclein

The key feature of ThT in respect to amyloid sensing is the specific fluorescence quantum yield enhancement attained upon binding to β-sheet containing species. Ideally, the new ThT analogues feature the same behaviour but with improved optical properties. Thus the next step was to test the library of charged and neutral ThT derivatives under physiological conditions in the presence of αSyn aggregates.

In agreement with the literature, ThT experienced a great enhancement in its quantum yield in the presence of αSyn ($\pi_{\mathrm{Fl},\alpha\mathrm{Syn}} = 0.24$ vs $\pi_{\mathrm{Fl,PBS}} < 0.01$) (Figure 4.8, Table 4.3). Likewise, the quantum yield of the charged mE analogous raised significantly when αSyn was added (Table 4.3, Figure 4.8, 4.10). However, the increase was not as pronounced as for ThT (Figure 4.10). Whereas ThT exhibited a $\sim$ 1000 fold higher quantum yield with αSyn compared to PBS, the highest enhancement of the mE analogues was $\sim$ 30-fold for mE13. The Stokes shift decreased slightly for ThT as well as all mE dyes, which is unfavourable since it results in a decrease in signal to noise ratio for fluorescence imaging. Among all the cationic dyes, mE10 attracted particular attention as not only its absolute quantum yield in presence of αSyn was $\sim$ 3-fold higher than that of ThT but also its brightness outperformed the brightness of ThT by $\sim$5-fold making mE10 a promising candidate for the detection of early oligomeric species with higher sensitivity.

The neutral ThT analogues also exhibited a fluorescence quantum yield enhancement upon binding to β-sheet containing species. However, the fluorescence increase accounted for less than 5-fold, making the E derivatives less suitable probes based on their fluorescence turn-on behaviour (Figure 4.10). This was manifested in their overall higher quantum yield in PBS as well as lower quantum yield in the presence of αSyn compared to the charged equivalents. As for ThT and the mE dyes, the Stokes shift decreased upon binding to protein aggregates. The results of the E derivatives, however, should be treated with caution due to the possible aggregation of these derivatives.

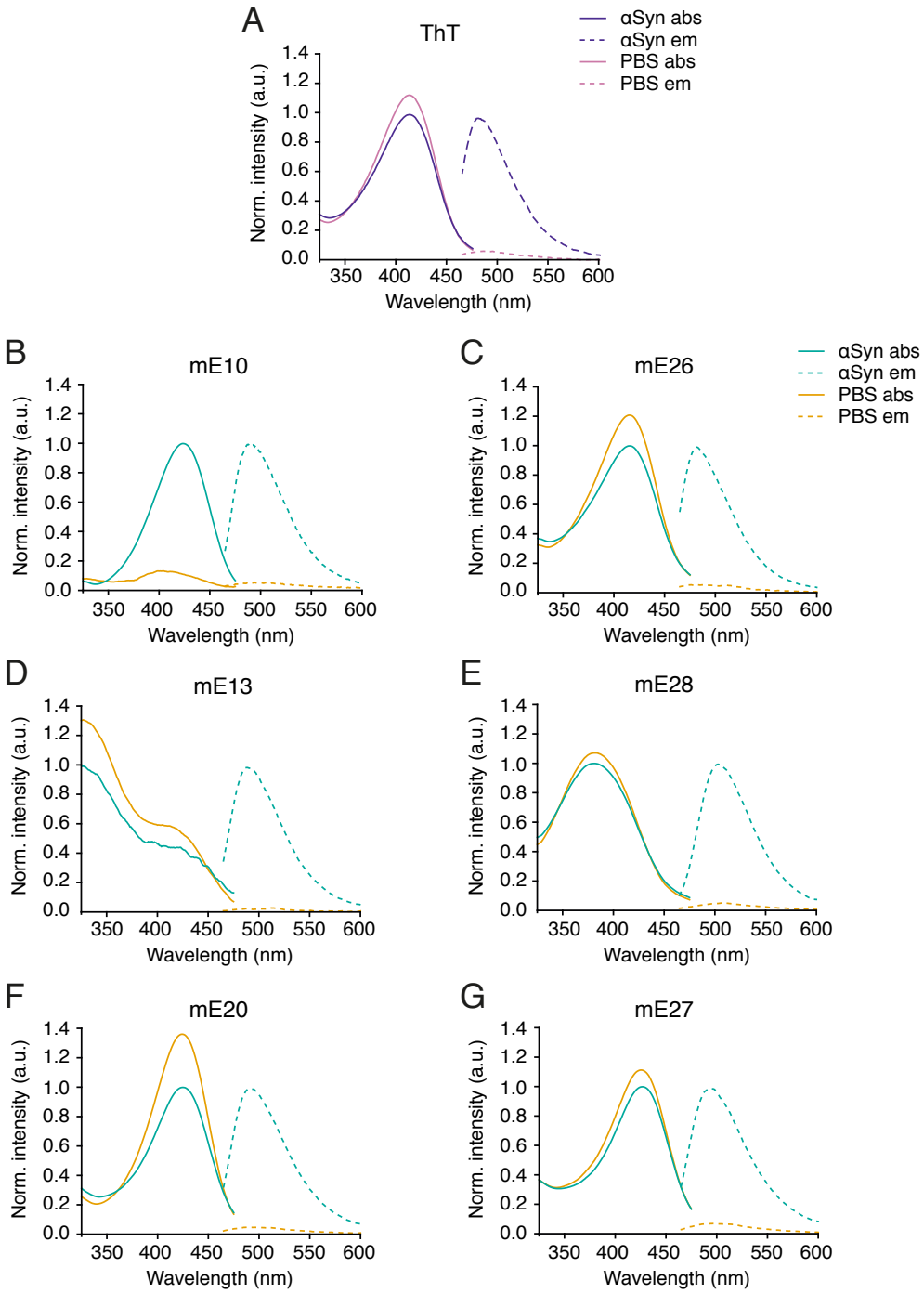

Figure 4.8 Absorption and emission spectra of 10 μM (A) ThT, (B) mE10, (C) mE26, (D) mE13, (E) mE28, (F) mE20 and (G) mE27 in PBS (orange) and in the presence of $\sim$2 μM recombinant αSyn aggregates (green). Normalisation of the absorption and fluorescence spectra was performed in respect to the maxima of the absorption/fluorescence maxima obtained in the presence of αSyn. Each spectrum represents the mean of results from 3 independent preparations of dye.

Table 4.3 Summary of photophysical properties of the charged mE derivatives and ThT in the presence of αSyn.[1]

Dye	λ_{abs} (nm)	λ_{em} (nm)	λ_{em} - λ_{abs} (nm)	ε_{abs} ($M^{-1}cm^{-1}$)	ϕ_{Fl}	B (a.u.)	R^1-structure
ThT	414	483	69	25283	0.24	6067	
mE26	420	483	63	14000	0.26	7070	
mE10	421	490	69	33107	0.81	31590	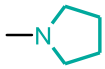
mE13	326 / 416	491	71	26400	0.61	16104	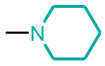
mE28	382	506	124	17000	0.58	9860	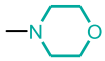
mE20	424	495	71	26400	0.61	16104	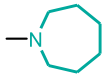
mE27	432	491	66	20300	0.58	9860	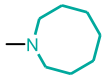

[1] Values were obtained from bulk UV-vis absorption and fluorescence measurements of the dyes (0.1 - 11 μM) in PBS buffer (pH 7.4) with recombinant αSyn aggregates (2 μM monomer concentration).

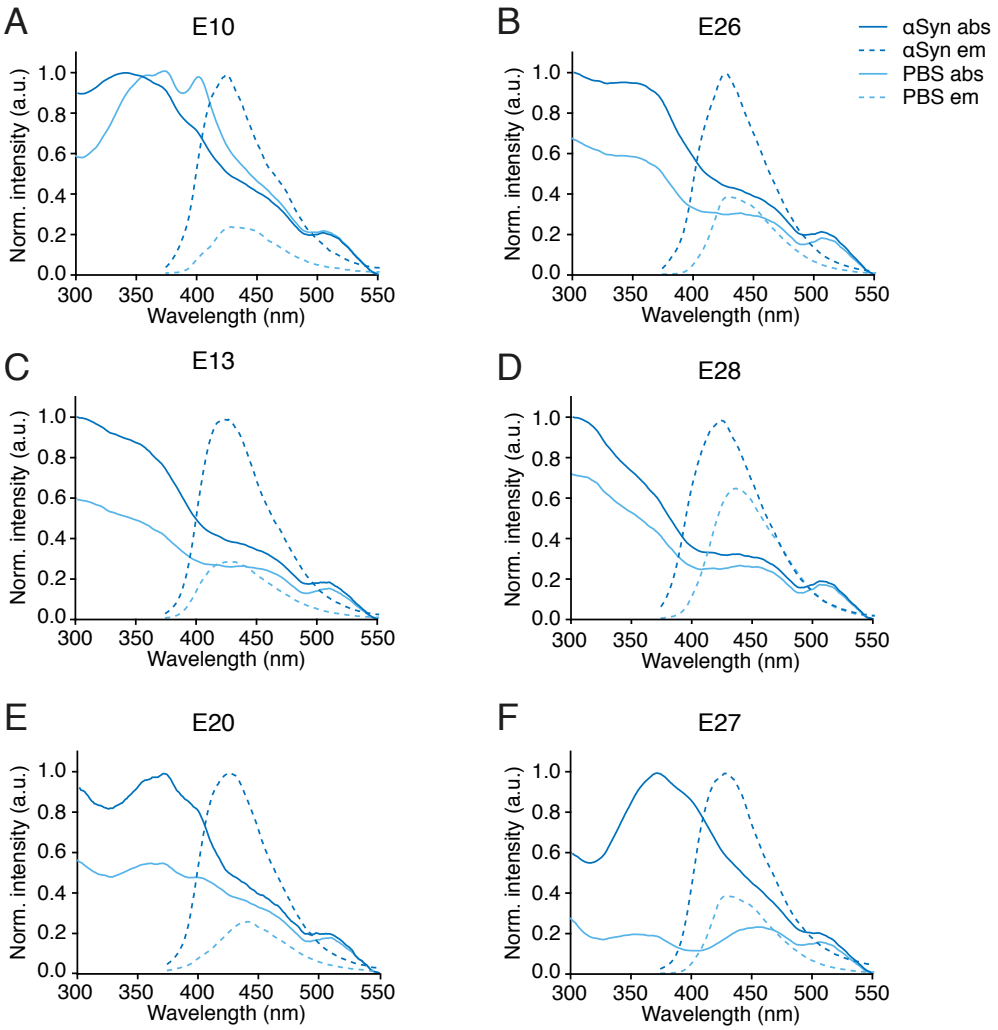

Figure 4.9 Absorption and emission spectra of 10 μM (A) E10, (B) E26, (C) E13, (D) E28, (E) E20 and (F) E27 in PBS (sky blue) and in the presence of $\sim$2 μM recombinant αSyn aggregates (blue). Normalisation of the absorption and fluorescence spectra was performed in respect to the maxima of the absorption/fluorescence maxima obtained in the presence of αSyn. Each spectrum represents the mean of results from 3 independent preparations of dye. (The spectral shapes were consistent across the measured concentration range 0.1 - 10 μM).

Table 4.4 Summary of photophysical properties of the neutral E derivatives and ThT in the presence of αSyn.[1]

Dye	λ_{abs} (nm)	λ_{em} (nm)	λ_{em} - λ_{abs} (nm)	ε_{abs} ($M^{-1}cm^{-1}$)	ϕ_{Fl}	B (a.u.)	R^1-structure
ThT	414	483	69	25283	0.24	6067	
E26	305	429	124	2000	0.11	220	
E10	367	425	58	1800	0.04	72	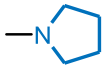
E13	330	425	95	3300	0.08	264	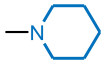
E28	320	427	107	4300	0.04	172	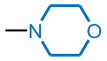
E20	373	427	54	3100	0.05	155	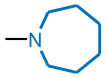
E27	374	431	57	1100	0.09	99	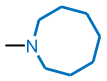

[1] Values were obtained from bulk UV-vis absorption and fluorescence measurements of the dyes in PBS buffer (pH 7.4) with 2 μM recombinant αSyn aggregates.

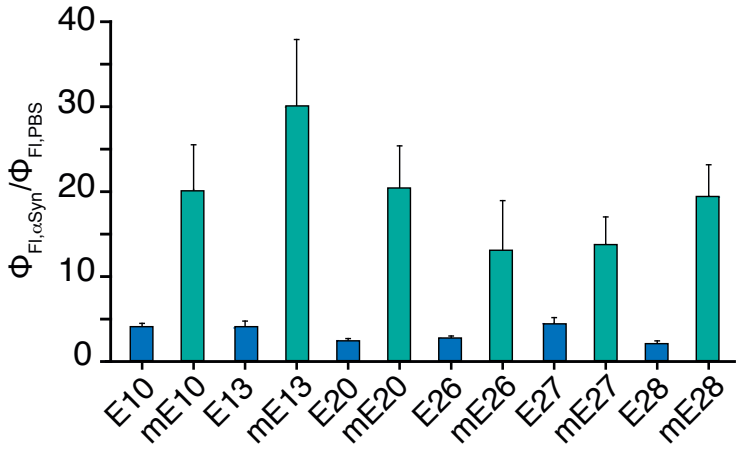

Figure 4.10 Quantum yield increase of mE and E derivatives upon αSyn binding (error are represented as propagated standard deviations of three measurements with separately prepared dye solutions).

In summary, all dyes were able to sense the presence of amyloid aggregates by an increase in their quantum yield. The mE derivatives manifested a greater fluorescence turn on response than the E derivatives, making them more suitable probes for fluorescence based imaging of amyloid. However, the photophysical properties obtained upon binding to αSyn must be viewed with caution as the amyloid aggregates are very heterogeneous and different binding affinities, binding sites and binding conformations have a great impact on the optical properties of dyes working as molecular rotors.

Binding Properties

Having gained an overview about the photophysical characteristics of the new ThT analogues, it was then necessary to examine their binding capabilities towards amyloid in order to deconvolute these from the optical properties. Thus, the next goal was to determine the binding affinities of the dyes towards αSyn and study the effect of different substituents towards their binding behaviour. It is worth emphasising that all binding affinity measurements were performed with αSyn aggregates obtained via a previously published protocol, that allows the generation of fibrils with a narrow size distribution and good reproducibility between independent batches [226].

Fluorescence-based Binding Affinities

One common way to experimentally measure the binding affinity of ThT towards fibrils is based on fluorescence spectroscopy exploiting the quantum yield increase upon protein binding. Thus, the binding affinities were measured through direct titration experiments,

in which an increasing amount of dye was added to a solution of constant concentration of αSyn.

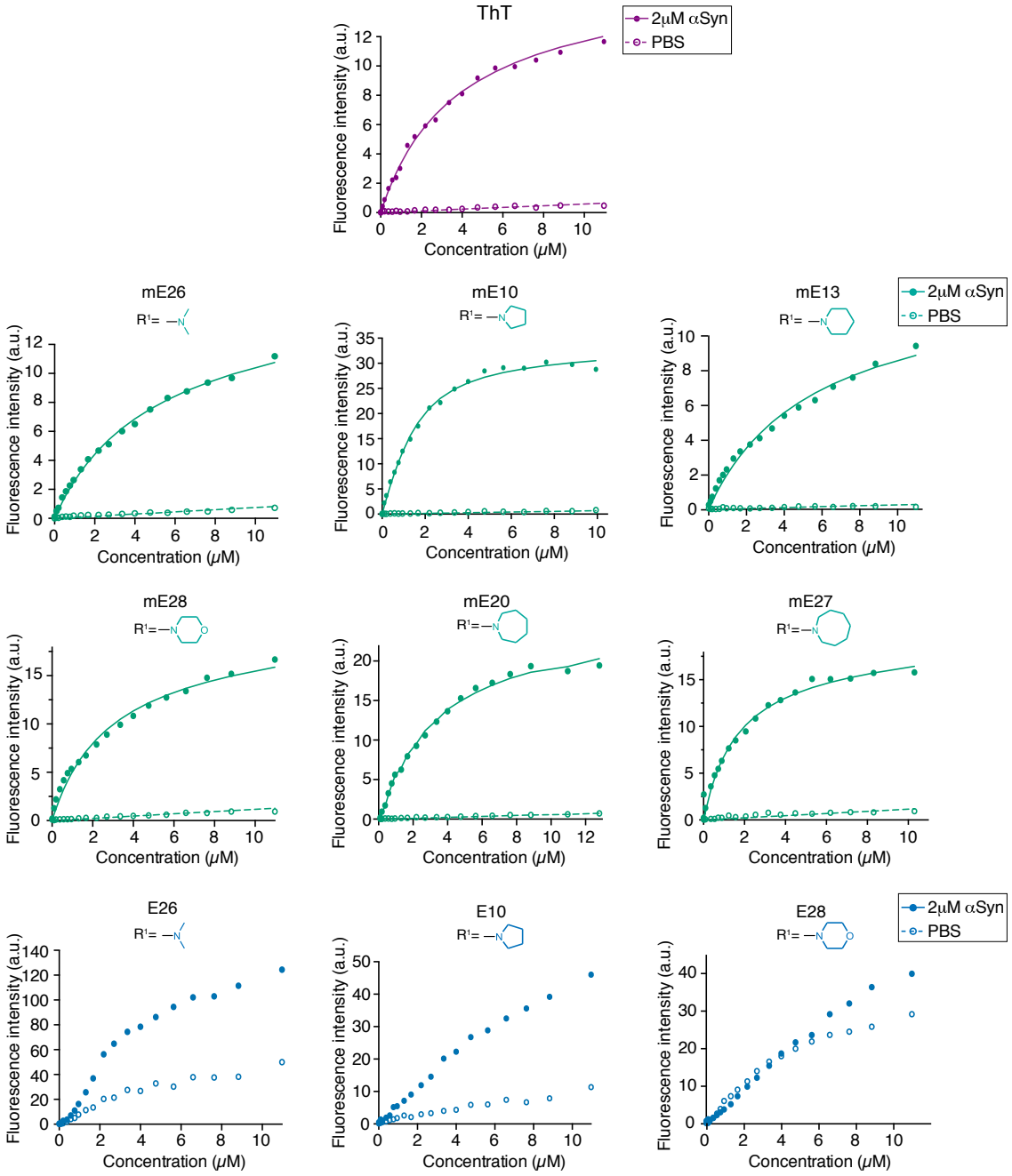

Figure 4.11 Representative binding curves of the mE derivatives and ThT obtained in the presence of 2 μM αSyn. The binding curves of 3 E derivatives are also shown to illustrate the difficulties to obtain useful data by direct titration due to the aggregation of the compound in PBS.

Table 4.5 Binding affinities obtained by fluorescence titration of the mE derivatives and ThT in the presence of 2 μM αSyn. The errors presenting standard deviations of 3 independent measurement.

K_D (μM)	ThT	mE26	mE10	mE13	mE28	mE20	mE27
mE	4.8 ± 1.3	6.21 ± 1.6	0.68 ± 0.1	4.74 ± 0.7	2.66 ± 0.9	1.53 ± 0.85	2.66 ± 0.09

The binding affinity of ThT was measured here to be $K_D = 4.8 \pm 1.3\,\mu$M, which agrees with previously measured values for other amyloid aggregates ranging from $K_D = 0.0035\,\mu$M (AS_{SAM} fibrils, pH 9) to $K_D = 64\,\mu$M (insulin fibrils, pH 1.6) [200]. All methylated, charged derivatives showed similar K_D values with the exception of mE10. With a K_D value of $0.68 \pm 0.1\,\mu$M, mE10 exhibited a one order of magnitude better binding affinity than ThT. As mE26, which only differs from ThT through the methoxy group on the benzothiazole ring, has a K_D value of $6.21 \pm 1.6\,\mu$M and thus similar to ThT, it is possible to exclude that the introduction of the oxygen and any implicated electrostatic interactions significantly impacts the binding of the dyes to αSyn. Thus, the origin of the improved binding of mE10 is probably result of the conversion of the dimethyl group into a 5-membered ring, which entails a more restricted conformation and may cause a greater sterical demand. However, increasing the ring size or adding an oxygen into the ring system did not result in improved binding affinities.

As highlighted previously, the neutral E analogues suffer from only a minor quantum yield increase upon binding to amyloid (Figure 4.10) as well as aggregation, which makes it difficult to obtain accurate binding affinities through direct titration experiments (Figure 4.11). Additionally, the E analogues did not exhibit a significant shift in their absorption profile when binding to αSyn (Figure 4.9). This, combined with the fact that they suffer from low extinction coefficients and tend to aggregate at higher concentrations meant absorption measurements were also not suitable to accurately determine the capability of the neutral derivatives to bind to αSyn. Hence, a competition assay was performed using ThT to measure the decrease in fluorescence signal as the compound competes for the ThT binding site. The binding affinities of the E derivatives obtained through the competition assay are summarised in Table 4.6.

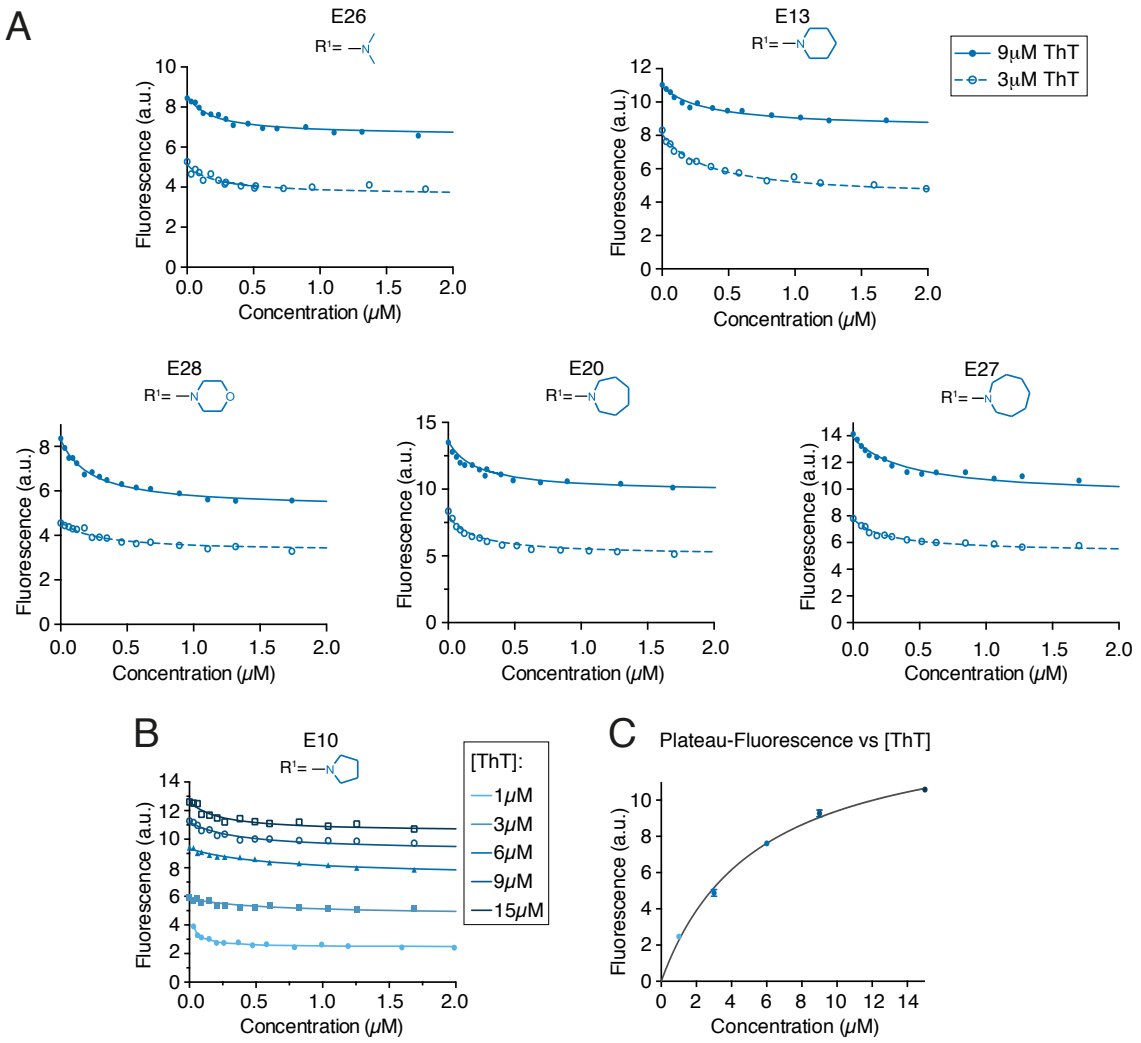

Figure 4.12 Fluorescence competition assay. A) Representative competition curves of E competing for the ThT binding site on αSyn. The curves obtain from 2 different ThT concentrations (3 μM (dashed line), 9 μM (solid line)) in the presence of 2 μM αSyn are illustrated as examples.B) Competition curves of E10 in the presence of 1 μM, 3 μM, 6 μM, 9 μM and 15 μM ThT as example of the influence of different ThT concentrations being present. C) Curve obtained when plotting the fluorescence intensities of the competition curves reached at the plateau against the ThT concentration being present.

Table 4.6 Binding affinities of E derivatives obtained by fluorescence competition assay with ThT in the presence of 2 μM αSyn. The errors presenting standard deviations of n $\geq$ 4 independent measurement.

Dye	ThT_{BS1}	ThT_{BS2}	E26	E10	E13	E28	E20	E27
K_D (μM)	3.1 ± 0.1	5.4 ± 0.2	0.09 ± 0.09	0.12 ± 0.08	0.17 ± 0.09	0.06 ± 0.04	0.06 ± 0.02	0.10 ± 0.03

The calculated K_D values suggest that the E derivatives are a significantly stronger binders than the mE equivalents and ThT in respect to αSyn aggregates. This is in agreement with the literature, which claims a greater stabilisation of the dye by the micro-environment in the binding channel due to the increased hydrophobicity of the neutral dyes and the loss of the positive charge [211].

As the quantum yield of unbound ThT is negligible and none of the E derivatives exhibits a significant fluorescence signal when excited at 440 nm, the signal intensity was expected to go down to nearly zero when all ThT molecules are displaced by the E derivative. Interestingly, the fluorescence intensity decreased in average only about 34% at most, indicating only a partial displacement of ThT by the E analogues (Figure 4.12A). This suggests different fluorescent binding sides of ThT as well as different binding affinities of ThT and the neutral dyes towards these binding sides. The E derivatives seem to mainly bind to one of the binding sites (in the following referred to as first binding site (BS1)) with binding affinities obtained through this competition assay. The affinity of the E dyes towards the other binding side ("second binding site" (BS2)) is too low to be measured, as the neutral dyes are not able to displace ThT from this position.

To support this hypothesis and to examine the binding affinity of ThT towards the second binding site, the competition assay was repeated with different concentrations of ThT ranging from 1 μM to 15 μM (Figure 4.12B). Fluorescence titration of ThT provided a K_D value of ThT of $4.8 \pm 1.3\,\mu$M (cf. Table 4.5) and thus the chosen concentration range covered concentration below and above the K_D value. The plateau of the competition curves was reached at different fluorescence intensities for the different ThT concentrations being present. This plateau intensity therefore provides a measure of how much of the second binding site is bound to ThT. When plotting the "plateau"-fluorescence intensities against the ThT concentration it was possible to calculate the K_D value for the second ThT binding site (Figure 4.12C). With a value of $K_{D,BS2} = 5.4 \pm 0.2\,\mu$M, the binding affinity of ThT towards the second biding side was close to the affinity obtained by direct titration of ThT ($K_{D,total} = 4.8 \pm 1.3\,\mu$M). As $K_{D,total}$ represents the weighted average of the two different binding sites (weighted by means of fluorescence intensity and the population of the two sites), this result indicates that the two different sites possess similar affinities for ThT.

Surface Plasmon Resonance based Binding Affinities

The results gained from fluorescence based binding affinity studies was especially useful to compare ThT and the charged mE derivatives and reveal different fluorescent binding sites of ThT, but to get an insight into non-fluorescent binding sites, further analysis, not

relying on the optical properties of the dyes, was needed. Thus, the binding capabilities of the mE and E derivatives towards αSyn aggregates was further assessed with surface plasmon resonance (SPR) spectroscopy. SPR is a surface method with high sensitivity and able to give insight into a) the rate of interaction between the target (αSyn aggregates) and ligand (dyes) and thus the kinetic rate constant, and b) the binding level, which then can then be used to determine the affinity constant [226].

To use this technology for our purpose, αSyn aggregates were covalently attached to a gold surface via an amide bound. The αSyn coated surface was then exposed to different concentrations of the dyes. Concentrations of the dyes tested covered a range between 0.25 μM and 30 μM. Data of lower concentrations were in the noise of the data acquisition, higher concentrations were avoided as titration experiments indicated micelle/aggregate formation starting around 30 μM. The binding experiments yielded good data quality for all all dyes, tested on three different chips and thus three different batches of immobilised αSyn. The results obtained were independent of the immobilization level and allowed a readout about the binding levels obtained for the different concentrations as well as the association and dissociation kinetics of the different dyes.

Examining the equilibrium resonance response in respect to the dye concentration enabled the calculation of K_D values for the different dyes (Figure 4.13, Table 4.7) in a similar way as for the fluorescence measurements. The K_D measured for ThT was 79.4 ± 6.1 μM, which was an order of magnitude higher than the value obtained by fluorescence titrations. However, care must be taken when comparing results from surface methods with results obtained in solution, as physical interactions might differ. During the SPR measurements, the fibrils are fixed on the surface and continuously exposed to a solvent flow whereas the fluorescence-based measurements were carried out in steady solution. Additionally, fluorescence based methods are limited to assess binding sites inducing a fluorescence increase, whereas SPR is able to take additional interactions into account. Nevertheless, overall the SPR results revealed similar trends as observed by fluorescence titrations (Table 4.7): mE26 and ThT showed the same K_D value (K_D(ThT) = 79.4 ± 6.1 μM, K_D(mE26) = 72.3 ± 6.68 μM) reinforcing that the ThT–amyloid interaction is tolerant against the methoxy substituent at position 6 of the benzothiazole ring. With a binding affinity of $K_D = 38.1 \pm 2.3$ μM, mE10 featured, as obtained earlier, the greatest affinity towards αSyn among the charged ThT analogues.

All E derivatives outperformed ThT as well as their corresponding mE partners by more than an order of magnitude, which was in agreement with the literature [211]. In addition, it was noticeable that whilst ThT and the mE dyes showed affinity curves best fitted by a one-binding side fit, all E derivatives revealed a hump between 1 μM and 5 μM dye concentration

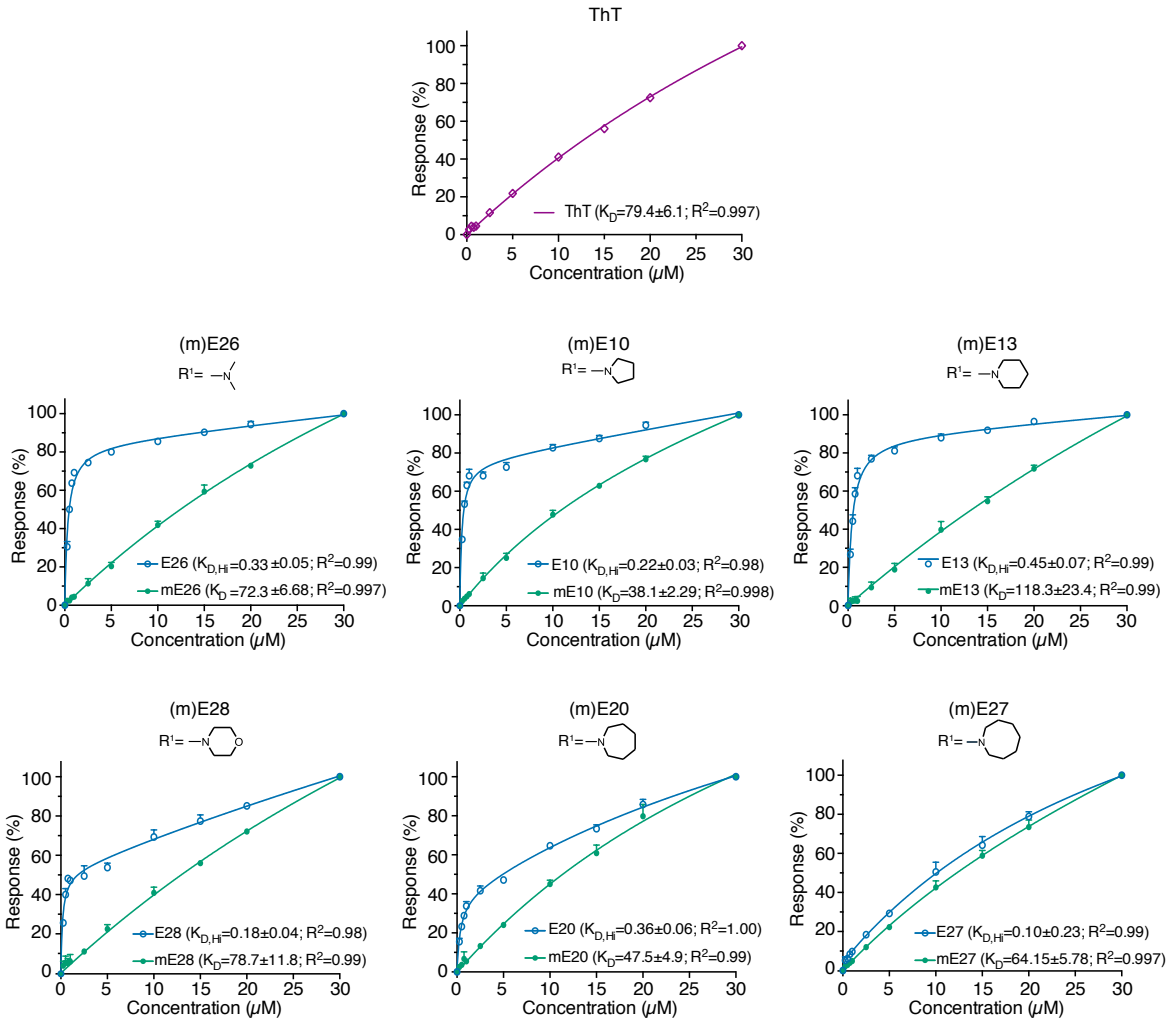

Figure 4.13 Binding affinity curves obtained from SPR experiments of ThT, mE and E derivatives binding to immobilised αSyn aggregates on a gold surface. Each spectrum represents the mean of results from 3 independent preparations of dye solutions and SPR chips; error bars are shown as standard deviations. One-site specific binding fit is shown for mE derivatives and ThT, two-site specific binding fits are applied for E derivatives. The $K_{D,Hi}$ value stated represents the K_D value towards the stronger binding site. $K_{D,Low}$ values can be found in Table 4.7.

and therefore a 2-binding side fit was better suited for their quantification. This supported the hypothesis that the neutral analogues feature different binding sites, of which the stronger binding site is less prone to bind ThT and the charged derivatives (cf. Figure 4.12).

Having studied the concentration dependent equilibrium affinities, the interaction between αSyn aggregates and the dyes was examined from a kinetics point of view. Representative sensograms for ThT, one mE and one E derivative are depicted in Figure 4.14. ThT and the charged dyes, showed an immediate association onto the surface bound αSyn aggregates with a steep association phase. mE10, with the highest calculated K_D value based on equilibrium affinity measurements, exhibited the steepest slope, which might indicate the fastest binding among the tested dyes (Figure 4.14 vs A and C). The dissociation of ThT and the mE dyes was very rapid, resulting in a negligible dissociation phase. This indicates a rather weak binding to the fibrils as they get washed of from their binding sites immediately.

On the contrary, the neutral analogues showed a distinct slower association to the fibrils with a clear dissociation phase. These findings are difficult to interpret as many factors can influence the on- and off-rate. However, one could speculate that the slower association might be caused by less accessible bindings sites or by some conformational changes after the initial binding. The slower dissociation points towards a stronger interaction of the E derivatives with the aggregates.

The response sensograms were further analysed using a heterogeneous ligand model (Figure 4.14). The goodness of the heterogeneous ligand fits were compared between ThT, the mE and E derivatives and did support the assumption that both, the charged and neutral ThT analogues, bind to multiple binding sites. However, even though the fits showed promising χ^2 values, especially for the charged dyes, the K_D values calculated from heterogeneous ligand fits were inconsistent when comparing the K_D values from runs of the same dye using different chips (cf. errors stated in Table 4.7). Thus there is some uncertainty associated with these results. The main reasons for the difficulty in modelling the dye-amyloid interaction with a kinetic approach arise from the high heterogeneity of the αSyn aggregates, the undefinable number of binding sites and the relative low affinity. It is also stated in the literature, that "because of the difficulties associated with obtaining definitive kinetic data on the BIAcore, equilibrium binding analysis is more reliable" [227]. Consequently, for further discussions only the binding affinities obtained through equilibrium binding analysis (Figure 4.13) are considered.

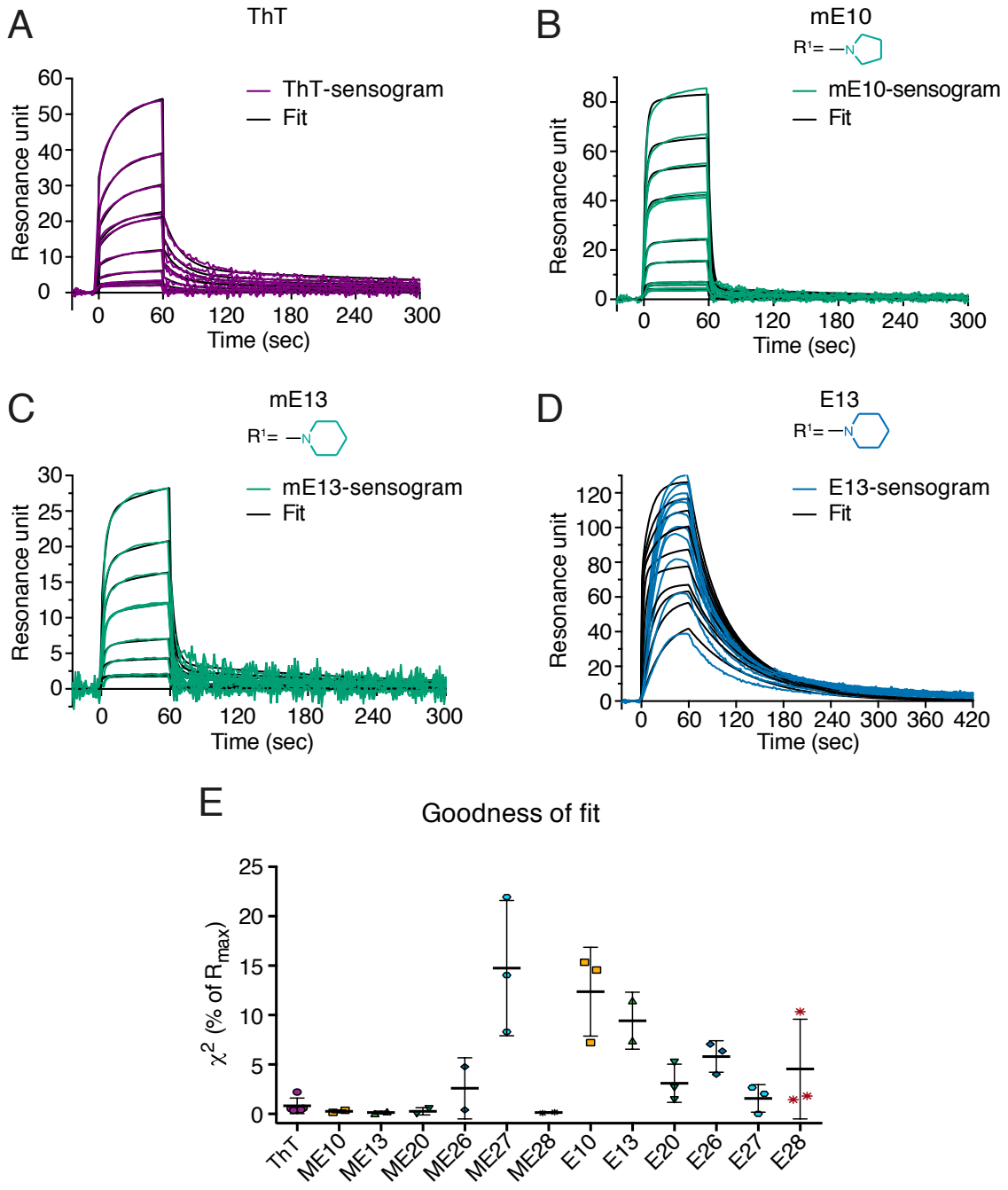

Figure 4.14 Representative SPR sensograms obtained from SPR experiments of A) ThT, B) mE10, C) mE13 and D) E13 binding to immobilised αSyn aggregates on a gold surface. E) Goodness of heterogeneous ligand fit. Error bars are represented as standard deviations of the χ^2 values obtained from fitting 3 independent SPR measurements using separately prepared dye solutions and different gold chips with immobilised αSyn aggregates. 2.8 μM αSyn aggregate solution was used for immobilisation; the dyes were tested at 11 different concentrations ranging from 0.1 μM to 30 μM.

Table 4.7 Binding affinities of ThT, mE and E derivatives towards immobilised αSyn aggregates on a gold surface obtained by SPR measurements.

Dye	ThT	mE26	mE10	mE13	mE28	mE20	mE27
$K_{D,Aff}$[1](μM)	79.4 ± 6.1	72.3 ± 6.7	38.1 ± 2.3	118 ± 23.4	78.7 ± 11.8	47.5 ± 4.9	64.2 ± 5.8
$K_{D1,Kin}$[2](μM)	7.55 ± 5.4	1.94 ± 2.7	11.9 ± 17.3	26.6 ± 22.5	0.9 ± 1.1	0.3 ± 0.1	2.9 ± 4.9
$K_{D2,Kin}$[2](μM)	90.2 ± 81.4	21.2 ± 29.8	143 ± 148	513 ± 136	776 ± 793	23.2 ± 18.5	8.5 ± 7.5

Dye	ThT	E26	E10	E13	E28	E20	E27
$K_{D1,Aff}$[3](μM)	79.4 ± 6.1	0.33 ± 0.03	0.22 ± 0.03	0.45 ± 0.07	0.18 ± 0.04	0.36 ± 0.06	0.10 ± 0.23
$K_{D2,Aff}$[3](μM)		-[4]	-[4]	-[4]	242 ± 451	65.0 ± 22.2	37.6 ± 6.0
$K_{D1,Kin}$ (μM)	7.55 ± 5.4	0.3 ± 0.02	0.1 ± 0.00	0.2 ± 0.02	0.7 ± 0.9	0.3 ± 0.08	7.1 ± 7.1
$K_{D2,Kin}$ (μM)	90.2 ± 81.4	39.5 ± 6.3	27.2 ± 9.7	27.4 ± 2.6	54.9 ± 16.3	23.2 ± 18.5	5330 ± 9188

[1] $K_{D,Aff}$ states the K_D value obtained by one-site specific binding fit of the equilibrium binding affinity curves.

[2] $K_{D1,Kin}$ states the K_D value of the stronger binding site, and $K_{D2,Kin}$ the K_D value of the weaker binding site obtained by heterogenous-ligand fit of the kinetic SPR curves.

[3] $K_{D1,Aff}$ states the K_D value of the stronger binding site, and $K_{D2,Aff}$ the K_D value of the weaker binding site obtained by two-site specific binding fit of the equilibrium binding affinity curves.

[4] Value too large.

Taken together, the results from the different binding studies, the neutral derivatives showed more than 10-fold higher binding affinities than ThT and their charged equivalents. Both, fluorescence based competition assay as well as SPR measurements reinforce the assumption of the presence of multiple binding sites on amyloid aggregates, of which not all trigger a fluorescence response. Among the charged dyes, mE10 possessed the highest binding affinity regardless of the method used.

Projecting the knowledge gained about the binding characteristics of the dyes onto the results from the previous photophysical quantifications, reveals a linear dependency between the binding affinity and the quantum yield in the presence of αSyn for the charged mE derivatives: a weaker binding resulted in a lower quantum yield. There was no correlation between the optical and binding properties observed for the E derivatives, which further affirms the occupation of different binding sites by the neutral and charged ThT analogous.

Interestingly, mE10 showed overall superior properties when compared to ThT and the other dyes: Its brightness in the presence of amyloid was ∼5-fold higher than the brightness of ThT and fluorescence titrations indicated a 7-fold improvement in its binding capabilities compared to ThT.

Monitoring Aggregation Kinetics

The comprehension of the aggregation process of amyloid proteins is a crucial requirement for the understanding of the diseases development.

All data obtained so far, indicated that mE10 exhibits improved features as amyloid stain compared to ThT. Hence, it was next tested whether mE10 can be used to monitor the aggregation process of amyloid proteins. First, bulk kinetic measurements of recombinant αSyn protein aggregation were performed with mE10 as the stain. ThT, the gold standard for monitoring amyloid fibril formation, and Nile red were chosen as positive controls. Nile red has been reported to bind earlier aggregates than ThT and thus should help to investigate the ability of mE10 to detect earlier aggregates [195].

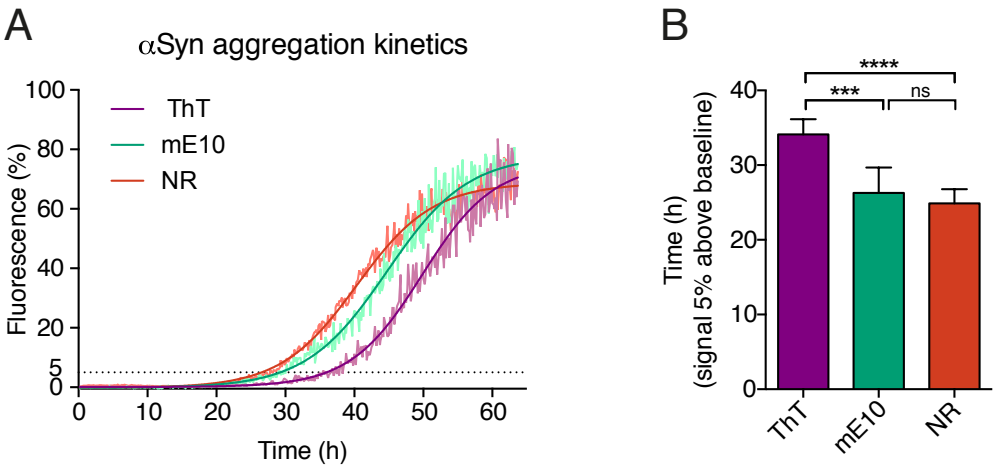

Figure 4.15 A) Kinetics of αSyn amyloid fibril formation (70 μM) monitored by mE10 (18 μM), ThT (18 μM) and Nile red (1 μM). The solid lines indicates the fitted sigmoidal growth curve, the lighter lines the averaged values obtained from minimum 7 independent αSyn aggregations. B) Bar graph indicating the time points, when the average fluorescence signal was 5% above the baseline signal. Error bars are represented as standard deviations of minimum 7 independent αSyn aggregations. Statistical significance was assessed by unpaired. two-tailed t-test; $****p < 0.0001$; $***p = 0.0003$.

αSyn amyloid fibril formation followed a sigmoidal growth curve where a 15-20 h lag phase was observed by mE10 and Nile red before a fluorescence change was detected (Figure 4.15A). For ThT, the lag phase appeared longer with 20-30 h. A clear signal, whose intensity was 5% above the baseline signal, was reached at 26.28 ± 1.4 h for mE10, at 24.89 ± 0.6 h for Nile red and 34.13 ± 0.8 h for ThT (Figure 4.15B). This data indicated that mE10 was able to detect aggregate formation significantly early than ThT, similar to the detection limit of Nile red.

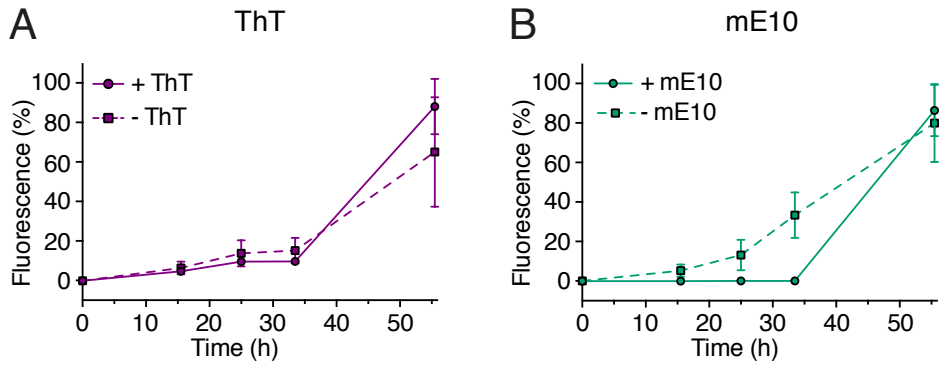

Figure 4.16 αSyn inhibition assay. The aggregation process of αSyn (70 μM) was monitored with and without A) ThT (18 μM) or B) mE10 (18 μM) being present to investigate the influence of the dyes toward aggregate formation. Error bars are represented as standard deviations of 3 independent aggregations.

The aggregation assay was performed whilst the dyes were present. Previously, it has been shown that the presence of dyes can influence the aggregation kinetics. Thus, it was necessary to examine the inhibitory effect on the aggregation of αSyn of mE10 in comparison to ThT to exclude that the earlier fluorescence response of mE10 is not caused by different abilities of mE10 and ThT to inhibit the aggregation. To test the inhibitory properties of mE10 and ThT, αSyn was aggregated under the same standard aggregation conditions for 55 h alone or in the presence of mE10 or ThT. At different time points of the aggregation process, aliquots were taken and imaged by bulk fluorescence measurements. Neither dye prevented the formation of fibrils at the concentration being used (Figure 4.16). However, mE10 seemed to have a stronger, slightly inhibitory effect on the formation of fibrils than ThT, which increases the emphasis on the ability of mE10 to detect even earlier aggregation species in the case of recombinant αSyn.

Having demonstrated that mE10 is able to report on earlier aggregation events of αSyn, it was then questioned if mE10 outperforms ThT in monitoring the aggregation process of other amyloid proteins. Thus, bulk kinetic measurements of synthetic Aβ42 protein aggregation were performed with mE10 and ThT. Aβ42 is deposited early and selectively in the senile plaques of Alzheimer′s disease and hence directly related to the pathogenesis [228].

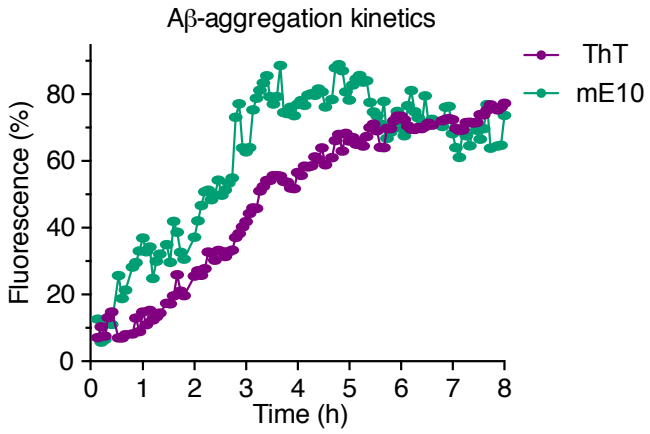

Figure 4.17 Kinetics of Aβ amyloid fibril formation (4 μM) monitored by 10 μM mE10 and ThT. The graph shows the average values of minimum 3 different aggregations.

The Aβ42 protein is known to exhibit a fast kinetic profile in comparison to αSyn, with a short lag phase between 1 - 2 h when measured in bulk with ThT [229]. The kinetic curve obtained with ThT was in accordance with these reports and did reveal a lag phase of $\sim$1 h with a plateau reached at $\sim$6 h. In comparison to this, nearly no lag phase was observed with mE10 and the plateau phase was reached after 3 - 3.5 h. These results further strengthened the assumption that mE10 is a promising candidate as new fluorescence probe for the detection of early oligomeric species with high sensitivity across different amyloid proteins.

Single Aggregate Fluorescence Anisotropy Imaging

Amyloid aggregates possess a large diversity in respect to their size, structure and formation mechanism [230]. Bulk measurements are able to characterise mE10 in respect to the average features of these heterogeneous species but to better understand the fundamentals behind this superior performance on a structural level, further analysis of the binding and fluorescence response on a single aggregate level is needed. Previously, high resolution fluorescence experiments have been able to investigate *in vitro* the structural changes in individual oligomers formed during the aggregation process. The results of these studies indicated a structural uniformity present in fibrils and a structural rearrangement of the aggregates before growing into these ordered fibrillar structures [188, 231, 232]. During the rearrangement and fibril growth the β-sheet content and the structural order increases.

ThT is thought to bind preferentially into the channel motif on the surface of the β-sheets with its long axis parallel to the long axis of the fibril (cf. section 4.1.3) [200]. Varela et al have previously provided evidence to reinforce this assumption of axial-specific binding

by using fluorescence anisotropy measurements combined with a single-aggregate imaging technology [231].

Within their set-up, a rotating polariser was placed between the tube lens and the dichroic of a total internal fluorescence microscopy (TIRF) arrangement (Figure 4.18), which enabled them to examine fluorescence specific to different polarisation states. When single αSyn fibrils stained with ThT were imaged under these conditions, the detected fluorescence intensity varied in a sinusoidal way as the polariser rotated resulting in a maximum when the polariser and the long axis of the fibril were aligned. As fluorophores that bind in a defined orientation, emit a highly polarised fluorescence, this result indicated that ThT is predominantly aligned with the axis of the αSyn fibril.

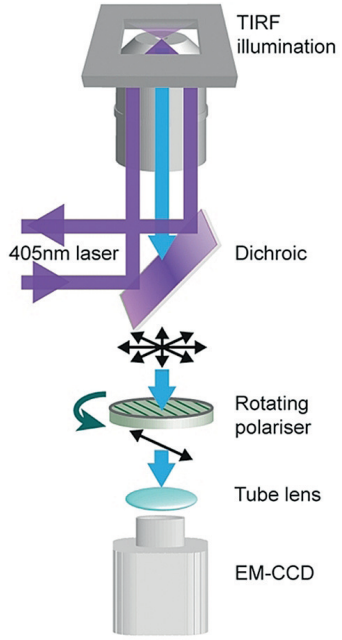

Figure 4.18 Schematic illustration of the fluorescence anisotropy set-up [231].

To find out whether mE10 binds in the same orientation to αSyn fibrils as ThT, fluorescence anisotropy measurements with the same imaging set-up were performed using late-stage recombinant aggregates of αSyn. For both dyes, mE10 and ThT, the fluorescence intensity modulated sinusoidally: a maximum signal intensity was reached when the axis was aligned with the fibril and a minimum intensity appeared when the axis of the polariser was perpendicular to the fibril (Figure 4.19). This was in agreement with previous published results for ThT. As the modulation phase was the same for ThT and mE10, it can be assumed that the two dyes are oriented the same way when bound to fibrils. Additionally, the intensity for both dyes went down to nearly zero when the polariser and the fibril axis were orthogonally placed. This indicates that the majority of dyes responsible for the fluorescence signal are bound in an ordered way, aligned with the axis of the late-stage recombinant αSyn aggregates. If other major fluorescent binding sites with different structural features were present for mE10, the fluorescence intensity of mE10 should manifest a constant offset in the sinusoidal response curve as some of the dye molecules would be binding to these additional binding sites in a different orientation. Taken together, these data indicated that the fluorescence turn-on response of mE10 and ThT is mostly based on the same binding order for the detection of late-stage amyloid aggregates. However, other binding sites might exist, which lead only to a weak or no fluorescence response.

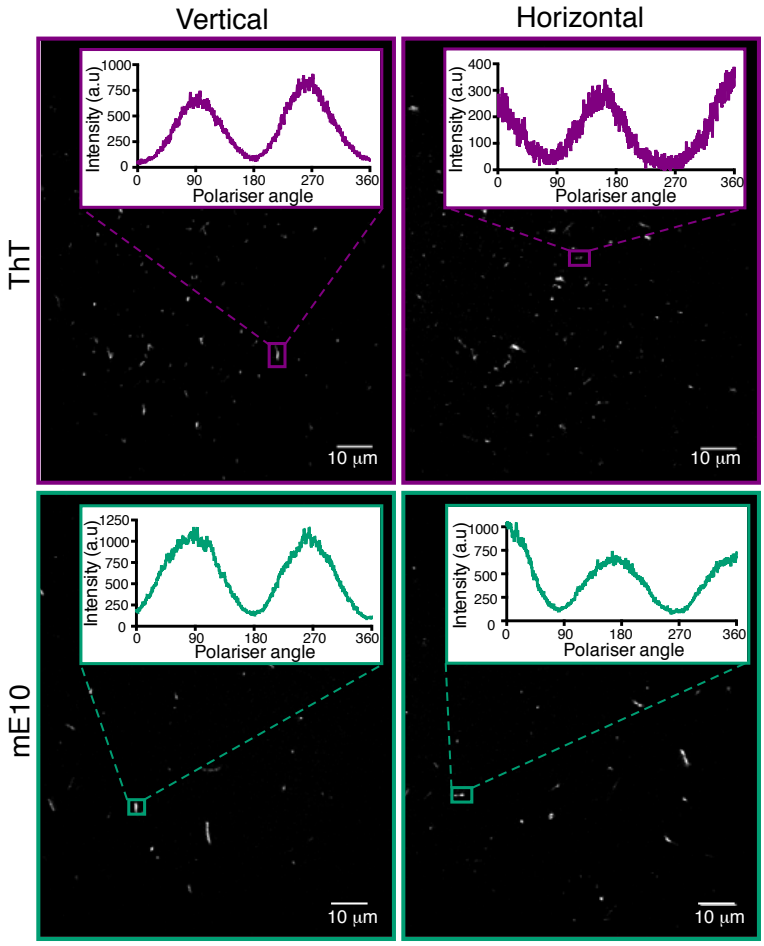

Figure 4.19 Fluorescence anisotropy measurements of late-stage αSyn (7 μM) aggregates with mE10 (5 μM) and ThT (5 μM). The detected fluorescence of mE10 and ThT modulated sinusoidally between a maximum when the polariser axis is aligned with the fibril and a minimum if the axis of the polariser is perpendicular to the fibril axis.

Previous aggregation kinetic measurements demonstrated that mE10 detects earlier aggregation events than ThT in bulk. Knowing now that mE10 and ThT are binding to β-sheet containing aggregates in the same ordered way, the cause for the earlier fluorescence response in bulk was further questioned by analysing the degree of modulation obtained by the anisotropy assay. It was reported, that the amplitude of the fluorescence signal of ThT obtained by fluorescence anisotropy measurements can be used as a measure of the extent of ordered β-sheet structures in individual aggregates [231]. Therefore, the fluorescence was fitted as described in the literature to $y = a\cos(bx + c) + d$, with a being the amplitude of the signal, b the angular frequency (constant, user-defined rotation speed of the polariser), c the phase and d an offset. The "modulation" value was then defined as $2a/(a + d)$. Aggregates that lead to a small modulation value (modulation < 0.5) were categorised as

non-modulating and thought to contain mostly disordered β-sheet units; species with a larger value (modulation > 0.5) are classified as modulating species owning spatially aligned β-sheet content. To apply this concept to deepen the understanding of the superior performance of mE10 above ThT, the fluorescence anisotropy measurements were repeated but with the focus of αSyn species being present in the lag phase of the aggregation process. More precisely, samples were taken from three different aggregation reactions at 6 hours. All the detected aggregates were then analysed separately to measure their degree of modulation (Figure 4.20).

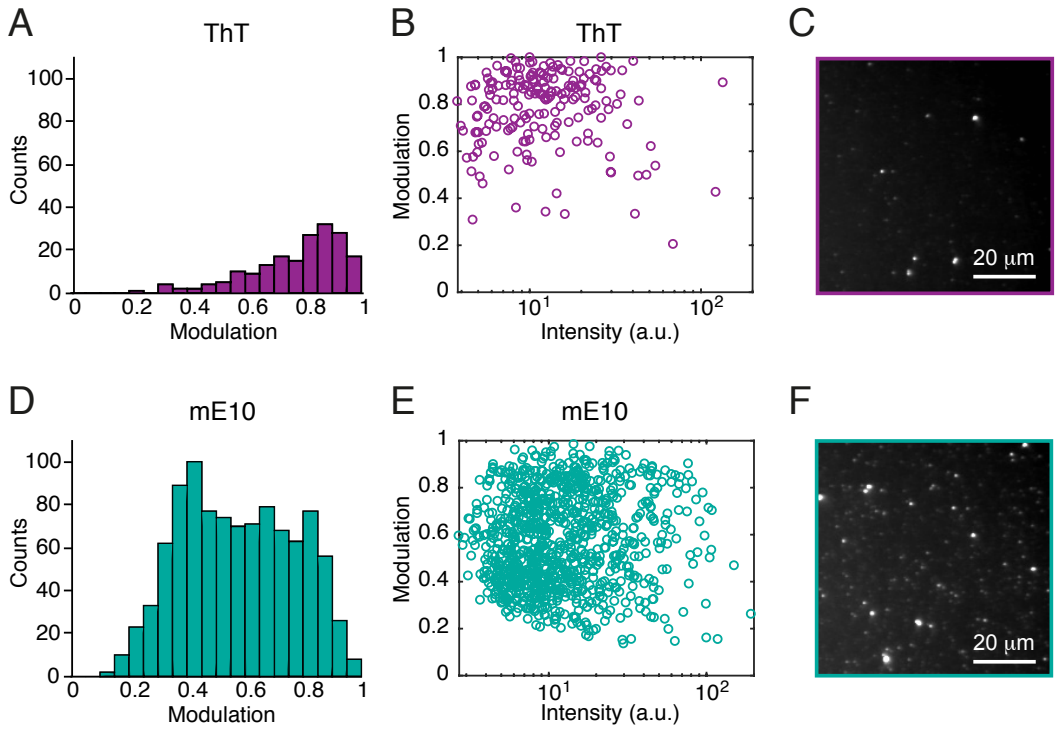

Figure 4.20 Fluorescence anisotropy measurements of αSyn aggregates (7 μM) in the aggregation lag phase with mE10 (5 μM) and ThT (5 μM). The response to anisotropy measurement was measured for the same number of fields of view for both A) ThT and D) mE10. Scatter plots of aggregate intensity vs modulation show that these parameters are not correlated for either B) ThT or E) mE10. Representative fluorescence images are shown for both C) ThT and F) mE10. The dyes were only added for the imaging and not present during the aggregation process.

mE10 showed an overall higher sensitivity in detecting aggregate species in this early stage samples compared to ThT (cf. count values in Figure 4.20A vs D). Furthermore, mE10 was able to detect both, modulating and non modulating species, whereas ThT reported mostly on modulating aggregates. This indicates that mE10 is not only able to detect more advanced aggregates, in which a certain degree of spatially aligned β-sheet content is already

present, but also possesses a high sensitivity towards earlier oligomeric species arising before the structural rearrangement and thus having mostly unordered β-sheet units. Another striking feature was that the degree of modulation was not correlated to the fluorescence signal intensity (Figure 4.20F), which suggests on the one hand, that the number of binding sites remains roughly constant during the structural rearrangement of the aggregates, and on the other hand that the ability of mE10 to detect the different species is not caused by the greater brightness of mE10. This was further investigated by imaging the samples from three different aggregation reactions with mE10 using lower excitation power in order to obtain emitted photon counts comparable to ThT imaging. The lowest laser power chosen was 5 times lower than the one used for ThT and hence should compensate for the $\sim$5-times greater brightness of mE10. By doing so, any effect towards the detection of different species relying on the greater brightness of mE10 should be excluded. Even though the number of detected aggregates ("counts", Figure 4.21) decreased with decreasing laser power, the histogram did continue to manifest the presence of modulating and non-modulating populations, ensuring that the ability of mE10 to detect more of these non-modulating species than ThT is not relying on its increased brightness.

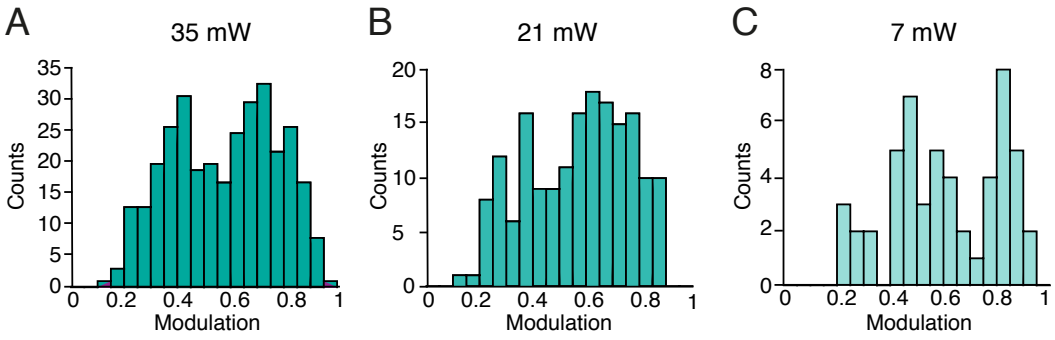

Figure 4.21 Fluorescence anisotropy measurements of αSyn aggregates (7 μM) in the lag phase with mE10 (5 μM) using different laser powers (A) 35 mW, B) 21 mW and C) 7 mW).

To cross validate that the applied definition of non-modulating species describes the signal response of amorphous oligomers, stable oligomers were imaged under the same conditions. Therefore, three different stable oligomeric αSyn species, wild-type (WT), E46K and H50Q, were tested [233]. All three stable oligomers had similar size (average diameter $\sim$20 nm), morphologies and secondary structures validated by dynamic light scattering, transmission electron microscopy and Fourier-transform infrared spectroscopy. Additionally, their β-sheet content was analysed to be between that of monomers and fibrils and arranged in an amorphous way. Thus, imaging these structures with mE10 and ThT should confirm, that a modulation value below 0.5 can be interpreted as signal generated by oligomeric species with

unordered arrangement of β-sheet units. As depicted in Figure 4.22, fluorescence anisotropy measurements of WT, E46K and H50Q resulted in modulation values centred between 0.2 and 0.3. These data confirmed the assumption that modulation values smaller than 0.5 can be correlated to non-modulating species.

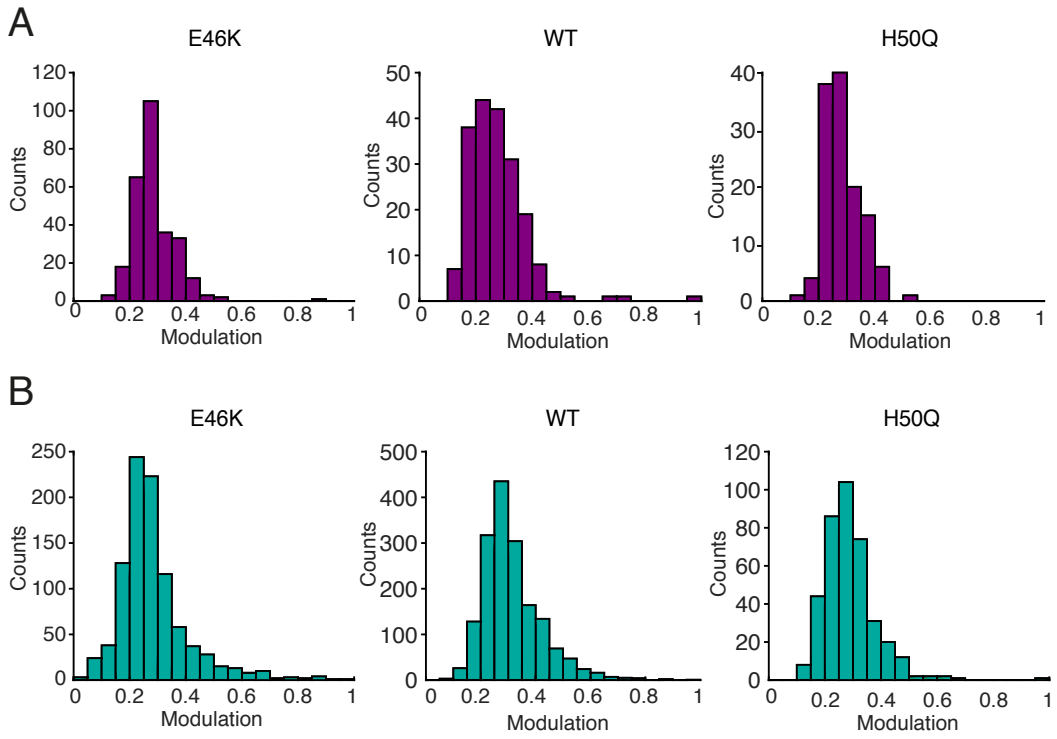

Figure 4.22 Fluorescence anisotropy measurements of stable αSyn oligomers with A) ThT and B) mE10. All individual species detected are plotted against the number of species being detected (counts).

Taken together, all the fluorescence anisotropy measurements indicate that, due to its higher affinity, mE10 is able to detect different and early arising aggregation events of αSyn aggregates, that might have a more disordered arrangement of cross-β motifs. This combined with its higher sensitivity makes mE10 a better αSyn stain than ThT, which might allow the study of the formation of these early species and their role in the pathogenesis of neurodegenerative disorders even at low concentrations in biological samples with higher background.

4.2.2 Improving Sensitivity and Resolution by DNA-PAINT

Another way to overcome the limitations of ThT based on its optical properties is to combine its binding specificity with other dyes featuring a higher extinction coefficient and

quantum yield at a different, preferentially red-shifted, wavelength. Since DNA-PAINT combines the high resolution of single-molecular localisation microscopy with the well known sensitivity and selectivity of DNA nanotechnology, it allows precise, programmable single-molecule imaging with sub-5-nm spatial resolution. Thus, DNA-PAINT methodology was considered as an alternative to development of new fluorescent probes in improving the sensitivity of ThT for small, low concentrated early stage oligomers. Using ThT as the targeting structure ensures β-sheet specificity and, additionally, can elucidate the binding behaviour of ThT. The signal generation is not based on the fluorescence increase of ThT and thus this approach might allow detection of ThT-binding sites, which have been kept in the dark due to their lack in introducing a ThT turn-on response.

To implement this method, a short DNA strand ("docking strand"), that can pair up with the complementary DNA strand linked to a dye ("imager strand"), needs to be attached to ThT without disturbing its binding affinities. The reported ThT dimers showed improved binding affinities and thus embodied a promising starting point [217]. In addition, the linker structure can be designed in a way to provide an easily accessible site for the attachment of the DNA docking strand. A chemically convenient way to conjugate biomolecules, such as DNA, to chemical scaffolds is click-chemistry. The classical click-reaction describes a 1,3-dipolar cycloaddition of azides and alkynes. Azides are chemical inert towards common biological moieties, meaning it does not interfer with any inherent functionalities of DNA, which makes them ideal groups for bio-orthogonal reactions [234]. Furthermore, even if no native peptide bond is formed at the ligation site, the resulting triazole moiety is considered to mimic an amide bond by electronic and steric means and thus should not disturb the binding towards protein aggregates [235].

To rationalise the concept, the linker was composed of two ethylene glycol units connected via a diethylamine bridge. The central amine functionality allowed then the attachment of the alkyne group, which presents the anchor point for the DNA docking strand. To further improve the binding affinity, an uncharged ThT analogue was chosen as targeting moiety. This decision was based on the $\sim$100-times higher binding affinity of the neutral aryl-benzothiazole PiB in comparison to ThT. The linker was attached on position 6 of the benzothiazole core structures as it was shown previously that modifications on this position do not interfere with the ThT - amyloid interaction [236, 217]. The design and synthesis is depicted in Figure 4.23.

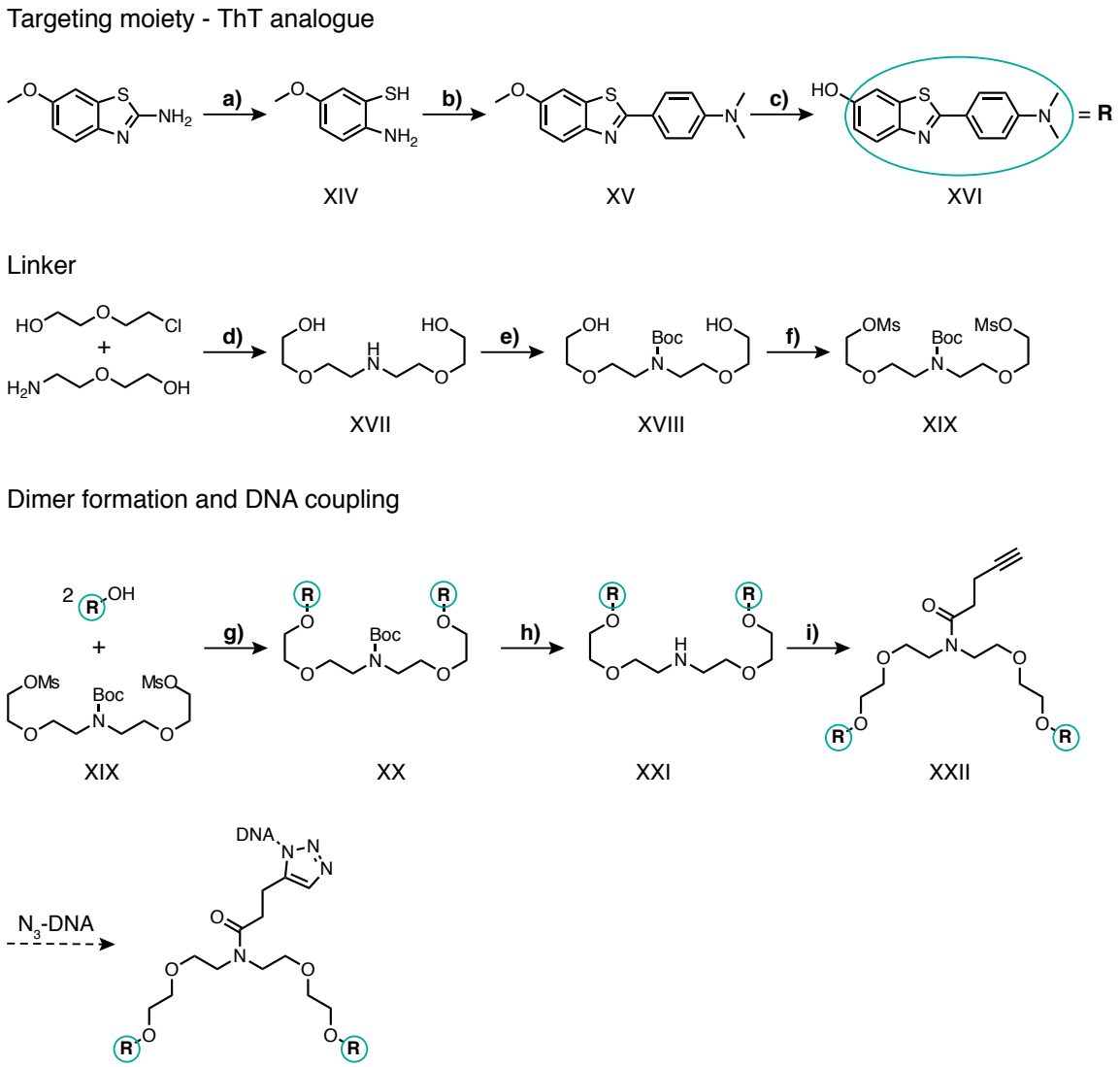

Figure 4.23 Synthesis scheme of DNA-PAINT probe. Reagents and conditions: (a) KOH, ethylene glycol, ΔT. (b) 4-(dimethylamino)benzaldehyde, DMSO, ΔT. (c) BBr_3, DCM. (d) Na_2CO_3, toluene, ΔT. (e) Boc_2O, $NaHCO_3$, THF. (f) MsCl, TEA, DCM. (g) NaH, DMF, ΔT. (h) HCl, MeOH (i) 4-Pentynoic acid, HATU, DIPEA, DMF. (Intermediates **XIX**, **XX** and **XXI** were synthesised with the guidance of previous synthetic routes from our collaborators in the lab of Thomas Neil Snaddon)

The neutral ThT analogue **XVI** was synthesised in 3 steps utilising a published procedure [236, 217]. Briefly, basic hydrolysis of 2-amino-6-methoxybenzothiazole resulted in the corresponding ortho-aminothiophenol **XIV**, which was subsequently reacted with 4-(dimethylamino)benzaldehyde and selectively O-demethylated at position 6 to yield the final aryl-benzothiazole **XVI** bearing a free hydroxy group for further modifications. The linker unit was synthesised starting with 2-(2-chloroethoxy)ethanol and 2-(2-aminoethoxy)ethanol followed by boc-protection of the nitrogen and subsequent activation of the hydroxy func-

tionalities as mesylates. Coupling of the deprotonated 6-hydroxy aryl-benzothiazole **XVI** to the dimesylated linker unit **XIX** and boc-deprotection of the linker nitrogen resulted in the ThT analogue dimer **XXI** carrying a free amine group, which was then used to incorporate the alkyne functionality via amide formation with 4-pentynoic acid.

Having successfully synthesised the dimeric ThT framework with the terminal alkyne group, the next step was to attach the DNA docking strand to it. As the docking strand, an 11 base pair long oligonucleotide with the sequence XTATACATCTA with X = 5'azidodT was chosen (MW = 3315 g/mol) as this sequence was shown to provide good blinking kinetics [218]. However, the sequence can readily be varied to tune the binding duration and thus the blinking kinetics to optimal conditions needed for different samples and dyes. The azide-DNA strand was aimed to be attached by simple click chemistry followed by size exclusion chromatography and LCMS validation. The general procedure was as follows: the azide DNA and alkyne compound were dissolved separately and degassed. The catalyst solution was prepared, degassed, added to the alkyne solution and the mixture was then degassed again. The mixture of catalyst and alkyne was added to the azide DNA solution, the reaction mixture was degassed and kept under shaking throughout the reaction. Different procedures have been reported in the literature for click reactions using oligonucleotides. A common approach is to use 1.1 eq. alkyne species, 1 eq. azide compound, a large excess of reducing agent (in general Na-ascorbate, 50 - 200 eq.) and $CuSO_4$ (50 - 70 eq.), and 5 eq. of Cu-stabilising ligand (e.g. TBTA, THPTA) [237–239]. The solvent systems used in the literature were adopted according to the solubility of the compounds and ranged from buffer to mixtures of organic solvent/H_2O/^{t}BuOH (3:1:1, v/v/v). As **XXII** was not soluble in aqueous solutions, DMSO was added as organic solvent to the reaction to ensure solubility of all compounds. To start with, the procedures described in the literature were applied using 1.1 eq. **XXII**, 1 eq. N_3-DNA, 50 eq. $CuSO_4$, 50 eq. Na-ascorbate as reducing agent and 5 eq. TBTA as Cu-stabilising ligand. Different variations of these "standard conditions" have been tried through changing:

1. reaction time: 1 h, 3 h, 7 h
2. reaction temperature: 25 °C, 37 °C, 45 °C, 60 °C
3. solvent system: 7:3 H_2O:DMSO, 1:1 H_2O:DMSO, 1:2 H_2O:DMSO, 12:7:21 H_2O:DMSO:^{t}BuOH
4. Cu-stabilising ligand: TBTA to THPTA
5. Cu(II): decreased $CuSO_4$ concentration (10 eq.); using $Cu(OAc)_2$ as Cu(II) compound.
6. Cu(I): using Cu(I) salts, CuBr and CuI, instead of Cu(II)
7. Alkyne equivalents: increased **XXII** concentration (10 eq., 50 eq)

Table 4.8 displays some of the conditions tried. Unfortunately, none of these approaches succeeded as either starting material or unspecific side product (mass increase compared to starting material: 98.02 g/mol) were isolated and identified by LCMS. As the work was carried out in small scales (2.25 μg N_3-DNA) the side product was not further analysed. To investigate the cause of the unspecific side product formation, the reactions were repeated with pentyonic acid instead of **XXII** (Figure 4.24). However, the same side product was obtained. Thus, the N_3-DNA was incubated without the alkyne compound in the presence of 50 eq. $CuSO_4$, 50 eq. Na-ascorbate and 5 eq. THPTA. This lead to the formation of the same side product, indicating unspecific adduct formation of the N_3-DNA. As the addition of a base in (DNA-)click chemistry was reported in the literature [240, 241] to accelerates the reaction rate, it was next investigated if the presence of a base (0.3 eq. DIPEA) or the use of buffer (66 mM TEA-AA buffer) instead of water might firstly increase the reactivity of the alkyne compound and secondly prevents the formation of this side product. This attempt also resulted in the formation of the side product. The current focus is placed on exploring different conditions to click other azides to compound **XXII** and if successful, the optimised conditions will then be tried with different azide-DNA strands.

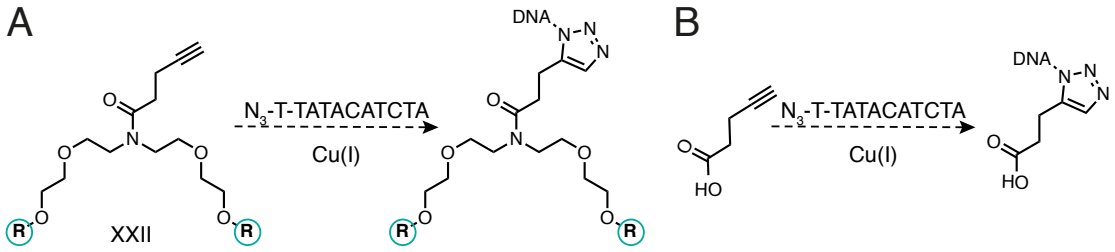

Figure 4.24 DNA-click reaction was tried with A) compound XXII and B) pent-4-ynoic acid.

Table 4.8 Exemplary conditions tried for DNA click chemistry

XXII	Cu-catalyst	Cu-ligand	Solvent	Reaction time [h]	Temp. [°C]	Others
1.1 eq.	$CuSO_4$ (50 eq.)	THPTA (5 eq.)	1:1 H_2O:DMSO	7	37	
50 eq.	$CuSO_4$ (50 eq.)	THPTA (5 eq.)	1:1 H_2O:DMSO	5	45	
1.1 eq.	$CuSO_4$ (10 eq.)	THPTA (5 eq.)	1:1 H_2O:DMSO	5	60	
1.1 eq.	$CuSO_4$ (50 eq.)	TBTA (5 eq.)	1:1 H_2O:DMSO	7	37	
10 eq.	$CuSO_4$ (50 eq.)	TBTA (5 eq.)	1:1 H_2O:DMSO	5	45	
1.1 eq.	$CuSO_4$ (50 eq.)	THPTA (5 eq.)	12:7:21 H_2O:DMSO:^{t}BuOH	5	45	
1.1 eq.	$CuSO_4$ (50 eq.)	THPTA (5 eq.)	12:7:21 H_2O:DMSO:^{t}BuOH	5	45	0.3 eq. DIPEA
1.1 eq.	$CuSO_4$ (50 eq.)	THPTA (5 eq.)	12:7:21 buffer:DMSO:^{t}BuOH	5	45	66 mM TEA-AA buffer
1.1 eq.	$Cu(OAc)_2$ (50 eq.)	THPTA (5 eq.)	12:7:21 H_2O:DMSO:^{t}BuOH	5	45	
1.1 eq.	CuBr (50 eq.)	THPTA (5 eq.)	12:7:21 H_2O:DMSO:^{t}BuOH	5	45	

However, the synthesised neutral ThT-dimer bearing an alkyne functionality cannot only be exploit for DNA-PAINT but also for attaching further targeting structures or other dyes to the framework. Furthermore, by varying the linker length and/or composition, further improvement of the binding affinity might be possible.

4.3 Summary and Conclusions

The comprehension of protein misfolding and formation of aggregates is a crucial requirement to expand our understanding of several neurodegenerative disorders, such as Parkinson′s and Alzheimer′s disease. Despite the success of ThT, the current most common fluorescent dye used for the detection of amyloid fibrils, it displays significant limitations. The most prominent ones are the selective labelling of only amyloid species present in the later stage of the aggregation process and its rather low quantum yield. As small soluble oligomeric species of misfolded proteins have recently been described as critical to the pathogenesis of neurodegenerative disorders, the inability of ThT to detect and assess these in biological samples represents a major limitation, hampering further research.

To address this unmet need, the goal of this chapter was to find fluorescence probes with improved optical and binding properties and higher sensitivity than ThT, which allow the detection and characterisation of earlier arising aggregation events at low concentrations. To pursue this objective two approaches were discussed: First, improving the photophysical properties and binding affinity/selectivity of ThT by modifying the substituents on the aryl nitrogen; secondly, utilising emerging high-resolution techniques, such as DNA-PAINT, and combining these with multivalent ThT-based targeting structures to merge the specific amyloid targeting ability of ThT with dyes with improved optical properties.

In search of structural modifications to improve ThT as an amyloid specific fluorescence probe, a library of charged and neutral ThT-derivatives were examined in respect to their photophysical properties and binding affinities. As the cationic (mE) and neutral (E) derivatives, were - apart from the methyl group on the benzothiazole nitrogen - structurally identical, this allowed further investigation of the importance of this structural feature, which differentiates also ThT and PiB. All structural modifications made, did not impact the ability of the dyes to act as molecular rotors. This was manifested by a low quantum yield in low viscosity solvents and a significant increase in fluorescence when surrounded by an environment with higher viscosity or bound to fibrils.

The E derivatives exhibited a much smaller extinction coefficient and fluorescence increase upon binding to αSyn aggregates compared to ThT making them poorly suitable

for fluorescence imaging. The cationic mE equivalents, by contrast, showed a fluorescence response suitable for imaging applications, even though the signal increase in the bound state was less than that achieved by ThT. As for probes acting as molecular rotors, the optical properties go hand in hand with their environment and thus their binding ability, different methods were exploited to validate the binding affinities of the mE and E derivatives towards recombinant αSyn aggregates. Fluorescence based assays as well as SPR measurements manifested a 1-2 orders of magnitude higher binding affinity of the neutral dyes as opposed to their charged analogues and ThT.

Outstanding throughout all optical and binding assay was the charged derivative mE10. The conversion of the dimethyl amino moiety into a pyrrolidine group generated a more restrained benzothiazole salt with increased lipophilicity improving the brightness upon binding to αSyn aggregates by 5-fold and enhancing the binding affinity compared to ThT. These improved proprieties enabled the detection of early oligomeric species with higher sensitivity in bulk aggregation kinetic assays as well as on a single aggregate level when looking at early stage αSyn aggregates. Furthermore, mE10 was able to sense different αSyn species in these early stage samples by quantifying the degree of modulation of individual aggregates. Following on from here, further characterisation should be carried out including monitoring the aggregation kinetics on a single aggregate level, exploring the detection limit by using single-aggregate techniques and evaluating the ability of mE10 to be used for high resolution single molecule imaging. Simultaneously, additional validation using other amyloid proteins should be performed. If this work yields positive results additional characterisation in biological samples such as human cerebrospinal fluid of Parkinson′s disease patients might be executed. However, taken all together, the results suggest that mE10 is a promising new fluorescence probe with improved photophysical and binding properties, which might allow the detection and characterisation of early oligomeric species and thus shine light onto their role in the pathogenesis of neurodegenerative disorders.

Combining new, high-affinity ThT-analogues with super-resolution microscopy using DNA-PAINT is a promising approach as it allows to finely tune the binding affinities of the ThT-derivatives without being considerate of influencing the optical properties of ThT. Thus, the focus of the future work of this project is divided into two parts. Further click-chemistry conditions including different DNA strands as well as other ways of covalently linking the docking strand onto the ThT-dimer should be explored. Should this succeed, subsequent DNA-PAINT imaging should be performed to prove the concept. Simultaneously, different linker length, linker compositions and topologies should be evaluated to find multivalent ThT-probes with high affinities towards protein aggregates. Additionally, it might be worth

trying to incorporate mE10 as targeting structure, as it shows increased binding affinity and, assumed from previous results, might additionally sense early stage amorphous oligomers. Similarly, integrating one charged dye (e.g. mE10) and one neutral dye (e.g. E10) as targeting structure might even allow to bind to two different binding sites and thus allowing the read out of different structural features of aggregates in different stages.

This project is ongoing and the group of Prof. C.A. Hunter is at the moment successfully developing and evaluating different multivalent ThT-structures. Thus, when combining all the different promising results it might be possible to find new amyloid probes with high sensitivity, selectivity to oligomeric structures and specificity towards the different pathological proteins (e.g. αSyn vs Aβ).

4.4 Material and Methods

4.4.1 Chemical Synthesis

General experimental details are the same as stated in Chapter 2, Materials and Methods 2.4.1

Synthesis of mE and E Derivatives

The synthesis of the mE and E derivatives was performed in the lab of T.N. Snaddon and adapted after a literature procedure [242]. An overview of the synthetic route including reactants and conditions is shown in Figure 4.25.

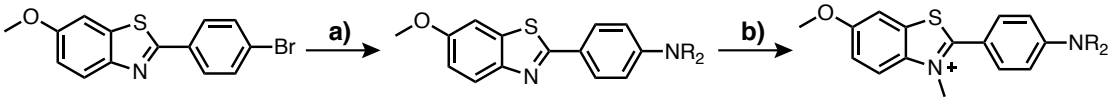

Figure 4.25 Synthesis scheme of mE and E derivatives. Reagents and conditions: (a) $Pd_2(dba)_3$ (1 mol%), BINAP (3 mol%), NaO*t*Bu (1.4 eq.), toluene, 80 °C, 18 h. (b) Methyl iodide (excess), PhCl, 110 °C, 18 h.

Synthesis for the DNA-PAINT Approach

Intermediates **XIV**, **XV** and **XVI** were synthesised following a previously reported procedures, the analytical data corresponded [236, 217]. Compounds **XIX**, **XX** and **XXI** were synthesised with the guidance of previous synthesis routes from our collaborators in the lab of Thomas Neil Snaddon.

Synthesis of XVII

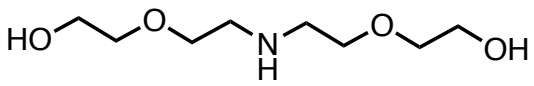

11.2 g (106.5 mmol) of 2-(2-Aminoethoxy)ethanol, 3 g (28.3 mmol) Na_2CO_3 and 60 mL toluene were refluxed for 5 min. 3.3 g (26.5 mmol) β-chloroethoxyethanol in 6 mL toluene was then added dropwise and the resulting solution was refluxed for 48 hours using a Dean-Stark apparatus. After cooling down to room temperature, the reaction was filtered and concentration in vacuo. The concentrate was then purified using a Kugelrohr apparatus. The desired product was obtained at 8 mbar and 270 °C as colorless oil (4.01 g, 20.74 mmol, 78%).

HRMS: m/z calculated for [M+H] = 194.13, found m/z = 194.1181.
^{1}H-NMR: (400 MHz, $CDCl_3$) δ [ppm] = 3.70 (t,$J_{H,H}$ = 4.7 Hz, 4H), 3.55 (t, $J_{H,H}$ = 4.7 Hz, 6H), 3.51 (t, $J_{H,H}$ = 5.4 Hz, 4H), 2.85 (t, $J_{H,H}$ = 5.4 Hz, 4H).

Synthesis of XVIII

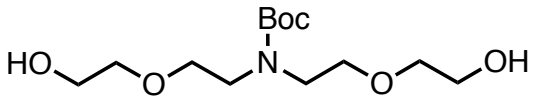

2 g (10.36 mmol) **XVII** and 4.2 g (50 mmol) $NaHCO_3$ were dissolved in 11 mL dry THF and cooled down to 0 °C. 2.7 g (12.4 mmol) Boc_2O was added and the reaction mixture was stirred at room temperature for 8 h. After concentration in vacuo, the residue was partitioned between EtOAc (10 mL) and H_2O (10 mL) and separated. The organic layer was washed once with brine and the combined aqueous layers were then re-extracted with EtOAc (3 x 10 mL). The combined organic fractions, were dried over anhydrous $MgSO_4$, filtered, and concentrated. The residue was purified by flash column chromatography (silica, hexane / (6:1 EtOAc:EtOH, gradient). The product was obtained as slightly yellow oil (2.53 g, 8.6 mmol, 83.2%).

HRMS: m/z calculated for [M+Na] = 316.1737, found m/z = 316.1732 matched M+Na.
^{1}H-NMR: (400 MHz, $CDCl_3$) δ [ppm] = 3.69 (m, 4H), 3.65 (bs, 4H), 3.57 (m, 4H), 3.45 (bs, 4H), 2.87 (t, $J_{H,H}$ = 5 Hz, 2H), 1.46 (s, 9H).

^{13}C NMR: (101 MHz, $CDCl_3$) δ [ppm] = 160.58, 84.74, 81.99, 77.16, 74.34, 66.46, 52.92, 33.21.

Synthesis of XIX

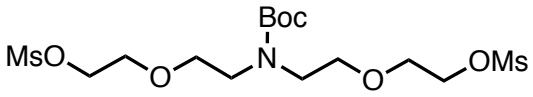

1.0 g (3.4 mmol) **XVIII** and 1.2 g (11.9 mmol) TEA were dissolved in 7 mL dry DCM and cooled down to 0 °C. 974 mg (8.5 mmol) methanesulfonyl chloride in 3 mL dry DCM was added dropwise and the reaction mixture was stirred at room temperature over night. 1N HCl (30 mL) was added while stirring and the mixture was extracted with DCM (4 x 25 mL). The combined organic layers were washed with $NaHCO_3$ solution, dried over $MgSO_4$, filtered, and concentrated to give the desired product as colourless oil (1.1 g, 2.4 mmol, 72%).

HRMS: m/z calculated for [M] = 472.1287, found m/z = 472.1284 matched M+Na.
^{1}H-NMR: (400 MHz, $CDCl_3$) δ [ppm] = 4.35 (m, 4H), 3.71 (m, 4H), 3.59 (m, 4H), 3.44 (m, 4H), 3.05 (s, 6H), 1.45 (s, 9H).

Synthesis of XX

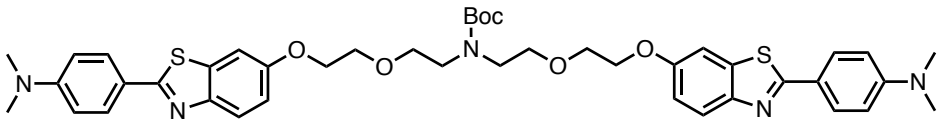

NaH (60% in mineral oil, 19mg, 0.44 mmol) was added to a solution of **XVI** (110 mg, 0.4 mmol) in dry DMF (4 mL). The reaction mixture was stirred at room temperature for 1 h before **XIX** (90 mg, 0.2 mmol) in 1 mL dry DMF was added. The reaction was then stirred at 80 °C for 18 h. After cooling down to room temperature, 15 mL H_2O was added and extracted with EtOAc (3 x 20 mL). The combined organic layers were washed with brine (1 x 15 mL), dried over $MgSO_4$, filtered, and concentrated to give the desired product as white solid (57.2 mg, 0.07 mmol, 35%).

HRMS: m/z calculated for [M+H] = 798.33, found m/z = 798.3370.
^{1}H-NMR: (400 MHz, $CDCl_3$) δ [ppm] = 7.95-7.87 (m, 6H), 7.34 (m, 2H), 7.05 (dd, $J_{H,H}$ = 9, 2.5 Hz, 2H), 6.76 (d, $J_{H,H}$ = 9 Hz, 4H), 3.73-3.68 (m, 4H), 3.67-3.56 (m, 4H), 3.52-3.43 (m, 4H), 3.07 (s, 12H), 1.48 (s, 9H).

^{13}C NMR: (101 MHz, $CDCl_3$) δ [ppm] = 166.6, 156.2, 155.5, 151.9, 149.1, 135.7, 128.5, 122.7, 115.4, 111.7, 105.4, 79.7, 70.1, 69.5, 69.4, 68.1, 48.0, 47.8, 40.2, 28.5.

Synthesis of XXI

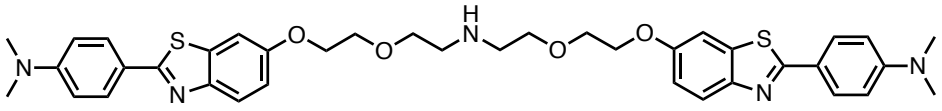

To 22 mg (0.028 mmol) **XX** was added 1.2 mL of 4M HCl in MeOH and the solution was stirred at room temperature for 1 h. The reaction was quenched with 3.3 mL 3M NaOH and the resulting suspension was extracted with EtOAc (3 x 3 mL), dried over $MgSO_4$, filtered, and concentrated to yield the desired product as white solid (16.8 mg , 0.024 mmol, 86%)

HRMS: m/z calculated for [M+H] = 697.28, found m/z = 697.2880.
^{1}H-NMR: (400 MHz, $CDCl_3$) δ [ppm] = 7.88 (d, $J_{H,H}$ = 9 Hz, 4H), 7.84 (d, $J_{H,H}$ = 9 Hz, 2H), 7.29 (d, $J_{H,H}$ = 2.5 Hz, 2H), 7.04 (dd, $J_{H,H}$ = 9, 2.5 Hz, 2H), 3.73-3.68 (m, 4H), 6.72 (d, $J_{H,H}$ = 9 Hz, 4H), 4.15 (t, $J_{H,H}$ = 5 Hz, 4H), 3.83 (t, $J_{H,H}$ = 5 Hz, 4H), 3.68 (t, $J_{H,H}$ = 5 Hz, 4H), 3.04 (s, 12H), 2.86 (t, $J_{H,H}$ = 5 Hz, 4H).
^{13}C NMR: (101 MHz, $CDCl_3$) δ [ppm] = 166.7, 156.3, 152.0, 149.2, 135.8, 128.6, 122.8, 121.7, 115.5, 111.8, 105.5, 71.0, 69.7, 68.2, 49.4, 40.3, 28.6.

Synthesis of XXII

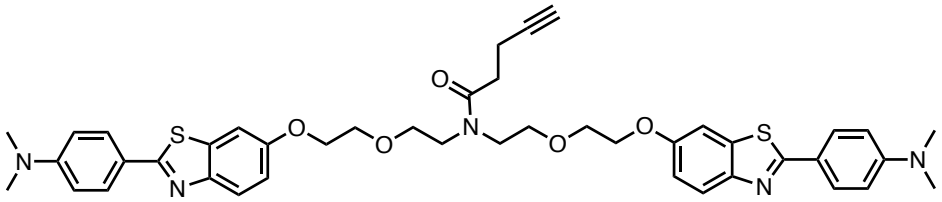

4-Pentynoic acid (6 mg, 0.06 mmol) and HATU (23.3 mg, 0.06 mmol) were dissolved in 1 mL dry DMF and stirred for 10 min at room temperature. 43 mg (0.06 mmol) **XXI** in 1 mL dry DMF was added and after 5 more minutes stirring at room temperature, DIPEA (19.4 mg, 15 mmol) was added. The resulting solution was stirred at room temperature for further 10 h. The reaction mixture was then partitioned between EtOAc and LiCl (5%), the aqueous layer was re-extracted with EtOAc and the combined organic fractions were dried over anhydrous $MgSO_4$, filtered, and concentrated. The residue was purified by flash column

chromatography (silica, DCM:(9:1 DCM:MeOH), gradient). The product was obtained as colourless oil (22.6 mg, 0.029 mmol, 48%).

MS: m/z calculated for [M+H] = 778.30, found m/z = 778.3034.
^{1}H-NMR: (400 MHz, $CDCl_3$) δ [ppm] = 7.86 (ddd, $J_{H,H}$ = 15, 9, 2.0 Hz, 6H), 7.31-7.27 (m, 2H), 7.03 (ddd, $J_{H,H}$ = 9, 4, 3 Hz, 2H), 6.72 (dd, $J_{H,H}$ = 9, 3 Hz, 4H), 4.12 (m, 4H), 3.79 (m, 4H), 3.70 (m, 4H), 3.62 (m, 4H), 3.04 (s, 12H), 2.66 (m, 2H), 2.51 (m, 2H), 1.92 (t, J = 2.5 Hz, 1H).
^{13}C NMR: (101 MHz, $CDCl_3$) δ [ppm] = 171.6, 166.7, 156.24, 156.1, 151.9, 149.1, 135.8, 128.5, 122.7, 121.6, 115.3, 111.7, 105.5, 89.3, 83.7, 69.9, 69.8, 69.6, 69.5, 68.6, 68.1, 68.0, 48.9, 46.7, 40.2, 32.2, 14.57.

Considerations for DNA-click Chemistry

Compound XXII was dissolved in the organic solvent and degassed using argon. N_3-DNA was dissolved in water and degassing was performed through freeze-pump-thaw cycles.

Size exclusion chromatography was performed using Bio-Rad Micro Bio-spin 6 Chromatography columns (Cat.no.732-6200).

Oligomer LC-MS analysiswas performed using a XTerra MS C18 column (2.5μM, 2.1x50 mm), using solvents A (100 mM 1,1,1,3,3,3-hexafluoro-2-propanol, 10 mM NEt_3) and B (MeOH), at a flow-rate of 0.2 mL/min, with a gradient 5%–30% B increasing at 1% per min. The signal was monitored at 260 nm. The identity of the compounds was assessed by ESI-MS with negative polarity in ultra-scan mode. Data was acquired between 1000-2800 m/z.

4.4.2 Preparation of αSynuclein Aggregates

The purification of monomeric wild-type αSyn from Escherichia coli was performed following a published protocol[243].

αSyn aggregates used for photophysical characterisation and binding affinity measurements were generated as described by Buell at al[226]. Briefly, monomeric αSyn was diluted into 50 mM sodium phosphate (pH 7.4) to reach a final concentration between 150 and 300 μM. Samples were incubated at 45 °C for in total 72 h whilst stirring at maximum speed with a Teflon flea. After every 24 h the aggregation reaction was sonicated (3 cycles of 10 sec at 30% power (Branson digital Sonifer, model 250, Branson, St Louis MO, USA). Finally, the aggregation mixture was aliquoted, flash frozen in liquid N_2 and stored at -80 °C till

used. The αSyn concentration stated in the different experiments is reported as the monomer equivalent concentration.

αSyn aggregates used for fluorescence anisotropy measurements were generated by diluting monomeric αSyn into 1x PBS buffer supplemented with with 0.01% NaN_3 to prevent bacterial growth. The solution was then incubated in the dark at 37 °C with constant shaking of 200 rpm for the time stated in the experiment.

4.4.3 Preparation of Synthetic Aβ42

The synthetic Aβ peptide (1-42, here called Aβ42), was purchased from Abcam (beta-Amyloid Peptide (1-42) (human) (ab120301)) and purified as described previously [244]. In short, the Aβ42 peptide was dissolved in 6 M GuHCl, purified with a Superdex 75 10/300 GL column (GE Healthcare Bio-Sciences AB SE-751 84 Uppsala, Sweden) and the centre of the elution peak was used for the experiments. To determine the concentration of the purified peptide, the known absorption at $\lambda = 280$ nm was used ($\varepsilon_{280} = 1490\,\mathrm{L\,mol^{-1}cm^{-1}}$).

4.4.4 Preparation of Dye Stock Solutions

Stock solutions of the different mE and E derivatives as well as ThT (Sigma-Aldrich, T3516) were prepared by dissolving solid into dry dimethyl sulfoxide (DMSO, Sigma Aldrich, 276855) to reach a final concentration of 10 mM. These were aliquoted and stored in the dark at -80 °C till used. Before the experiment, the stock solutions were diluted into filtered (0.02 μm syringe filter, Whatman, 6809-1102) PBS (pH 7.4), sonicated and filtered (0.02 μm syringe filter, Whatman, 6809-1102). For ThT, the final concentration was determined from the absorbance at 412 nm, using an extinction coefficient of 36 000 $\mathrm{M^{-1}cm^{-1}}$.

4.4.5 Photophysical Characterisation

Absorption and fluorescence spectra were recorded at 25 °C using a fluorescence spectrophotometer (Cary Eclipse, Varian) and an UV-VIS spectrophotometer (Cary 300 Bio, Varian). Therefore, samples were placed into Suprasil® quartz cuvettes with a 10 mm path length. Fluorescence and absorption spectra of E, mE dyes and ThT were recorded at various concentrations free in PBS (1x, pH 7.4) and in the presence of 2 μM late stage αSyn aggregates. Each condition was measured with a minimum of 3 separately prepared dye samples. Buffer blanks and blanks of 2μM late stage αSyn aggregates were collected for both fluorescence and absorption spectra and used for background correction. The fluorescence and absorption

measurements in 2-propanol (99.5%, Sigma-Aldrich 278475) were performed at a final concentration of 10 μM.

Photophysical properties, including absorption maxima (λ_{abs}), emission maxima (λ_{em}), Stokes shift, molar extinction coefficient (ε), fluorescence quantum yield (ϕ_{Fl}) and brightness ($B = \varepsilon \cdot \phi_{Fl}$), were determined from bulk absorption and fluorescence measurements using a custom Matlab script. Stokes shifts were calculated as the difference of λ_{em} and λ_{abs}, absorption coefficients were determined from the absorbance of solutions with known concentrations and sample path length using the Beer–Lambert law. The quantum yield of the dyes were calculated by referencing against quinine sulfate (Sigma-Aldrich, Q0132) in 0.1 M H_2SO_4 ($\phi_{Fl} = 0.5$) (see Appendix A.4, Figure A.11 for calibration curve). Discrepancies in absorbency and solvent refractive index were corrected for (cf. 2.4.3) [160].

4.4.6 Fluorescence based Binding Assays

All samples were prepared in low-binding Eppendorf tubes (Eppendorf AG, Hamburg, Germany).

Fluorescence and absorption titrations were recorded at 25 °C using a fluorescence spectrophotometer (Cary Eclipse, Varian) and a Varian Cary 300 Bio UV-VIS spectrophotometer, using standard titration protocols. Typical procedure: 4 μM αSyn dilutions were prepared by dilution of the corresponding amount of stock solution in filtered (0.02 μm syringe filter, Whatman, 6809-1102) PBS 1X. Dye stock solutions were diluted into filtered (0.02 μm syringe filter, Whatman, 6809-1102) PBS 1X to prepare seven solutions with concentrations ranging between 19.5 μM and 1 mM, which were then sonicated carefully. 0.1 mL of the 4 μM αSyn dilution was removed, diluted down to 2 μM, transferred into a Suprasil® quartz cuvette and the fluorescence and absorption spectrum were recorded. Defined volumes of dye dilutions were then added to the same volume of 4 μM αSyn dilutions to avoid dilution of αSyn during the titration. Aliquots of this solution were successively added to the cuvette, the solution was thoroughly mixed and the spectra were recorded after each addition. The same protocol was carried out without the presence of αSyn. Fluorescence spectra of ThT and the mE10 derivatives were acquired with an excitation wavelength of 440-5 nm and emission was collected between 465 nm and 600 nm with an emission slit of 5 nm. For the neutral E derivatives the samples were additionally recorded with an excitation wavelength of 355-5 nm and emission collection between 375 nm and 600 nm. Fluorescence spectra were analysed using a Microsoft Excel spreadsheet to fit the changes in fluorescence intensity

at fixed wavelengths to a 1:1 binding isotherm by optimising the association constant and fluorescence intensity of the free and bound dye using purpose written VBA macros.

The fluorescence competition assays were carried out in a similar way but with different, constant concentrations of ThT (1-15 μM) being present. This implicates that the 4 μM αSyn dilution was supplemented with double the ThT concentration aimed for in the final sample (e.g. in case of a final ThT concentration of 3 μM, the 4 μM αSyn dilution would be supplemented with 6 μM ThT to avoid dilution of αSyn and ThT during the titration). As a control, the same protocol was carried out with a constant ThT concentration in PBS and subsequent addition of solutions of E derivatives. Fluorescence spectra were analysed using a Microsoft Excel spreadsheet to fit the changes in fluorescence intensity at fixed wavelengths to an isotherm that allowed for both ThT and dye binding in competition to the first protein binding site (BS1). The value of $K_{A,ThT}$ (the association constant for ThT binding to the first binding site) was fixed at the value measured by direct titration. For each point in the titration an iterative procedure implemented as VBA macros was used to solve simultaneous equations 1-5 for the concentrations of all of the species present.

(1) $[BS1 \cdot ThT] = K_{A,ThT}[BS1_{free}] \cdot [ThT_{free}]$

(2) $[BS1 \cdot dye] = K_{A,dye}[BS1_{free}] \cdot [dye_{free}]$

(3) $[dye_{total}] = [dye_{free}] + [BS1 \cdot dye]$

(4) $[ThT_{total}] = [ThT_{free}] + [BS1 \cdot ThT]$

(5) $[BS1_{total}] = [BS1_{free}] + [BS1 \cdot dye] + [BS1 \cdot ThT]$

(6) $[I]_{obs} = I(BS1 \cdot ThT) \cdot [BS1 \cdot ThT] + I_0$

Equation 6 was then used to calculate the fluorescence intensity. A simplex optimisation was used to obtain values of $K_{A,dye}$ (and thus $K_{D,dye}$), $[BS1]_{total}$, I(BS1·ThT) and I_0 that provided the best fit to the experimental data. I_0 is the plateau fluorescence intensity due to ThT bound to the second binding site BS2.

4.4.7 Surface Plasmon Resonance Measurements

SPR studies were performed at 25 °C using a Biacore T200 in HBS-EP+ buffer (10 mM HEPES, 150 mM sodium chloride, 3 mM EDTA, and 0.05% v/v surfactant P20 in MQ water; filtered through a vacuum driven 0.22 μm filter system from Millipore) containing 5% v/v DMSO. αSyn, prepared as described prior, were covalently coupled to a Research Grade CM5 sensor chip (BIAcore) via primary amino functionalities of the fibrils using the amine coupling kit provided by BIAcore. For surface coating, αSyn was injected at a concentration

of 2.8 μM in 10 mM sodium acetate buffer (pH 4.0) at a flow rate of 10 μL/min for 12 minutes. Coupling levels ranged from 2146 to 11350 RU. A second flow cell was treated identically including all immobilisation chemistry but without αSyn to function as reference for analysis.

30 μM dye solutions were prepared by dilution 10 M dye stock solutions into down to HBS-EP+ buffer with a final concentration 5% DMSO. The concentration series (30 μM, 20 μM, 15 μM, 10 μM, 5 μM, 2.5 μM, 1 μM, 0.75 μM, 0.5 μM, 0.25 μM, 0.1 μM) was then prepared by further diluting the 30 μM solution.

To correct for the DMSO content in the samples, a solvent correction assay was performed at the beginning and at the end of each measurement set. After stabilisation of the baseline, response units for each dye sample were acquired by using a flow rate of 30 μL/min for 60 seconds. Dissociation time was set to 400 seconds. No further regeneration step was needed. The measurements of each dye concentration series was conducted in a randomised order and the 10 μM sample was measured a second time after the whole concentration series of the dye to prove consistency. In between the measurements of different dyes a 5 μM ThT sample was measured as control sample. The whole SPR measurement set for each dye was at least repeated three times on different flow cells with fresh immobilised αSyn and new prepared concentration series.

All data are solvent corrected and reference subtracted. Equilibrium binding analysis was performed by normalising the obtained binding levels at the equilibrium from each concentration series and averaging the normalised values over the replicates ($n \geq 3$). The averaged values were then plotted as a function of concentration (Figure 4.13). K_D values were obtained with GraphPad Prism 6 by non-linear curve fitting to these values using the equation $Y = B_{max} * X / [K_D + X]$, where Y is the response, X the concentration, B_{max} the maximum specific binding response (same unit as Y) and K_D is the equilibrium binding constant (in the same units as X). Kinetic analysis was performed using the heterogeneous ligand fit provided in the Biacore software.

4.4.8 Measuring Aggregation Kinetics of wild-type αSyn

To study the aggregation kinetics of αSyn, wild-type αSyn monomers were diluted into filtered (0.2 μm syringe filter, Whatman, 6780-1302) PBS (pH 7.4) supplemented with 0.01% NaN_3 and 18 μM ThT, 18 μM mE10 or 1 μM Nile red to reach a final concentration of 70 μM. Each sample was then pipetted into multiple wells of a 96-well, low-binding polyethylene glycol coating plate (Corning 3881, Kennebuck ME, USA) with a clear bottom,

at 100 μL per well. The 96-well plate was sealed with a gas permeable plate seal, placed in a plate reader (CLARIOstar; BMG Labtech, Ortenberg, Germany) and incubated at 37 °C. Fluorescence was measured using excitation and emission filters of 440-10 nm and 490-15 nm for mE10 and ThT, and 520-10 nm (ex) with 660-20 nm (em) for Nile red. Measurements were performed every 10 min for a period of up to 63.5 h. Plates were subjected to double orbital shaking at 200 rpm for 540 sec after each reading.

To investigate the inhibitory effect of mE10 and ThT, wild-type αSyn monomer were diluted into filtered (0.2 μm syringe filter, Whatman, 6780-1302) PBS (pH 7.4) supplemented with 0.01% NaN_3 and divided into 12 aliquots. 3 of the aliquots were supplemented with 18 μM ThT and 3 with 18 μM mE10. The remaining 6 aliquots served as controls. All samples were prepared in low-binding Eppendorf tubes (Eppendorf AG, Hamburg, Germany) and the final concentration of αSyn monomer in each aliquot was 70 μM. The solutions were then incubated in the dark at 37 °C with constant agitation (200 rpm) for 55 h. The dye solutions used to supplement the aggregation mixtures mentioned above, was also incubated under the same conditions and used for supplementing the control samples before imaging. At t = 0, 15, 25, 33 and 55 h, samples of the different aggregation reactions were taken and mE10 or ThT were added to the control samples. Each sample was then pipetted into multiple wells of a 384-well plate (Corning, black polysterene, clear bottom) at 20 μL per well. The plates were placed into a plate reader (CLARIOstar; BMG Labtech, Ortenberg, Germany) using excitation and emission filters of 440-10 nm and 490-15 nm. It was ensured that the concentration of αSyn was the same for all samples thought the process and the concentration of dye while imaging was 18 μM in all cases.

4.4.9 Measuring Aggregation Kinetics of Synthetic Aβ42

For kinetic experiments, the synthetic Aβ42 monomer was diluted with filtered (0.2 μm syringe filter, Whatman, 6780-1302) PBS (pH 7.4) to a concentration of 4 μM and supplemented with 10 μM ThT or 10 μM mE10. All samples were prepared in low-binding Eppendorf tubes (Eppendorf AG, Hamburg, Germany) on ice. Each sample was then pipetted into multiple wells of a 96-well, low-binding polyethylene glycol coating plate (Corning 3881, Kennebuck ME, USA) with a clear bottom, at 70 μL per well. The 96-well plate was placed in a plate reader (CLARIOstar; BMG Labtech, Ortenberg, Germany) and incubated at 37 °C under quiescent conditions using the bottom reading mode (ThT/mE10: 440-15 nm excitation, 480-15 nm emission)For each new preparation of protein, the aggregation kinetics

were checked by performing aggregation reactions at different concentrations of Aβ and a minimum of three replications per condition.

4.4.10 Fluorescence Anisotropy Measurements

Sample preparation

General Consideration

All samples were prepared in low-binding Eppendorf tubes (Eppendorf AG, Hamburg, Germany).

Borosilicate glass coverslips (VWR international, 22 x 22 mm, product number 631-0124) were cleaned using an argon plasma cleaner (PDC-002, Harrick Plasma) for at least 1 h to ensure that any fluorescent residues are removed from the coverslip. Frame-Seal slide chambers (9 x 9 mm, Bio-Rad, Hercules,CA, product number SLF-0201) were attached to the coverslip, and 50 μL of poly-L-lysine (70-150 kDa, Sigma-Aldrich, product number P4707-50 ML) was added on the inside of the slide chamber. After incubation for 20-30 min, the surplus of poly-L-lysin was aspirated carefully and gently washed three times with filtered PBS.

To correct for any fluorescent artefacts caused by the coverslips or any of the solutions being used, dye solutions (5 μM, 50 μL) in PBS without αSyn were imaged for each experiment and used as blanks.

Samples for Evaluation of Binding Order of mE10 on Late Stage αSyn Aggregates

αSyn was aggregated under the conditions stated before for 48 h and stored in the dark at 4 °C for several weeks. The 70 μM αSyn samples were diluted into filtered PBS supplemented with 5 μM dye to yield a final concentration of 7 μM αSyn. 50 μL of this solution was then added on the inside of the slide chamber and imaged. For each condition a minimum of 2 different coverslips were imaged at 3-5 different positions per slide.

Samples for Evaluating Modulation Degree on Early Stage αSyn Aggregates

αSyn was aggregated under the conditions stated before for 6 h. After 6 h, they were put on ice and subsequently used for imaging. Therefore, the 70 μM αSyn samples were diluted into filtered PBS to yield a final concentration of 7 μM αSyn. 50 μL of this solution was then added on the inside of the slide chamber and incubated for 10 min at room temperature. After 10 min, the surplus was carefully removed and the slide was washed twice with PBS. Finally, 50 μL of 5 μM dye solution was added and images recorded. For each dye, three separate

aggregation reactions were tested and slides were imaged at minimum three different frames.

Stable Oligomers

The stable oligomers were supplied in PBS (pH 7.4) containing 0.01% NaN_3 at concentrations of 52.4 μM (E46K), 18.4 μM (WT) and 31.1 μM (H50Q). The samples were diluted into filtered PBS supplemented with 5 μM dye to yield final concentrations of either 1 μM (E36K+mE10, E46K+ThT, WT+mE10) or 0.5 μM (WT+ThT, H50Q+mE10, H50Q+ThT). 50 μL of this solution was then added on the inside of the slide chamber and imaged. For each condition 2 different coverslips were imaged at minimum 3 different positions per slide.

Imaging

The imaging set up was the same as described in the literature [231]. Briefly, Imaging was performed on a total internal reflection fluorescence microscope using a 405 nm laser (LBX-405-50-CIR-PP, Oxxius), which was passed through a quarter wave plate (WPQ05M-405, Thorlabs) aligned parallel to the optical axis at the edge of a 60x Plan Apo TIRF, NA 1.45 oil-immersion objective lens, (Nikon Corporation) mounted on an Eclipse TE2000-U microscope (Nikon Corporation). Fluorescence emission was also collected by the same objective and selected by the presence of a dichroic (ZT 405/532 rpc) and subsequently passed through an emission filter (FF01-480/40/25). A polariser (10LP-VIS-B, Newport) mounted on a stepper motor rotation mount (K10CR1/M, Thorlabs) was placed between tube lens and the microscope body. During image acquisition, the polariser was rotated 360 degrees at 2 degrees per second for each field of view and images were recorded on an EMCCD camera (Evolve 512, Photometrics) at 20 frames per second with an exposure time of 50 ms during a full 360 $^\circ$ spin. Each pixel was 241 nm. Micromanager software was used to control the microscope [245]. The excitation power was 35 W/cm^2 measured in epifluorescence mode for all samples. For mE10 samples studying the modulation degree, the same samples were additionally imaged by using a laser power of 21 and 7 W/cm^2 for each frame.

Image Analysis

The image stacks corresponding to the full spin of the polariser were denoised in ImageJ (NIH, Bethesda) by sub-averaging 30 frames. To correct for the small circular drift caused by the rotation of the polariser, the images were aligned using “Align Images” plug-in available in GDSC utility plug-ins from the University of Sussex (http://www.sussex.ac.uk/gdsc/-

intranet/microscopy/imagej/utility). After alignment, the entire stack was averaged and by using the Find Maxima function in ImageJ each protein aggregate was detected. The threshold was set to 50. To obtain the sinusoidal fluorescence response of the dyes bound to fibrils, ROIs were drawn on different horizontally and vertically orientated fibrils and the signal intensity at these ROIs was plotted against the polariser angle.

To obtain the modulation signal for each species detected, analysis was performed by Juan Varela as described in the literature [231]. Shortly, the signal intensity of a 3×3 pixels square in each detected species was calculated and the local background was subtracted. The resulting signal was then plotted and fitted with a cosinusoidal curve of the form $y = acos(bx + c) + d$. In case of the phase c of the aggregate being similar to the phase c of the background, the aggregate was not considered in the analysis. If quality was appropriate, modulation was calculated by $modulation = 2a\,/\,(a + d)$.

Chapter 5

Bifunctional Fluorescent Probes for β-Amyloids and Hydrogen Peroxide Detection

The results presented in this chapter are published in the paper "Bifunctional fluorescent probes for detection of amyloid aggregates and reactive oxygen species"[246], listed in the publication section. The synthesis of the dyes was performed by James Fyfe, Omaru Kabia and Dung Do. αSyn was purified by Ewa Klimont. Lisa-Maria Needham performed fluorescence measurements; the data was analysed by Lisa-Maria and myself. Margarida Rodrigues and I prepared the αSyn fibrils. I performed binding assays, LCMS measurements, NMR stability studies.

5.1 Introduction and Motivation

Having found the ThT-analogue mE10 with superior photophysical and binding properties, the aim of this chapter was to apply this knowledge and integrate it into a bifunctional fluorescence probe able to detect amyloid aggregates and reactive oxygen species (ROS) simultaneously.

ROS are endogenously produced oxidising agents important in essential biological processes. However, high levels of ROS can induce, among others, protein alternations, DNA mutations and impair mitochondrial function, all of which are known to contribute to the development of neurodegenerative diseases. Thus, oxidative stress has long been suggested to play an important role in the pathogenesis in a range of neurodegenerative

disorders [247, 13, 248]. Conversely, it was also shown that amyloid species formed in neurodegenerative diseases are capable of inducing free radical production [249]. Together, this generates a bidirectional relationship between protein aggregation and oxidative stress.

Even though it is possible to detect both oxidative stress and amyloid aggregates, separately in *in vitro* and *in vivo* models of neurodegeneration as well as in post-mortem brains [250, 13], the interplay between ROS and the pathogenesis of neurodegeneration remains poorly understood: What is causation, what is correlation and how exactly do the different developmental stages of the disease vary from each other in respect of their amyloid species and redox biology [250, 13]? Thus, the ability to image increased levels of specific ROS together with amyloid aggregates could help to elucidate this complex interplay.

As highlighted in previous chapters, assessing ROS levels is technically challenging due to their short half-life and high reactivity, demanding non-interruptive methods with high spatial and temporal resolution. High-resolution fluorescence imaging operates on a temporal and spatial scale highly suited to meet this needs. Additionally, it enables visualisation and quantification of amyloid aggregates on a single aggregate level [216]. Therefore, the goal of this work was to combine single-molecule fluorescence instrumentation with new bifunctional fluorescence probes to enable the concurrent readout detailing both the presence and characteristics of different amyloid species as well as a specific ROS.

5.1.1 Approach

ThT is the most common fluorescent dye used for the detection of amyloid fibrils. As previously confirmed by the results in Chapter 4, mE10 has been demonstrated to outperform ThT in respect to its optical and binding properties while maintaining the most significant property of ThT, the fluorescence quantum yield enhancement attained upon binding to β-sheet containing species. In addition to a 5-fold increase in brightness and a 7-fold higher binding affinity, the results described in chapter 4 indicated the suitability of mE10 for the detection of early arising aggregation events including amorphous oligomers. These features make the mE10 scaffold a promising base for the generation of a new bifunctional contrast agent.

Hydrogen peroxide (H_2O_2) is generated in numerous biological processes and represents an important biological ROS, which is highly involved in redox signalling. Additionally, the often relatively high activation energy of reactions with H_2O_2 leads to an increased stability in the biological environment, which results in greatly enhanced *in vivo* concentrations in several diseases including neurodegenerative disorders [251–253]. H_2O_2-mediated conversion of

aryl boronic acids and esters has been broadly used as strategy to generate probes that respond effectively and selectively to H_2O_2 over other competing ROS [19, 20].

Based on this foreknowledge, the goal of this work was to design new H_2O_2-reactive, amyloid sensitive fluorescence probes based on the mE10 benzothiazole core for amyloid targeting and aryl boronic esters for H_2O_2 sensing (Figure 5.1). The presence of H_2O_2 should trigger the conversion of the boronic ester functionality into the corresponding phenol, thereby causing a change in the sterical and electronical properties of the dye. This, in turn, should lead to a change in the optical profile of the probes while maintaining their capability to bind to amyloid aggregates.

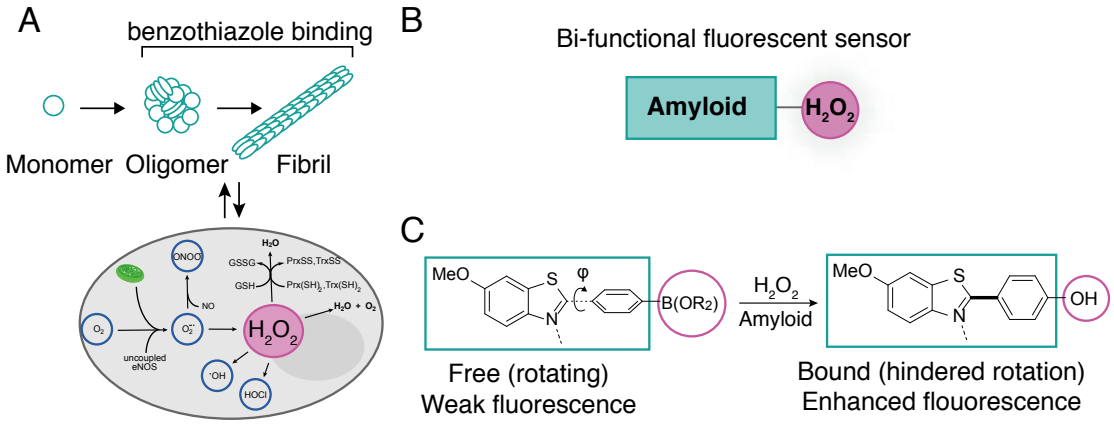

Figure 5.1 Background and concept of the bifunctional fluorescence sensor design. A) Pathway of amyloid fibril formation starting from the monomeric protein and the suggested interplay with oxidative stress. B) Schematic illustration of the bifunctional fluorescence sensor design. One part of the sensor allows amyloid sensing by binding towards amyloid fibrils, which leads to an increase in fluorescence, whereas the other part of the sensor is sensitive to H_2O_2 and causes a change in the optical properties of the sensor after reacting with H_2O_2. C) Molecular structure of the bi-functional fluorescence sensor. In the unbound state, the sensor shows low fluorescence intensity, which increases when bound to amyloid aggregates. Additionally, in the presence of H_2O_2 the boronic ester undergoes oxidative cleavage forming the corresponding phenol, which causes a change in the optical properties of the sensor.

Converting the aryl dimethyl amino group of ThT into a pyrrolidine unit (mE10), showed promising results. Thus, the boronic ester equivalent to mE10, mBE1, was designed, in which the pyrrolidine functionality was converted into a boronic acid pinacol ester. As this modification introduces sterical and especially electronical alternations, which are likely to influence the behaviour of the bifunctional probe, the approach was complemented by synthesising the 6-membered ring analogue, mBE2, as well as the corresponding neutral derivatives, BE1 and BE2 (Figure 5.2), to gain an insight into the relationship between the chemical structure, reactivity and specificity.

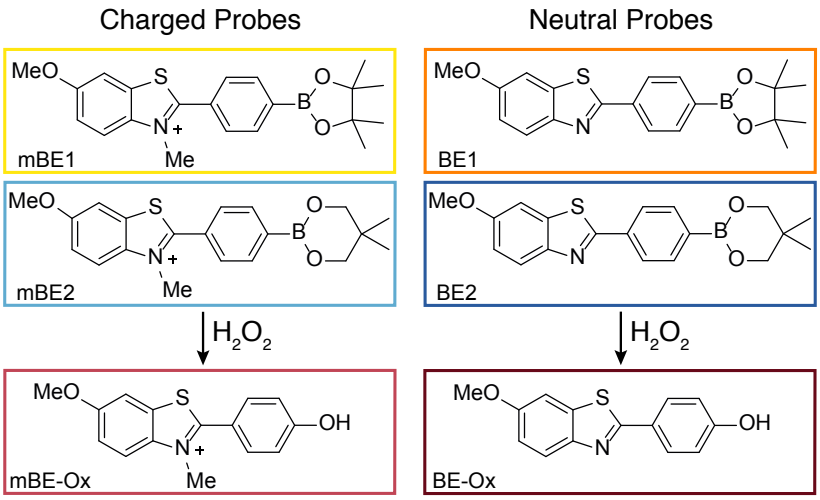

Figure 5.2 Chemical structure of the four bifunctional probes, of which mBE1 and mBE2 are the charged derivatives and BE1 and BE2 the neutral equivalents. The chemical structure of the dyes after the reaction with H_2O_2 are also shown, which are referred as mBE-Ox and BE-Ox.

5.2 Results and Discussion

5.2.1 Photophysical Properties

The foundation of the success of ThT as amyloid stain relies on its low fluorescence in its free state and the turn on response upon binding to amyloid aggregates. Thus, in order to sense amyloid species, the new bifunctional probes need to fulfil these criteria. To prove that the boronic ester modifications did not impact the underlying molecular rotor behaviour, the four new derivatives were first examined towards their bulk fluorescence and absorption properties in PBS without the presence of protein aggregates.

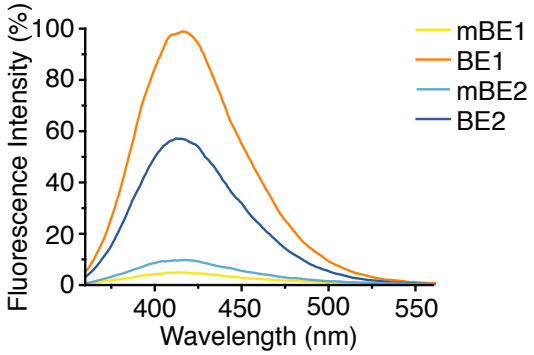

Figure 5.3 Fluorescence spectra of the four bifunctional probes free in PBS (5 μM). The intensities are normalised towards the maximum intensity of BE01.

As for the mE and E derivatives described in Chapter 4, the four dyes showed low quantum yield values in PBS ($\sim$ 0.01 for mBE dyes, 0.04-0.06 for BE dyes), even though the dyes showed over 10-times greater quantum yields than that of ThT (Table 5.1). Additionally, their extinction coefficients were decreased compared with ThT and mE10, leading to a over 4-times higher brightness than ThT but more than 3-fold lower brightness than mE10, making the four dyes promising probes for the purpose of this study as low brightness is desirable. Overall, the neutral derivatives exhibited overall higher quantum yields compared to the cationic equivalents but with overall lower extinction coefficients. These findings correlated well to previous results obtained from the E and mE derivatives and reinforce the assumption of a higher energy barrier between the non-fluorescent twisted intramolecular charge transfer (TICT) and the fluorescent locally excited (LE) state in the neutral derivatives as well as a reduced oscillator strength in absence of the positive charge.

Through scrutinising the effect of the exchange of the aryl nitrogen against electron withdrawing groups it was shown that the charged derivatives are influenced by modifications on this position to a greater extent than the neutral analogues. The absorption and fluorescence maxima of the cationic probes experienced a hypsochromic shift of 90 nm and 77 nm respectively when compared to mE10, making the absorption and emission wavelength range equivalent to those of the neutral analogues. For the non-charged dyes, the maxima shifted hypsochromically to a lesser extent (40 nm (abs), 12 nm (em)) compared to the neutral mE10 equivalent, E10. The conversion of the aryl boronic esters into the phenol did not significantly alter the appearance of the maxima of the charged mBE dyes. The BE derivatives experienced a minor chromatic shift in their emission maximum of 6 -10 nm, which is not significant to be used as readout for the conversion of the boronic ester into the phenol. These findings together suggest that the electron withdrawing nature of the substituent decreases the extent of electron delocalisation significantly whereas sterical modifications show minor impact. In respect to the extinction coefficient, the data suggested that the more electron deficient and sterically demanding the group, the lower the extinction coefficient (ε(mE10) > ε(mBE-Ox) > ε(mBE1) > ε(mBE2)). This resulted in a $\sim$ 4.5-fold increase in brightness for the charged probes, and a greater than 2.7-fold increase for the neutral probes when converting the aryl boronic ester into its phenol. The increase in brightness can serves as basis for the readout of the presence of H_2O_2 in biological environment and thus supports the probe design to be useful for specific ROS sensing.

Table 5.1 Summary of photophysical properties[1] of mBE and BE derivatives in PBS compared to ThT and mE10.

Dye	λ_{abs} (nm)	λ_{em} (nm)	λ_{em} - λ_{abs} (nm)	ε_{abs} ($M^{-1}cm^{-1}$)	ϕ_{Fl}	B (a.u.)	R^1-structure
ThT	413	488	75	36000	0.00	39.4	
mE10	420	494	74	31130	0.04	1245.2	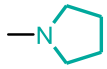
mBE1	330	417	87	16800	0.010	174	
mBE2	330	417	87	14800	0.010	152	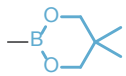
BE1	330	416	86	6400	0.061	390	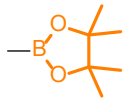
BE2	330	412	82	4200	0.041	172	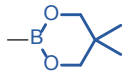
mBE-Ox	328	416	88	20500	0.083	782	
BE-Ox	325	406	81	12700	0.037	1059	

[1] Values were obtained from bulk UV-vis absorption and fluorescence measurements of the dyes in PBS buffer (pH 7.4).

5.2.2 H_2O_2 Sensing

Having established the suitable photophysical properties of the new bifunctional probes, characterised by a relative low quantum yield in PBS and a greater brightness of the phenol derivatives, it was necessary to prove the ability of the dyes to react with H_2O_2 and hence triggering a change in the photophysical properties. This was initially evaluated with bulk fluorescence spectroscopy and liquid chromatography mass spectrometry (LCMS) upon the addition of a physiologically realistic H_2O_2 concentration of 100 μM [163]. To control for external factors such as photobleaching and ROS generated though oxygen quenching by the triplet state of the fluorophore, the same assay was performed with all dyes in the absence of H_2O_2.

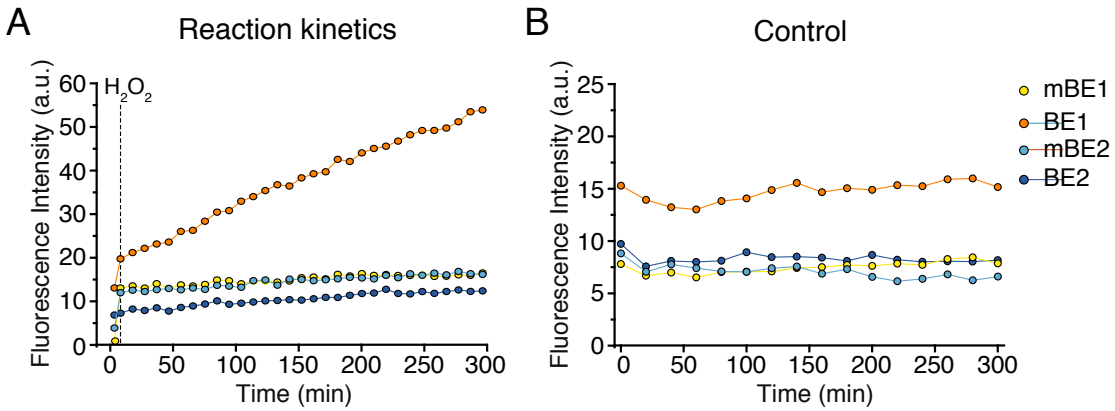

Figure 5.4 A) Reaction kinetics of the four bifunctional probes (5 μM) upon addition of 100 μM H_2O_2. The dashed line indicates the time point at which H_2O_2 was added. B) Fluorescence intensity of the four dyes vs time of control experiment in PBS.

Fluorescence data showed an instant enhancement in signal intensity within less than 30 seconds resulting in an fluorescence increase of 15.4-, 3.3-, 1.5- and 1.1-fold for mBE1, mBE2, BE1 and BE2 respectively (Figure 5.4). After this initial boost, the reaction was further monitored for 5 h leading to a final fluorescence enhancement of 19.6-fold for mBE1, 4.6-fold for mBE2, 4.2-fold for BE1 and 1.9-fold for BE2. The corresponding kinetic profile displayed linear increase for all four dyes over the monitored time range, but with different rates (mBE1 = 0.011 min^{-1}, mBE2 = 0.015 min^{-1}, BE1 = 0.112 min^{-1}, BE2 = 0.017 min^{-1}). These findings indicate that mBE1 is the most promising dye in respect to its signal-to-noise ratio as the presence of H_2O_2 triggered an over 4-times greater turn on response as opposed to the other dyes. Unexpectedly, BE1, which possesses the same boronic ester functionality as mBE1, showed the greatest reaction kinetic, which was $\sim$ 10-times faster compared to mBE1. It was shown that the oxidation rate is strongly dependent on the para substituent,

which is here represented by the benzothiazole unit [107]. Based on the results from the literature as well as the mechanism behind the oxidative cleavage, the mBE derivatives were thought to show a higher reaction rate, as the positive charge makes the benzothiazole more electron withdrawing and thus should facilitate the nucleophilic attack of H_2O_2. However, as highlighted before and indicated by the lower quantum yield, it is likely that the methyl-group reduces the energy difference between the LE and the TICT state. This in turn would lead to a more pronounced TICT state conformation and consequently a reduced conjugation between the aryl and benzothiazole system decreasing the influence of the benzothiazole unit on the boronic ester reactivity.

To cross validate that the observed increase in fluorescence intensity is based on the oxidative cleavage of the boronic ester by H_2O_2, the dyes were analysed via LCMS before and after 60 min incubation with 100 μM H_2O_2. 60 min incubation in PBS without H_2O_2 served as control. A summary of the LCMS results can be found in the Appendix. The data confirmed the conversion of the boronic esters of all four probes into the corresponding phenols. Opposed to this, no phenol formation was detected after 1 hour without H_2O_2 reinforcing that the changes observed in the optical measurements are based on the oxidative cleavage of the boronic esters by H_2O_2.

However, the conversion rate for the four derivatives was different. BE1 was converted to 100%, whereas mBE1 was only 73% converted into the corresponding phenol. The conversion rates for the 6-membered ring analogues BE2 and mBE2 were 90% and 88% respectively. This correlates with the reaction kinetics of BE1 from fluorescence measurements but contrasts to the continuous fluorescence increase of BE1 over 5 hours. Additionally, as BE1 and BE2 get converted into the same phenol derivative, the fluorescence intensities should have been relatively close in case of a 90%-oxidation of BE2 into BE-Ox. This was not the case for the kinetic fluorescence study, as the signal of BE1 was ~ 3 times greater than the one for BE2 after 60 min. A number of repetitions of both, fluorescence and LCMS measurements, showed significant variability especially in the fluorescence data. This might be caused by several factors including errors caused by the limited sensitivity of the bulk fluorescence spectrometer as the signal changes are rather small, balancing errors when preparing the different stock solutions for extinction coefficient calculations and inherent sensitivity of the dyes to competing processes.

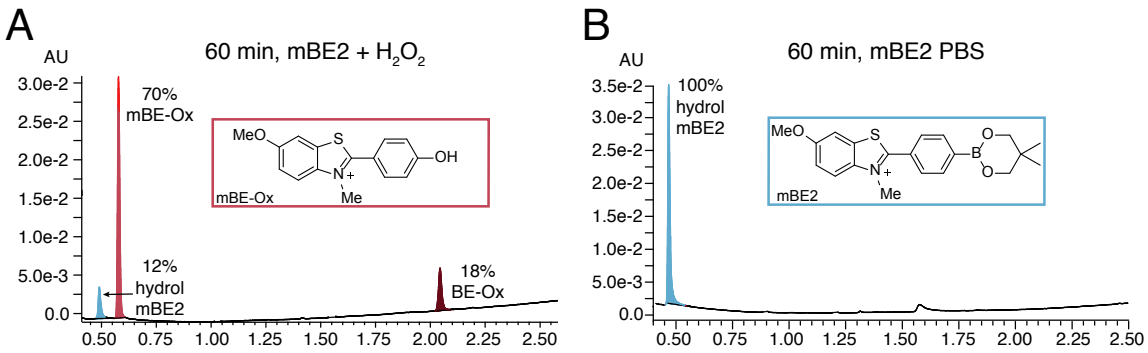

Figure 5.5 Representative LCMS traces of mBE2 after 60 min incubation with A) 100 μM H_2O_2 in PBS and B) PBS. The values are representing relative area under the curve in the UV chromatogram monitored at 254 nm.

It was noticeable that for all samples - at t = 0 min and t = 60 min, with and without the presence of H_2O_2 - the boronic acid instead of the boronic ester was detected via LCMS (Figure 5.5). This is often perceived due to on-column hydrolysis of the boronic esters, which is promoted by the acidic pH of the mobile phase, the column as well as the column temperature, as well as partial in situ hydrolysis of the esters under the aqueous conditions [254, 255]. However, as it is known that boronic esters have a tendency to hydrolyse under biological conditions, which would lead to mBE1 and mBE2 as well as BE1 and BE2 being the same molecules, it was necessary to ensure that the boronic acid generation happened predominantly during LCMS analysis. Therefore, direct mass spectrometry (ESI and ESCI) as well as LCMS analysis of the samples diluted in MeCN were performed. Both confirmed the contribution of the acidic solvent, on-column hydrolysis and ionisation towards the detection of the boronic acid instead of the ester. Further LCMS and NMR studies in DMSO as well as D_2O/d_6-DMSO confirmed the stability of the four dyes under these conditions. Taken together, it can be assumed that the boronic esters are the predominant species present during the studies.

Besides of the detection of the hydrolysed product, it was further detected that in the mBE samples which were exposed to H_2O_2, up to $\sim$ 19% of the oxidised product was de-methylated (Figure 5.5A). De-methylation did not appear in the samples without H_2O_2 (Figure 5.5B) and hence the partial demethylation can be attributed to the presence of H_2O_2. However, the fluorescence emission of the BE and mBE samples in PBS did not show any change in signal intensity over the course of 5 hours, which indicates that these extraneous factors could be neglected. As a further control, the fluorescence of ThT was also measured

before and after the addition of H_2O_2 and as expected no effect on the emission or LCMS signal was detected.

Among the four probes, BE1 showed the highest fluorescence signal, which is promising for sensitive detection of lower quantities of H_2O_2. Thus, the reaction of BE1 was additionally monitored with different concentrations of H_2O_2 ranging from 1 μM to 100 μM (Figure 5.6. The results after 5 h manifested a graduated increase in the emission reaching a plateau between 25 μM and 60 μM H_2O_2 and thus allowing the readout of different amounts of H_2O_2.

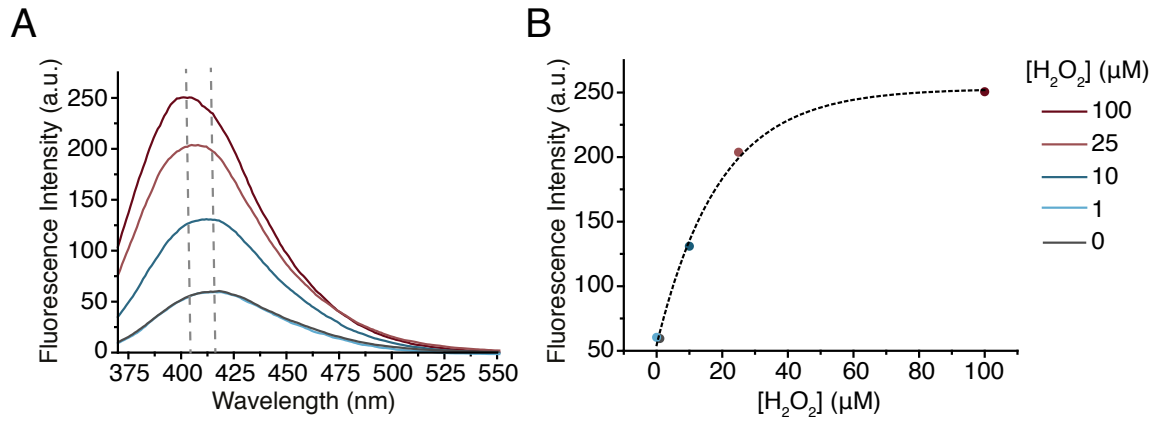

Figure 5.6 H_2O_2 sensitivity of BE1. A) Fluorescence spectra of BE01 (5 μM) after 5 h incubation with H_2O_2 at concentrations from 0 - 100 μM. B) H_2O_2 response curve of BE1 (5 μM) after 5 h incubation with different concentrations of H_2O_2.

Taken together, even though hydrolysis in aqueous solutions and variability in the reaction kinetics occurred, both, fluorescence and LCMS measurements confirmed the ability of the new bifunctional probes to sense physiologically realistic H_2O_2 concentrations. Additionally, BE1 appeared to be promising for the sensitive detection of H_2O_2 at quantities smaller than 100 μM.

5.2.3 Amyloid Sensing

The bifunctional probes were designed to respond to H_2O_2 as well as the presence of amyloid sprecies. Thus, after having established their ability to function as H_2O_2 sensors, it was then necessary to examine the capability of the dyes to report on the presence and characteristics of amyloid species. Therefore, the optical properties of the dyes in the presence of late stage αSyn aggregates were examined (Table 5.2).

Table 5.2 Summary of photophysical properties[1,2] of mBE and BE derivatives in the presence of αSyn compared to ThT and mE10.

Dye	λ_{em} (nm)	$\lambda_{em,PBS}$ - $\lambda_{em,\alpha Syn}$ (nm)	ϕ_{Fl}	$\phi_{Fl,\alpha Syn}/\phi_{Fl,PBS}$	B (a.u.)	$B_{\alpha Syn}/B_{PBS}$ (a.u.)	R^1-structure
ThT	483	5	0.24	~1000	6067	154.0	
mE10	490	4	0.81	20.3	31590	25.4	
mBE1	386	31	0.013	1.3	218	1.3	
mBE2	392	25	0.022	2.1	325	2.1	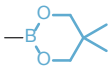
BE1	391	25	0.110	1.8	704	1.8	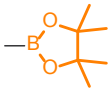
BE2	393	19	0.140	3.4	588	3.4	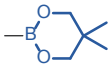

[1] Values were obtained from bulk UV-vis absorption and fluorescence measurements of the dyes in the presence of 10 μM late stage αSyn aggregates. [2] Due to the significant overlap of the absorption spectrum of the dyes and αSyn aggregates, it was not possible to determine accurate extinction coefficient values for the dyes bound to amyloid.

All four probes exhibited an increase in their quantum yield and brightness upon binding to late stage αSyn aggregates. However, the increase was relatively low compared to mE10 and especially ThT. Whereas mE10 experienced a more than 20-fold increase in its quantum yield and an 25.4-fold increase in brightness, the greatest difference in quantum yield and brightness of the four probes bound to amyloid compared to PBS was reached for BE2 with an increase of 3.4-fold. This was in reverse to what was previously found for the mE and E analogues, for which the neutral derivatives exhibited a smaller fluorescence response than the charged equivalents. Additionally, the 6-membered ring mBE/BE dyes showed a stronger response towards αSyn aggregates than the 5-membered boronic ester derivatives, which was also in contrast to previous findings (mE10 vs mE13, Chapter 4). Besides the greater quantum yield of the pinacol boronic esters in their free state, this could be the result of different interactions of the dyes with the protein aggregates which may have contributed to changes in their ground and excited states.

Furthermore, it was striking that the quantum yield and brightness ratios for the boronic ester probes yielded the same values. This was similar to the findings for mE10 and was caused by an increase in extinction coefficient upon binding. For ThT the brightness ratio was much smaller than that of the quantum yield, which could be linked to the decrease in its extinction coefficient upon binding. Thus, it is likely that the boronic ester derivatives experience an increase in their extinction coefficient in the presence of αSyn aggregates.

Even though the fluorescence response was smaller than that observed for mE10 and ThT, all four bifunctional probes did manifest a significant shift in their fluorescence maxima between 19 nm and 31 nm. This led to 7.8-fold greater shift in the fluorescence maximum of the bound versus the unbound dye when comparing mE10 and its boronic ester equivalent mBE1. Such offset between the free and bound state might offer an additional quantification of the binding towards protein aggregates and thus complement the fluorescence turn on response.

5.2.4 Binding Affinities

The optical properties of fluorescence dyes are often very sensitive towards their environment, especially fluorophores acting as molecular rotors [207]. Thus, to better understand the observations about the optical properties of the bifunctional dyes upon binding to amyloid species, the next goal was to determine the binding affinities of the dyes towards αSyn. The binding affinity measurements were performed with αSyn aggregates obtained via a previously published protocol, that allows the generation of fibrils with a narrow size distribution and good reproducibility between independent batches [226].

As discussed in Chapter 4, fluorescence based measurements of binding affinities are limited by the performance of the dyes as emitters and are only able to report on binding sites triggering a fluorescence response. Since the four bifunctional probes responded towards the presence of αSyn aggregates with a distinct but rather low fluorescence increase and the main purpose of the affinity measurements was to compare all four dyes and their phenol equivalents. Surface plasmon resonance (SPR) measurements were performed to assess the binding affinities. αSyn aggregates were covalently attached to a gold surface via an amide bond and exposed to different concentrations of the dyes (cf. Chapter 4 for more details). The SPR binding experiments yielded good data quality for all dyes with very minor error bars obtain across three different chips (represented as standard deviations).

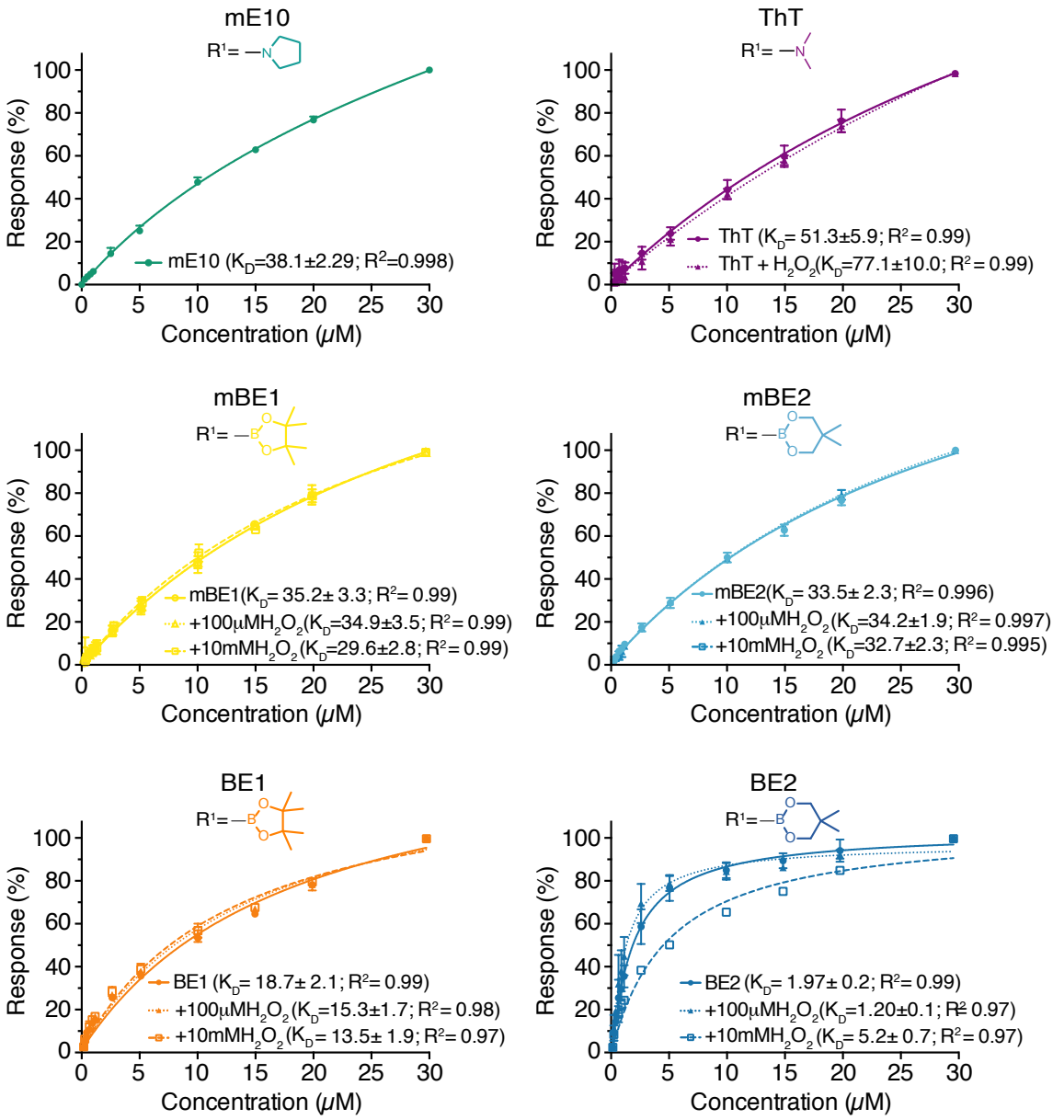

Figure 5.7 Binding affinity curves obtained from SPR experiments of mBE and BE dyes (before and after incubation with H_2O_2 (100 μM and 10 mM)), ThT and mE10 binding to immobilised αSyn aggregates on a gold surface. Each spectrum represents the mean of results from 3 independent preparations of dye solutions and SPR chips; error bars are shown as standard deviations.

Analysing the equilibrium resonance response in respect to the dye concentration yielded binding affinities for the four dyes with K_D values between $1.97 \pm 0.15\,\mu$M (BE2) and $35.2 \pm 3.3\,\mu$M (mBE1) and thus below the K_D of ThT and mE10 (Figure 5.7). In accordance with previous findings, the neutral analogues, BE1 and BE2, appeared to bind more strongly to αSyn aggregates than the charged dyes (mBE1, mBE2, mE10, ThT) but around

one order of magnitude weaker than their E-derivatives (E10 ($K_D = 0.22 \pm 0.03$) and E13 ($K_D = 0.45 \pm 0.07$), Chapter 4). This confirms the hypothesis, that the gain in hydrophobicity by the loss of the positive charge supports the insertion of the dye into the binding groove and strengthens the protein-dye interactions [211]. The decreased binding abilities of BE1 and BE2 as opposed to their E analogues further reinforced the enhanced interactions of more hydrophobic dyes with the amino acid side chains of the binding sites, as the incorporation of the two oxygen atoms through the boronic ester entity decreases the hydrophobicity. The change in hydrophobicity and steric did not significantly influence the binding of the charged mBE derivatives. This might be explained by the less deep binding of the charged dyes accompanied with less distinct interactions with the predominant hydrophobic amino acid side chains, which could generate a greater tolerance towards the modifications.

In line with the strongest fluorescence turn on response among the four bifunctional dyes, BE2 exhibited the strongest binding affinity. Thus, BE2 appeared to be promising for sensitive detection of lower concentrations of amyloid aggregates.

It was not only important to prove the binding affinities of the new probes towards amyloid but also to show that this property stays unaffected by the transformation of the boronic ester into the phenol triggered by H_2O_2. Therefore, the dyes were incubated for 1 h with 100 μM H_2O_2 prior to SPR analysis. None of the four dyes showed a significant change in their binding affinities (Figure 5.7). Interestingly, BE1 and BE2 persisted to show different equilibrium response curves and thus affinities after the incubation with 100 μM H_2O_2. This was unexpected as both dyes convert into the same phenol. However, as mentioned before, the reaction rate between the dyes varies and thus the phenol might have been present to different degrees. Thus, the experiment was repeated with 10 mM H_2O_2 to ensure complete conversion. LCMS analysis was performed beforehand to ensure that 10 mM H_2O_2 does not cause any other transformations of the dyes. Under these conditions the response curves of BE1 and BE2 converged, as expected. No significant change was observed in the mBE derivatives as they appeared alike under all conditions.

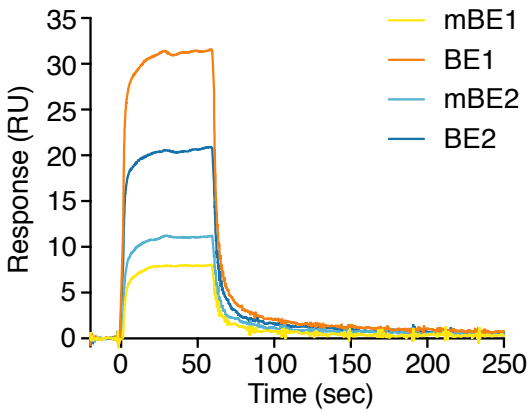

Figure 5.8 Representative SPR sensogram obtained from SPR experiments of 10μM mBE1, mBE2, BE1 and BE2 binding to immobilised αSyn aggregates on a gold surface.

After having examined the concentration dependent equilibrium affinities, the kinetics of the interaction between αSyn aggregates and the new bifunctional probes was questioned. Representative sensograms for the four dyes are depicted in Figure 5.8. No significant difference in their on and off rate behaviour was noticeable: all boronic esters as well as their oxidised analogues showed an immediate association onto the surface bound αSyn aggregates with a steep association phase. The dissociation was very rapid, resulting in a negligible dissociation phase. This mirrors the behaviour of the mE dyes and indicates a rapid exchange of dye molecules.

Taken together, the data suggested that any change in the fluorescence signal upon addition of H_2O_2 was not due to affinity changes but rather a modification of a fluorescence property of the dye itself.

5.2.5 Bifunctional Sensing

Having validated the ability of all four boronic ester derivatives to detect H_2O_2 and the presence of αSyn separately, it was essential to prove the feasibility of simultaneous detection of these two crucial factors common in most neurological pathologies.

Assessing the bulk fluorescence response of the four dyes when H_2O_2 was combined with αSyn aggregates manifested a striking enhancement in the total fluorescence emission of the two neutral dyes, BE1 and BE2 (Figure 5.9). Upon binding to αSyn species the signal intensity of BE1 increased 3.3-fold, BE2 4.8-fold. In the presence of H_2O_2, the emission signal of BE1 was enhanced by 2.0-fold, whereas the emission of BE2 showed no significant change. However, adding both simultaneously resulted in a total rise of the fluorescence signal of 7.5-fold for BE1 and 19.6-fold for BE2, which indicates their great suitability as

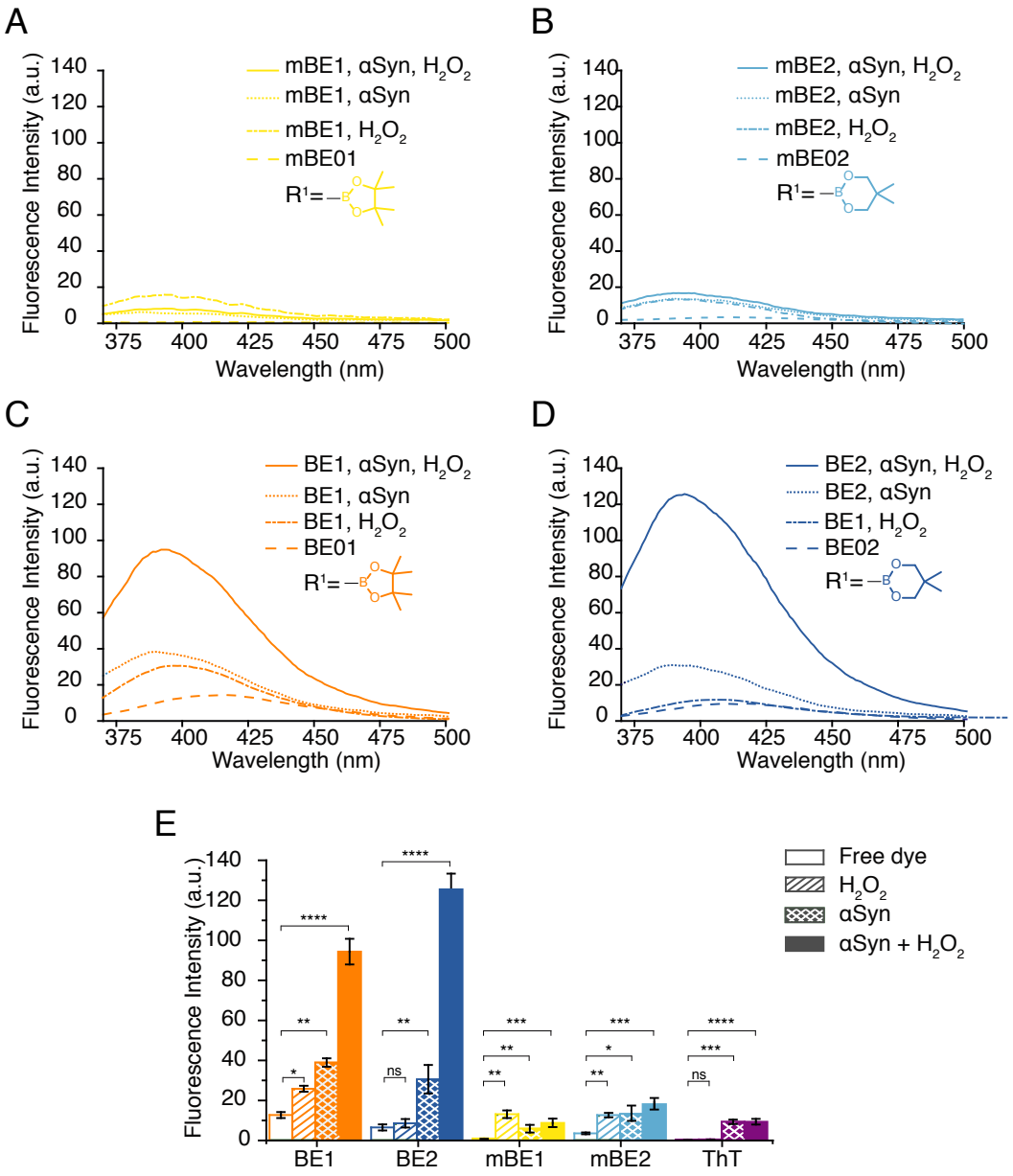

Figure 5.9 Fluorescence response of mBE and BE dyes towards H_2O_2, αSyn and $\alpha\text{Syn} + H_2O_2$. Bulk fluorescence spectra of A) mBE1, B) mBE2 C) BE1 and D) BE2 free in PBS and in the presence of H_2O_2, αSyn and $\alpha\text{Syn} + H_2O_2$. E) Bar graph indicating the fluorescence response of the different dyes towards H_2O_2, αSyn and $\alpha\text{Syn} + H_2O_2$.

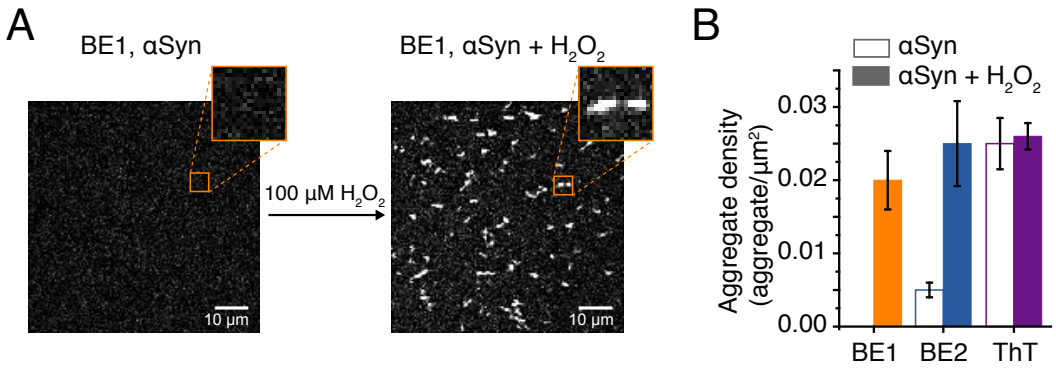

Figure 5.10 A) Representative average intensity SAVE image of BE1 with αSyn before and after H_2O_2 addition. B) Bar graph illustrating the aggregate density detected by BE1, BE2 and ThT before and after H_2O_2 addition.

bifunctional fluorescence sensors for concomitant detection of H_2O_2 and αSyn aggregates. Another beneficial feature, which facilitates their use as bifucntional probes, results from their shift in emission maximum in the presence of αSyn aggregates and H_2O_2 (Figure 5.9). In contrast to the neutral BE probes, the cationic mBE derivatives did not display a strong change in their emission properties when H_2O_2 and αSyn were present simultaneously compared to the response to H_2O_2 or αSyn aggregates alone. Thus, mBE1 and mBE2 were able to function as sensors for H_2O_2 and αSyn aggregates independently but did not allow a readout of the concomitant presence of these pathogenic factors.

The superior fluorescence response of the neutral BE derivatives might be caused, among others, by their stronger binding towards αSyn aggregates. This could lead to different interactions with functional groups in the protein binding site affecting the polarity and reactivity of the boronic ester and thus their optical properties and conversion rate.

The distinct fluorescence response as well as overall greater integrated fluorescence intensity of BE1 and BE2 enabled further verification of their bifunctionality on the single aggregate level using single-aggregate visualisation by enhancement (SAVE) imaging. Without the presence of H_2O_2, BE1 did not enable the detection of any αSyn aggregate. However, after the addition of H_2O_2 BE1 visualised 0.020 ± 0.004 aggregates/μm^2 (Figure 5.10). Similarly, BE2 only detected a minor quantity of aggregates (0.005 ± 0.004 aggregates/μm^2) to begin with but increased its sensitivity by 5-fold to 0.025 ± 0.004 aggregates/μm^2 upon the addition of H_2O_2. These results indicate that both dyes can function as bifunctional H_2O_2 and αSyn aggregate sensors in bulk as well as on single aggregate level.

5.3 Summary and Conclusion

The accumulation of abnormally aggregated proteins and high levels of ROS are key features of many neurodegenerative disorders including Parkinson's and Alzheimer's disease. Thus, new methods able to detect the presence of amyloid aggregates and ROS simultaneously will be critical to expand our understanding of their interplay and their role in the pathogenesis of neurodegenerative disorders.

To address this unmet need, the design and successful application of new bifunctional fluorescence probes for the concomitant detection of αSyn aggregate and H_2O_2 were described in this chapter. Combining established structures for the independent detection of amyloid aggregates and H_2O_2 resulted in four dyes, mBE1, mBE2, BE1 and BE2, composed of a β-sheet sensitive aryl-benzothiazole core and H_2O_2-reactive boronic ester moiety. The mBE and BE derivatives differ from each other only in the N-methylation of the benzothiazole unit resulting in one charged and one neutral analogue. This minor structural change appeared to have a pronounced effect on the binding and optical properties as well as the bifunctional capabilities of the dyes. Despite showing weaker binding affinities and a less distinct fluorescence turn on response in the presence of either H_2O_2 or amyloid aggregates, the charged mBE dyes were able to sense αSyn aggregates and H_2O_2 independently. However, the combination of both, protein aggregates and H_2O_2 did not result in a signal change making them poor bifunctional probes. Opposed to this, the neutral dyes exhibited stronger binding affinities and beneficial optical properties compared to their charged analogues. Most strikingly was their large increases in ensemble fluorescence intensity when αSyn aggregates and H_2O_2 were present at the same time. This not only indicated the great potential of the two BE probes as bifunctional sensors but also allowed their application on a single aggregate level. Taken together, the neutral boronic ester aryl-benzothiazoles, BE1 and BE2, represent promising bifunctional dyes which possess the potential to study protein aggregation and oxidative stress simultaneously in *in vitro* models of neurodegeneration.

Despite their promise, further work is required to better understand the non-linear changes in the emission properties of BE1 and BE2 in the presence of the two species simultaneously and to evaluate their feasibility to differentiate the presence of H_2O_2, αSyn aggregates or $H_2O_2 + \alpha$Syn aggregates. Also, it might be useful to perform anisotropy measurements similar to those described for mE10 to question the binding mode of these dyes under different redox conditions as well as in the presence of amyloid species at different aggregation stages. Following on from this the same experiments may be carried out with other proteins known to form amyloid aggregates and associated with neurodegeneration (e.g. Aβ, tau) to asses

selectivity and specificity. Additionally, studies with patient derived samples (e.g. CSF, brain tissue) would allow insight into their binding properties in a patho-physiological environment and thus also reveal non-specific binding to proteins, enzymes and cell components. Furthermore, additional modifications on the benzothiazole core or the aryl unit linked to the boronic ester might be explored to tune the optical properties as well as reactivity of the dyes. This may allow the generation of new analogues with an increased turn on response and distinct H_2O_2 reactivities, which then could allow more effective and sensitive bifunctional sensing.

5.4 Material and Methods

5.4.1 Chemical Synthesis

The synthesis of the mBE and BE derivatives was performed in the lab of T.N. Snaddon and adapted a procedure previously described by Wolfe et al [242]. An overview of the synthetic route including reactants and conditions is shown in Figure 5.11.

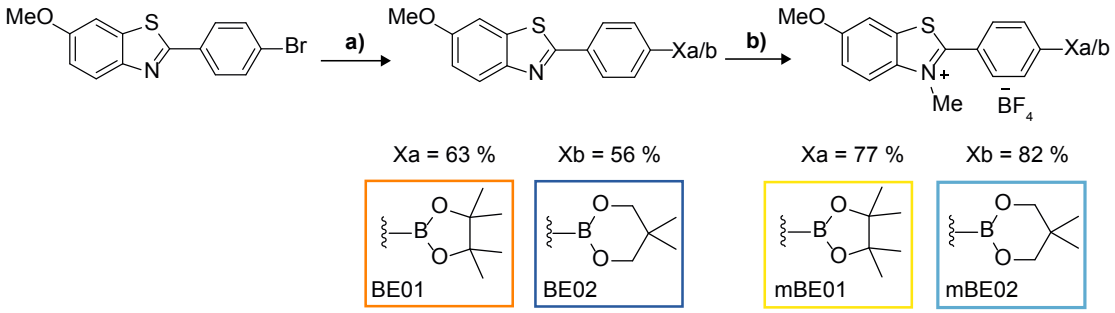

Figure 5.11 Synthesis scheme of mBE and BE derivatives. Reagents and conditions: (a) $Pd(dppf)Cl_2{*}CH_2Cl_2$, $B_2(OR)_2$, 1,4-dioxane, 100 °C, 18 h. (b) Me_3OBF_4, DCM, 25 °C, 24 h.

5.4.2 Photophysical Characterisation

All solvents were filtered (0.2 μm syringe filter, Whatman, 6780-1302) before used.

Samples were placed into a quartz fluorescence cuvette (Hellma Analytics, 3 x 3 mm) and bulk fluorescence spectra were recorded using a fluorescence spectrophotometer (Cary Eclipse, Varian). Fluorescence spectra of BE, mBE dyes and ThT (5 μM) were recorded free in PBS (pH 7.4), in the presence of H_2O_2 (100 μM), in the presence of αSyn aggregates ($\sim$ 10 μM) and in the in the presence of both H_2O_2 and αSyn aggregates simultaneously at excitation maxima. The response towards H_2O_2 was recorded at 20-minute intervals over a 5

hour time period; the response towards αSyn aggregates was measured instantly. To assess the bulk fluorescence response towards both, H_2O_2 and αSyn aggregates, the dyes (25 μM) were incubated with H_2O_2 (100 μM) for 60 minutes, diluted to 5 μM and the emission spectra were recorded with αSyn aggregates. The error bars represent standard deviations from experiments with n = 3 separately prepared dye samples.

Form these data and bulk absorption measurements, several photophysical quantities were determined as described in Chapter 4 (4.4.5).

5.4.3 Surface Plasmon Resonance Measurements

The binding affinities were assessed analogue to the procedure described in Chapter 4 (4.4.7). To acquire the binding curves of the oxidised dyes, the 30 μM sample was incubated for 1 h with 100 μM or 10 mM H_2O_2 before further dilution.

5.4.4 LCMS Quantification of Reaction with H_2O_2

LCMS analysis of the reaction of the dyes with H_2O_2 was performed using a Waters Acquity H-class UPLC coupled with a single quadrupole Waters SQD2. ACQUITY UPLC CSH C18 Column, 130Å, 1.7 μm, 2.1 mm x 50 mm was used as the UPLC column. The conditions of the UPLC method are as follows: Solvent A: Water +0.1% Formic acid; Solvent B: Acetonitrile +0.1% Formic acid; Gradient of 0-4 minutes 5% - 100% B + 1 minute 100% B with re-equilibration time of 2 minutes. Flow rate: 0.6 mL/min; Column temperature of 40 °C; Injection volume of 2 mL. The signal was monitored at 254 nm. Samples were prepared by diluting the stock solutions of the BE and mBE compounds into PBS (pH 7.4) or MeCN to a concentration of 30 °CM. The diluted dye solutions were analysed via LCMS directly after dilution (t = 0) as well as 1 hour after dilution (t = 1h). To prove the oxidative cleavage of the boronic esters to a phenol triggered by H_2O_2, the diluted dye solutions were exposed to 100 μM H_2O_2 and analysed via LCMS after 1 hour of incubation. To ensure stability of the dyes in the presence of 10 mM the same procedure was repeated with 10 mM H_2O_2.

To question to which degree the stationary phase of the column affects the boronic ester hydrolysis, the samples were also injected directly into the MS without the chromatographic separation. ESI and ESCI were used as ionisation methods.

5.4.5 NMR Stability Tests

The dyes (1 mg in 700 μL) were incubated for 5 h in D_2O spiked with d-DMSO till fully dissolved. BE2 was not fully solvable at this concentration even with 50% d-DMSO and thus no NMR spectrum was recorded. After incubation, NMR spectra were recorded on a Bruker AVANCE III HD (500 MHz, DUL $^{13}C/^{1}H$) at room temperature and compared with the original NMR spectra. Calibration of the spectra was achieved using the solvent signals.[150] All chemical shifts (δ) are quoted in ppm and coupling constants given in Hz. Splitting patterns are given as follows: s (singlet), bs (broad singlet), d (doublet), t (triplet), q (quadruplet), m (multiplet). The ^{1}H-NMR signals after 5 h incubation were as follows:

mBE1
^{1}H-NMR: (500 MHz, D_2O) δ [ppm] = 8.15 (d, $J_{H,H}$ = 9.5 Hz, 1H), 8.09 (d, $J_{H,H}$ = 8.0 Hz, 2H), 7.90 – 7.88 (m, 2H), 7.83 (d, $J_{H,H}$ = 2.5 Hz, 1H), 7.60 (dd, $J_{H,H}$ = 9.5, 2.5 Hz, 1H), 4.30 (s, 3H), 4.02 (s, 3H), 1.23 (s, 12H).

mBE2
^{1}H-NMR: (500 MHz, D_2O) δ [ppm] = 8.15 (d, $J_{H,H}$ = 9.5 Hz, 1H), 8.09 (d, $J_{H,H}$ = 8.0 Hz, 2H), 7.90 – 7.89 (d, $J_{H,H}$ = 8.0 Hz, 2H), 7.83 (d, $J_{H,H}$ = 2.5 Hz, 1H), 7.60 (dd, $J_{H,H}$ = 9.5, 2.5 Hz, 1H), 4.31 (s, 3H), 4.02 (s, 3H), 3.38 (s, 4H), 0.89 (s, 6H).

BE1
^{1}H-NMR: (500 MHz, D_2O) δ [ppm] = 8.03 (d, $J_{H,H}$ = 8 Hz, 2H), 7.94 (d, $J_{H,H}$ = 9 Hz, 1H), 7.81 (d, $J_{H,H}$ = 8 Hz, 2H), 7.67 (d, $J_{H,H}$ = 2.5 Hz, 1H), 7.14 (dd, $J_{H,H}$ = 9, 2.5 Hz, 1H), 1.29 (s, 13H).

5.4.6 Single-Aggregate Fluorescence Imaging

In short, single aggregate fluorescence imaging experiments were carried out in total internal reflection fluorescence (TIRF) mode microscopy with the bespoke inverted microscope (Olympus, IX73) set-up. Excitation of BE, mBE compounds and ThT in the presence of αSyn aggregates were performed with a collimated 405 nm laser (Oxxius, Laserboxx, LBX- 405-50-CIR-PP) which was aligned parallel to the optical axis and directed into an oil immersion objective lens (1.45 NA, 60×, Plan Apo, TIRF, Nikon) above the critical angle to ensure TIR at the coverslip–sample (glass/water) interface. Fluorescence emission was also collected by the same objective and selected by the presence of a dichroic (Di01-

R405/488/561/635, Semrock) and subsequently passed through appropriate emission filters (BLP01-488R-25, Semrock). Images were then recorded by an EMCCD camera (Evolve delta 512, Photometrics) with an electron multiplication gain of 250 running in frame transfer, clear presequence mode. Each pixel on the image was 275 nm. Images were recorded at 100 ms exposure for 200 frames using automation through Micro-manager software [245].

Images were analysed with a bespoke ImageJ macro. Image stacks of 200 frames taken as 100 ms per frame of the BE dyes and ThT with αSyn aggregates and either in the presence or absence of H_2O_2 were compressed in time to create single frame images representing the average pixel intensities. Pixels of intensity above background were determined with a fixed threshold and αSyn aggregate species in each field of view identified and counted. The density of species was determined from the division of the number of species by the area of the field of view (4726 μm^2). Five fields of view in the presence of H_2O_2 and five in the absence of H_2O_2 were analysed for each dye. Error bars represent the standard deviations of the species density between the five fields of view.

Chapter 6

Conclusion and Future Work

Reactive oxygen species (ROS) and associated oxidative stress contribute to dysfunction and cell death in nearly all pathologies [256, 257]. However, the lack of tools for measuring defined redox species in normal and diseased states has been a profound limitation for fundamental research in redox biology as well as clinical studies. Most approaches disrupt cellular integrity, influences the redox state themselves, lack specificity, possess insufficient spatiotemporal resolution or have limited potential for *in vivo* imaging. To overcome this unmet need, the fundamental objective of this thesis was to develop new optical probes for the specific detection of ROS in cancer and neurodegenerative disorders and combine these with suitable technologies allowing a specific readout with high spatial and temporal resolution under biological relevant conditions.

ROS encompass a broad and diverse range of species from which each molecule has unique reaction properties (pathway, kinetics, rate) and distinctive spatial and temporal distribution [2]. Therefore, it is crucial to focus on a particular molecule when questioning their physiological and pathological impact. H_2O_2 is a major and abundant ROS in living organisms and plays an important role as a second messenger in physiological as well as pathological processes. Hence, H_2O_2 was chosen as the ROS of interest in the work presented in this thesis.

Although mostly assigned to oxidative stress and damage, ROS play an important role as regulatory molecules in a range of biological processes, which results in a ubiquitous presence of ROS [2]. To study the impact of oxidative stress towards a particular disease, the location of the probe within the organism and the cell must be understood to detangle physiological ROS generation from pathological. This makes a bifunctional probe design crucial as it allows the simultaneous detection of a disease specific marker and the ROS of interest. The main approach used in this thesis for this purpose was to combine a targeting

moiety specific towards a disease inherent biomarker with a H_2O_2 reactive boronic ester. Together, this ascertained a disease specific binding/accumulation of the dye and a prescribed signal change in the presence of H_2O_2. Prior to the application of the bifunctional probes, it was crucial to understand the photophysical and biological properties of the new dyes and how they interact with their environment. Only an in-depth understanding of these underlying factors enables the accurate interpretation of the data and precise tailoring of the photophysical and biological features of the dye through chemical modifications to maximise sensitivity and selectivity.

Different pathological conditions entail different challenges and thus not only is the probe design is crucial for a successful implementation but also the technology used for the assessment. As the scope of this work spanned two separate pathologies, cancer and neurodegenerative diseases, with different research foci, photoacoustic (PA) imaging and single aggregate fluorescence imaging were exploited as imaging modalities.

PA imaging is an emerging method that combines the high contrast of optical imaging with the high temporal and spatial resolution of ultrasound [54]. Since sound waves are less scattered and diffracted by biological tissues than photons, this technique bypasses some of the drawbacks of traditional optical imaging techniques, which makes it suited to study complex disease, such as cancer, *in vivo* in real-time with high spatial resolution. Additionally, PA imaging uses non-ionising radiation in the near infrared range and thus does not influence the redox state during image requisition. Taking all these features together, PA imaging is highly qualified to study oxidative stress in cancer.

The development of single-molecule fluorescence techniques is fundamentally changing biological research as it allows visualisation nano-scale biological structures and dynamic processes with unrivalled resolution in both time and space [87]. This is of great importance when questioning pathological changes on the molecular level. One main application of single-molecule fluorescence imaging is the study of diseases associated with the aberrant aggregation of misfolded proteins, such as Parkinson's and Alzheimer's diseases. Due to the highly transient and heterogeneous nature of protein aggregates and their small size of less than 200 Å, conventional techniques fail to identify and characterise these pathological species. Thus, due to its unprecedented spatial resolution combined with its high temporal resolution, single-molecule fluorescence microscopy is well suited to question the interaction of ROS and protein aggregation during the pathogenesis of neurodegenerations.

6.1 Imaging Oxidative Stress in Cancer using PA Imaging

Oxidative stress and increased levels of ROS have long been linked to cancer initiation, progression and therapy response. However, whether the increased levels of ROS observed in cancer are cause or correlation and how they affect the different disease stages and treatment response is still an open question. Consequently, one aim of the work presented in this thesis was to develop a bifunctional probe for PA imaging to characterise and define the pathology of ROS in cancer *in vivo*.

This work was introduced with the characterisation of heptamethine cyanine dyes and the synthesis and detailed investigation of structural modifications on a heptamethine cyanine backbone that enable the development of a PA probe encompassing: good peak absorption in the NIR window, efficient PA signal generation, sufficient photostability, water solubility, cancer targeting and the ability to exhibit a signal change upon the reaction with H_2O_2. The results allowed for greater understanding of the relationships between structure and photophysical and biological function laying the foundations for the design and synthesis of a new bifunctional, H_2O_2-activatable PA probe based on a heptamethine carbocyanine dye scaffold. The new bifunctional probe uses glucose for cancer localisation and a boronic ester moiety for the rapid and specific detection of physiological amounts of H_2O_2 via PA, absorption and fluorescence spectroscopy. *In vitro* studies indicated no significant toxicity of the new bifunctional probe and demonstrated the specific uptake of the dye into the cytosol of cells. *In vivo* and *ex vivo* studies showed promising results with the absence of toxicity over four weeks, accumulation of the probe in tumour tissue accompanied with specific changes in the PA tumour spectra and the H_2O_2-dependent conversion of the activatable dye. Additionally, spectral unmixing approaches were introduced to successfully generate images indicating the presence of the new activatable contrast agent and its conversion product.

The results presented here, suggest the promising application of this approach for studying the interplay between tumourigenesis and oxidative stress *in vivo* with high spatial and temporal resolution. Building up from here, further work is required to improve the dye-structure to generate narrower absorption and PA peaks and greater spectral differences between the capped and uncapped dye, which would improve the applicability for further *in vivo* studies. Furthermore, it is necessary to advance the unmixing approach described in this thesis, for example by applying a fluence correction to the data. Should this work yield positive results, additional *in vivo* studies in more realistic orthotopic and transgenic mouse models should be carried out to investigate the feasibility of the approach to monitor tumour development and treatment response. Moreover, the contrast agent could then be combined

with the endogenous contrast of haemoglobin and oxyhaemoglobin to allow the visualisation of oxidative stress, tumour vascularisation and hypoxia at the same time *in vivo* (Figure 6.1).

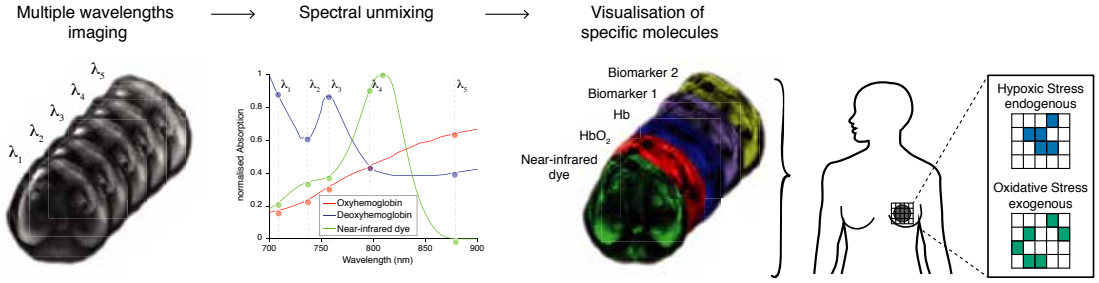

Figure 6.1 Multispectral optoacoustic tomography and its application for simultaneous visualisation of oxidative and hypoxic stress (adapted from ref. [258]).

Finally, different disease-specific targeting moieties should be explored to extend the use of this new activatable PA probe to the study of oxidative stress in a broad range of pathological conditions. This would facilitate the measurement and thus the investigation of the impact of H_2O_2 towards a specific pathological progress *in vivo*. The consequent knowledge about the interplay between ROS and disease development might then open new doors for therapeutic approaches.

6.2 Imaging Oxidative Stress and Amyloid Aggregates in Neurodegenerative Diseases with Single-Molecule Fluorescence Imaging.

Protein aggregation into amyloid deposits and oxidative stress are key features of many neurological disorders. Thus, new methods for the detection of ROS and protein aggregates are critical to advance our clinical understanding of neurodegeneration. Accordingly, the work presented here demonstrated bifunctional fluorescent probes for the simultaneous detection of both amyloid aggregates and H_2O_2.

A set of novel neutral and cationic fluorescent dyes derived from Thioflavin-T (ThT), the most common fluorescent dye used for the detection of amyloid fibrils, were first investigated in terms of their amyloid binding properties and unique bulk and single-aggregate fluorescence properties to gain a better understanding of the relationships between the chemical structure and these features. The neutral analogues, although exhibiting impaired optical

properties compared to ThT, revealed different binding sites compared to ThT and the charged derivatives. The charged dyes showed overall optical and binding properties competitive with ThT. Interestingly, one dye, mE10, showed superior properties and allowed the detection of early arising and more amorphous amyloid aggregates on a bulk and single aggregate level. Moreover, it has laid the foundation for the development of four bifunctional probes for amyloid aggregate and H_2O_2 sensing. These probes were based on the mE/E scaffold for amyloid detection and combined with a H_2O_2 reactive boronic ester functionality. Bulk and single aggregate measurements showed that two probes, BE1 and BE2, were able to successfully detect the simultaneous presence of both H_2O_2 and αSyn aggregates *in vitro*.

These findings form a promising foundation for studying earlier arising amyloid species as well as their interplay with increased levels of H_2O_2 *in vitro*. Continuing from here, further characterisation of mE10 as well as BE1 and BE2 using other amyloid proteins, cellular studies of neurodegeneration and human cerebrospinal fluid of patients would help to validate the feasibility of these new probes to detect and characterise potentially toxic oligomeric species and their interactions with H_2O_2. Furthermore, applying high resolution single molecule imaging techniques would enhance the sensitivity of the new probes and get a better insight into the aggregate-dye-H_2O_2 interaction during the different stages of protein aggregation. Therefore, it would also be necessary to interrogate more deeply the anti-aggregation properties of the dyes and how they are related to their chemical structure. This might additionally reveal a new avenue for new therapies. Finally, the knowledge gained about the relationship between chemical structure and photophysical and binding properties can now be implemented into multivalent probes. Combining the features of mE10 and BE1/2 into a such a multivalent probe design and expanding it to other high resolution imaging techniques, such as DNA-PAINT, might allow the development of multi-functional probes with superior binding and optical properties and to tune the selectivity to specific oligomeric structures and pathological proteins.

6.3 Concluding Remarks

ROS are critical biological parameters and play a dual role as both physiological and pathological agents. However, studying ROS generation and its function is limited by the current state-of-the-art methods.

Thus, there is a urgent need for better approaches to detect and quantify the different types of ROS in biological systems, especially *in vivo*. In developing such new probes it is important to understand the location of the probe within the organism and cell, the chemistry, reaction

kinetics and selectivity of the probe as well as its metabolism/decomposition. Furthermore, to minimise misinterpretation, it is crucial to understand the signal generation process, effects of the biological environment on the signal and the limitations of the applied detection method. Combining these considerations and applying them to biological validation studies in realistic animal models of disease, might allow a robust readout of the levels of a particular ROS within various tissues and cell types and how these levels change during disease development and treatment. This will then not only help to unravel the physiological and pathological roles of specific ROS *in vivo* but also allow one to assess the efficacy of redox-based therapies.

It is through the development and detailed characterisation of new ROS- and disease-specific imaging probes combined with suitable imaging technologies that research in the oxidative stress and free radical field will progress and new frontiers are reached.

Bibliography

[1] Judith Weber, Paul C Beard, and Sarah E Bohndiek. Contrast agents for molecular photoacoustic imaging. *Nature Methods*, 13(8):639–650, 7 2016.

[2] Michael P. Murphy, Arne Holmgren, Nils-Goran Larsson, Barry Halliwell, Christopher J. Chang, Balaraman Kalyanaraman, Sue Goo Rhee, Paul J. Thornalley, Linda Partridge, David Gems, Thomas Nystrom, Vsevolod Belousov, Paul T. Schumacker, and Christine C. Winterbourn. Unraveling the Biological Roles of Reactive Oxygen Species. *Cell Metabolism*, 13:361–366, 2011.

[3] Simone Reuter, Subash C. Gupta, Madan M. Chaturvedi, and Bharat B. Aggarwal. Oxidative stress, inflammation, and cancer: How are they linked? *Free Radical Biology and Medicine*, 49(11):1603–1616, 2010.

[4] G Dakubo. Mitochondrial reactive oxygen species and cancer. *Handbook of Free Radicals: Formation, Types and Effects*, pages 99–116, 2010.

[5] David Bar-or, Raphael Bar-or, Leonard T Rael, and Edward N Brody. Redox Biology Oxidative stress in severe acute illness. *Redox Biology*, 4:340–345, 2015.

[6] Lien Ai Pham-Huy, Hua He, and Chuong Pham-Huy. Free radicals, antioxidants in disease and health. *International journal of biomedical science : IJBS*, 4(2):89–96, 2008.

[7] Manish Mittal, Mohammad Rizwan Siddiqui, Khiem Tran, Sekhar P Reddy, and Asrar B Malik. Reactive oxygen species in inflammation and tissue injury. *Antioxidants & redox signaling*, 20(7):1126–67, 2014.

[8] Anu Rahal, Amit Kumar, Vivek Singh, Brijesh Yadav, Ruchi Tiwari, Sandip Chakraborty, and Kuldeep Dhama. Oxidative stress, prooxidants, and antioxidants: The interplay. *BioMed Research International*, 2014, 2014.

[9] Gregg L. Semenza. Hypoxia-inducible factors in physiology and medicine. *Cell*, 148(3):399–408, 2012.

[10] Lewis C. Cantley. The phosphoinositide 3-kinase pathway. *Science*, 296(5573):1655–1657, 2002.

[11] S. Perwez Hussain and Curtis C. Harris. Inflammation and cancer: An ancient link with novel potentials. *International Journal of Cancer*, 121(11):2373–2380, 2007.

[12] Alberto Mantovani, Alberto Mantovani, Paola Allavena, Paola Allavena, Antonio Sica, Antonio Sica, Frances Balkwill, and Frances Balkwill. Cancer-related inflammation. *Nature*, 454(7203):436–44, 2008.

[13] Sonia Gandhi and Andrey Y. Abramov. Mechanism of oxidative stress in neurodegeneration. *Oxidative Medicine and Cellular Longevity*, 2012.

[14] Bayani Uttara, Ajay V Singh, Paolo Zamboni, and R T Mahajan. Oxidative Stress and Neurodegenerative Diseases: A Review of Upstream and Downstream Antioxidant Therapeutic Options. *Current Neuropharmacology*, 7:65–74, 2009.

[15] Daria Ezeriņa, Bruce Morgan, and Tobias P. Dick. Imaging dynamic redox processes with genetically encoded probes. *Journal of Molecular and Cellular Cardiology*, 73:43–49, 2014.

[16] Jeroen Frijhoff, Paul Winyard, Neven Zarkovic, Sean Davies, Roland STocker, David Cheng, Annie Knight, Emma Taylor, Jeantette Oettrich, Tatjana Ruskova, Harald Schmidt, and Pietro Ghezzu. Clinical relevance of biomarkers of oxidative stress. *Antioxidants & redox signaling*, 2015.

[17] Barry Halliwell and Matthew Whiteman. Measuring reactive species and oxidative damage in vivo and in cell culture: how should you do it and what do the results mean? *British journal of pharmacology*, 142(2):231–55, 5 2004.

[18] Balaraman Kalyanaraman, Victor Darley-Usmar, Kelvin J.a. Davies, Phyllis a. Dennery, Henry Jay Forman, Matthew B. Grisham, Giovanni E. Mann, Kevin Moore, L. Jackson Roberts, and Harry Ischiropoulos. Measuring reactive oxygen and nitrogen species with fluorescent probes: challenges and limitations. *Free Radical Biology and Medicine*, 52(1):1–6, 2012.

[19] Evan W. Miller, Aaron E. Albers, Arnd Pralle, Ehud Y. Isacoff, and Christopher J. Chang. Boronate-based fluorescent probes for imaging cellular hydrogen peroxide. *Journal of the American Chemical Society*, 127(47):16652–16659, 2005.

[20] Bryan C. Dickinson, Calvin Huynh, and Christopher J. Chang. A palette of fluorescent probes with varying emission colors for imaging hydrogen peroxide signaling in living cells. *Journal of the American Chemical Society*, 132(23):5906–5915, 2010.

[21] Jennifer L. Martindale and Nikki J. Holbrook. Cellular response to oxidative stress: Signaling for suicide and survival. *Journal of Cellular Physiology*, 192(1):1–15, 2002.

[22] H. Zhao, J. Joseph, H. M. Fales, E. A. Sokoloski, R. L. Levine, J. Vasquez-Vivar, and B. Kalyanaraman. Detection and characterization of the product of hydroethidine and intracellular superoxide by HPLC and limitations of fluorescence. *Proceedings of the National Academy of Sciences*, 102(16):5727–5732, 2005.

[23] Peter Wardman. Fluorescent and luminescent probes for measurement of oxidative and nitrosative species in cells and tissues: Progress, pitfalls, and prospects. *Free Radical Biology and Medicine*, 43(7):995–1022, 2007.

[24] B. Halliwell and J.M.C. Gutteridge. *Free Radicals in Biology and Medicine.* Oxford University Press, Oxford, 4 edition, 2007.

[25] Bryan C Dickinson, Vivian S Lin, and Christopher J Chang. Preparation and use of MitoPY1 for imaging hydrogen peroxide in mitochondria of live cells. *Nature protocols*, 8(6):1249–59, 2013.

[26] Colette T. Dooley, Timothy M. Dore, George T. Hanson, W. Coyt Jackson, S. James Remington, and Roger Y. Tsien. Imaging dynamic redox changes in mammalian cells with green fluorescent protein indicators. *Journal of Biological Chemistry*, 279(21):22284–22293, 2004.

[27] Bruce Morgan, Mirko C. Sobotta, and Tobias P. Dick. Measuring EGSH and H2O2 with roGFP2-based redox probes. *Free Radical Biology and Medicine*, 51(11):1943–1951, 2011.

[28] Vladimir L Kolossov, Bryan Q Spring, Robert M Clegg, Jennifer J Henry, Anna Sokolowski, Paul J a Kenis, and H Rex Gaskins. Development of a high-dynamic range, GFP-based FRET probe sensitive to oxidative microenvironments. *Experimental biology and medicine (Maywood, N.J.)*, 236(6):681–691, 2011.

[29] Evan W. Millera, Bryan C. Dickinson, and Christopher J. Chang. Aquaporin-3 mediates hydrogen peroxide uptake to regulate downstream intracellular signaling. *PNAS*, 107(36):15681–15686, 2010.

[30] Valerie Carroll, Brian W Michel, Joseph Blecha, Henry Vanbrocklin, Kayvan Keshari, David Wilson, and Christopher J Chang. A Boronate-Caged [18 F]FLT Probe for Hydrogen Peroxide Detection Using Positron Emission Tomography. *Journal of the American Chemical Society*, 136:14742–14745, 2014.

[31] Fuminori Hyodo, Ryan M. Davis, Emi Hyodo, Shingo Matsumoto, Murali C. Krishna, and James B. Mitchell. The relationship between tissue oxygenation and redox status using magnetic resonance imaging. *International Journal of Oncology*, 41(6):2103–2108, 2012.

[32] Sarah E Bohndiek, Mikko I Kettunen, De-en Hu, Brett W C Kennedy, Joan Boren, Ferdia a Gallagher, and Kevin M Brindle. Hyperpolarized [1-13C]-ascorbic and dehydroascorbic acid: vitamin C as a probe for imaging redox status in vivo. *Journal of the American Chemical Society*, 133(30):11795–801, 2011.

[33] M. L. James and S. S. Gambhir. A Molecular Imaging Primer: Modalities, Imaging Agents, and Applications. *Physiological Reviews*, 92(2):897–965, 2012.

[34] M. a. Pysz, S. S. Gambhir, and J. K. Willmann. Molecular imaging: current status and emerging strategies. *Clinical Radiology*, 65(7):500–516, 2010.

[35] Liming Nie, Shouju Wang, Xiaoyong Wang, Pengfei Rong, Ying Ma, Gang Liu, Peng Huang, Guangming Lu, and Xiaoyuan Chen. In vivo volumetric photoacoustic molecular angiography and therapeutic monitoring with targeted plasmonic nanostars. *Small*, 10(8):1585–1593, 2014.

[36] T. Ido, C-N. Wan, V. Casella, J. S. Fowler, A. P. Wolf, M. Reivich, and D. E. Kuhl. Labeled 2-deoxy-D-glucose analogs. 18F-labeled 2-deoxy-2-fluoro-D-glucose, 2-deoxy-2-fluoro-D-mannose and 14C-2-deoxy-2-fluoro-D-glucose. *Labelled Compounds and Radiopharmaceutics*, 1978.

[37] Anca Dragulescu-Andrasi, Sri Rajasekhar Kothapalli, Grigory a. Tikhomirov, Jianghong Rao, and Sanjiv S. Gambhir. Activatable oligomerizable imaging agents for photoacoustic imaging of furin-like activity in living subjects. *Journal of the American Chemical Society*, 135:11015–11022, 2013.

[38] Yasuteru Urano, Daisuke Asanuma, Yukihiro Hama, Yoshinori Koyama, Tristan Barrett, Mako Kamiya, Tetsuo Nagano, Toshiaki Watanabe, Akira Hasegawa, Peter L Choyke, and Hisataka Kobayashi. Selective molecular imaging of viable cancer cells with pH-activatable fluorescence probes. *Nature medicine*, 15(1):104–109, 2009.

[39] W.E Klunk, H. Engler, A. Nordberg, Y. Wang, G. Blomqvist, D.P. Holt, M. Bergstroem, I. Savitcheva, G.F. Huang, S. Estrada, and B. Ausen. Imaging Brain Amyloid in Alzheimer's Disease with Pittsburgh Compound-B. *Annals of Neurology*, 55:306–319, 2004.

[40] Minsig Choi, Lance K. Heilbrun, Raghu Venkatramanamoorthy, Jawana M. Lawhorn-Crews, Mark M. Zalupski, and Anthony F. Shields. Using 18F-fluorodeoxyglucose positron emission tomography to monitor clinical outcomes in patients treated with neoadjuvant chemo-radiotherapy for locally advanced pancreatic cancer. *American Journal of Clinical Oncology: Cancer Clinical Trials*, 33(3):257–261, 2010.

[41] Christian Tiede, Anna a S Tang, Sarah E. Deacon, Upasana Mandal, Joanne E. Nettleship, Robin L. Owen, Suja E. George, David J. Harrison, Raymond J. Owens, Darren C. Tomlinson, and Michael J. McPherson. Adhiron: A stable and versatile peptide display scaffold for molecular recognition applications. *Protein Engineering, Design and Selection*, 27(5):145–155, 2014.

[42] J. Löfblom, J. Feldwisch, V. Tolmachev, J. Carlsson, S. Ståhl, and F. Y. Frejd. Affibody molecules: Engineered proteins for therapeutic, diagnostic and biotechnological applications. *FEBS Letters*, 584(12):2670–2680, 2010.

[43] Hongguang Sun, Xun Zhu, Patrick Y Lu, Roberto R Rosato, Wen Tan, and Youli Zu. Oligonucleotide aptamers: new tools for targeted cancer therapy. *Molecular therapy. Nucleic acids*, 3(April):e182, 2014.

[44] Tove Olafsen and Anna M. Wu. Antibody Vectors for Imaging. *Seminars in Nuclear Medicine*, 40(3):167–181, 2010.

[45] Seulki Lee, Jin Xie, and Xiaoyuan Chen. Peptides and peptide Hormones for Molecular Imaging and Disease Diagnosis. *Chemical Reviews*, 110(5):3087–3111, 2011.

[46] Y Matsumura and H Maeda. A new concept for macromolecular therapeutics in cancer chemotherapy: mechanism of tumoritropic accumulation of proteins and the antitumor agents Smancs. *Cancer research*, 46(December):6387– 6392, 1986.

[47] Joseph W. Nichols and You Han Bae. EPR: Evidence and fallacy. *Journal of Controlled Release*, 190:451–464, 2014.

[48] Mark W Dewhirst, Yiting T Cao, and Benjamin Moeller. Cycling hypoxia and free radicals regulate angiogenesis and radiotherapy response. *Nature reviews. Cancer*, 8(june):425–437, 2008.

[49] R K Jain. Vascular and interstitial barriers to delivery of therapeutic agents in tumors. *Cancer metastasis reviews*, 9:253–266, 1990.

[50] Jesse V. Jokerst, Adam J. Cole, Dominique Van De Sompel, and Sanjiv S. Gambhir. Gold nanorods for ovarian cancer detection with photoacoustic imaging and resection guidance via Raman imaging in living mice. *ACS Nano*, 6(11):10366–10377, 2012.

[51] Kengo Kanazaki. Development of human serum albumin conjugated with near-infrared dye for photoacoustic tumor imaging with near-infrared dye for photoacoustic tumor. *Journal of Biomedical Optics*, 19(9):096002–1, 2014.

[52] Naama Karton-Lifshin, Ehud Segal, Liora Omer, Moshe Portnoy, Ronit Satchi-Fainaro, and Doron Shabat. A unique paradigm for a turn-ON near-infrared cyanine-based probe: Noninvasive intravital optical imaging of hydrogen peroxide. *Journal of the American Chemical Society*, 133(28):10960–10965, 2011.

[53] Vsevolod V. Belousov, Arkady F. Fradkov, Konstantin A. Lukyanov, Dmitry B. Staroverov, Konstantin S. Shakhbazov, Alexey V. Terskikh, and Sergey Lukyanov. Genetically encoded fluorescent indicator for intracellular hydrogen peroxide. *Nature Methods*, 3(4):281–286, 2006.

[54] Vasilis Ntziachristos, Jorge Ripoll, Lihong V Wang, and Ralph Weissleder. Looking and listening to light: the evolution of whole-body photonic imaging. *Nature biotechnology*, 23(3):313–320, 2005.

[55] Pc Beard. Biomedical Photoacoustic Imaging. *Interface Focus*, 1(4):602–631, 2011.

[56] Yi Wang and Ruikang Wang. Photoacoustic recovery of an absolute optical absorption coefficient with an exact solution of a wave equation. *Phys. Med. Biol.*, 53(21):6167–77, 2008.

[57] G M Hale and M R Querry. Optical Constants of Water in the 200-nm to 200-microm Wavelength Region. *Applied optics*, 12(3):555–563, 1973.

[58] R. L. P. van Veen, H. J. C. M. Sterenborg, A. Pifferi, A. Torricelli, E. Chikoidze, and R. Cubeddu. Determination of visible near-IR absorption coefficients of mammalian fat using time- and spatially resolved diffuse reflectance and transmission spectroscopy. *Journal of Biomedical Optics*, 10(5):054004, 2005.

[59] Ben Cox, Jan G. Laufer, Simon R. Arridge, and Paul C. Beard. Quantitative spectroscopic photoacoustic imaging: a review. *Journal of Biomedical Optics*, 17(6):061202, 2012.

[60] Stéphanie Vial, Christelle Mansuy, Sandrine Sagan, Theano Irinopoulou, Fabienne Burlina, Jean Paul Boudou, Gérard Chassaing, and Solange Lavielle. Peptide-grafted nanodiamonds: Preparation, cytotoxicity and uptake in cells. *ChemBioChem*, 9(13):2113–2119, 2008.

[61] Shai Ashkenazi. Photoacoustic lifetime imaging of dissolved oxygen using methylene blue. *Journal of biomedical optics*, 15(4):040501, 2010.

[62] Satoru Onoe, Takashi Temma, Yoichi Shimizu, Masahiro Ono, and Hideo Saji. Investigation of cyanine dyes for in vivo optical imaging of altered mitochondrial membrane potential in tumors. *Cancer medicine*, 3(4):775–86, 2014.

[63] Nam-Young Kang, Sung-Jin Park, Xiao Wei Emmiline Ang, Animesh Samanta, Wouter H P Driessen, Vasilis Ntziachristos, Kristine O Vasquez, Jeffrey D Peterson, Seong-Wook Yun, and Young-Tae Chang. A macrophage uptaking near-infrared chemical probe for in vivo imaging of inflammation. *Chemical communications (Cambridge, England)*, 50:6589–91, 2014.

[64] N. Beziere and V. Ntziachristos. Optoacoustic Imaging of Naphthalocyanine: Potential for Contrast Enhancement and Therapy Monitoring. *Journal of Nuclear Medicine*, 56(2):323–328, 2014.

[65] Helena de Puig, Justina O. Tam, Chun-Wan Yen, Lee Gehrke, and Kimberly Hamad-Schifferli. Extinction Coefficient of Gold Nanostars. *The Journal of Physical Chemistry C*, 119(30):17408–17415, 2015.

[66] Kanyi Pu, Adam J Shuhendler, Jesse V Jokerst, Jianguo Mei, Sanjiv S Gambhir, Zhenan Bao, and Jianghong Rao. Semiconducting polymer nanoparticles as photoacoustic molecular imaging probes in living mice. *Nature nanotechnology*, 9(3):233–9, 2014.

[67] Jonathan F Lovell, Cheng S Jin, Elizabeth Huynh, Honglin Jin, Chulhong Kim, John L Rubinstein, Warren C W Chan, Weiguo Cao, Lihong V Wang, and Gang Zheng. Porphysome nanovesicles generated by porphyrin bilayers for use as multimodal biophotonic contrast agents. *Nature materials*, 10(4):324–332, 2011.

[68] Lule Beqa, Zhen Fan, Anant Kumar Singh, Dulal Senapati, and Paresh Chandra Ray. Gold nano-popcorn attached SWCNT hybrid nanomaterial for targeted diagnosis and photothermal therapy of human breast cancer cells. *ACS Applied Materials and Interfaces*, 3(9):3316–3324, 2011.

[69] Jesse V Jokerst, Dominique Van de Sompel, Sarah E Bohndiek, and Sanjiv S Gambhir. Cellulose Nanoparticles are a Biodegradable Photoacoustic Contrast Agent for Use in Living Mice. *Photoacoustics*, 2(3):119–127, 2014.

[70] Avinash Srivatsan, Samir V. Jenkins, Mansik Jeon, Zhijin Wu, Chulhong Kim, Jingyi Chen, and Ravindra K. Pandey. Gold nanocage-photosensitizer conjugates for dual-modal image-guided enhanced photodynamic therapy. *Theranostics*, 4(2):163–174, 2014.

[71] Alexei P. Leonov, Jiwen Zheng, Jeffrey D. Clogston, Stephan T. Stern, Anil K. Patri, and Alexander Wei. Detoxification of gold nanorods by treatment with polystyrenesulfonate. *ACS Nano*, 2(12):2481–2488, 2008.

[72] Juan Hu, Xianglong Zhu, Hui Li, Zhenghuan Zhao, Xiaoqin Chi, Guoming Huang, Dengtong Huang, Gang Liu, Xiaomin Wang, and Jinhao Gao. Theranostic Au cubic nano-aggregates as potential photoacoustic contrast and photothermal therapeutic agents. *Theranostics*, 4(5):534–545, 2014.

[73] Wei Lu, Marites P. Melancon, Chiyi Xiong, Qian Huang, Andrew Elliott, Shaoli Song, Rui Zhang, Leo G. Flores, Juri G. Gelovani, Lihong V. Wang, Geng Ku, R. Jason Stafford, and Chun Li. Effects of photoacoustic imaging and photothermal ablation therapy mediated by targeted hollow gold nanospheres in an orthotopic mouse xenograft model of glioma. *Cancer Research*, 71:6116–6121, 2011.

[74] T. Stahl, T. Allen, and P. Beard. Characterization of the thermalisation efficiency and photostability of photoacoustic contrast agents. *Proc. of SPIE*, 8943:89435H, 2014.

[75] Muhammad Rameez Chatni, Jun Xia, Rebecca Sohn, Konstantin Maslov, Zijian Guo, Yu Zhang, Kun Wang, Younan Xia, Mark Anastasio, Jeffrey Arbeit, and Lihong V. Wang. Tumor glucose metabolism imaged in vivo in small animals with whole-body photoacoustic computed tomography. *Journal of Biomedical Optics*, 17:076012, 2012.

[76] Hua Gong, Ziliang Dong, Yumeng Liu, Shengnan Yin, Liang Cheng, Wenyao Xi, Jian Xiang, Kai Liu, Yonggang Li, and Zhuang Liu. Engineering of multifunctional nanomicelles for combined photothermal and photodynamic therapy under the guidance of multimodal imaging. *Advanced Functional Materials*, pages 1–11, 2014.

[77] Neus Lozano, Zahraa S. Al-Ahmady, Nicolas S Beziere, Vasilis Ntziachristos, and Kostas Kostarelos. Monoclonal antibody-targeted PEGylated liposome-ICG encapsulating doxorubicin as a potential theranostic agent. *International Journal of Pharmaceutics*, 482(1-2):2–10, 2015.

[78] Mohammad Eghtedari, Mohammad Eghtedari, Anton V Liopo, Anton V Liopo, John a Copland, John a Copland, Alexander a Oraevsky, Alexander a Oraevsky, Massoud Motamedi, and Massoud Motamedi. Engineering of hetero-functional gold nanorods for the in vivo molecular targeting of breast cancer cells. *Nano letters*, 9(1):287–91, 2009.

[79] Jing Lin, Shouju Wang, Peng Huang, Zhe Wang, Shouhui Chen, Gang Niu, Wanwan Li, Jie He, Daxiang Cui, Guangming Lu, Xiaoyuan Chen, and Zhihong Nie. Photosensitizer-loaded gold vesicles with strong plasmonic coupling effect for imaging-guided photothermal/photodynamic therapy. *ACS Nano*, 7(6):5320–5329, 2013.

[80] Zannatul Yasmin, Edward Khachatryan, Yuan-hao Lee, Saher Maswadi, Randolph Glickman, and Kelly L Nash. In vitro monitoring of oxidative processes with self-aggregating gold nanoparticles using all-optical photoacoustic spectroscopy. *Biosensors and Bioelectronic*, 64:676–682, 2015.

[81] Peter P. Fu, Qingsu Xia, Huey Min Hwang, Paresh C. Ray, and Hongtao Yu. Mechanisms of nanotoxicity: Generation of reactive oxygen species. *Journal of Food and Drug Analysis*, 22(1):64–75, 2014.

[82] Satoru Onoe, Takashi Temma, Kengo Kanazaki, Masahiro Ono, and Hideo Saji. Development of photostabilized asymmetrical cyanine dyes for in vivo photoacoustic imaging of tumors. *Journal of Biomedical Optics*, 20(9):096006, 2015.

[83] Ga Reynolds and Kh Drexhage. Stable heptamethine pyrylium dyes that absorb in the infrared. *The Journal of Organic Chemistry*, 42(5):885–888, 1977.

[84] A.J.M. Wollman and M.C Leake. *Single-Molecule Narrow-Field Microscopy of Protein–DNA Binding Dynamics in Glucose Signal Transduction of Live Yeast Cells.* Humana Press, New York, vol 1431 edition, 2016.

[85] Susan Cox. Super-resolution imaging in live cells. *Developmental biology*, 401(1):175–81, 2015.

[86] Lothar Schermelleh, Rainer Heintzmann, and Heinrich Leonhardt. A guide to super-resolution fluorescence microscopy. *The journal of cell biology*, 190(2):165–175, 2010.

[87] Bo Huang, Hazen Babcock, and Xiaowei Zhuang. Breaking the diffraction barrier: Super-resolution imaging of cells. *Cell*, 143(7):1047–1058, 2010.

[88] Raimund J. Ober, Sripad Ram, and E. Sally Ward. Localization Accuracy in Single-Molecule Microscopy. *Biophysical Journal*, 86(2):1185–1200, 2004.

[89] Michael J. Rust, Mark Bates, and Xiaowei Zhuang. Sub-diffraction-limit imaging by stochastic optical reconstruction microscopy (STORM). *Nature Methods*, 3(10):793–795, 2006.

[90] E Betzig, G H Patterson, R Sougrat, O W Lindwasser, S Olenych, J S Bonifacino, M W Davidson, J Lippincott-Schwartz, and H F Hess. Imaging Intracellular Fluorescent Proteins at Nanometer Resolution. *Science*, 313(5793):1642–1645, 2006.

[91] Samuel T. Hess, Thanu P.K. Girirajan, and Michael D. Mason. Ultra-high resolution imaging by fluorescence photoactivation localization microscopy. *Biophysical Journal*, 91(11):4258–4272, 2006.

[92] A. Sharonov and R. M. Hochstrasser. Wide-field subdiffraction imaging by accumulated binding of diffusing probes. *Proceedings of the National Academy of Sciences*, 103(50):18911–18916, 2006.

[93] Daniel Axelrod. Total internal reflection fluorescence microscopy in cell biology [Review]. *Traffic*, 2(2):764–774, 2001.

[94] Bernard Valeur. *Molecular Fluorescence Principles and Applications*. Wiley, 2001.

[95] Sebastian Van De Linde and Markus Sauer. How to switch a fluorophore: From undesired blinking to controlled photoswitching. *Chemical Society Reviews*, 43(4):1076–1087, 2014.

[96] Masafumi Minoshima and Kazuya Kikuchi. Photostable and photoswitching fluorescent dyes for super-resolution imaging. *Journal of Biological Inorganic Chemistry*, 22(5):639–652, 2017.

[97] Rob Zondervan, Florian Kulzer, Sergei B. Orlinskii, and Michel Orrit. Photoblinking of Rhodamine 6G in Poly(vinyl alcohol): Radical Dark State Formed through the Triplet. *J. Phys. Chem. A*, 107:6770–6776, 2003.

[98] Mark A. Haidekker and Emmanuel A. Theodorakis. Environment-sensitive behavior of fluorescent molecular rotors. *Journal of Biological Engineering*, 4:1–14, 2010.

[99] K.H. Drexhage. Fluorescence efficiency of laser dyes. *Journal of Research of the National Bureau of Standards Section A: Physics and Chemistry*, 80A(3):421, 1976.

[100] Andrey S. Klymchenko. Solvatochromic and Fluorogenic Dyes as Environment-Sensitive Probes: Design and Biological Applications. *Accounts of Chemical Research*, 50(2):366–375, 2017.

[101] Steven F. Lee, Quentin Vérolet, and Alexandre Fürstenberg. Improved super-resolution microscopy with oxazine fluorophores in heavy water. *Angewandte Chemie - International Edition*, 52(34):8948–8951, 2013.

[102] Lubert Stryer. Excited-State Proton-Transfer Reactions. A Deuterium Isotope Effect on Fluorescence. *Journal of the American Chemical Society*, 88(24):5708–5712, 1966.

[103] Venus Sosa, Teresa Moliné, Rosa Somoza, Rosanna Paciucci, Hiroshi Kondoh, and Matilde E. LLeonart. Oxidative stress and cancer: An overview. *Ageing Research Reviews*, 12(1):376–390, 2013.

[104] Joshua a. Hess and Mohamad K. Khasawneh. Cancer metabolism and oxidative stress: Insights into carcinogenesis and chemotherapy via the non-dihydrofolate reductase effects of methotrexate. *BBA Clinical*, 3:152–161, 2015.

[105] Xuan Zhang, Lun Zhang, Yaqian Liu, Bin Bao, Yi Zang, Jia Li, and Wei Lu. A near-infrared fluorescent probe for rapid detection of hydrogen peroxide in living cells. *Analyst*, 141:2380–2383, 2016.

[106] Dongjian Zhu, Guoping Li, Lin Xue, and Hua Jiang. Development of ratiometric near-infrared fluorescent probes using analyte-specific cleavage of carbamate. *Organic and Biomolecular Chemistry*, 11(28):4577–4580, 2013.

[107] Sheng Cao, Robin Christiansen, and Xiaohua Peng. Substituent effects on oxidation-induced formation of quinone methides from arylboronic ester precursors. *Chemistry - A European Journal*, 19(27):9050–9058, 2013.

[108] Yunyan Kuang, Kumudha Balakrishnan, Varsha Gandhi, and Xiaohua Peng. Hydrogen peroxide inducible DNA cross-linking agents: Targeted anticancer prodrugs. *Journal of the American Chemical Society*, 133(48):19278–19281, 2011.

[109] James Joseph, Kevin N. Baumann, Philipp Koehler, Tim J. Zuehlsdorff, Daniel J. Cole, Judith Weber, Sarah E. Bohndiek, and Silvia Hernández-Ainsa. Distance dependent photoacoustics revealed through DNA nanostructures. *Nanoscale*, 9(42):16193–16199, 2017.

[110] Kai Yang, Lei Zhu, Liming Nie, Xiaolian Sun, Liang Cheng, Chenxi Wu, Gang Niu, Xiaoyuan Chen, and Zhuang Liu. Visualization of protease activity in vivo using an activatable photo-acoustic imaging probe based on CuS nanoparticles. *Theranostics*, 4(2):134–141, 2014.

[111] Jelena Levi, Sri-Rajashekar Kothapalli, Sarah Bohndiek, Joon-Kee Yoon, Anca Dragulescu-Andrasi, Carsten Nielsen, Aleksandra Tisma, Sunil Bodapati, Gayatri Gowrishankar, Xinrui Yan, Carmel Chan, Daniela Starcevic, and Sanjiv Sam Gambhir.

Molecular Photoacoustic Imaging of Follicular Thyroid Carcinoma. *Clinical Cancer Research*, 19:1494–1502, 2013.

[112] Christopher J. Reinhardt, Effie Y. Zhou, Michael D. Jorgensen, Gina Partipilo, and Jefferson Chan. A Ratiometric Acoustogenic Probe for in Vivo Imaging of Endogenous Nitric Oxide. *Journal of the American Chemical Society*, 140(3):1011–1018, 2018.

[113] Jelena Levi, Sri-Rajashekar Kothapalli, Sarah Bohndiek, Joon-Kee Yoon, Anca Dragulescu-Andrasi, Carsten Nielsen, Aleksandra Tisma, Sunil Bodapati, Gayatri Gowrishankar, Xinrui Yan, Carmel Chan, Daniela Starcevic, and Sanjiv Sam Gambhir. Molecular photoacoustic imaging of follicular thyroid carcinoma. *Clinical Cancer Research*, 19(6):1494–1502, 2013.

[114] Anurag Mishra, Yuanyuan Jiang, Sheryl Roberts, Vasilis Ntziachristos, and Gil G. Westmeyer. Near-infrared photoacoustic imaging probe responsive to calcium. *Analytical Chemistry*, 88(22):10785–10789, 2016.

[115] Sheryl Roberts, Markus Seeger, Yuanyuan Jiang, Anurag Mishra, Felix Sigmund, Anja Stelzl, Antonella Lauri, Panagiotis Symvoulidis, Hannes Rolbieski, Matthias Preller, X. Luís Deán-Ben, Daniel Razansky, Tanja Orschmann, Sabrina C. Desbordes, Paul Vetschera, Thorsten Bach, Vasilis Ntziachristos, and Gil G. Westmeyer. Calcium Sensor for Photoacoustic Imaging. *Journal of the American Chemical Society*, 140(8):2718–2721, 2018.

[116] Hailey J. Knox, Jamila Hedhli, Tae Wook Kim, Kian Khalili, Lawrence W. Dobrucki, and Jefferson Chan. A bioreducible N-oxide-based probe for photoacoustic imaging of hypoxia. *Nature Communications*, 8(1), 2017.

[117] Alexander P. Gorka, Roger R. Nani, and Martin J. Schnermann. Cyanine polyene reactivity: scope and biomedical applications. *Organic and Biomolecular Chemistry*, 13(28):7584–7598, 2015.

[118] A. Mishra, R.K. Behera, P.K. Behera, B.K. Mishra, and B.B. Gopa. Cyanines during the 1990a: A Review. *Chemical Reviews*, 100:1973–2011, 2000.

[119] Heinz Mustroph, Knut Reiner, Jürgen Mistol, Steffen Ernst, Dietmar Keil, and Lothar Hennig. Relationship between the Molecular Structure of Cyanine Dyes and the Vibrational Fine Structure of their Electronic Absorption Spectra. *ChemPhysChem*, 10(5):835–840, 2009.

[120] Ragheb F. Atmeh, Isam M. Arafa, and Maysoon Al-Khateeb. Albumin Aggregates: Hydrodynamic Shape and Physico-Chemical Properties. *Jordan Journal of Chemistry*, 2(2):169–182, 2007.

[121] Swati R. Mujumdar, Ratnakar B. Mujumdar, Charsetta M. Grant, and Alan S. Waggoner. Cyanine-labeling reagents: Sulfobenzindocyanine succinimidyl esters. *Bioconjugate Chemistry*, 7(3):356–362, 1996.

[122] Kada Yesudas. Cationic cyanine dyes: Impact of symmetry-breaking on optical absorption and third-order polarizabilities. *Physical Chemistry Chemical Physics*, 15(44):19465–19477, 2013.

[123] Narasimhachari Narayanan and Gabor Patonay. A New Method for the Synthesis of Heptamethine Cyanine Dyes: Synthesis of New Near-Infrared Fluorescent Labels. *J. Org. Chem.*, 60(17):2391–2395, 1995.

[124] Zongren Zhang and Samuel Achilefu. Synthesis and evaluation of polyhydroxylated near-infrared carbocyanine molecular probes. *Organic letters*, 6(12):2067–2070, 2004.

[125] Jun Yin, Younghee Kwon, Dabin Kim, Dayoung Lee, Gyoungmi Kim, Ying Hu, Ji Hwan Ryu, and Juyoung Yoon. Cyanine-based fluorescent probe for highly selective detection of glutathione in cell cultures and live mouse tissues. *Journal of the American Chemical Society*, 136:5351–5358, 2014.

[126] Xu Wang, Jianzheng Lv, Xueying Yao, Yong Li, Fang Huang, Mengmeng Li, Jie Yang, Xiuyun Ruan, and Bo Tang. Screening and investigation of a cyanine fluorescent probe for simultaneous sensing of glutathione and cysteine under single excitation. *Chem. Commun.*, 50(97):15439–15442, 2014.

[127] Soo Yeon Lim, Keum Hee Hong, Dae Il Kim, Hyockman Kwon, and Hae Jo Kim. Tunable heptamethine-azo dye conjugate as an NIR fluorescent probe for the selective detection of mitochondrial glutathione over cysteine and homocysteine. *Journal of the American Chemical Society*, 136:7018–7025, 2014.

[128] Dabin Kim, Gyoungmi Kim, Sang-Jip Nam, Jun Yin, and Juyoung Yoon. Visualization of Endogenous and Exogenous Hydrogen Peroxide Using A Lysosome-Targetable Fluorescent Probe. *Scientific Reports*, 5:8488, 2015.

[129] Banghe Zhu, John Rasmussen, Litorja Maritoni, and Eva Sevick-Muraca. Determining the Performance of Fluorescence Molecular Imaging Devices using Traceable Working Standards with SI Units of Radiance. *IEEE Transactions on Medical Imaging*, 0062(c):1–1, 2015.

[130] Hirendra N. Ghosh, Katrin Adamczyk, Sandeep Verma, Jens Dreyer, and Erik T J Nibbering. On the role of hydrogen bonds in photoinduced electron-transfer dynamics between 9-fluorenone and amine solvents. *Chemistry - A European Journal*, 18(16):4930–4937, 2012.

[131] Kaushik Thanki, Varun Kushwah, and Sanyog Jain. *Targeted Drug Delivery : Concepts and Design*. Springer, 2015.

[132] Federico Lucantoni, Heiko Dussmann, and Jochen H. M. Prehn. Metabolic Targeting of Breast Cancer Cells With the 2-Deoxy-D-Glucose and the Mitochondrial Bioenergetics Inhibitor MDIVI-1. *Frontiers in Cell and Developmental Biology*, 6(September):1–12, 2018.

[133] Joy L. Kovar, William Volcheck, Eva Sevick-Muraca, Melanie a. Simpson, and D. Michael Olive. Characterization and performance of a near-infrared 2-deoxyglucose optical imaging agent for mouse cancer models. *Analytical Biochemistry*, 384(2):254–262, 2009.

[134] J Czernin. Clinical applications of FDG-PET in oncology. *Acta medica Austriaca*, 29(5):162–70, 2002.

[135] Matthew Vander Heiden, Lewis Cantley, and Craig Thompson. Understanding the Warburg effect: The metabolic Requiremetns of cell proliferation. *Science*, 324(5930):1029–1033, 2009.

[136] Min Yu, Han Yongzhi, Shengying Chen, Xiaodan Luo, Ye Lin, Yu Zhou, Haosheng Jin, Baohua Hou, Yanying Deng, Lei Tu, and Zhixiang Jian. The prognostic value of GLUT1 in cancers: a systematic review and meta-analysis. *Oncotarget*, 8(26):43356–43367, 2017.

[137] Hongming Zhuang, Michael Pourdehnad, Eric S. Lambright, Alvin J. Yamamoto, Michael Lanuti, Peiyong Li, P. David Mozley, Milton D. Rossman, Steven M. Albelda, and Abass Alavi. Dual Time Point 18F-FDG PET Imaging for Differentiating Malignant from Inflammatory Processes. *J Nucl Med*, 42(9):1412–1417, 2001.

[138] H. Jadvar, A. Alavi, and S. S. Gambhir. 18F-FDG Uptake in Lung, Breast, and Colon Cancers: Molecular Biology Correlates and Disease Characterization. *Journal of Nuclear Medicine*, 50(11):1820–1827, 2009.

[139] L. Sokoloff, M. Reivich, C. Kennedy, M. H.Des Rosiers, C. S. Patlak, K. D. Pettigrew, O. Sakurada, and M. Shinohara. the [14C]Deoxyglucose Method for the Measurement of Local Cerebral Glucose Utilization: Theory, Procedure, and Normal Values in the Conscious and Anesthetized Albino Rat. *Journal of Neurochemistry*, 28(5):897–916, 1977.

[140] H. Lodish, A. Berk, and S.L. Zipursky. *Molecular Cell Biology - Uniporter-Catalyzed Transport*. W. H. Freeman and Company, New York, 4th editio edition, 2000.

[141] Jeffery S. Reynolds, Tamara L. Troy, Ralf H. Mayer, Alan B. Thompson, David J. Waters, Karen K. Cornell, Paul W. Snyder, and Eva M. Sevick-Muraca. Imaging of spontaneous canine mammary tumors using fluorescent contrast agents. *Photochemistry and Photobiology*, 70(1):87–94, 1999.

[142] Vasilis Ntziachristos and Daniel Razansky. Molecular imaging by means of multispectral optoacoustic tomography (MSOT). *Chemical reviews*, 110(5):2783–94, 5 2010.

[143] M. L. Landsman, G. Kwant, G. A. Mook, and W. G. Zijlstra. Light-absorbing properties, stability, and spectral stabilization of indocyanine green. *Journal of applied physiology (Bethesda, Md. : 1985)*, 40(4):575–583, 1976.

[144] K Licha, B Riefke, Vasilis Ntziachristos, A Becker, B Chance, and W Semmler. Hydrophilic cyanine dyes as contrast agents for near-infrared tumor imaging: synthesis, photophysical properties and spectroscopic in vivo characterization. *Photochemistry and photobiology*, 72(3):392–398, 2000.

[145] Megan S. Michie, Ralph Götz, Christian Franke, Matthew Bowler, Nikita Kumari, Valentin Magidson, Marcia Levitus, Jadranka Loncarek, Markus Sauer, and Martin J. Schnermann. Cyanine Conformational Restraint in the Far-Red Range. *Journal of the American Chemical Society*, 139(36):12406–12409, 2017.

[146] R. Nikolai, A. Carole, and L. Xiaohai. Dyes for labelling molecular ligands., 2013.

[147] Shen Gene and Yue Stephen. Functionalized cyanine dyes., 2012.

[148] Vikram Dogra, Bhargava Chinni, Shalini Singh, Hans Schmitthenner, Navalgund Rao, John J. Krolewski, and Kent L. Nastiuk. Photoacoustic imaging with an acoustic lens detects prostate cancer cells labeled with PSMA-targeting near-infrared dye-conjugates. *Journal of Biomedical Optics*, 21(6):066019, 2016.

[149] James Joseph, Philipp Koehler, Tim J Zuehlsdorff, Daniel J Cole, Kevin N Baumann, Judith Weber, Sarah E Bohndiek, and Silvia Hernández-ainsa. Photoacoustic molecular rulers based on DNA nanostructures. pages 1–15, 2017.

[150] Hugo E Gottlieb, Vadim Kotlyar, and Abraham Nudelman. NMR Chemical Shifts of Common Laboratory Solvents as Trace Impurities. *The Journal of Organic Chemistry*, 62(3):7512–7515, 1997.

[151] Ajay K. Bose, Maghar S. Manhas, Suhas Pednekar, Subhendu N. Ganguly, Hoang Dang, William He, and Arun Mandadi. Large scale Biginelli reaction via water-based biphasic media: A green chemistry strategy. *Tetrahedron Letters*, 46(11):1901–1903, 2005.

[152] Yoichi Shimizu, Takashi Temma, and Isao Hara. Development of Novel Nanocarrier-Based Near-Infrared Optical Probes for In Vivo Tumor Imaging. pages 719–727, 2012.

[153] Nicola J. Clegg, Sreenivasan Paruthiyil, Dale C. Leitman, and Thomas S. Scanlan. Differential response of estrogen receptor subtypes to 1,3-diarylindene and 2,3-diarylindene ligands. *Journal of Medicinal Chemistry*, 48(19):5989–6003, 2005.

[154] M. J. Frisch, G. W. Trucks, H. B. Schlegel, G. E. Scuseria, M. A. Robb, J. R. Cheeseman, J. A. Montgomery, Jr., T. Vreven, K. N. Kudin, J. C. Burant, J. M. Millam, S. S. Iyengar, J. Tomasi, V. Barone, B. Mennucci, M. Cossi, G. Scalmani, N. Rega, G. A. Petersson, H. Nakatsuji, M. Hada, M. Ehara, K. Toyota, R. Fukuda, J. Hasegawa, M. Ishida, T. Nakajima, Y. Honda, O. Kitao, H. Nakai, M. Klene, X. Li, J. E. Knox, H. P. Hratchian, J. B. Cross, V. Bakken, C. Adamo, J. Jaramillo, R. Gomperts, R. E. Stratmann, O. Yazyev, A. J. Austin, R. Cammi, C. Pomelli, J. W. Ochterski, P. Y. Ayala, K. Morokuma, G. A. Voth, P. Salvador, J. J. Dannenberg, V. G. Zakrzewski, S. Dapprich, A. D. Daniels, M. C. Strain, O. Farkas, D. K. Malick, A. D. Rabuck, K. Raghavachari, J. B. Foresman, J. V. Ortiz, Q. Cui, A. G. Baboul, S. Clifford, J. Cioslowski, B. B. Stefanov, G. Liu, A. Liashenko, P. Piskorz, I. Komaromi, R. L. Martin, D. J. Fox, T. Keith, M. A. Al-Laham, C. Y. Peng, A. Nanayakkara, M. Challacombe, P. M. W. Gill, B. Johnson, W. Chen, M. W. Wong, C. Gonzalez, and J. A Pople. Gaussian 03 Revision C. *Gaussian, Inc., Wallingford CT*, 2004.

[155] Thom H. Dunning. Gaussian basis sets for use in correlated molecular calculations. I. The atoms boron through neon and hydrogen. *The Journal of Chemical Physics*, 90(2):1007–1023, 1989.

[156] P. J. Stephens, F. J. Devlin, C. F. Chabalowski, and M. J. Frisch. Ab Initio calculation of vibrational absorption and circular dichroism spectra using density functional force fields. *Journal of Physical Chemistry*®, 98(45):11623–11627, 1994.

[157] Stefan Morscher, Wouter H P Driessen, Jing Claussen, and Neal C. Burton. Semi-quantitative multispectral optoacoustic tomography (MSOT) for volumetric PK imaging of gastric emptying. *Photoacoustics*, 2(3):103–110, 2014.

[158] Alexander Dima, Neal C. Burton, and Vasilis Ntziachristos. Multispectral optoacoustic tomography at 64, 128, and 256 channels. *Journal of biomedical optics*, 19(3):36021, 3 2014.

[159] J. X. Duggan, J. DiCesare, and J. F. Williams. *New Directions in Molecular Luminescence - Investigations on the use of laser dyes as quantum counters for obtaining corrected fluorescence spectra in the near infrared*. ASTM International, Philadelphia, 1983.

[160] J. R. Lakowicz. *Principles of Fluorescence Spectroscopy*. Springer New York, New York, 2006.

[161] James Joseph, Michal R. Tomaszewski, Isabel Quiros-Gonzalez, Judith Weber, Joanna Brunker, and Sarah E. Bohndiek. Evaluation of Precision in Optoacoustic Tomography for Preclinical Imaging in Living Subjects. *Journal of Nuclear Medicine*, 58(5):807–814, 2017.

[162] Eran Elinav, Roni Nowarski, Christoph a Thaiss, Bo Hu, Chengcheng Jin, and Richard a Flavell. Inflammation-induced cancer: crosstalk between tumours, immune cells and microorganisms. *Nature reviews. Cancer*, 13(11):759–71, 2013.

[163] Barry Halliwell, Marie Veronique, Lee Hua, Marie Celement Veronique, and Hua Long Lee. Hydrogen peroxide in the human body. *FEBS Letters*, 486:14–17, 2000.

[164] Fabio Hecht, Juliana M. Cazarin, Carlos Eduardo Lima, Caroline C. Faria, Alvaro Augusto da Costa Leitão, Andrea C.F. Ferreira, Denise P. Carvalho, and Rodrigo S. Fortunato. Redox homeostasis of breast cancer lineages contributes to differential cell death response to exogenous hydrogen peroxide. *Life Sciences*, 158:7–13, 2016.

[165] P. Laudański, J. Swiatecka, O. Kovalchuk, and S. Wołczyński. Expression of GLUT1 gene in breast cancer cell lines MCF-7 and MDA-MB-231. *Ginekol Pol.*, 74(9):782–5, 2003.

[166] Leonardo Venturelli, Silvia Nappini, Michela Bulfoni, Giuseppe Gianfranceschi, Simone Dal Zilio, Giovanna Coceano, Fabio Del Ben, Matteo Turetta, Giacinto Scoles, Lisa Vaccari, Daniela Cesselli, and Dan Cojoc. Glucose is a key driver for GLUT1-mediated nanoparticles internalization in breast cancer cells. *Scientific Reports*, 6:1–14, 2016.

[167] Joy L. Kovar, William Volcheck, Eva Sevick-Muraca, Melanie a. Simpson, and D. Michael Olive. Characterization and performance of a near-infrared 2-deoxyglucose optical imaging agent for mouse cancer models. *Analytical Biochemistry*, 384(2):254–262, 2009.

[168] Denise A. Chan, Patrick D. Sutphin, Phuong Nguyen, Sandra Turcotte, Edwin W. Lai, Alice Banh, Gloria E. Reynolds, Jen Tsan Chi, Jason Wu, David E. Solow-Cordero, Muriel Bonnet, Jack U. Flanagan, Donna M. Bouley, Edward E. Graves, William A.

Denny, Michael P. Hay, and Amato J. Giaccia. Targeting GLUT1 and the Warburg effect in renal cell carcinoma by chemical synthetic lethality. *Science Translational Medicine*, 3(94), 2011.

[169] Patrícia Meireles, Joana Sales-Dias, Carolina M. Andrade, João Mello-Vieira, Liliana Mancio-Silva, J. Pedro Simas, Henry M. Staines, and Miguel Prudêncio. GLUT1-mediated glucose uptake plays a crucial role during Plasmodium hepatic infection. *Cellular Microbiology*, 19(2), 2017.

[170] Eunice E. Lee, Jing Ma, Anastasia Sacharidou, Wentao Mi, Valerie K. Salato, Nam Nguyen, Youxing Jiang, Juan M. Pascual, Paula E. North, Philip W. Shaul, Marcel Mettlen, and Richard C. Wang. A Protein Kinase C Phosphorylation Motif in GLUT1 Affects Glucose Transport and is Mutated in GLUT1 Deficiency Syndrome. *Molecular Cell*, 58(5):845–853, 2014.

[171] Fabrizio D'Anselmi, Maria Grazia Masiello, Alessandra Cucina, Sara Proietti, Simona Dinicola, Alessia Pasqualato, Giulia Ricci, Gabriella Dobrowolny, Angela Catizone, Alessandro Palombo, and Mariano Bizzarri. Microenvironment promotes tumor cell reprogramming in human breast cancer cell lines. *PLoS ONE*, 8(12):1–12, 2013.

[172] G.S. Choudhar, S. Al-harbi, and A Almasan. *Caspase-3 Activation Is a Critical Determinant of Genotoxic Stress-Induced Apoptosis. In: Apoptosis and Cancer. Methods in Molecular Biology*. Humana Press, New York, 1219 edition, 2015.

[173] Peijuan Zhu, Tomoyuki Oey, and Ian A. Blair. Determination of cellular redox status by stable isotope dilution liquid chromatography/mass spectrometry analysis of glutathione and glutathione disulfide. *Rapid Commun. Mass Spectrom*, 22:432–440, 2008.

[174] Thomas Köcher, Peter Pichler, Remco Swart, and Karl Mechtler. Quality control in LC-MS/MS. *Proteomics*, 11(6):1026–1030, 2011.

[175] Ann Van Eeckhaut, Katrien Lanckmans, Sophie Sarre, Ilse Smolders, and Yvette Michotte. Validation of bioanalytical LC-MS/MS assays: Evaluation of matrix effects. *Journal of Chromatography B: Analytical Technologies in the Biomedical and Life Sciences*, 877(23):2198–2207, 2009.

[176] Kerstin N. Timm, Brett W. C. Kennedy, Piotr Dzien, Timothy J. Larkin, Sarah E. Bohndiek, Alan J. Wright, Mikko I. Kettunen, De-En Hu, Michael Williams, Irene Marco-Rius, and Kevin M. Brindle. Assessing Oxidative Stress in Tumors by Measuring the Rate of Hyperpolarized [1- 13 C]Dehydroascorbic Acid Reduction Using 13 C Magnetic Resonance Spectroscopy . *Journal of Biological Chemistry*, 292(5):1737–1748, 2016.

[177] K. Böhme and H. D. Brauer. Generation of Singlet Oxygen from Hydrogen Peroxide Disproportionation Catalyzed by Molybdate Ions. *Inorganic Chemistry*, 31(16):3468–3471, 1992.

[178] Richard G. Zepp, Bruce C. Faust, and Hoigné Jürg. Hydroxyl Radical Formation in Aqueous Reactions (pH 3-8) of Iron(II) with Hydrogen Peroxide: The Photo-Fenton Reaction. *Environmental Science and Technology*, 26(2):313–319, 1992.

[179] P. Workman, E. O. Aboagye, F. Balkwill, A. Balmain, G. Bruder, D. J. Chaplin, J. A. Double, J. Everitt, D. A.H. Farningham, M. J. Glennie, L. R. Kelland, V. Robinson, I. J. Stratford, G. M. Tozer, S. Watson, S. R. Wedge, S. A. Eccles, V. Navaratnam, and S. Ryder. Guidelines for the welfare and use of animals in cancer research. *British Journal of Cancer*, 102(11):1555–1577, 2010.

[180] James Joseph, Michal R. Tomaszewski, Isabel Quiros-Gonzalez, Judith Weber, Joanna Brunker, and Sarah E Bohndiek. Evaluation of Precision in Optoacoustic Tomography for Preclinical Imaging in Living Subjects. *Journal of Nuclear Medicine*, 58(5):807–814, 5 2017.

[181] Adriano Aguzzi and Tracy O'Connor. Protein aggregation diseases: pathogenicity and therapeutic perspectives. *Nature reviews. Drug discovery*, 9(3):237–248, 2010.

[182] Massimo Stefani. Protein misfolding and aggregation: New examples in medicine and biology of the dark side of the protein world. *Biochimica et Biophysica Acta - Molecular Basis of Disease*, 1739(1):5–25, 2004.

[183] Robin Roychaudhuri, Mingfeng Yang, Minako M. Hoshi, and David B. Teplow. Amyloid β-protein assembly and Alzheimer disease. *Journal of Biological Chemistry*, 284(8):4749–4753, 2009.

[184] Vijay Kumar, Neha Sami, Tara Kashav, Asimul Islam, Faizan Ahmad, and Md Imtaiyaz Hassan. Protein aggregation and neurodegenerative diseases: From theory to therapy. *European Journal of Medicinal Chemistry*, 124:1105–1120, 2016.

[185] David Balchin, Manajit Hayer-Hartl, and F. Ulrich Hartl. In vivo aspects of protein folding and quality control. *Science (New York, N.Y.)*, 353(6294):aac4354, 2016.

[186] D. A. Kirschner, C. Abraham, and D. J. Selkoe. X-ray diffraction from intraneuronal paired helical filaments and extraneuronal amyloid fibers in Alzheimer disease indicates cross-beta conformation. *Proceedings of the National Academy of Sciences*, 83(2):503–507, 1986.

[187] Fabrizio Chiti and Christopher M Dobson. Protein Misfolding, Functional Amyloid, and Human Disease. *Annu. Rev. Biochem*, 75:333–66, 2006.

[188] Nunilo Cremades, Samuel I A Cohen, Emma Deas, Andrey Y. Abramov, Allen Y. Chen, Angel Orte, Massimo Sandal, Richard W. Clarke, Paul Dunne, Francesco A. Aprile, Carlos W. Bertoncini, Nicholas W. Wood, Tuomas P J Knowles, Christopher M. Dobson, and David Klenerman. Direct observation of the interconversion of normal and toxic forms of α-synuclein. *Cell*, 149(5):1048–1059, 2012.

[189] Lauren M. Billings, Salvatore Oddo, Kim N. Green, James L. McGaugh, and Frank M. LaFerla. Intraneuronal Aβ causes the onset of early Alzheimer's disease-related cognitive deficits in transgenic mice. *Neuron*, 45(5):675–688, 2005.

[190] Roland Riek and David S. Eisenberg. The activities of amyloids from a structural perspective. *Nature*, 539(7628):227–235, 2016.

[191] Tuomas P J Knowles, Michele Vendruscolo, and Christopher M Dobson. The amyloid state and its association with protein misfolding diseases. *Nature reviews. Molecular cell biology*, 15(6):384–96, 2014.

[192] Alexander J. Howie and Douglas B. Brewer. Optical properties of amyloid stained by Congo red: History and mechanisms. *Micron*, 40(3):285–301, 2009.

[193] Therése Klingstedt, Andreas Åslund, Rozalyn A. Simon, Leif B.G. Johansson, Jeffrey J. Mason, Sofie Nyström, Per Hammarström, and K. Peter R. Nilsson. Synthesis of a library of oligothiophenes and their utilization as fluorescent ligands for spectral assignment of protein aggregates. *Organic and Biomolecular Chemistry*, 9(24):8356–8370, 2011.

[194] Alexander J. Howie, Douglas B. Brewer, Daniel Howell, and Adrian P. Jones. Physical basis of colors seen in Congo red-stained amyloid in polarized light. *Laboratory Investigation*, 88(3):232–242, 2008.

[195] Rajesh Mishra, Daniel Sjölander, and Per Hammarström. Spectroscopic characterization of diverse amyloid fibrils in vitro by the fluorescent dye Nile red. *Molecular BioSystems*, 7(4):1232–1240, 2011.

[196] Jeppe T. Pedersen and Niels H.H. Heegaard. Analysis of protein aggregation in neurodegenerative disease. *Analytical Chemistry*, 85(9):4215–4227, 2013.

[197] Michelle A. Poirier, Huilin Li, Jed Macosko, Shuowei Cai, Mario Amzel, and Christopher A. Ross. Huntingtin spheroids and protofibrils as precursors in polyglutamine fibrilization. *Journal of Biological Chemistry*, 277(43):41032–41037, 2002.

[198] Barthélemy Demeule, Robert Gurny, and Tudor Arvinte. Detection and characterization of protein aggregates by fluorescence microscopy. *International Journal of Pharmaceutics*, 329(1-2):37–45, 2007.

[199] Milos D. Ikonomovic, William E. Klunk, Eric E. Abrahamson, Chester A. Mathis, Julie C. Price, Nicholas D. Tsopelas, Brian J. Lopresti, Scott Ziolko, Wenzhu Bi, William R. Paljug, Manik L. Debnath, Caroline E. Hope, Barbara A. Isanski, Ronald L. Hamilton, and Steven T. DeKosky. Post-mortem correlates of in vivo PiB-PET amyloid imaging in a typical case of Alzheimer's disease. *Brain*, 131(6):1630–1645, 2008.

[200] Minna Groenning. Binding mode of Thioflavin T and other molecular probes in the context of amyloid fibrils-current status. *Journal of Chemical Biology*, 3(1):1–18, 2010.

[201] Anna I. Sulatskaya, Irina M. Kuznetsova, and Konstantin K. Turoverov. Interaction of thioflavin T with amyloid fibrils: Fluorescence quantum yield of bound dye. *Journal of Physical Chemistry B*, 116(8):2538–2544, 2012.

[202] Christine Xue, Tiffany Yuwen Lin, Dennis Chang, and Zhefeng Guo. Thioflavin T as an amyloid dye: Fibril quantification, optimal concentration and effect on aggregation. *Royal Society Open Science*, 4(1), 2017.

[203] Matthew Biancalana and Shohei Koide. Molecular mechanism of Thioflavin-T binding to amyloid fibrils. *Biochimica et Biophysica Acta - Proteins and Proteomics*, 1804(7):1405–1412, 2010.

[204] Vitali I. Stsiapura, Alexander A. Maskevich, Sergey A. Tikhomirov, and Oleg V. Buganov. Charge transfer process determines ultrafast excited state deactivation of thioflavin T in low-viscosity solvents. *Journal of Physical Chemistry A*, 114(32):8345–8350, 2010.

[205] Wojciech Dzwolak and Magdalena Pecul. Chiral bias of amyloid fibrils revealed by the twisted conformation of Thioflavin T: An induced circular dichroism/DFT study. *FEBS Letters*, 579(29):6601–6603, 2005.

[206] Vitali I. Stsiapura, Alexander A. Maskevich, Valery A. Kuzmitsky, Konstantin K. Turoverov, and Irina M. Kuznetsova. Computational study of thioflavin T torsional relaxation in the excited state. *Journal of Physical Chemistry A*, 111(22):4829–4835, 2007.

[207] Nadav Amdursky, Yuval Erez, and Dan Huppert. Molecular rotors: What lies behind the high sensitivity of the thioflavin-T fluorescent marker. *Accounts of Chemical Research*, 45(9):1548–1557, 2012.

[208] Anna I. Sulatskaya, Alexander A. Maskevich, Irina M. Kuznetsova, Vladimir N. Uversky, and Konstantin K. Turoverov. Fluorescence quantum yield of thioflavin T in rigid isotropic solution and incorporated into the amyloid fibrils. *PLoS ONE*, 5(10):1–7, 2010.

[209] H. LeVine. Thioflavine T interaction with amyloid β-sheet structures. *Amyloid*, 2(1):1–6, 1995.

[210] M. R H Krebs, E. H C Bromley, and A. M. Donald. The binding of thioflavin-T to amyloid fibrils: Localisation and implications. *Journal of Structural Biology*, 149(1):30–37, 2005.

[211] Chun Wu, Michael T. Bowers, and Joan Emma Shea. On the origin of the stronger binding of PIB over Thioflavin T to protofibrils of the Alzheimer Amyloid-β peptide: A molecular dynamics study. *Biophysical Journal*, 100(5):1316–1324, 2011.

[212] Minna Groenning, Mathias Norrman, James M. Flink, Marco van de Weert, Jens T. Bukrinsky, Gerd Schluckebier, and Sven Frokjaer. Binding mode of Thioflavin T in insulin amyloid fibrils. *Journal of Structural Biology*, 159(3):483–497, 2007.

[213] Harry Levine. Multiple ligand binding sites on Aβ(1-40) fibrils. *Amyloid*, 12(1):5–14, 2005.

[214] Naoto Iwakawa, Daichi Morimoto, Erik Walinda, Yasushi Kawata, Masahiro Shirakawa, and Kenji Sugase. Real-time observation of the interaction between thioflavin T and an amyloid protein by using high-sensitivity Rheo-NMR. *International Journal of Molecular Sciences*, 18(11):1–8, 2017.

[215] Ji-Eun Lee, Jason C. Sang, Margarida Rodrigues, Alexander R. Carr, Mathew H. Horrocks, Suman De, Marie N. Bongiovanni, Patrick Flagmeier, Christopher M. Dobson, David J. Wales, Steven F. Lee, and David Klenerman. Mapping Surface Hydrophobicity of α-Synuclein Oligomers at the Nanoscale. *Nano Letters*, page acs.nanolett.8b02916, 2018.

[216] Mathew H. Horrocks, Steven F. Lee, Sonia Gandhi, Nadia K. Magdalinou, Serene W. Chen, Michael J. Devine, Laura Tosatto, Magnus Kjaergaard, Joseph S. Beckwith, Henrik Zetterberg, Marija Iljina, Nunilo Cremades, Christopher M. Dobson, Nicholas W. Wood, and David Klenerman. Single-Molecule Imaging of Individual Amyloid Protein Aggregates in Human Biofluids. *ACS Chemical Neuroscience*, 7(3):399–406, 2016.

[217] Luoheng Qin, Julian Vastl, and Jianmin Gao. Highly sensitive amyloid detection enabled by thioflavin T dimers. *Molecular bioSystems*, 6:1791–1795, 2010.

[218] Joerg Schnitzbauer, Maximilian T. Strauss, Thomas Schlichthaerle, Florian Schueder, and Ralf Jungmann. Super-resolution microscopy with DNA-PAINT. *Nature Protocols*, 12(6):1198–1228, 2017.

[219] Koichi Wakabayashi, Kunikazu Tanji, Fumiaki Mori, and Hitoshi Takahashi. The Lewy body in Parkinson's disease: Molecules implicated in the formation and degradation of α-synuclein aggregates. *Neuropathology*, 27(5):494–506, 2007.

[220] Jack C.C. Hsu, Eric H.L. Chen, Robert C. Snoeberger, Frederick Y. Luh, T. S. Lim, C. P. Hsu, and Rita P.Y. Chen. Thioflavin T and its photoirradiative derivatives: Exploring their spectroscopic properties in the absence and presence of amyloid fibrils. *Journal of Physical Chemistry B*, 117(13):3459–3468, 2013.

[221] Alexander A. Maskevich, Vitali I. Stsiapura, Valeriy A. Kuzmitsky, Irina M. Kuznetsova, Olga I. Povarova, Vladimir N. Uversky, and Konstantin K. Turoverov. Spectral properties of thioflavin T in solvents with different dielectric properties and in a fibril-incorporated form. *Journal of Proteome Research*, 6(4):1392–1401, 2007.

[222] Gebhard Haberhauer, Rolf Gleiter, and Christoph Burkhart. Planarized Intramolecular Charge Transfer: A Concept for Fluorophores with both Large Stokes Shifts and High Fluorescence Quantum Yields. *Chemistry - A European Journal*, 22(3):971–978, 2016.

[223] C. Cazeau-Dubroca, G. Nouchi, M. Ben Brahim, M. Pesquer, D. Grose, and Ph Cazeau. Dual fluorescence of 4-N,N-dimethylaminopyridine. Role of hydrogen-bonded complex in the ground state. *Journal of Photochemistry and Photobiology, A: Chemistry*, 80(1-3):125–133, 1994.

[224] C. Cazeau-Dubroca, A. Peirigua, M. Ben Brahim, G. Nouchi, and Ph Cazeau. Hydrogen bonding and TICT molecules in ground state. *Proceedings of the Indian Academy of Sciences - Chemical Sciences*, 104(2):209–217, 1992.

[225] Marie N. Bongiovanni, Julien Godet, Mathew H. Horrocks, Laura Tosatto, Alexander R. Carr, David C. Wirthensohn, Rohan T. Ranasinghe, Ji Eun Lee, Aleks Ponjavic, Joelle V. Fritz, Christopher M. Dobson, David Klenerman, and Steven F.

Lee. Multi-dimensional super-resolution imaging enables surface hydrophobicity mapping. *Nature Communications*, 7:1–9, 2016.

[226] A. K. Buell, C. Galvagnion, R. Gaspar, E. Sparr, M. Vendruscolo, T. P. J. Knowles, S. Linse, and C. M. Dobson. Solution conditions determine the relative importance of nucleation and growth processes in -synuclein aggregation. *Proceedings of the National Academy of Sciences*, 111(21):7671–7676, 2014.

[227] P.A. Van der Merwe. Surface plasmon resonance. *Semantic Scholar*, pages 1–50, 2002.

[228] S.G Younkin. The role of Abeta42 in Alzheimer ' s disease. *J Physiology*, 92:289–292, 1998.

[229] Patrick Flagmeier, Suman De, David C. Wirthensohn, Steven F. Lee, Cécile Vincke, Serge Muyldermans, Tuomas P.J. Knowles, Sonia Gandhi, Christopher M. Dobson, and David Klenerman. Ultrasensitive Measurement of Ca2+Influx into Lipid Vesicles Induced by Protein Aggregates. *Angewandte Chemie - International Edition*, 56(27):7750–7754, 2017.

[230] A. Orte, N. R. Birkett, R. W. Clarke, G. L. Devlin, C. M. Dobson, and D. Klenerman. Direct characterization of amyloidogenic oligomers by single-molecule fluorescence. *Proceedings of the National Academy of Sciences*, 105(38):14424–14429, 2008.

[231] Juan A. Varela, Margarida Rodrigues, Suman De, Patrick Flagmeier, Sonia Gandhi, Christopher M. Dobson, David Klenerman, and Steven F. Lee. Optical Structural Analysis of Individual α-Synuclein Oligomers. *Angewandte Chemie - International Edition*, 57(18):4886–4890, 2018.

[232] Julien Duboisset, Patrick Ferrand, Wei He, Xiao Wang, Hervé Rigneault, and Sophie Brasselet. Thioflavine-T and Congo Red reveal the polymorphism of insulin amyloid fibrils when probed by polarization-resolved fluorescence microscopy. *Journal of Physical Chemistry B*, 117(3):784–788, 2013.

[233] O. Coskuner and O. Wise-Scira. Structures of the E46K mutant-type alpha-synuclein protein and impact of E46K mutation on the structures of the wild-type alpha-synuclein protein. *ACS Chem Neurosci*, 4:1101–1113, 2013.

[234] Sander S. Van Berkel, Mark B. Van Eldijk, and Jan C M Van Hest. Staudinger ligation as a method for bioconjugation. *Angewandte Chemie - International Edition*, 50(38):8806–8827, 2011.

[235] Victoria D. Bock, Henk Hiemstra, and Jan H. Van Maarseveen. Cu I-catalyzed alkyne-azide click cycloadditions from a mechanistic and synthetic perspective. *European Journal of Organic Chemistry*, (1):51–68, 2006.

[236] Chester A. Mathis, Yanming Wang, Daniel P. Holt, Guo Feng Huang, Manik L. Debnath, and William E. Klunk. Synthesis and evaluation of 11C-labeled 6-substituted 2-arylbenzothiazoles as amyloid imaging agents. *Journal of Medicinal Chemistry*, 46(13):2740–2754, 2003.

[237] Pawan Kumar, Lynda Truong, Ysobel Ruth Baker, Afaf Helmy El-Sagheer, and Tom Brown. Synthesis, Affinity for Complementary RNA and DNA, and Enzymatic Stability of Triazole-Linked Locked Nucleic Acids (t-LNAs). *ACS Omega*, 3(6):6976–6987, 2018.

[238] Jinfeng Chen, Ysobel R Baker, Asha Brown, Afaf Helmy El-Sagheer, and Tom Brown. Enzyme-free synthesis of cyclic single-stranded DNA constructs containing a single triazole, amide or phosphoramidate backbone linkage and their use as templates for rolling circle amplification and nanoflower formation. *Chemical Science*, pages 8110–8120, 2018.

[239] Benjamin P. Duckworth, Yan Chen, James W. Wollack, Yuk Sham, Joachim D. Mueller, T. Andrew Taton, and Mark D. Distefano. A universal method for the preparation of covalent protein-DNA conjugates for use in creating protein nanostructures. *Angewandte Chemie - International Edition*, 46(46):8819–8822, 2007.

[240] Franck Amblard, Jong Hyun Cho, and Raymond F Schinazi. Cu (I) -Catalyzed Huisgen Azide - Alkyne 1 , 3-Dipolar Cycloaddition Reaction in Nucleoside , Nucleotide , and Oligonucleotide Chemistry. (I):4207–4220, 2009.

[241] Fahmi Himo, Timothy Lovell, Robert Hilgraf, Vsevolod V. Rostovtsev, Louis Noodleman, K. Barry Sharpless, and Valery V. Fokin. Copper(I)-catalyzed synthesis of azoles. DFT study predicts unprecedented reactivity and intermediates. *Journal of the American Chemical Society*, 127(1):210–216, 2005.

[242] John P Wolfe and Stephen L Buchwald. Improved FunctionalGroup Compatibilityin the Palladium- Catalyzed Amination of Aryl Bromides. *Tetrahedron Letters*, 38(36):6359–6362, 1997.

[243] Wolfgang Hoyer, Thomas Antony, Dmitry Cherny, Gudrun Heim, Thomas M Jovin, and Vinod Subramaniam. Dependence of a -Synuclein Aggregate Morphology on Solution Conditions. 2836(02):383–393, 2002.

[244] Dominic M. Walsh, Eva Thulin, Aedín M. Minogue, Niklas Gustavsson, Eric Pang, David B. Teplow, and Sara Linse. A facile method for expression and purification of the Alzheimer's disease-associated amyloid β-peptide. *FEBS Journal*, 276(5):1266–1281, 2009.

[245] Arthur D Edelstein, Mark A Tsuchida, Nenad Amodaj, Henry Pinkard, Ronald D Vale, and Nico Stuurman. Advanced methods of microscope control using μManager software. *Journal of Biological Methods*, 1(2):10, 2014.

[246] Lisa-Maria Needham, Judith Weber, W B Fyfe, Omaru M Kabia, Dung T Do, Yu Zhang, Margarida Rodrigues, Christopher M Dobson, Sonia Ghandi, E Bohndiek, Thomas N Snaddon, and F Lee. Bifunctional fluorescent probes for detection of amyloid aggregates and reactive oxygen species. *R. Soc. open sci.*, 5:171399, 2018.

[247] Aashiq Hussain Bhat, Khalid Bashir Dar, Suhail Anees, Mohammad Afzal Zargar, Akbar Masood, Manzoor Ahmad Sofi, and Showkat Ahmad Ganie. Oxidative stress, mitochondrial dysfunction and neurodegenerative diseases; a mechanistic insight. *Biomedicine and Pharmacotherapy*, 74:101–110, 2015.

[248] Piotr Czarny, Paulina Wigner, Piotr Galecki, and Tomasz Sliwinski. The interplay between inflammation, oxidative stress, DNA damage, DNA repair and mitochondrial dysfunction in depression. *Progress in Neuro-Psychopharmacology and Biological Psychiatry*, (February):0–1, 2017.

[249] Emma Deas, Nunilo Cremades, Plamena R. Angelova, Marthe H.R. Ludtmann, Zhi Yao, Serene Chen, Mathew H. Horrocks, Blerida Banushi, Daniel Little, Michael J. Devine, Paul Gissen, David Klenerman, Christopher M. Dobson, Nicholas W. Wood, Sonia Gandhi, and Andrey Y. Abramov. Alpha-Synuclein Oligomers Interact with Metal Ions to Induce Oxidative Stress and Neuronal Death in Parkinson's Disease. *Antioxidants & Redox Signaling*, 24(7):376–391, 2016.

[250] Mark A. Lovell, William D. Ehmann, Steven M. Butler, and William R. Markesbery. Elevated thiobarbituric acidreactive substances and antioxidant enzyme activity in the brain in Alzheimer's disease. *Neurology*, 45:1594–1601, 1995.

[251] Moon Hee Lee, Dong Hoon Hyun, Barry Halliwell, and Peter Jenner. Effect of overexpression of wild-type and mutant Cu/Zn-superoxide dismutases on oxidative stress and cell death induced by hydrogen peroxide, 4-hydroxynonenal or serum deprivation: Potentiation of injury by ALS-related mutant superoxide dismutases and pro. *Journal of Neurochemistry*, 78(2):209–220, 2001.

[252] Christine C. Winterbourn. The biological chemistry of hydrogen peroxide. *Methods in Enzymology*, 528:3–25, 2013.

[253] Julie K Andersen. Oxidative stress in neurodegeneration: cause or consequence? *Nature Reviews Neuroscience*, 10(7):S18–S25, 2004.

[254] Archana Kumar, Tania Ng, Sushant Malhotra, Jason Gruenhagen, and Larry Wigman. Accurate analysis of boronic pinacol esters using low residual silanol silica based reversed phase HPLC. *Journal of Liquid Chromatography and Related Technologies*, 37(14):1985–1998, 2014.

[255] Jing Xu, D Duran, and Bing Mao. On - Column Hydrolysis Kinetics Determination of Boronic Pinacol Ester Intermediates for Use in Optimization of Fast HPLC Methods On-Column Hydrolysis Kinetics Determination of Boronic Pinacol Ester. 6076(November 2016), 2006.

[256] Barry Halliwell. Oxidative stress and neurodegeneration: Where are we now? *Journal of Neurochemistry*, 97(6):1634–1658, 2006.

[257] Michael P. Murphy. Antioxidants as therapies: Can we improve on nature? *Free Radical Biology and Medicine*, 66:20–23, 2014.

[258] Adrian Taruttis and Vasilis Ntziachristos. Advances in real-time multispectral optoacoustic imaging and its applications. *Nature Photonics*, 9(April):219–227, 2015.

Appendix A

Appendix

A.1 Chapter 2

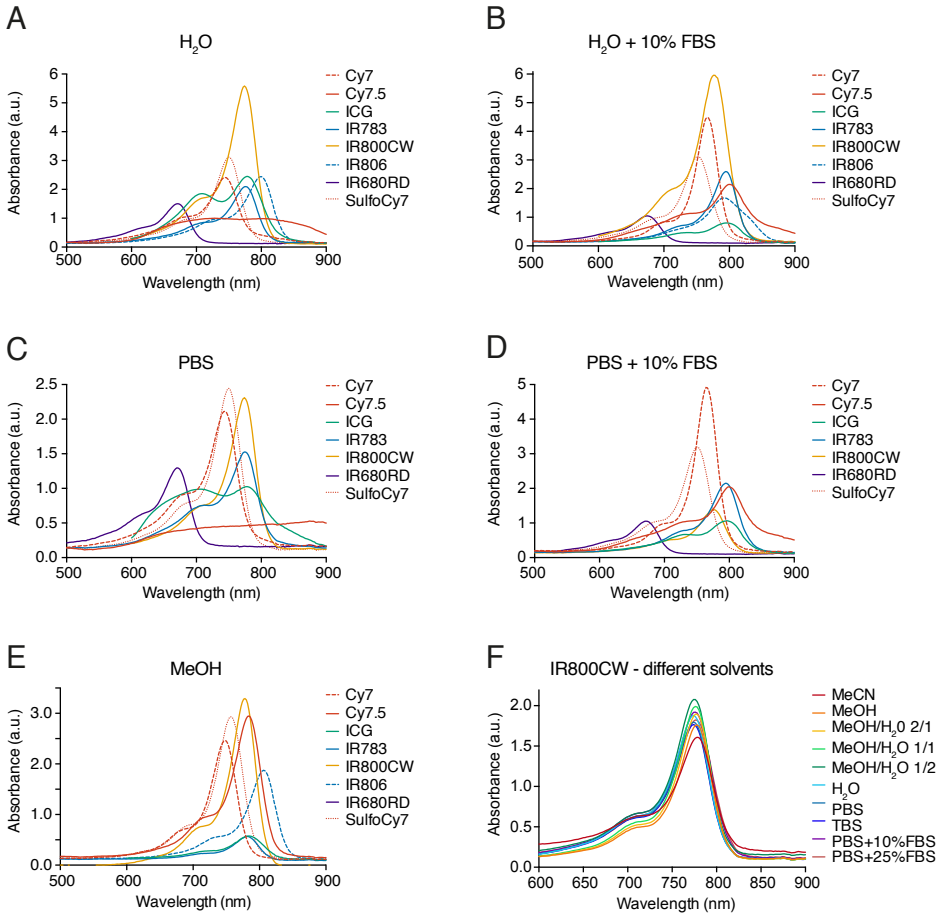

Figure A.1 Representative spectra of commercial cyanine dyes (20 μM) in A) H_2O, B) H_2O + 10%FBS C) PBS, D) PBS + 10%FBS, E) MeOH. D) Spectra of 5 μM IR800CW in different solvents showing that neither ions nor proteins do influence the spectra of sulfo-dyes.

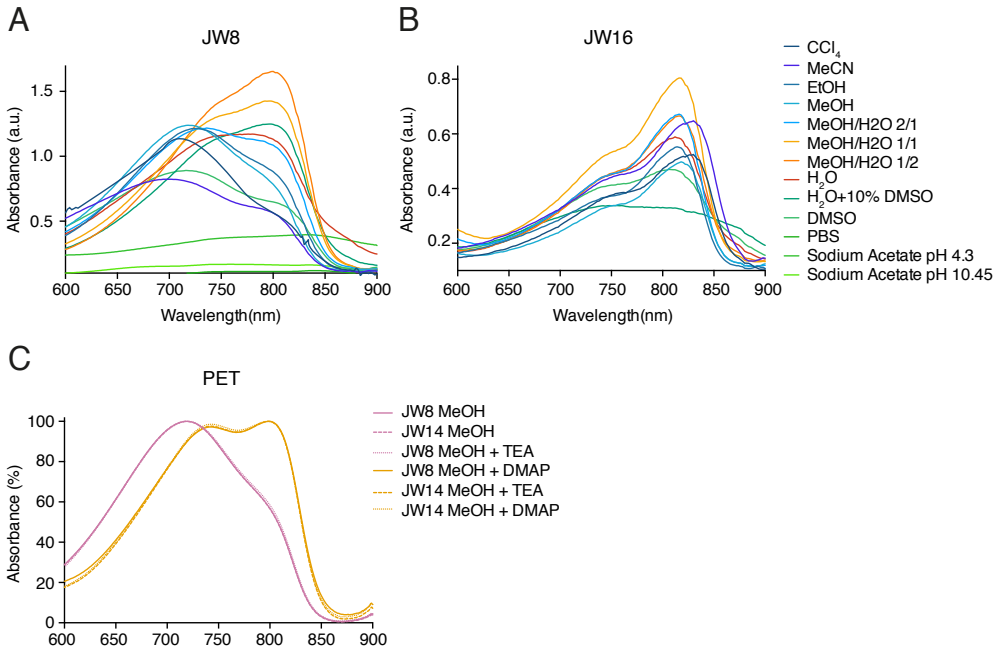

Figure A.2 Representative spectra of the piperazine-linker derivatives, JW8 (A, 20 μM) and JW16 (B, 20 μM), in different solvents. Interestingly, the absorption shape of JW8 changed in the different solvents whereas the absorption spectra of JW16 stayed mostly constant in the solvents, in which JW16 was solvable. The changes in different solvents was questioned with DFT calculations shown in Figure A.3. C) The influence of PET towards the absorption properties is demonstrated for representative absorption spectra of JW8 (5 μM) and JW14 (5 μM) in MeOH, MeOH + TEA (50 μM) and MeOH + DMAP (50 μM). No changes were observed under the different tested conditions.

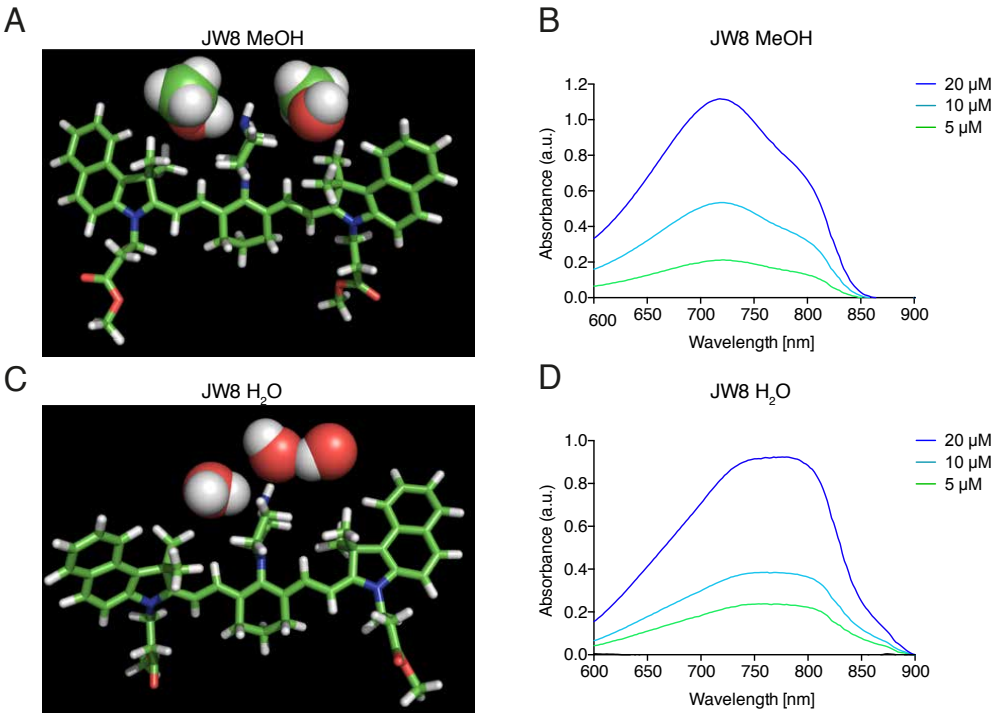

Figure A.3 Computational investigation of the geometrical properties of JW8 in A) MeOH and C) H_2O illustrating how the different solvent molecules are interacting with the amine functionality of the piperazine unit leading to a different twist in the dye backbone structure. This twist can be used to explain the different absorption shapes of JW8 in MeOH (B) and H_2O (C).

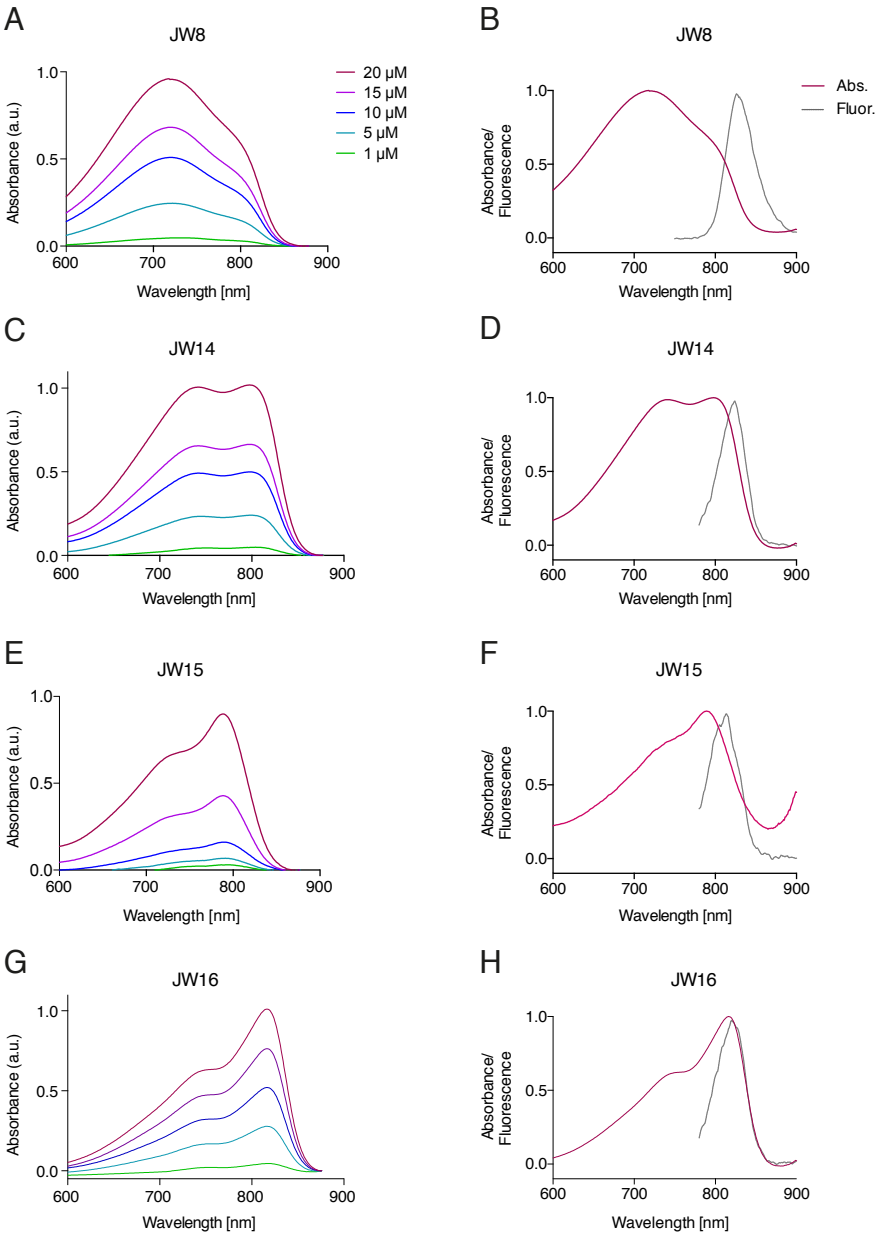

Figure A.4 Representative spectra of the four piperazine-linker derivatives, JW8 (A), JW14 (C), JW15 (D), JW16 (E), at different concentrations (20 μM, 15 μM, 10 μM, 5 μM, 1 μM) in MeOH. The corresponding normalised fluorescence and absorption spectra are shown in B), D), F) and H).

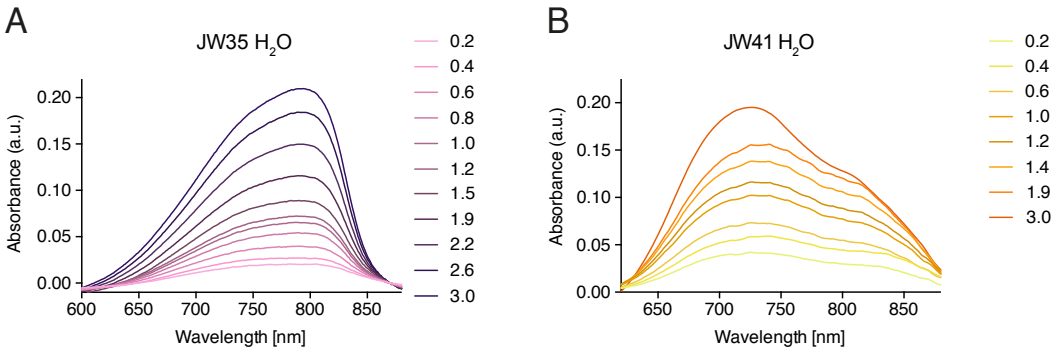

Figure A.5 Representative spectra of JW41 and JW35 in H_2O in different concentrations indicating that the different shapes in their absorption spectra are not concentration and thus aggregation based.

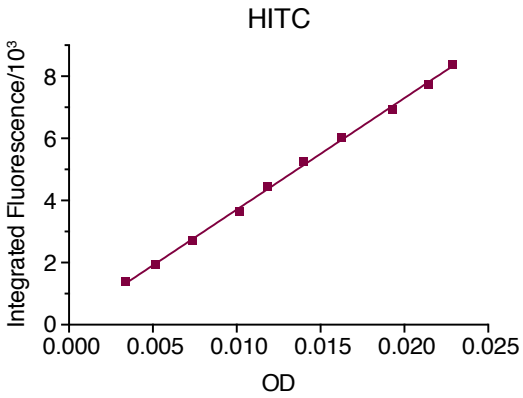

Figure A.6 Calibration curve of fluorescence standard HITC. Linear regression (y=mx + c) resulting in an average slope 3.68 x 10^5.

A.2 Chapter 3

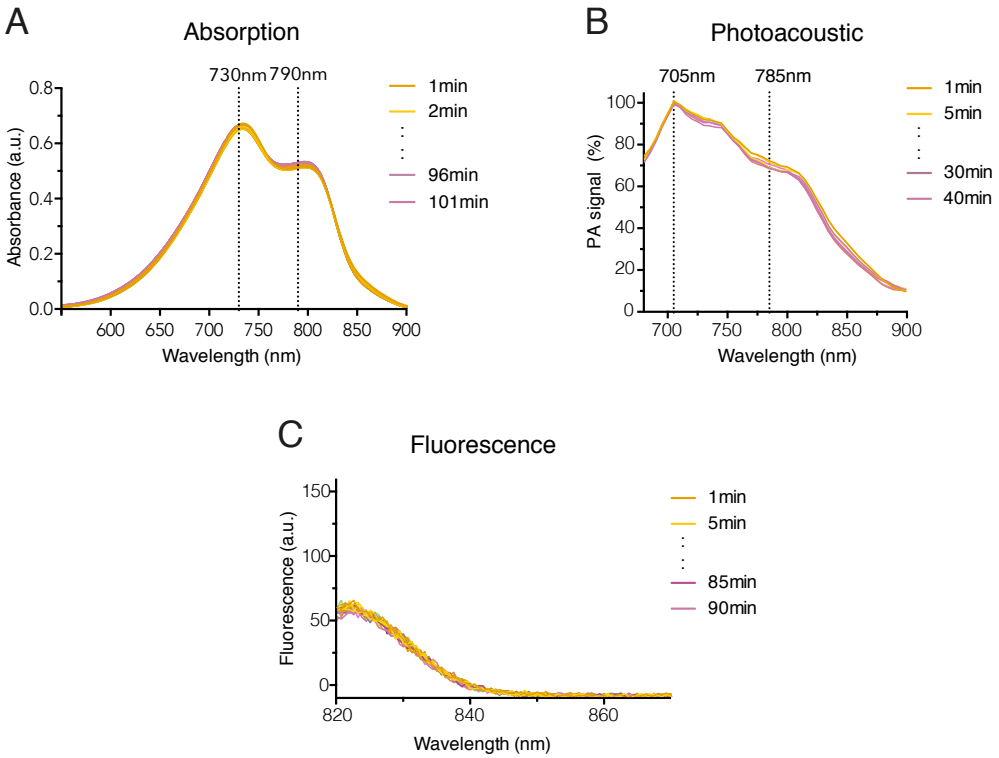

Figure A.7 H_2O_2 reactivity controls: Absorption (A), photoacoustic (B) and fluorescence (C) spectra of JW41 (10 μM) in water monitored over up to 100 min confirming that the partial hydrolysis of JW41 to the hydrolysed boronic acid, $JW41_{hydro}$, does not influence the photophysical properties of the dye.

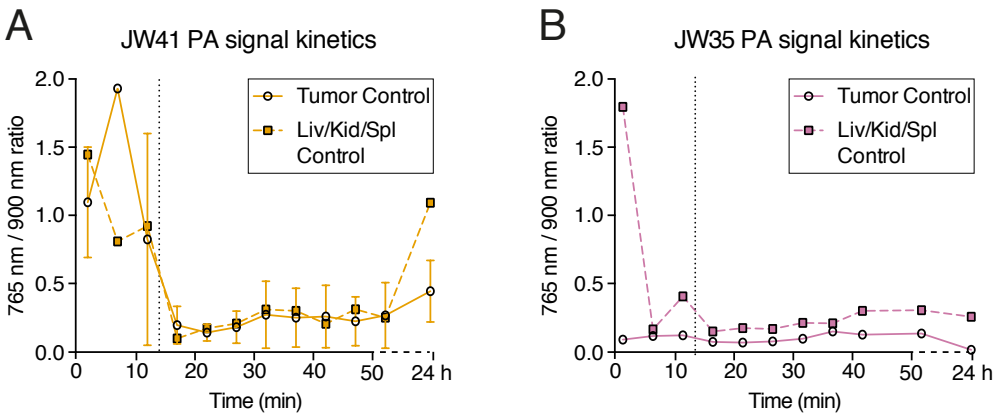

Figure A.8 PA signal kinetics of control regions illustrated in Figure 3.13 and 3.15.

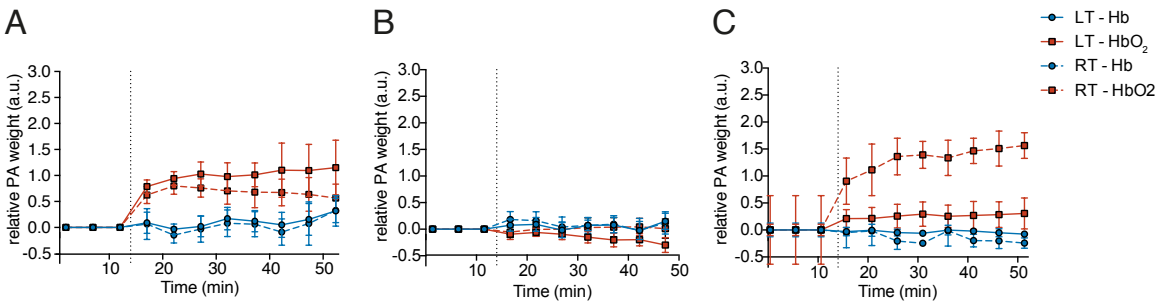

Figure A.9 *In vivo* spectral unmixing of Hb and HbO_2. Representative kinetics curves of the PA weight of Hb and HbO_2 obtained by spectrally unmixing of the outlined tumour ROIs in A) Figure 3.17A, B) Figure 3.17B and C) Figure 3.17C.

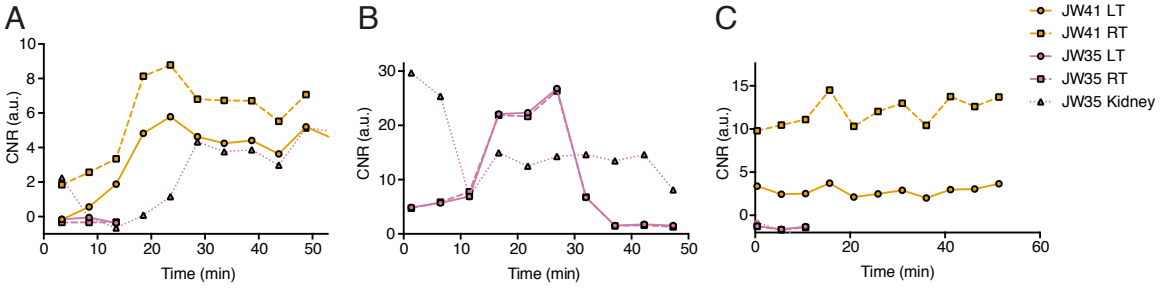

Figure A.10 Contrast to noise (CNR) spectra of the *in vivo* spectra of JW41 and JW35 obtained by spectral unmixing of the outlined tumour and kidney ROIs in A) Figure 3.17A, B) Figure 3.17B and C) Figure 3.17C. The CNR was calculated as follows: CNR = (dye mean signal of the tumour or kidney ROI - dye mean signal of the control ROI) / SD of the dye signal in the control ROI.

A.3 Chapter 4

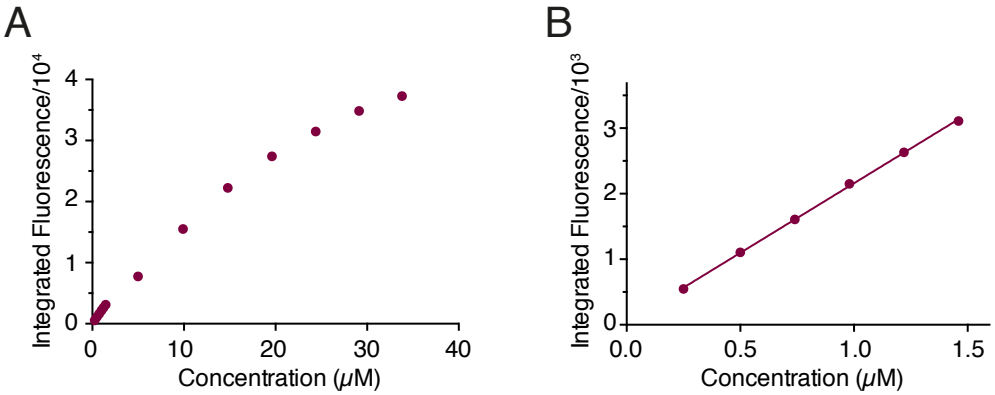

Figure A.11 A) Calibration curve of fluorescence standard quinine sulfate. B) The linear parts of the curves were fitted with linear regression (y=mx + c) resulting in a slope 2.12 x 10^3.

A.4 Chapter 5

	Time point (minutes)	Hydrolyzed Mass ($gmol^{-1}$)	Hydrolyzed Retention Time (minutes)	Hydrolyzed Rel. Area (%)	Boronate ester Mass ($gmol^{-1}$)	Boronate ester Retention Time (minutes)	Boronate ester Rel. Area (%)	Oxidized Mass ($gmol^{-1}$)	Oxidized Retention Time (minutes)	Oxidized Rel. Area (%)
BE01	0	286.26	1.88	65	368.24	3.34	35			
BE01	60	286.18	1.88	47	368.40	3.34	53			
BE01 and 100 µM H_2O_2	60							258.14	2.04	100
BE02	0	286.26	1.88	100						
BE02	60	286.26	1.88	100						
BE02 and 100 µM H_2O_2	60	286.34	1.88	10				258.22	2.04	90
mBE01	0	300.28	0.49	100						
mBE01	60	300.28	0.49	100						
mBE01 and 100 µM H_2O_2	60	300.12	0.49	27				272.24	0.58	64
mBE02	0	300.20	0.49	100						
mBE02	60	300.28	0.49	100						
mBE02 and 100 µM H_2O_2	60	300.28	0.49	12				272.32	0.58	70

	Oxidized, de-methylated			
	Time point (minutes)	Mass (gmol-1)	Retention Time (minutes)	Rel. Area (%)
mBE01 and 100 µM H_2O_2	60	258.22	2.04	9.47
mBE02 and 100 µM H_2O_2	60	258.22	2.04	18.63

Figure A.12 LCMS validation of the reaction of the mBE and BE probes with H_2O_2. Mass: mass detected with LCMS; Rel. Area: relative area under the curve in the UV chromatogram (monitored at 254 nm). Hydrolysed: boronic acid derivative of dye; Boronate ester: dye with boronate ester functionality; Oxidized: phenol derivative of the dye after oxidative cleavage. Oxidized, de-methylated: phenol derivative of the dye after oxidative cleavage and loss of methyl group on Nitrogen.